Experimental study on inertial effects in liquid-solid flows

Thesis by

Esperanza Linares-Guerrero

In Partial Fulfillment of the Requirements

for the Degree of

Doctor of Philosophy

California Institute of Technology

Pasadena, California

2015

(Defended May 6, 2015)

To my family

Dedicado a mi familia

Acknowledgments

My sincerest gratitude to my advisor, Professor Melany Hunt, for her support and guidance throughout my PhD. I deeply appreciate all the freedom that Professor Hunt gave me to conduct this research. Her understanding and encouragement were essential to overcome all the challenges and the many technical difficulties I encountered with the experiments. She has been a constant source of wisdom and perspective. Her critical thinking is something I hope to be able to emulate, and I am truly grateful and fortunate to have had the opportunity to work under her supervision. I also want to thank my former advisor Professor Roberto Zenit for introducing me to the fascinating world of multi-phase flows, and for co-advising me during the last year of my PhD. I am immensely grateful for his amazing sense of humor, wisdom, and talent for teaching fluid mechanics. During my PhD, I had the privilege to discuss my work with Professor Chris Brennen. I am thankful for his mentorship, encouragement and captivating life stories. I would like to acknowledge Professor John Brady and Professor Michael Lamb for serving on my thesis committee and for their helpful suggestions and interest in my research.

I am thankful to the Roberto Rocca Education Program for granting me a full scholarship during my first year at Caltech and continued support throughout my PhD.

Even though for the most part of my PhD I was the only member of my research group, I was fortunate to have arrived at Caltech just in time to be welcomed by the previous members of the granular flows group and to whom I want to thank: Dr. Xiaobai Li, Dr. Nathalie Vriend and Dr. Angel Ruiz-Angulo. Special thanks to Dr. Erin Koos, my predecessor on this project, for her mentorship, immense patience and for introducing me to the apparatus used for these experiments.

I owe a debt of gratitude to Michael Gerfen and John Van Deusen for helping me fix the experimental apparatus and for answering all my technical questions. I also want to thank Corey Campbell and Moisés García for charmingly supplying the materials needed for the experiments and helping me find technical support at Caltech. I would also like to thank Felicia Hunt and Natalie Gilmore in the Dean's office for all their help, support, and understanding.

I was blessed with an amazing group of friends at Caltech. They were not only a source of emotional support, but also a source of talented minds and extra hands whenever I needed them in the lab. I particularly thank my dear friend Andrew Richards for the enormous amount of time

he spent discussing my research and helping me mount and unmount the apparatus. I learned so much from him and got a great ego boost every time I defeated him playing rummikub (which was always). I also want to thank Romelia Salomón for all the advice she gave me on how to navigate the PhD. I am deeply grateful to Indrat Aria, Michio Inoue, Kaway Kwok, Ivan Szelengowicz, Francisco Montero, and Liza Santoso for all the long nights we spent together having fun or doing homework. I want to thank Paloma de la Puente, Alejandro López, Pablo Guerrero, Ludovica Lattanzi, Chengyun Chua, Katrine Hansen, Oziel García and my academic little sister Monica Wilhelmusmtz for getting their hands dirty helping me in the lab and for making me feel so loved.

I want to thank my dear aerialist friends Libby Schultz, Lisa Nghe and Natalie Becerra for helping me indirectly to stay motivated and gather the needed energy for the completion of my PhD by facilitating me with the beautiful distraction of aerial silks.

Finally, I want to thank my family. The visualizations presented in Chapter 6 were done with the help of my father. I wouldn't be here if it weren't for the constant support of my mother to whom I am deeply grateful. I also want to thank my brother and sister for cheering me up whenever it was needed. Special thanks to all my fabulous aunts for believing in me and encouraging me to pursue my dreams. *Gracias papá por visitarme y ayudarme con los experimentos. Fue todo un placer trabajar contigo, hacemos un gran equipo. Gracias mamá por siempre estar a mi lado aún en la distancia y por ser mi principal fuente de apoyo, inspiración y apapachos. A todas mis tías por ser tan lindas y motivarme a seguir mis sueños. No lo hubiese logrado sin todo su apoyo y amor. Les estaré eternamente agradecida.*

Abstract

This thesis presents experimental measurements of the rheological behavior of liquid-solid mixtures at moderate Reynolds (defined by the shear rate and particle diameter) and Stokes numbers, ranging from $3 \leq Re \leq 1.6 \times 10^3$ and $0.4 \leq St \leq 195$. The experiments use a specifically designed Couette cylindrical rheometer that allows for probing the transition from transporting a pure liquid to transporting a dense suspension of particles. Measurements of the shear stress are presented for a wide range of particle concentration (10 to 60% in volume) and for particle to fluid density ratio (ρ_p/ρ) between 1 and 1.05. The effective relative viscosity exhibits a strong dependence on the solid fraction for all density ratios tested. For $\rho_p/\rho = 1$ the effective viscosity increases with Stokes number (St) for volume fractions (ϕ) lower than 40% and becomes constant for higher ϕ. When the particles are denser than the liquid, the effective viscosity shows a stronger dependance on St. An analysis of the particle resuspension for the case with $\rho_p/\rho = 1.05$ is presented and used to predict the local volume fraction where the shear stress measurements take place. When the local volume fraction is considered, the effective viscosity for settling and no settling particles is consistent, indicating that the effective viscosity is independent of differences in density between the solid and liquid phase. Shear stress measurements of pure fluids (no particles) were performed using the same rheometer, and a deviation from laminar behavior is observed for gap Reynolds numbers above 4000, indicating the presence of hydrodynamic instabilities associated with the rotation of the outer cylinder. The increase on the effective viscosity with Stokes numbers observed for mixtures with $\phi \leq 30\%$ appears to be affected by such hydrodynamic instabilities. The effective viscosity for the current experiments is considerably higher than the one reported in non-inertial suspensions.

Experiment - where theory comes to die

-Sidney R. Nagel

Contents

[1] Some of the material that is summarized in this section is taken from a paper by Koos, Linares-Guerrero, Hunt, and Brennen (2012)

List of Tables

List of Figures

List of Symbols

$\bar{\phi}$	Loading volume fraction
δ	Depletion layer thickness
$\dot{\gamma}$	Shear rate
μ_{app}	Apparent suspension viscosity from smooth wall measurements
μ	Suspending liquid viscosity
μ'	Suspension effective viscosity
μ'^{*}_{min}	Lowest effective viscosity for each volume fraction $\rho_p/\rho = 1.05$
μ'_{min}	Lowest effective viscosity for each volume fraction and $\rho_p/\rho = 1$
ω	Rotational speed
ϕ	Volume fraction
ϕ_m	Maximum volume fraction
ϕ_{RCP}	Random close packing
ϕ_{RLP}	Random loose packing
ψ	Sphericity
ρ	Suspending liquid density
ρ_p	Particle density
τ	Shear stress
b	Shear gap width
d	Particle diameter
H	Height of test cylinder

h	Height reached by particles
h_s	Height of settled particles
h_T	Total annulus height
h_{tm}	Height measured from porous medium surface to annulus top
M	Measured torque
$M_{eff,\,laminar}$	Effective laminar torque based on effective viscosity, $M_{eff,\,laminar} = 2\pi r_i^2 H \dot{\gamma} \mu'_{min}$
$M_{laminar}$	Torque from laminar theory, $M_{laminar} = 4\pi\mu H\omega r_i^2 r_o^2/(r_o^2 - r_i^2)$
Pe	Péclet number, $Pe = 6\pi\mu d^3\dot{\gamma}/kT$
r_i	Inner cylinder radius
r_o	Outer cylinder radius
Re	Reynolds number based on shear rate and particle diameter, $Re = \rho\dot{\gamma}d^2/\mu$
$Re^*_{b,\,eff}$	Modified effective Reynolds, $Re^*_{b,\,eff} = \rho\omega b/\mu'^*_{min}$
Re^*_b	Modified gap Reynolds number based on rotational speed, $Re^*_b = \rho r_o \omega b/\mu$
Re_b	Gap Reynolds number based on shear rate, $Re_b = \rho\dot{\gamma}b^2/\mu$
$Re_{b,\,eff}$	Effective Reynolds number, $Re_{b,\,eff} = \rho\omega r_o b/\mu'$
Sc	Schmidt number, $Sc = Pe/Re$
St	Stokes number, $St = \rho_p Re/9\rho$
V_p	Volume of particles

Chapter 1

Introduction

Granular materials and their suspension in liquids are prevalent in a wide range of natural and man-made processes. These include the industrial handling of seeds and slurries, clogging of drilling wells, and geological phenomena such as landslides and debris flows. Because of the complexity of having more than one phase (the solid and the fluid one), most of the understanding of how these materials flow is based on empirical observations, hampering, for example, the design of efficient transport of a suspension of solids in a fluid medium. Therefore the goal of this research is to help develop constitutive models that predict how liquid-solid mixtures behave when sheared as a function of various physical parameters, using carefully controlled experiments to validate and refine such models. The work presented in this thesis focuses on liquid-solid mixtures, and unlike the mechanics of dry granular material flows which are dominated by collisions and friction, the mechanics for these mixtures involve the interaction between the solid particles, the inertial effects from both liquid and solid phase, and viscous effects of the liquid. In particular, the effects of particle concentration and the density ratio between the two phases are studied under shear conditions where particle collisions might become important. A review of previous rheological experiments and the key parameters that govern the behavior of liquid-solid mixtures is presented.

1.1 Rheology of non-inertial suspensions

There is an extensive work done in the rheology of suspensions; however, most of these studies cover mixtures with low Reynolds number (Re) (from 10^{-6} to 10^{-3}), where Re is defined as $Re = \rho\dot{\gamma}d^2/\mu$, ρ and μ are the density and dynamic viscosity of the suspending liquid, $\dot{\gamma}$, is the shear rate and d is the particle diameter. Rutgers (1962) and Barnes (1989) did a summary of earlier studies where emphasis was made on the relationship between the particle concentration and the effective relative viscosity (μ'). The latter is defined as the proportionally function between the shear stress (τ) and

shear rate of the mixture assuming that the mixture is Newtonian,

$$\tau = \mu' \dot{\gamma}$$

Rutgers (1962) examined the dependence of the relative viscosity on concentration for rigid spheres of more or less monodisperse character. He observed that with good dispersion, no structure-formation, no adsorption or solvation, and no electrical disturbance, the relation between the relative viscosity and the volume fraction may be independent of sphere size, in the size range of $0.264\mu m$ to $177\mu m$. Three regimes were recognized: (i) a dilute regime for volume fractions (ϕ) less than 0.02, where the relative viscosity (μ'/μ) depends almost linearly on ϕ and the dilute suspension exhibits a Newtonian behavior; (ii) a semi-dilute regime for $\phi \leq 0.25$, where μ'/μ exhibits a higher dependance on the particle concentration but the suspension behavior is still approximately Newtonian; (iii) a concentrated regime for $\phi \geq 0.25$, where μ'/μ increases rapidly with volume fraction and exhibits a shear thinning behavior. These studies cover a range of vanishingly small Re numbers only ($1.2 \times 10^{-6} \leq Re \leq 2 \times 10^{-5}$).

Effective viscosity models

The first person to address theoretically the suspension behavior in the dilute limit was Einstein (1906). Based on the hydrodynamics around a single sphere, Einstein derived the relative viscosity of such dilute suspension:

$$\frac{\mu'}{\mu}(\phi) = 1 + B\phi$$

where B is often referred as Einstein coefficient or 'intrinsic viscosity' and its value has not been validated (Mueller et al., 2010). Numerous expressions have been proposed to extend the range of validity of Einsteins expression to higher concentrations (Cheng and Law, 2003). They are either theoretical expansions or empirical expressions. The theoretical expansions are usually expressed in the form of power series:

$$\frac{\mu'}{\mu}(\phi) = 1 + k_1\phi + k_2\phi^2 + k_3\phi^3 + ...$$

This relation does not hold for volume fractions higher than 0.25 and even for $\phi < 0.25$, the polynomial relationship describe experimental data poorly (Rutgers, 1962; Thomas, 1965; Barnes, 1989; Mueller et al., 2010; Abedian and Kachanov, 2010). One reason for this is that the polynomial relation predicts a finite value of the relative viscosity for solid fractions close to one, which is physically impossible given that the maximum volume fraction for spherical particles of the same diameter is $\phi_m \approx 0.74$ (hexagonally close-packed arrangement). At this high solid fraction the relative viscosity must be infinite. For particles that are randomly distributed, the densest packing (random close packing) obtained is lower. Experimentally, the value of the random close packing ranges between

0.627 and 0.64 (Scott, 1960; Haughey and Beveridge, 1966; Scott and Kilgour, 1969); numerically, ϕ_m has been reported to be between 0.61 and 0.648 (Finney, 1970; Bennett, 1972; LeFevre, 1973; Torquato et al., 2000; O'Hern et al., 2002). Physically, ϕ_m represents the limiting fraction above which flow is no longer possible. However, higher packing is observed for particles that had been sheared (Rutgers, 1962; Tsai and Gollub, 2004). This suggests that shearing imposes additional structure to the particles distribution, and for high shear rates the particles are at volume fractions higher than the ϕ_m found for zero and moderate shear rates (der Werff and de Kruif, 1989). The model that best fits the experimental data for non-Brownian suspensions at higher solid fractions includes ϕ_m as a parameter. Considering a suspension with uniformly distributed particles, Krieger and Dougherty (1959) expanded Einstein's equation to higher concentration. Their equation relates the relative viscosity with ϕ_m as follows:

$$\frac{\mu'}{\mu}(\phi) = \left(1 - \frac{\phi}{\phi_m}\right)^{-C\phi_m}.$$

This equation tends to Einstein's equation when ϕ tends to zero and it has been used widely to fit experimental data (Jeffrey and Acrivos, 1976; Pabst, 2004; Pabst et al., 2006; Mueller et al., 2010), where C and ϕ_m are used as fitting parameters. Different theoretical and empirical correlations for the relative viscosity have been proposed with the same functional form as the Krieger-Dougherty equation (Maron and Pierce, 1956; Jeffrey and Acrivos, 1976; Quemada, 1977; Leighton and Acrivos, 1987a,b) .

Zarraga et al. (1999) studied the total stress of concentrated non-Brownian suspensions of spheres (43 μm glass beads) in Newtonian fluids. Using three different geometries (rotating rod, parallel plate, and cone and plate measurements), they measured the relative viscosity and proposed an empirical model in the form of Krieger-Dougherty equation:

$$\frac{\mu'}{\mu}(\phi) = \frac{\exp(-2.34\phi)}{\left(1 - \frac{\phi}{\phi_m}\right)^3},$$

where $\phi_m = 62\%$ for the particles used in their experiments. Their empirical model is in good agreement with other non-Brownian suspensions (Acrivos et al., 1993; Ovarlez et al., 2006; Bonnoit et al., 2010) for a Reynolds number range of 1×10^{-6} to 3×10^{-2}. Similarly, exponential formulas for computing the relative viscosity of the form

$$\frac{\mu'}{\mu}(\phi) = exp\Big(\frac{D\phi}{1 - \phi/\phi_m}\Big)$$

have been developed both theoretically and empirically, where D and ϕ_m are used as fitting parameters(Vand, 1948; Mooney, 1951; Cheng and Law, 2003).

All of these formulations are done under the assumption that the effective viscosity of the suspension is only a function of particle concentration. Other approaches on how to deal with the shear viscosity on concentrated suspensions include energy dissipation in the space between particles (Frankel and Acrivos, 1967; Hoffmnn and Kevelam, 1999), and the re-organization of particles in plane sheets that move one on top of another (Hoffmann, 1972).

Non-Newtonian behavior for concentrated non-inertial suspensions

Non-Newtonian behaviors had been observed in semi-dilute and concentrated suspensions at low Reynolds number. The shear thickening behavior was well reviewed by Barnes (1989) and it was found that there is a wide variety of suspensions that show a shear thickening behavior. Barnes' observations suggest that given the right circumstances, *all* suspensions of solid particles will show the phenomenon. Nevertheless, Barnes' review only covered particle size smaller than $100\mu m$, where the Brownian motion is present (Stickel and Powell, 2005). Evidence of the presence of a yield stress and shear-thinning behavior has also been extensively reported (Rutgers, 1962; Acrivos et al., 1994). Acrivos et al. (1994) studied the quasi-static regime of a suspension of rigid, non-colloidal particles immersed in a Newtonian fluid. They found a shear thinning behavior even for values of the solid fraction as low as 0.20. They explained such observations by means of particle distributions, which occurred due to a slight mismatch in the densities of the two phases.

Heymann et al. (2002) found the presence of a yield stress that was not single value for high volume fractions. This suggested that at high concentrations there is an elasto-viscous region where the particles form a network that deforms elastically at low shear rates and breaks up when the yield stress is reached.

Another factor that can influence the behavior of the suspension is Brownian motion: irregular motion of particles suspending in a fluid due to their colliding, thermally excited atoms and molecules. At room temperature and when particles are smaller than 100 μm, Brownian motion is present. The presence of Brownian motion is dictated by the Péclet number (Pe), which relates the rate of advection of a flow to its thermal diffusion and is defined as:

$$Pe = \frac{6\pi\mu d^3\dot{\gamma}}{kT},$$

where k is the Boltzmann constant and T is the absolute temperature. Suspensions with $Pe > 10^3$ are considered non-Brownian (Stickel and Powell, 2005). The present work deals with liquid-solid mixtures with Péclet numbers higher than 10^{10} where the effects from Brownian motion are negligible.

1.2 Rheology of inertial suspensions

The studies described in Section 1.1 were done in the limit of zero Reynolds number. Most of the work done on suspensions are often done in this limit (Brady and Bossis, 1988; Ladd, 1994; Zarraga et al., 1999; Brady, 2001; Sierou and Brady, 2002; Brady et al., 2006). Non-inertial suspensions represent one extreme of the studies of particulate flows. On the other extreme are studies of granular flows, which, unlike non-inertial suspensions where the particle inertia is negligible and the mechanics of the flow are dominated by hydrodynamic forces, the momentum transfer in granular flows is governed by particle collisions, and the interstitial fluid interaction with the particles is generally assumed to be negligible. Studies of granular flows have also been done extensively (Forterre and Pouliquen (2008) presents a review on such studies). However, there are fewer studies between these two extremes where both the inertia of one or both phases and the viscous effects of the fluid are important.

Stickel and Powell (2005) summarized the different types of non-Newtonian behavior observed in suspensions in terms of the effects of Brownian motion and the effects of inertia. Stickel and Powell (2005) considered that at steady state, the viscosity of a suspension is a function of 5 dimensionless numbers:

$$\frac{\mu'}{\mu} = f(\phi, Pe, Re, St, Ar),$$

where St is the Stokes number defined as:

$$St = \frac{1}{9}\frac{\rho_p}{\rho_f}Re,$$

and Ar is the Archimedes number which describes the ratio of gravitational forces to viscous forces and it is defined as:

$$Ar = \frac{gd^3\rho|\rho_p - \rho|}{\mu^2}.$$

Based on dimensionless analysis, Stickel and Powell (2005) constructed a "phase diagram", where the suspension may be expected to behave as a Newtonian fluid for large ranges of Pe and vanishingly small Re number, shear thickening for large Pe and Re, and shear thinning for both Pe and Re vanishingly small, as depicted in Figure 1.1. For non-Brownian systems (Pe$\rightarrow \infty$) the Peclet number can be neglected; therefore, the relative viscosity is a function of only the volume fraction, Archimedes, Stokes and Reynolds number ($\mu'/\mu = f(\phi, Re, St, Ar)$). For systems where the density of the two phases match, and considering a steady-state, the density ratio can be neglected and consequently so can the Stokes and Archimedes number. In the regime of $Re \ll 10^{-3}$ and $Pe \gg 10^3$, the dependance on the Reynolds and Peclet number can be neglected (Chang and Powell, 2002; Probstein et al., 1994; Shapiro and Probstein, 1992). The limits for this regime are determined by the Schmidt number, $Sc = \frac{Pe}{Re}$. As shown in Figure 1.1, the suspension is expected to be Newtonian

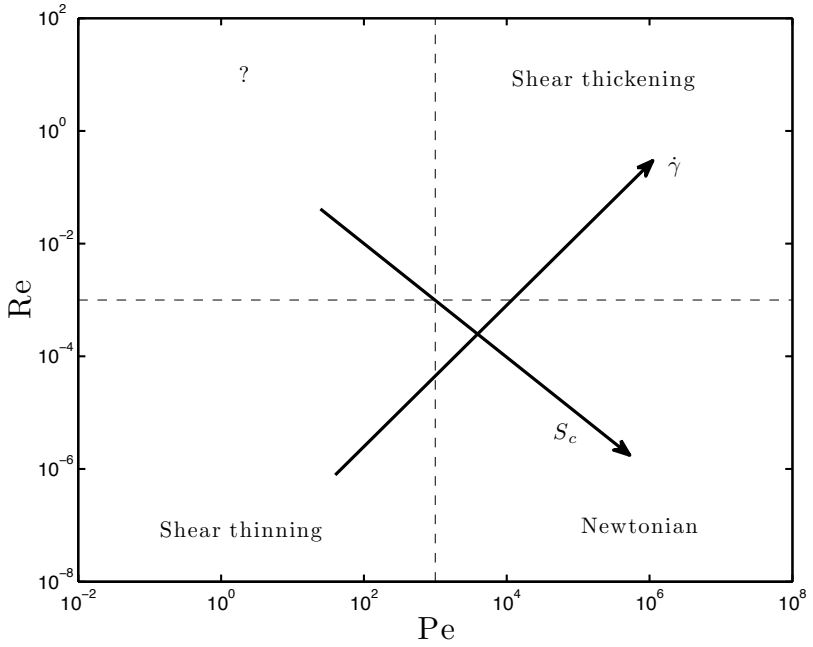

Figure 1.1: Flow pattern for suspension rheology, based solely on a dimensional analysis. Diagram from Stickel and Powell (2005).

for a certain range of shear rates and diminishing Schmidt number (Stickel and Powell, 2005). Under these conditions the relative viscosity of the suspension depends solely on the volume fraction,

$$\frac{\mu'}{\mu_f} = f(\phi).$$

Therefore, at a constant particle concentration, the suspension is expected to exhibit a constant relative viscosity and hence a Newtonian behavior. However, the effective viscosity of the suspension cannot be a function of the volume fraction alone. From the mixture theory viewpoint, the effective properties of the suspension depends on all the details of the microstructure and the particle concentration is not the only microstructure measure. Parameters like particle size distribution, temperature, porosity, etc. would determine the effective viscosity (Pabst, 2004). The extent of inertial effects is dictated by the Reynolds number. Stickel and Powell (2005) suggests that the shear thickening behavior observed in the review of Barnes (1989) and Hoffmann (1972) is due to such effects and considers that for $Re > 10^{-3}$, the inertial effects become important. The reason why shear thickening is linked to inertial effects is because when inertial effects are present, the interactions between particles increase and this changes the mechanism in which the momentum is transferred. The change in momentum due to collisions and the frequency of those collisions is proportional to the relative velocity of the particles, giving rise to stresses that depend on the square of the shear rate. However, the regime where this occurs is still not well established because it is difficult, as shown in the next section, to make direct comparisons between experiments.

In the following section, a description of the previous studies concerning suspensions with non-Brownian particles and Reynolds number higher than 1×10^{-3} is presented. The range of experimental parameters for the current study and those earlier studies are summarized in table 1.1.

Previous experiments [1]

As summarized by Koos et al. (2012), one of the earliest and most extensive experiments dealing with flows with Reynolds number greater than one was performed by Bagnold (1954). He used a small Couette flow rheometer with the inner cylinder fixed and the outer cylinder rotating. The top and bottom end caps were also rotating. Using this device he measured the shear and normal stresses for suspensions with a density ratio between the liquid and solid phase equal to one, over a range of shear rates and particle concentrations. He identified two flow regimes: (i) macro-viscous, where the suspension behaves like a Newtonian fluid and is considered non-collisional; and (ii) grain-inertia, where the interstitial fluid plays a minor role and the main contributions to the stresses are attributed to inter-particle friction and collisions.

The macro-viscous regime was found at low shear rates and the tangential stresses were linearly proportional to the dynamic viscosity of the liquid, the shear rate, and a function of solid fraction:

$$\tau \approx \mu\dot{\gamma} f_1(\phi).$$

The grain-inertia regime occurred at larger shear rates, similar to the results found for highly concentrated non-inertial suspensions, the stresses were independent of fluid viscosity and depended on the square of the shear rate, the square of the particle diameter, the particle density, and displayed a stronger dependence on the solid fraction:

$$\tau \approx {\rho_p}^2 d^2 \dot{\gamma}^2 f_2(\phi).$$

Bagnold distinguished the two regimes by defining a parameter, N, from the ratio of the scaling of the stresses,

$$N = \frac{\rho_p d^2 \dot{\gamma}^2 f_1(\phi)}{(\mu\dot{\gamma} f_2(\phi))} = \rho_p d^2 \dot{\gamma} g(\phi)/\mu,$$

where $g(\phi)$ is a function that increases with solid fraction. The parameter, N, has been referred to as the Bagnold number, and according to Bagnold $N \approx 450$ marked the transition from the viscous regime to the inertial regime. Zeininger and Brennen (1985) found a similar transitional Bagnold number for their hopper flows experiments. However, it is important to note that Bagnold's experiments involved neutrally buoyant particles so that the fluid and solid densities matched, $\rho_f =$

[1] Some of the material that is summarized in this section is taken from a paper by Koos, Linares-Guerrero, Hunt, and Brennen (2012)

ρ_p. In addition, Bagnold used only 1mm deformable wax beads. Hence, in these experiments only the shear rate and the fluid viscosities were varied; the density and the particle size were fixed.

Savage and McKeown (1983) tried to replicate Bagnold's experiments using a concentric cylinder rheometer. Their experimental setup differed from the one used by Bagnold. The flow was sheared by the rotation of the inner cylinder instead of the outer cylinder. Using a neutrally-buoyant liquid-solid suspension, they varied the particle size from 1 to 2 mm diameter and the roughness of the driving surfaces. They found higher shear stresses than Bagnold and although they found that shear stress varied with the square of the shear rate, they did not find a dependence on the square of the particle diameter. They concluded that the shear cells as well as the particles were sufficiently different from those used by Bagnold that direct comparisons cannot be made, even though the apparatus was just 3 cm higher and had a shear gap 6 millimeters wider than the one used by Bagnold. As it is discussed later in Section 1.3, rotating the inner cylinder is known to destabilize secondary flows (Mullin and Benjamin, 1980; Andereck et al., 1986; Conway et al., 2004). Hence, the work of Savage and McKeon suggested that the flow was governed not only by the length scale of the particles but also by the scale of the experimental apparatus.

One of the challenges that is encountered with inertial suspensions is that the experimental design may influence the measurements of the stresses. For example, in a flow with rotation, the radial inertia can induce a radial velocity within the flow (Taylor, 1936a,b). At low Reynolds number, the viscosity can suppress this radial motion, but as the Reynolds number increases, secondary flows, often referred to as Taylor vortices, may change the character of the flow field from a simple shear flow; this change in flow character can affect the measurement of the stresses. Hunt et al. (2002) made a detailed analysis of Bagnold's work and demonstrated that his experimental results were marred by the presence of secondary flows that developed at the boundaries of the rheometric device. By accounting for the contribution of the vortices to the shear stress, Hunt *et al.* demonstrated that Bagnold's linear to quadratic transition could be explained by assuming a laminar Newtonian flow with an effective viscosity that depended on the solid concentration. The presence of shear thickening can often be attributed to the improper design of the experiment, that is, machine artifacts mistaken for shear thickening. These phenomena could explain the results which otherwise show no relationship to other data in the literature, and does not dismiss the shear thickening behavior of concentrated suspensions.

Other experiments involving particles that are unaffected by Brownian motion have been done later are the ones done by Hanes and Inman (1985). They used glass spheres and water as the interstitial fluid in their rheological measurements ($\rho_p/\rho = 2.48$). They used an annular configuration where the sides and bottom rotated. The top did not rotate and was allowed to displace upwards in response to the normal stress generated by the mixture. They examined a narrow range of volume fractions between 0.49 and 0.58. The experiments used glass beads of two sizes in both water and air.

The particles used were denser than the surrounding fluid. The shearing surfaces were roughened by cementing one to two grain layers of the particles. According to the authors, the rotational speeds and applied normal stresses used in these experiments were selected to ensure that the centrifugal stress was always much less than the normal stress. The secondary flows were small compared with the primary flow and did not affect the stress measurements (Hanes and Inman, 1985). The shear stress was measured on the top wall. Their flow curves show slopes between 1 and 2, suggesting that the flow studied was in a transition regime. They observed the formation of a layer of static particles above which the granular material deformed rapidly. The presence of this layer suggests that the nature of the boundaries can have a significant effect upon the dynamics of the entire flow. In all of their experiments, the stresses were found to be weakly dependent on the volume concentration up to approximately 0.5, and strongly dependent above this concentration.

Similar to the work done by Acrivos et al. (1994), but with much larger particles ($d = 3.175$ mm vs $d = 0.14$ mm used by Acrivos *et al.*), Prasad and Kytömaa (1995) studied the transition between the quasi-static and the viscous regimes of dense particle suspension. They measured the effective viscosity of acrylic particles in an aqueous glycerine mixture ($\rho_p/\rho_f = 1.12$). In this study, only high solid fractions ($0.493 \leq \phi \leq 0.561$) were considered. They used an annular gap where the bottom was allowed to rotate and the top and sides remained fix. The stress measurements were made on the top surface. The upper and bottom walls were rough with a roughness scale of the order of the particle diameter. Their results show no evidence of secondary flows present ($9.3 \leq Re_b \leq 328$). Their device allowed them to conduct two kinds of experiments: constant normal stress and constant volume fraction. The first kind revealed that the maximum packing fraction (ϕ_m), defined as that solid fraction at which the mixture cannot be sheared, is not constant and increases with the normal stress, reaching a maximum with the shear rate. This observation was also done by Rutgers (1962) and later by Tsai and Gollub (2004). For the constant volume fraction experiments they found a shear thinning behavior for volume fractions above 0.543, and a Newtonian behavior for the set of runs below that value. Finally, they studied the influence of fluid viscosity by conducting experiments with a fluid viscosity one order of magnitude lower than that used in the earliest experiments. They did not find differences in their results, which is somewhat counterintuitive since the overall viscosity of the suspension is almost a direct function of the continuous phase viscosity.

In the recent years, a number of studies have attempted to unify the rheology of suspensions with the rheology of dry granular flows. However, such efforts have been limited to dense suspensions, where the volume fraction is higher than 50 %. Therefore, the link found between the two rheologies deals with the transition from friction dominated flow at low shear rates to viscous dominated at higher shear rates, rather than the transition from viscous dominated to inertia dominated flows. A summary of the studies regarding dense non-Brownian suspensions with moderate Reynolds number is presented below.

In a suspension with perfectly matched densities and volume fractions close to the random close packing, a presence of yield stress is expected to occur provided that normal stress is applied (Coussot and Ancey, 1999; Prasad and Kytömaa, 1995; Huang et al., 2005). However, the presence of yield stress has been observed in volume fractions looser than the random close packing. Fall et al. (2009) showed that the presence of yield stress in volume fractions lower than the random close packing is due to a density mismatch between the fluid and the solid particles. By carefully matching the two phase densities, rheological measurements on non-Brownian suspensions were performed using 40 μm in diameter polystyrene particles suspended in a NaI solution. They studied the effect of a slight density difference ($\Delta\rho = 0.15 g/cm^3$) and found that when the particles are perfectly buoyant, there is no presence of yield stress until volume fractions of 62%. Using magnetic resonance imaging in a wide-gap Couette geometry, they observed no presence of shear banding in suspensions with matched density, but for $\Delta\rho = 0.15 g/cm^3$, the flow is not homogeneous at low shear rates. As the shear rate increases the suspension becomes more homogeneous and the presence of shear bands disappear. This study suggests that the reason for the presence of yield stresses observed in the previous works at lower volume fractions is due to a slight density mismatch. Sedimentation or creaming may lead to the formation of more concentrated zones in which the particles are packed enough that a yield stress emerges. The presence of shear banding has also the same origin, where the normal stresses generated by the flow at low shear rates can no longer balance the gravity force. At higher shear rates, the shear induced resuspension of the particles prevent shear banding from occurring, making the flow to be homogeneous. In the current work, the effect of density mismatch is also studied where the presence of yield stress is observed, indicating that there is a slight difference in density for the matched density experiments.

Dijksmann et al. (2010) studied the rheology of non-Brownian suspensions with settling particles using a "split-bottom" geometry. Their experimental setup consisted on a square box with a rotating disk at the bottom. The radius of the disk is 4.5 cm and the width of the box is 15 cm. The suspension has a free surface the top and the height of the suspension is varied. They used acrylic particles with a diameter of 4.6 mm in an aqueous mixture of Triton X-100 and ZnCl2. The density ratio is $\rho_p/\rho = 1.1$. Based on the hypothesis that for vanishingly flow speeds, hydrodynamics effects are expected to be negligible and the behavior of the suspensions becomes similar to the behavior of dry granular materials. Dijksmann et al. (2010) derived a constitutive equation for their suspension using the modified inertial number approach proposed by Cassar et al. (2005),

$$\tau = A_o P + A_1 \frac{\mu\dot{\gamma}}{\alpha},$$

where P and α are pressure and porosity; and A_o and A_1 are empirical friction functions. Their constitutive model is reminiscent of the rheology of a Bingham fluid. Their results for suspensions

sheared at low rotational speeds (driving rotating disk rates goes from $8.3 \times 10^{-5} \leq \dot{\gamma} \leq 8.2 \times 10^{-2}$ rps) compare favorably with the predicted flow field for slow dry flows, suggesting that the effect of interstitial fluid is negligible and that the mechanism of the suspension flow is dictated by friction. At higher shear rates, the flow behavior of the suspension is Newtonian and it compared favorably with the predicted flow field determined by a finite element software package. The stresses become rate dependent for driving rates of approximately 0.01 rps, and increase linearly with increasing shear rates. The torques measured for the suspensions in the Newtonian regime were compared with the torque for just the suspending liquid, and it was found that the effective viscosity of their suspension is only three to five times higher than the viscosity of the suspending liquid. Such values are far below what Krueger-Dougherty formula would predict. However, due to the non-confinement of their flow, the effective volume fraction of their suspension is not fixed, which complicates the analysis. The effect of interstitial fluid viscosity was also studied by using a different suspension with 2 mm glass beads and glycerol as the suspending liquid. The suspending liquid viscosity was varied by more than a decade by increasing the temperature from 4 to 37 $^{\circ}C$. Their results show that once the measured torque is scaled with the change in viscosity, the data collapses into one single curve, where the flow exhibits a Bingham fluid-like behavior for low shear rates and a Newtonian behavior for higher shear rates. Decreasing the viscosity would also decrease the Reynolds number, and considering the highest driving rates tested, the range of Reynolds number goes from 1.26 to 26 for this set of experiments.

Boyer et al. (2011) made an analysis similar to Dijksmann et al. (2010) where the modified inertial number is used to unify the rheology of dense suspensions and dry granular flows. Using a pressure-imposed shear cell, measurements of the shear and normal stress were performed. The top boundary of their apparatus was free to displace in the vertical direction; thus the volume fraction tested varied accordingly to the normal pressure applied. At an initial stage, the volume fraction was chosen to be 56.5 % for most of their experiments. Two types of particles were used: (i) polymethyl methacrylate (PMMA) (d=1.1$\pm$0.05 mm) in triton X-100/water/zinc solution, and (ii) polystyrene (d=0.58 $\pm$0.01 mm) in polyethylene glycol-ran-propylene glycol moonlitylether. The density ratio for both set of experiments was equal to one and settling effects were neglected together with the presence of particle migration. Using the modified inertial number (I_v) proposed by Cassar et al. (2005),

$$I_v = \frac{\eta(I_v)\dot{\gamma}}{P^p},$$

where P^p is the particle pressure, Boyer et al. (2011) proposed a constitutive model for the suspensions where the shear stress is proportional to the particle pressure. The coefficient of proportionality is given by the effective friction (η) that depends solely on the modified inertial number and can be inferred by the ratio of shear and normal stresses ($\eta = \tau/P^p$). For the two particles tested, the co-

efficient of friction for different particle pressures, liquid viscosity, and shear rates collapses into one single curve when plotted against I_v. The volume fraction can be calculated from the displacement of the top plate and it was found to be a decreasing function of I_v. Boyer et al. (2011) showed that this apparent frictional behavior of dense suspensions can be reconciled with the classical view that considers an effective viscosity if the suspensions is sheared at constant volume fraction, in which case, the shear and normal stresses depend on the viscosity of the fluid and the shear rate,

$$\tau = \mu_s(\phi)\mu\dot{\gamma} \text{ and } P^p = \mu_n(\phi)\mu\dot{\gamma},$$

where $\mu_s(\phi)$ and $\mu_n(\phi)$ are the dimensionless effective shear and normal viscosities. Equating the proposed constitutive equation with the classical view leads to the following relation:

$$\mu_s(\phi) = \frac{\eta[I_v(\phi)]}{I_v(\phi)} \text{ and } \mu_n(\phi) = \frac{1}{I_v(\phi)},$$

and therefore the rheology of the suspension is dictated by an effective viscosity that depends solely on the volume fraction and the effective friction. Their experimental results agrees with the correlation of Krieger and Dougherty for the limited range of volume fractions tested.

Trulsson et al. (2012) studied the transition from viscous to inertial regime in dense suspensions via numerical simulations, where it was found that the transition from Newtonian to shear thickening behavior is dictated by the ratio of the inertial number I defined as

$$I = \sqrt{\frac{\rho\dot{\gamma}^2 d^2}{P^p}},$$

and the modified inertial number I_v used by Boyer et al. (2011). In their simulations the lubrication interactions between the particles are considered and it was found that the transition from viscous to inertial regime is unaffected by it. The shear stress was found to be a sum of viscous forces and the forces due to particle interactions that depend quadratically with the shear rate, as proposed by Bagnold (1954),

$$\tau = f(\phi)(\mu\dot{\gamma} + k\rho d^2\dot{\gamma}^2)$$

where k is a constant of order 1 that encodes the details of dissipative mechanisms. While the work of Boyer et al. (2011) focused on the quasi-static viscous regime, the simulations of Trulsson et al. (2012) considered higher shear rates where the inertia becomes important. Trulsson et al. (2012) explained that the reason why the data of Boyer et al. (2011) collapses with just the modified inertial number is because they studied a regime with vanishingly shear rates.The quadratic dependance on the shear rate found by the numerical simulations of Trulsson et al. (2012) is limited to high volume fractions that are close to the jamming transition. In such case, the effective viscosity of the

Experiment	**d(mm)**	$\dot{\gamma}$ (s^{-1})	**Re**	**St**	ρ_p/ρ	**Flow behavior**
Bagnold (1954)[a]						
50 % paraffin wax	1.32	7.34 - 52	14.94 - 89.62	1.66 - 9.95	1	Newtonian-Shear thickening
and lead stearate						
Savage *et al. (1983)*						
	0.97	7.86 - 59.78	7.12 - 54.09	0.79 - 6.01		
polystyrene	1.24	5.018 - 71.15	7.42 - 105.22	0.82 - 11.69	1	Newtonian-Shear thickening
	1.78	8.04 - 65.57	24.50 - 199.79	2.722 - 22.20		
Hanes *et al. (1985)*						
glass beads	1.1	35.60 - 263.00	43 - 317	11.88 - 87.65	2.48	Newtonian-Shear thickening
	1.85	34.4 - 127	118.00 - 434.00	36.37 - 134.25	2.78	Newtonian-Shear thickening
Acrivos *et al (1994)*						
PMMA [a]	0.1375	0.45 - 5.374	8×10^{-4} - 3×10^{-2}	8×10^{-5} - 3×10^{-3}	1	Shear thinning
acrylic	0.0905	0.135 - 44.13	3×10^{-6} - $9.\times10^{-4}$	3×10^{-7} - 1×10^{-4}	0.95	Shear thinning
Prasad *et al. (1995)*						
glass beads	2	1 - 100	1.37-13.7	0.32-3.2	2.09	Shear thinning - Newtonian
acrylic	3.175	0.50 - 16.00	0.09 - 2.89	0.01 - 0.36	1.12	Shear thinning - Newtonian
Fall *et al. (2009)*						
polystyrene	0.04	$1\times10^{-4}-10$	$4\times10^{-6}-4\times10^{-3}$	$5\times10^{-7}-5\times10^{-4}$	0.85 and 1	Viscoplastic
Dijksman *et al. (2010)*						
acrylic	4.6	$2\times10^{-3}-10.4$	$4\times10^{-4}-0.72$	$5\times10^{-5}-0.09$	1.1	Viscoplastic-Newtonian
glass	2	$5\times10^{-3}-31.4$	$6\times10^{-5}-2.4$	$1\times10^{-5}-0.53$	$1.88-1.92$	Viscoplastic-Newtonian
Boyer *et al. (2011)*						
polystyrene	0.58	0.1-2.5	$1\times10^{-5}-4\times10^{-4}$	$2\times10^{-6}-5\times10^{-5}$	1	Viscoplastic-Newtonian
PMMA	1	0.1-2.5	$4\times10^{-5}-1\times10^{-3}$	$4\times10^{-6}-1\times10^{-4}$	1	Viscoplastic-Newtonian
Koos *et al. (2012)*						
polystyrene	3.34	2.19 - 74.87	18.05 - 782.04	2.04 - 89.46	1 and 1.009	Newtonian
nylon	6.36	7.77 - 70.24	50.36 - 718.31	5.65 - 81.21	1	Newtonian
SAN [b]	3.22	4.72 - 83.04	23.21 - 539.08	2.58 - 60.19	1	Newtonian

Table 1.1: Previous experiments properties.

[a]Macro-viscous regime
[a]polymethyl methacrylate
[b]styrene acrylonitrile

suspension diverges leading to vanishingly Reynolds numbers. Therefore, the transition from the viscous to the inertial regime at high volume fractions is of a different nature that the transition formulated by Bagnold (1954), where particle collisions control the regime.

Kulkarni and Morris (2008), Yeo and Maxey (2013), and Picano et al. (2013) studied the rheology of inertial suspensions for a wider range of volume fractions by means of numerical simulations. In these three studies the Reynolds number was larger than 10^{-3} and both the inertia of the particles and the fluid are considered. The simulations considered a density ratio equal to one. The common result between these simulations is the increase of effective relative viscosity with Reynolds number. Figure 1.2 shows the results from these numerical works.

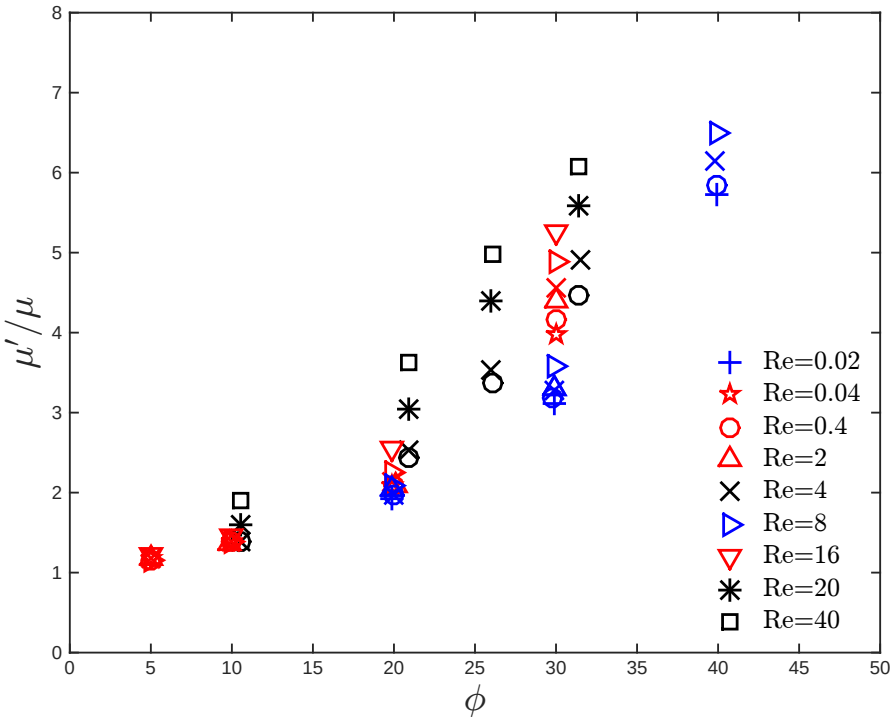

Figure 1.2: Predicted effective relative viscosity for inertial suspensions from numerical studies. Symbols denote the Reynolds numbers according to figure legend. Red symbols are from Kulkarni and Morris (2008), blue symbols are from Yeo and Maxey (2013), and black symbols are from Picano et al. (2013).

The previous work of Koos et al. (2012) showed a different result. In the range of Reynolds number tested (20 to 800), the effective viscosity of the suspensions with neutrally buoyant particles showed no dependance on the Reynolds number. The reason for this difference in results is still not clear but it is believed that the transition from macro viscous to inertial regime is dictated by the Stokes number and that for the range of Stokes numbers tested the particle interactions are damped by viscous dissipation of the interstitial fluid. A detailed description of this study is presented in Chapter 3.

The present work is a continuation of the work done by Koos et al. (2012). Koos performed

rheological measurements of liquid solid mixtures with relatively large particles (ranging from 3.34 to 6.36 mm) with a density ratio of one. The range of Reynolds and Stokes numbers tested were between $20 \leq Re \leq 800$ and $3 \leq St \leq 90$ respectively. The effective viscosity for all the mixtures tested showed no dependance with the Reynolds and equivalently with Stokes numbers. A further detail of the work of Koos is presented in Chapter 3.

Table 1.1 shows the regimes for this kind of suspensions and the flow behavior observed in previous experiments. Based on the phase diagram proposed by Stickel and Powell (2005), all the mixtures were expected to exhibit a shear thickening behavior. This suggests that this phase diagram needs to be re-scaled. Based on Table 1.1, a suspension may be expected to exhibit a Newtonian behavior for greater ranges of shear rates as particle size and fluid viscosity increase.

The diagram shown in Figure 1.3 summarizes the Reynolds and volume fractions regions studied in the previous experimental studies along with the range covered in the current work.

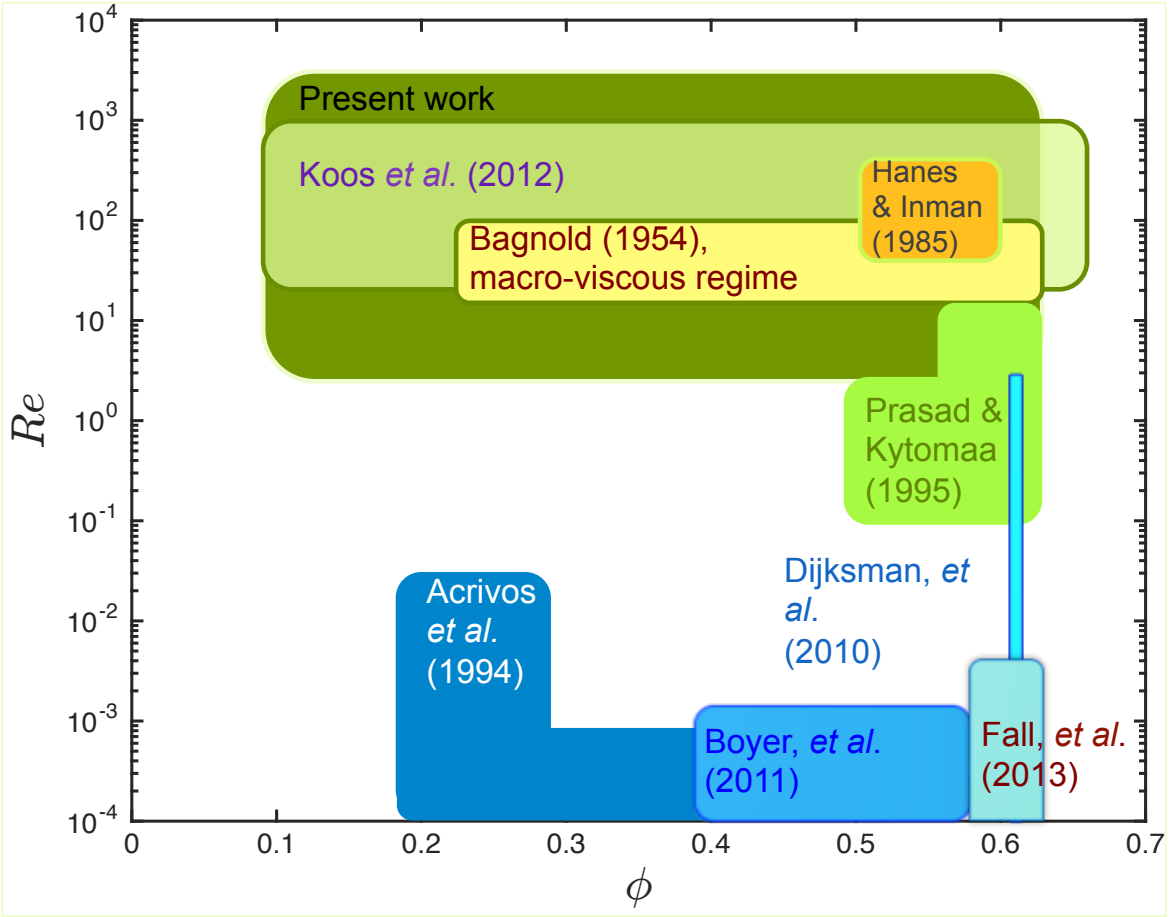

Figure 1.3: Diagram of previous and current experimental work done in inertial suspensions in terms of Re. The properties of the previous experiments can be found in table 1.1

Particle interactions

The Stokes number is a dimensionless number that gives a measure of the ratio of available momentum in the solid phase that sustains the particle motion through the liquid to the liquid viscous forces (Yang and Hunt, 2006). In several studies (MacLaughlin, 1968; Davis et al., 1986; Joseph et al., 2001; Joseph and Hunt, 2004; Yang and Hunt, 2006), the Stokes number has been used to characterize the collision of particles immersed in a viscous fluid. The energy loss during the collision is described by the effective coefficient of restitution (e). It has been found that with diminishing Stokes number, a monotonic decrease in e is observed (Joseph et al., 2001; Joseph and Hunt, 2004; Yang and Hunt, 2006). This dependence is the same for normal and oblique collisions between pairs of identical and dissimilar spheres, as well as for sphere-wall collisions. For St>2000, the effect of the fluid becomes negligible, resulting in a nearly unity restitution coefficient that approximates a dry impact. However, with increasing liquid viscosity or decreasing particle inertia, the sphere can no longer sustain its motion through the liquid and a critical particle Stokes number, St ≈ 10, exists below which no rebound occurred. These findings suggest that for dense suspensions there will be a critical Stokes number below which the collisions of the particles will be damped by the liquid, and above it there will be a decrease of energy lost during the particle collisions.

The Stokes number tested in the current experiments vary from 2.5 to 195 and it is expected that the particle collisions in these regime become important.

The diagram shown in Figure 1.4 summarizes the Stokes and volume fractions regions studied in the previous and in the present experimental work.

Particle settling

When the particles are denser than the suspending liquid, the particles can settle depending on the shearing conditions and the density ratio. The mechanical properties of liquid-solid flows can be strongly affected in the presence of settling since the mixture is no longer homogeneous. When sheared, the particles can re-suspend. The resuspension of particles at vanishingly Reynolds number was first observed by Gadala-Maria and Acrivos (1980). This phenomena called *viscous resuspension* has been modeled by balancing gravitational and shear induced particle migration by Leighton and Acrivos (1986) and it was successfully employed by Acrivos et al. (1993). In the model of Leighton and Acrivos (1986), the particle terminal velocity (v_{ter}) was given by Stokes flow:

$$v_{ter} = \frac{2}{9}\frac{a^2 g(\rho_p - \rho)}{\mu}$$

where a is the particle radius and g is the gravitational acceleration.

The particles can be fluidized with increasing shear rate. King (2001) categorizes the liquid-solid

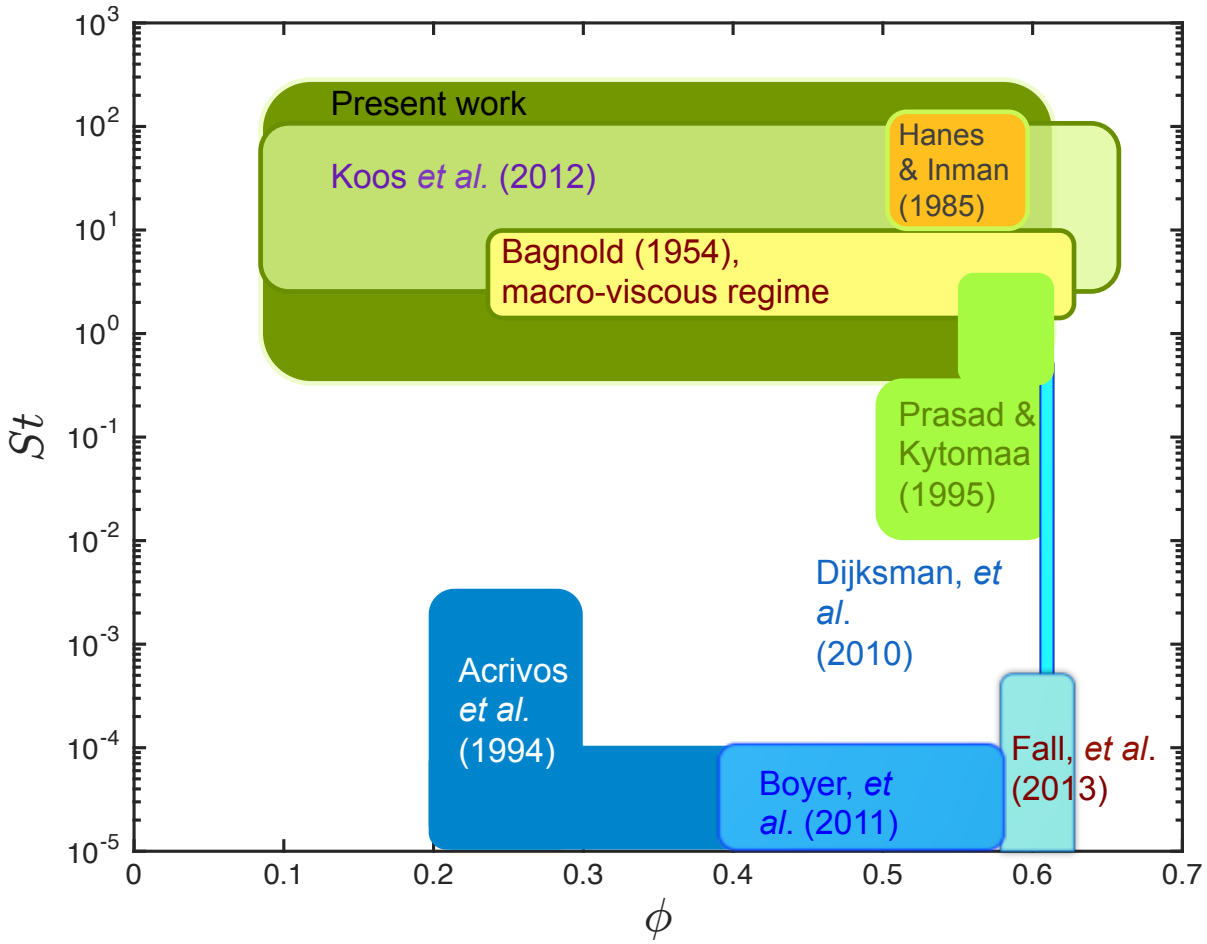

Figure 1.4: Diagram of previous and current experimental work done in inertial suspensions in terms of St. The properties of the previous experiments can be found in table 1.1

flows based on variation of Archimedes number and Reynolds number, where the suspension would be homogenous for low Ar and moderate Re, and become heterogeneous with increasing Ar. As the ρ_p/ρ increases, the required Reynolds number to fluidize the particles also increases (Bi and Fan, 1992; King, 2001). The effective viscosity of the suspension depends strongly on the volume fraction which can vary when the particles are denser than the liquid. To account for such variations, in the present experiments visualizations of the flow are made allowing to infer the local volume fraction and correlate it to the measured effective viscosity.

1.3 Secondary flows

In a rotating flow, instabilities due to the deviation from the azimuthal direction of the flow occur. This deviation is primarily due to centripetal forces generated in a rotating fluid. Taylor (1936a) observed that in a coaxial cylindrical Coquette flow, counter rotating laminar tori develop. When the flow was driven by the rotation of the inner cylinder, the development of highly ordered patterns formed after the inner cylinder rotation rate exceeded a critical value. When the flow was driven by the rotation of the outer cylinder and the inner cylinder remained fixed, such transitions occurred more gradually. Under this configuration, the formation of a recirculating flow at the top and bottom boundaries occurred. Taylor (1936a,b) observed that under the rotation of the outer cylinder the circulatory motion is stable to infinitesimal disturbances and also that there is an intermediate range of Reynolds number in which the flow is in transition and stable. Instabilities of the flow occur at much lower Reynolds numbers when the inner cylinder drives the flow due to centrifugal forces. Conway et al. (2004) observed the formation of Taylor like vortices in a dry granular flow at slightly lower Reynolds number, proving that such instabilities are also likely to occur in granular materials.

The presence of these flows increases the shear stress on the cylinder walls. Coles (1965) showed that the measured torque under the presence of secondary flows can increase in a nonlinear manner. Therefore, care should be taken to avoid the effect of the presence of these secondary flows when acquiring rheological data. In the current work, the rheometer used was specifically designed to delay the presence of such effects. However, how the presence of particles influence the strengthening or weakening of these flows is difficult to estimate. Matas et al. (2003) summarized the effects of the presence of particles in a horizontal pipe flow. The transition from laminar to turbulent depends on the ratio between the particle and pipe diameter. When this ratio increases, the critical Reynolds number decreases for volume fractions less than 10, and it increases as the volume fraction increases and the ratio of particle and pipe diameter increases. Gore and Crowe (1991) observed that turbulence was strengthened by small particles and attenuated by large ones.

Effect of rough boundaries

To avoid slip at the wall (a condition where the solid phase of the mixture can roll and slide at the wall or move away from it), the current experiments were performed using rough walls. The presence of rough boundaries can impact the stability of the fluid. Cadot et al. (1997) performed experiments on Couette-Taylor flow with smooth and rough walls. In these experiments the flow was driven by either counter-rotating the cylinders or by the rotation of the inner one. The presence of roughness at the wall did not change the transition but it did increase the measured torques after the threshold was reached. Similar to what was found by Cadot et al. (1997), van den Berg et al. (2003) and Lee et al. (2009) examined the differences in transition for walls with different roughness and found that the critical Reynolds number is the same regardless of the presence or absence of roughness.

All these studies considered the rotation of the inner cylinder, where the transition occurs abruptly and the flow is more unstable. It is possible that under the rotation of the outer cylinder the range of Reynolds number at which the flow is in transition but stable can be affected by the presence of roughness.

1.4 Thesis outline

The primary objective of this thesis is to investigate the inertial effects in liquid-solid flows. The current work is a continuation of the work done by Koos (2009), and emphasis has been focused on extending the Stokes and equivalently the Reynolds number regime studied previously via experiments. Rheological measurements using a concentric cylinder apparatus equipped with rough walls were performed for particles with the same or higher density than the suspending liquid.

The description of the rheometer and the methods for measuring the rheological properties of the liquid-solid flow is presented in Chapter 2. Measurements of the torque for pure fluid (no particles) is also presented where the presence of hydrodynamics instabilities is discussed and analyzed. The results from the previous experimental work done by Koos et al. (2012) is reported in Chapter 3. In Chapter 4 the torque measurements for particulate flows with density ratio (ρ_p/ρ) equal to 1 and 1.05 are described. Chapter 5 presents the results for flows with $\rho_p/\rho = 1.05$ over a porous medium.

For the experiments with settling particles, a characterization of the particle resuspension is performed and presented in Chapter 6. The measurements of the settling particles' expansion are used to predict the effective volume fraction for the experiments with $\rho_p/\rho = 1.05$. Chapter 7 presents a discussion and analysis of the obtained results. A comparison between the results with different density ratio is presented and the effect of hydrodynamics instabilities is analyzed.

Chapter 8 summarizes the results obtained from this investigation. Topics for future work are

discussed as well.

Chapter 2

Experimental setup

The current experiments are designed to examine the effect of volume fraction and Stokes number (and equivalently the Reynolds number) at shear rates sufficiently high enough so that particle interactions are expected to become important. Neutrally buoyant and settling particles are used (ρ_p/ρ from 1 to 1.4). In this chapter the rheometer and the method used for making the torque measurements are described (Section 2.1). Subsequently, the particles and the interstitial liquids that were employed to create the liquid-solid mixtures are reported in Section 2.2. Finally, the modification of the experimental apparatus for making visualizations of the flow and its procedure is specified in Section 2.6.

2.1 Rheometer

In Figure 2.1 a schematic of the concentric-cylinder rheometer is shown. The rheometer is designed to measure the shear stress of liquid-solid mixtures that feature relatively large particles (the order of mm size) and are sheared at considerably shear rates. One of the difficulties that arises with high shear rates flows is the presence of secondary flows. As shown by the review of Hunt et al. (2002), an improper design of an experiment can result in observations that do not reflect the behavior of the particulate flow itself. For this reason, the rheometer is designed to delay the presence of secondary flows (Taylor vortices). This is the same experimental apparatus used by Koos (2009). It consists of a rotational outer cylinder and an inner cylinder that consists of three parts: the top and bottom static cylinders (fixed guard cylinders), and the middle cylinder (test cylinder) which is instrumented to make measurements of the torque. The concentric and rotating outer cylinders are all made of stainless steel.

The liquid-solid mixture is sheared by the rotation of the outer drum and the torque measurements take place at the test cylinder. This cylinder is supported by a central shaft, which, in turn, has ball bearings mounted to allow the free deflection of this cylinder. A set of ball bearings is also located between the rotating outer cylinder and the fixed guard cylinders to reduce friction. The

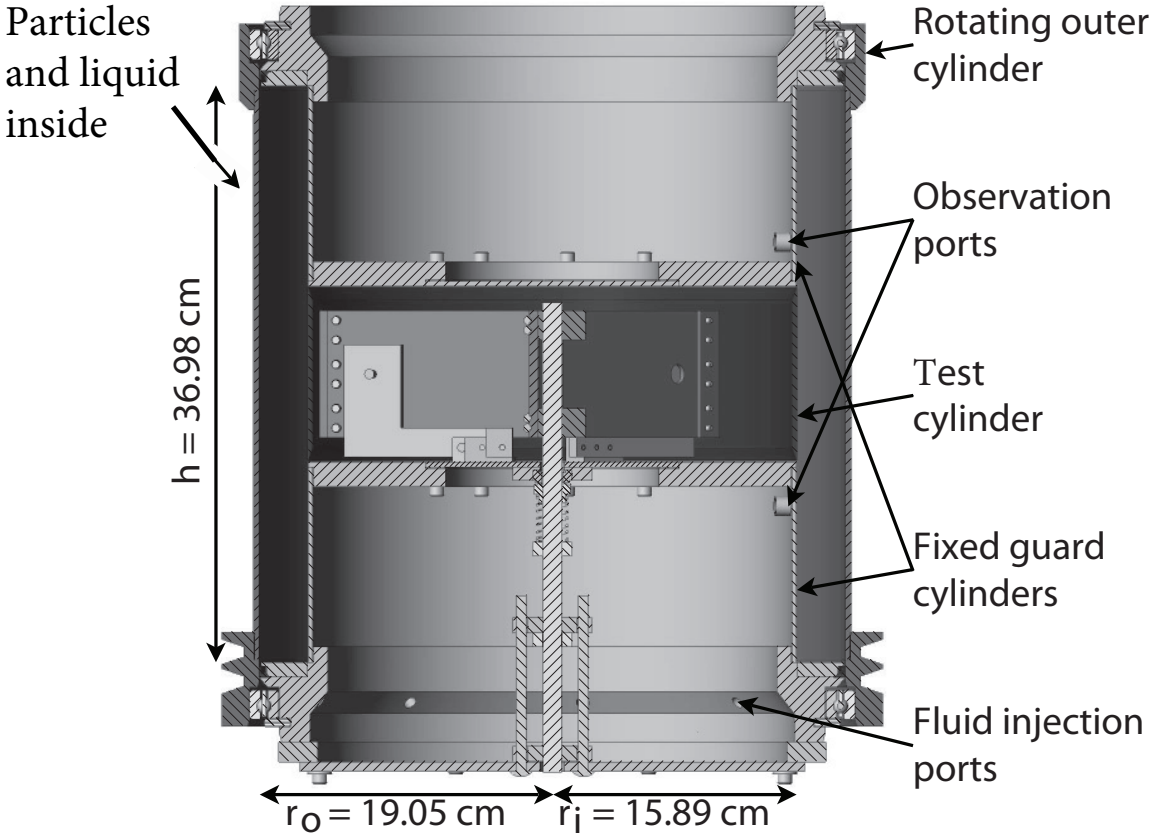

Figure 2.1: Rheometer, Couette flow device. The liquid-solid mixture is sheared by the rotation of the outer cylinder. The top and bottom cylinders are fixed. The inner middle cylinder (test cylinder) is free to rotate slightly so as to measure the torques created by the flow.

Property	**Smooth walls**	**Rough walls**
Annulus height (h_T)	36.98 cm	36.98 cm
Test cylinder height	11.22 cm	11.22 cm
Fixed guards height	12.7 cm	12.7 cm
Annulus inner radius (r_i)	15.89 cm	16.22 cm
Annulus outer radius (r_o)	19.05 cm	18.72 cm
Annulus gap (b)	3.16 cm	2.49 cm
Ratio of height to gap (h_T/b)	11.7	14.84
Ratio of gap to outer radius (b/r_o)	0.166	0.133
Maximum rotational speed (ω)	14.9 rad s^{-1}	14.9 rad s^{-1}
Re critical	1.6×10^4	1.1×10^4

Table 2.1: Rheometer properties and dimensions

fixed guards and the central shaft are equipped with seals that prevent the fluid from entering the bearings. The fixed guard cylinders are separated from the test cylinder by a knife edge gap (0.7 mm) to prevent the particles from exiting the annulus gap but allowing the test cylinder to rotate freely. The height of the test cylinder, H, is 11.22 cm, the inner radius of the annulus, r_i, is 15.89 cm, the outer radius of the annulus, r_o, is 19.05 cm, and the width of the annulus between the cylinders when the walls are smooth, b, is 3.16 cm. The outer cylinder is driven by a belt connected to a motor; the maximum rotational speed is $\omega = 14.8$ rad s^{-1}. Hence, the maximum shear rate, $\dot{\gamma} = 2\omega r_o^2/(r_o^2 - r_i^2)$, is 123 s^{-1}. The experiment dimensions and its range of speeds are listed in Table 2.1. Mechanical drawings of the rheometer parts can be found in the thesis of Koos (2009). To avoid slip at the wall, the inner and outer cylinder walls are roughened by coating them with polystyrene particles. The particles are glued to thin waterproof vinyl sticker sheets (commonly used as aquarium backgrounds), which covered both surfaces. The glued particles are oriented randomly and have a surface area fraction of 0.70. The decrease in gap thickness due to the rough walls is considered when calculating the shear rate and the change in dimensions is reported in table 2.1.

Shearing the mixture by rotating the outer cylinder is preferred over shearing it by rotating the inner one because Taylor vortices develop at lower rotational speeds in the latter case due to centripetal forces (Taylor, 1936a,b; Wendt, 1933). Besides delaying the presence of secondary flows by rotating the outer cylinder, the rheological measurements are made away from the top and bottom boundary where the secondary flows develop. The contribution to the measured torque by end effects is attenuated by increasing the ratio of height and shearing gap width, ($H/b = 11.7$). Further delay

is achieved through the increase in the ratio of gap width to outer radius (b/r_o). By using a modified gap Reynolds number ($Re_b^* = \rho r_o \omega b/\mu$, where ω is the angular velocity of the outer cylinder), it is possible to determine the critical Re_b^* at which these secondary flows occur (Taylor, 1936a,b). Using the data of Taylor, a critical modified gap Reynolds number of 1.6×10^4 is found for this apparatus when the walls are smooth and 1.1×10^4 when the reduction in gap width due to added roughness is considered. The modified gap Reynolds number range for a pure fluid (no particles) in the current experiments is $1.0 \times 10^3 \leq Re_b^* \leq 7.2 \times 10^4$, and thus some of the experiments are above the critical Reynolds number; however, the presence of solid particles increases the effective viscosity of the flow and hence decreases the Reynolds number.

2.2 Torque measurements

Unlike Bagnold (1954), in which the torque was not measured directly, the torque measurements in this work are directly taken in the test section located in the middle of the inner cylinder (see Figure 2.1) without removing any possible contribution to friction or fluid. The test cylinder is allowed to deflect rotationally due to the torque applied by the flow. The rotation of the test cylinder is opposed by a linear spring that is connected to a static reference. The spring connects to the test cylinder through a torque arm. The torque is measured by measuring the elongation of the spring. Different springs with different stiffness are used depending on the torque applied by the flow. To overcome the spring initial tension every spring is preloaded. A pulley is used to direct the preload and reduce friction. An optical probe and a fotonic sensor (MTI 0623H and MTI KD-300, respectively) is mounted on a static reference to measure the spring displacement. The arm that connects the test cylinder to the spring is equipped with a mirror that is used as the moving target for the optic probe. A sketch of the torque measurement setup is shown in Figure 2.2. The calibrations of the optical probe and the springs are discussed in Subsection 2.2 and 2.2, respectively, followed by the methodology for measuring the rheometer angular speed.

Optical probe calibration

The optical probe contains a set of light transmitting and light receiving fibers that are aligned in a hemispherical configuration. Light is fed to the transmit fibers, where it exits the probe tip and hits the target. Light that is reflected from the target is captured by the receive fibers and transmitted to the fotonic sensor that converts the light intensity to voltage. The output voltage is proportional to the distance between the probe tip and the target being monitored. Figure 2.3 shows a diagram of the fotonic sensor output as a function of target displacement. When the target is in contact with the optic probe, no light is received by the fibers, giving an output signal of zero. The voltage increases with increasing distance reaching a maximum. Past the optical peak, there is

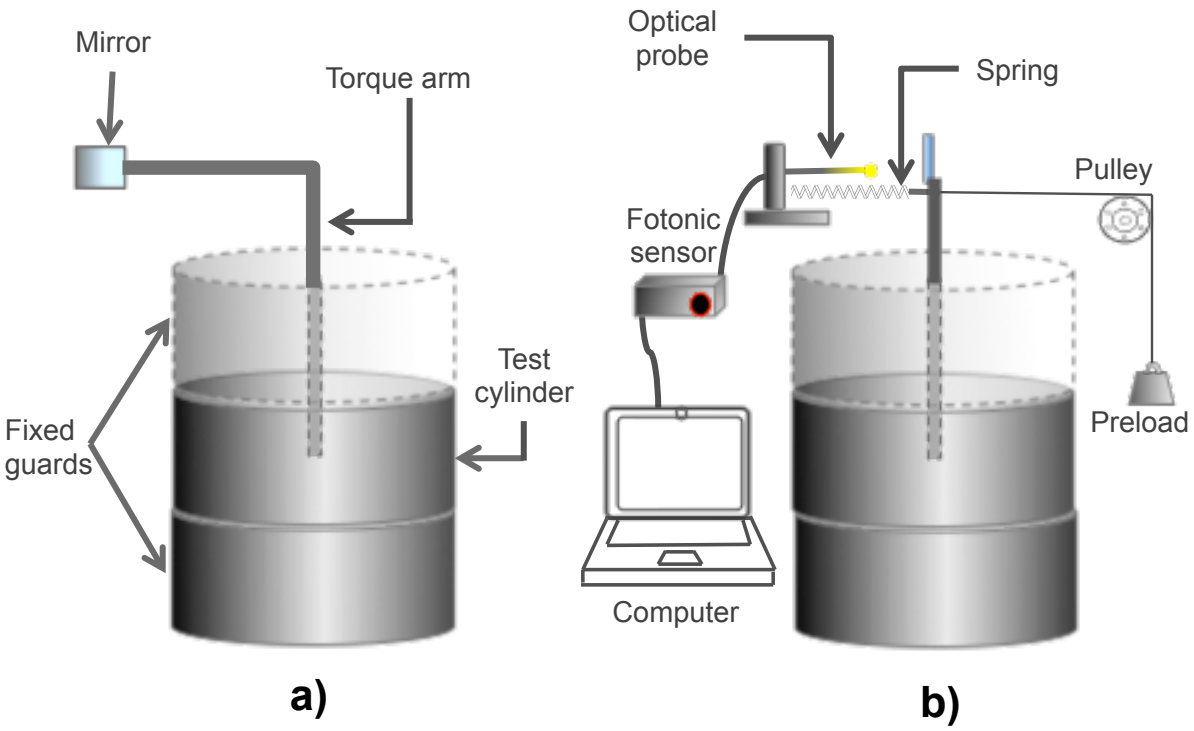

Figure 2.2: Torque measurement system. The outer rotating cylinder is left out of the drawing for clarity. (a) Front view of inner cylinder. The mirror attached to the torque arm is the target monitored by the optical probe. (b) Side view of the inner cylinder. The optical probe and the spring are attached to a stationary frame. The spring is connected to the test cylinder through the torque arm. The signal from the fotonic sensor is read out and stored in the computer.

a sensitive linear output response (Range 2). The optical probe is positioned far enough from the moving target to make sure that the sensor output is in this range. The optical probe sensitivity post the optical peak is 30 $\mu m/mV$. The optical probe is calibrated using a dial gage. A typical calibration curve is shown in Figure 2.4. The curve that best fits the data is a rational polynomial and its coefficients depend on the initial target position. The optical probe is calibrated prior to every set of experiments and when a spring is changed. This calibration is repeated at least 10 times and the final calibration curve is the average of these calibration curves. The fotonic sensor records the optical probe signal for 10 seconds with a frequency sample of 10,000 Hz. The sensor output is then averaged and coverted it to displacement using the calibration curve.

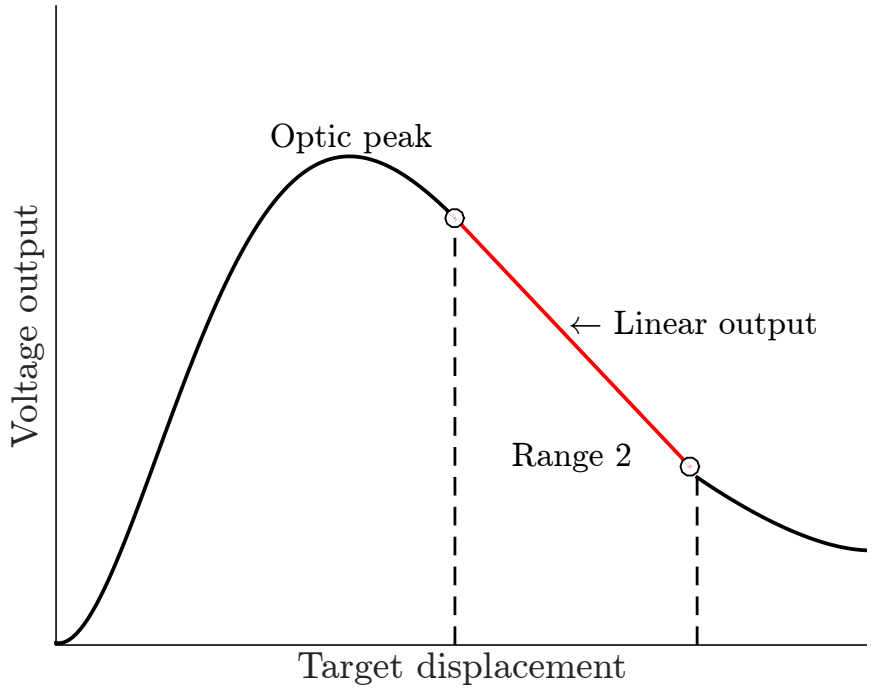

Figure 2.3: Diagram of an MTI KD-300 fotonic sensor output as a function of target displacement.

Springs calibration

The springs used to measure the torque were manufactured by *Century springs*. The calibration of the spring is carried out by loading the spring with known masses. The masses are weighted prior to each calibration using a scale with a resolution of 0.05 grams. The masses are attached to the torque arm through a fishing line that runs through a pulley (see Figure 2.2). The torque arm is connected to the spring and hence the spring can be loaded and its displacement measured for different masses. Springs with different stiffness are used to allow a range of torques (M) between $1.3 \times 10^{-3} \leq M \leq 2.7$ Nm to be measured. The calibration curves for all of the springs used are shown in Figure 2.5. The spring calibration is performed while the rheometer is filled with

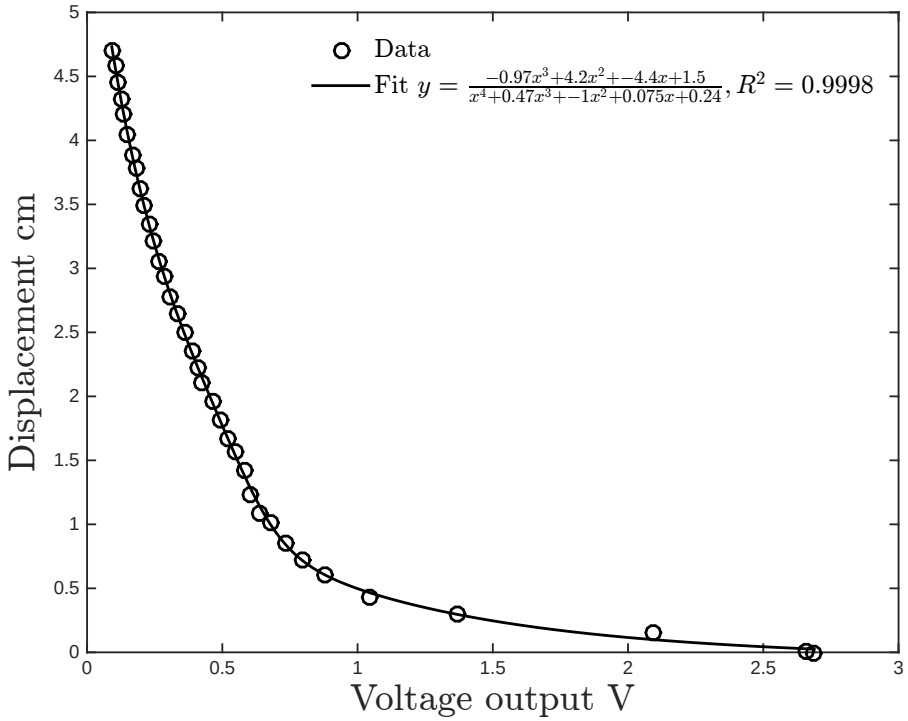

Figure 2.4: An example of a fotonic sensor calibration curve. All the calibration curves are best fitted by a rational polynomial. The order of the polynomial numerator and denominator is 3 and 4, respectively.

water and running at different speeds. Each point represents the mean of at least 15 individually recorded measurements; the error bars represent the standard deviation in these measurements. The R-squared average for all the linear fits is 0.999. The lowest R-squared corresponds to the spring with the highest slopes (and equivalently with the highest sensitivity). An initial torque is required to start the displacement of the spring; this torque is given by the x-intercept of the calibration curve. All the experiments are preloaded with the corresponding spring initial torque to guarantee maximum sensitivity. The calibration curve for the spring with the highest resolution and sensitivity is shown in Figure 2.6. The initial torque has been subtracted to show the maximum resolution of this spring. A maximum deviation from the linear fit of 17% occurs at the lowest torques applied.The R-squared value of this fit is 0.9988.

During the torque measurements, the displacement of the spring is also recorded with a digital camera to account for any possible mis-calibration of the optical probe. The photos taken of the spring are used to measure its displacement and double check the sensor output.

Angular speed measurements

The rotation of the outer cylinder is measured using a magnetic sensor and a laser tachometer. The two devices are used to account for uncertainties in the speed measurements. For the lowest

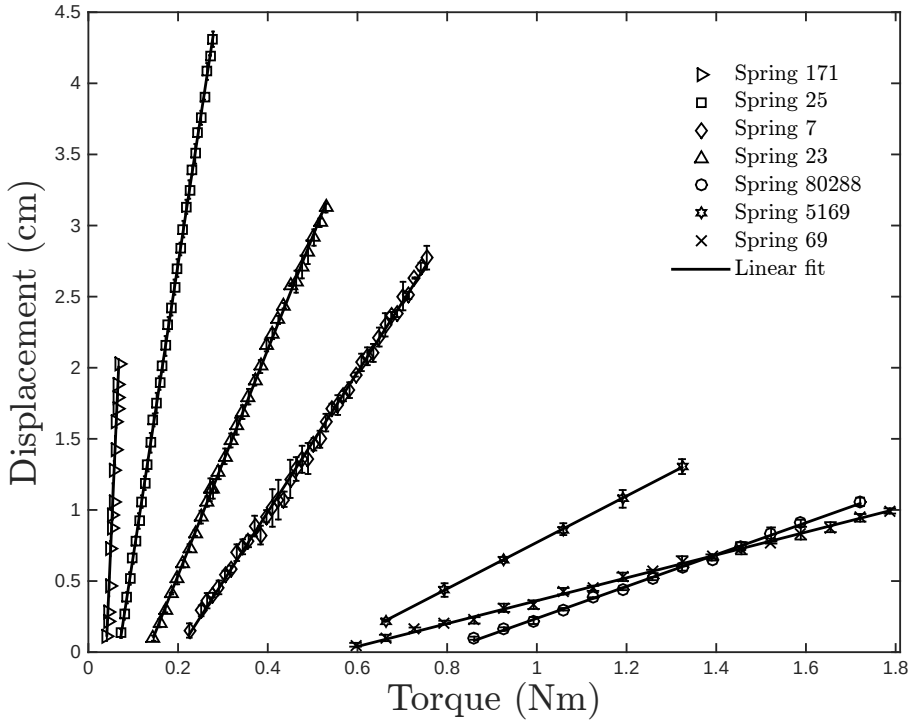

Figure 2.5: Springs calibration curves. The spring constant and its sensitivity are given by the slope of the linear fit. The error bars correspond to the standard deviation of the measurements.

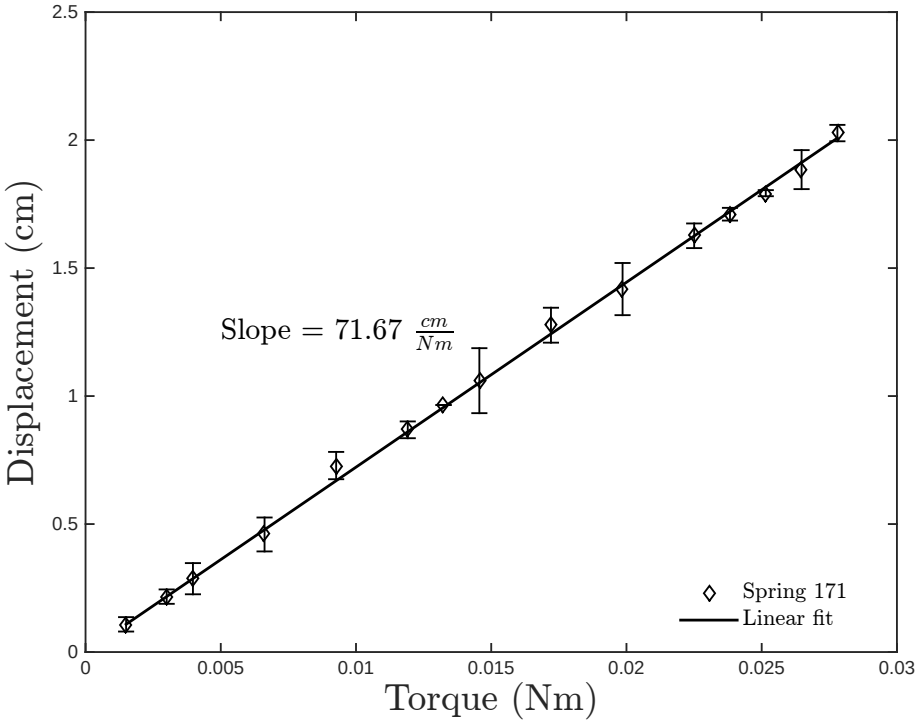

Figure 2.6: Calibration curve for spring 171-b (highest sensitivity). The spring constant and its sensitivity are given by the slope of the linear fit. The error bars correspond to the standard deviation.

rotational speeds, a chronometer is also used to account for the reduction of accuracy of the laser tachometer. The magnetic sensor does not work for rotational speeds below 2.87 rad s^{-1}. To increase the accuracy of the laser tachometer at low speeds, 8 reflective marks were evenly spaced and placed on the outer cylinder. Due to the high reflectiveness of stainless steel, the laser is pointed to a black stripe painted on the outer cylinder where the reflective marks are located. Figure 2.7 shows a sketch of the rotational speed measurement system. In the previous work of Koos (2009),

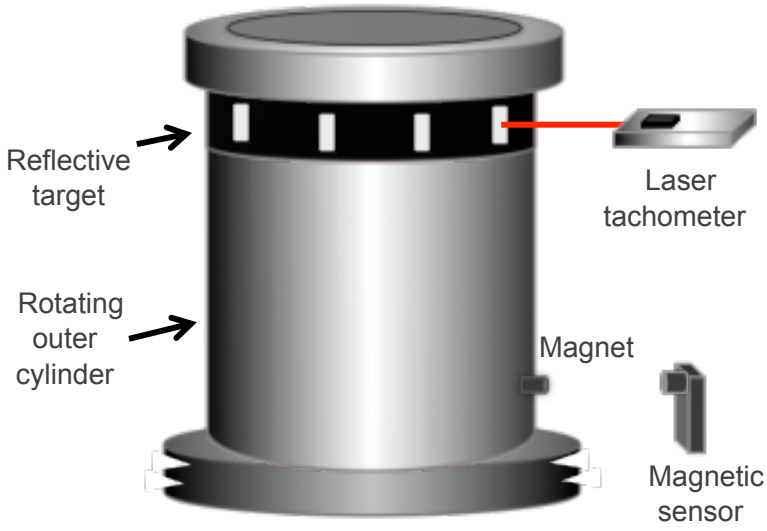

Figure 2.7: Sketch of the rotational speed measurement system. The rotational speed is measured with a laser tachometer and a magnetic sensor.

the angular speed was measured by counting the outer cylinder revolutions and measuring the time with a chronometer. Measurements of the angular speed using this method were performed while measuring the angular speed with the laser and magnet sensor to measure the uncertainty on the previous speed measurements. The outer cylinder is driven by a belt connected to a motor; the motor speeds are controlled via a Bardac drive that allows the gradual increase of the speed. To test that the rheometer runs at a constant speed, rotational speed measurements for the laser, magnet sensor, and chronometer were recorded for a period of 1.5 hours for 9 different speeds. Figure 2.8 shows the rotational speed measurements for each instrument. The measurements are in good agreement; the highest deviation is found at the highest rotational speeds for the measurements that used the chronometer. The outer cylinder angular speed is shown to maintain a constant speed for all the different speeds tested. Figure 2.9 shows the measured angular speed for each control speed tested. Each point represents the mean of all the measurements taken from the 3 instruments. Even when the chronometer method exhibits the biggest deviation, this deviation is no larger than 6% of the average speed measured using the laser tachometer. Hence, the maximum uncertainty in the speed measurements from the previous work of Koos (2009) is less than 6%.

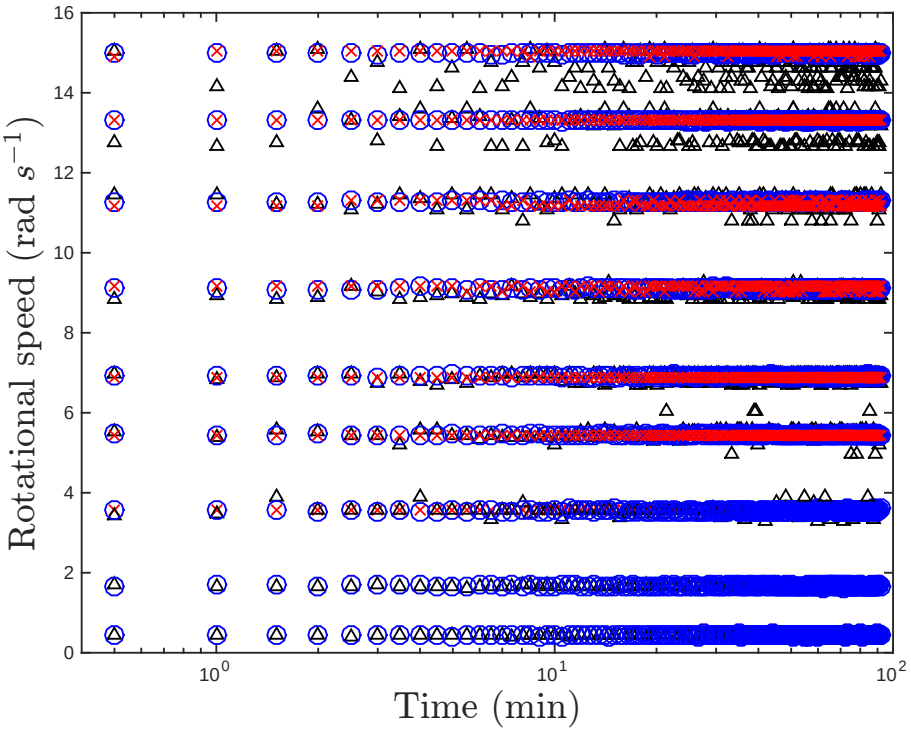

Figure 2.8: Measured rotational speed as a function of time for each measurement device. x , ◯ and △ symbols correspond to the rotational speed measurements used using the magnetic sensor, laser tachometer, and chronometer, respectively.

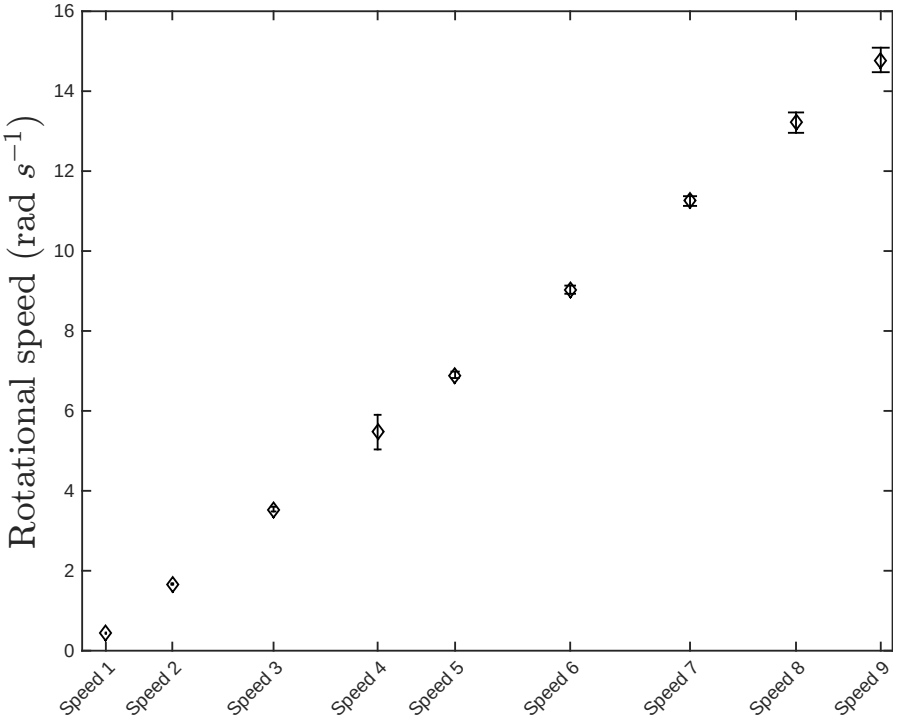

Figure 2.9: The mean rotational speed measured with the three different instruments as a function of the motor speed tested. The error bars represent the standard deviation in these measurements.

2.3 Error analysis

The uncertainty contributions considered for the torque measurements are:

- Uncertainty in spring constant measurement
- Uncertainty in distance measurement
- Uncertainty in optical probe calibration curve

A set of several repeated readings has been taken for each contribution. The mean and standard deviation are calculated for each set. The estimated standard uncertainty for each contribution is calculated as follows:

$$u = \frac{\sigma}{\sqrt{n}}, \tag{2.1}$$

where u is the standard uncertainty of the measurement, σ is the standard deviation, and n is the number of measurements. Each individual standard uncertainty is then combined in terms of relative uncertainty . The combined uncertainty is given in root mean squared (RMS) of each individual uncertainty terms,

$$u_T = \sqrt{\left(\frac{u(K)}{K}\right)^2 + \left(\frac{u(D)}{D}\right)^2 + \left(\frac{u(V)}{V}\right)^2} \tag{2.2}$$

where $u(K)$, $u(D)$, and $u(V)$ are the standard uncertainty of the spring constant, distance, and optical probe calibration, respectively. As mentioned in Subsection 2.2, the calibration curve of the optical probe used for each experiment is the mean of at least 10 curves obtained prior to each experiment. The distance uncertainty corresponds to the spring elongation measurements performed to measure the torque of the flow. At least five torque measurements are taken for each speed tested. To estimate the spring constant uncertainty, at least ten measurements of the calibration curves are considered for each spring. The uncertainty of the rotational speed is estimated as the standard deviation in the speed measurements. Both the laser tachometer and the magnet sensor are used to record the outer cylinder speed for each torque measurement. The change in suspending liquid temperature is recorded thoughout the duration of the experiments. The variation in temperature and consequently the variation in suspending liquid density and viscosity, contributes to the uncertainty in Stokes and Reynolds number (u_{St}, u_{Re}). For these dimensionless numbers the combined uncertainty is given by

$$u_{St} = u_{Re} = \sqrt{\left(\frac{u(\omega)}{\omega}\right)^2 + \left(\frac{u(\mu)}{\mu}\right)^2 + \left(\frac{u(\rho)}{\rho}\right)^2}, \tag{2.3}$$

where $u(\omega)$, $u(\mu)$, and $u(\rho)$ are the standard uncertainty of the rotational speed, viscosity, and density of the liquid, respectively.

2.4 Pure fluid torque measurements

To test the experimental method, torque measurements are performed for an aqueous-glycerine mixture with no particles and plain water. These measurements are taken with rough walls. The temperature of the fluid and density are monitored and considered when calculating the fluid properties. The range of gap Reynolds number tested is $3.6 \times 10^2 \leq Re_b \leq 8.3 \times 10^4$. The torque measurements are compared with the theoretical results for Couette flow. Considering an infinitely long cylindrical Couette device with the outer cylinder rotating and the inner cylinder being held stationary, the torque applied by a laminar flow to the inner cylinder considering smooth walls is (Schlichting, 1951)

$$M_i = -M_o = 4\pi\mu H \frac{\dot{\omega} r_i^2 r_o^2}{r_o^2 - r_i^2} = M_{laminar}, \tag{2.4}$$

where H is the height of the test cylinder, μ and ρ are the viscosity and density of the fluid, respectively, and r_i and r_o are the inner and outer cylinder radius. The decrease in gap thickness due to the rough walls have been taken into account for the values of r_i and r_o. The effect of rough walls is discussed later in this section. Figure 2.10 shows the torque as a function of the shear rate for a 77% and 21% in volume aqueous-glycerine mixture and for plain water. Each point represents the mean of 10 individually recorded measurements; the vertical error bars represent the combined torque uncertainty. The uncertainty of the shear rate is represented by the horizontal error bars. The theoretical results for Couette flow are also shown in Figure 2.10. For an aqueous glycerine mixture of 77%, the torque measurements are in good agreement with the theoretical laminar Couette solution. The maximum deviation from the laminar solution is 14%. For the lower glycerine percentage of 21% and plain water, the measured torques do not compare favorably with the torques corresponding to laminar flow theory. For both liquids the measured torques are considerably higher than the one predicted for laminar flow. The measured torques for water are very close in value to the ones measured for the 21% aqueous-glycerine mixture, even though the aqueous glycerine mixture is 1.8 times more viscous than water.

Figure 2.11 shows the measured torques normalized by the theoretical torque as a function of the gap Reynolds number defined as

$$Re_b = \frac{\rho \dot{\gamma} b^2}{\mu} \tag{2.5}$$

The reduction in shear gap width due to the rough walls has been considered when calculating the gap Reynolds number. For the case with the highest percentage of glycerine (and thus the lower gap Re range), the normalized torque is close to one. The maximum uncertainty for this case occurs at the lowest gap Reynolds number. For the case of 21% of glycerine, the normalized torque is between 4 and 15 times higher than the theoretical torque, while the normalized torque for water is between 9 and 29 times higher.

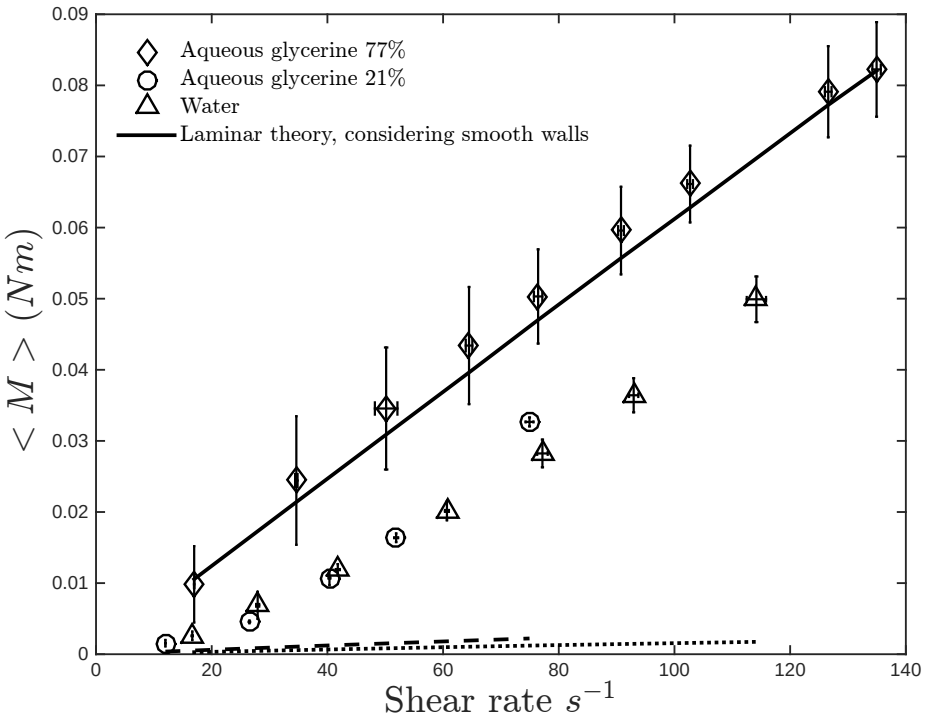

Figure 2.10: Measured torque as a function of the shear rate for an aqueous-glycerine mixture with no particles. The percentage in volume of glycerine is 77% and 21% for the aqueous-glycerine mixtures. The lines correspond to the theoretical Couette solution for a laminar flow with a viscosity corresponding to the liquid at the recorded temperatures. Continuous and dash lines correspond to 77% and 21% aqueous glycerine. Dotted line is the theoretical torque for plain water.

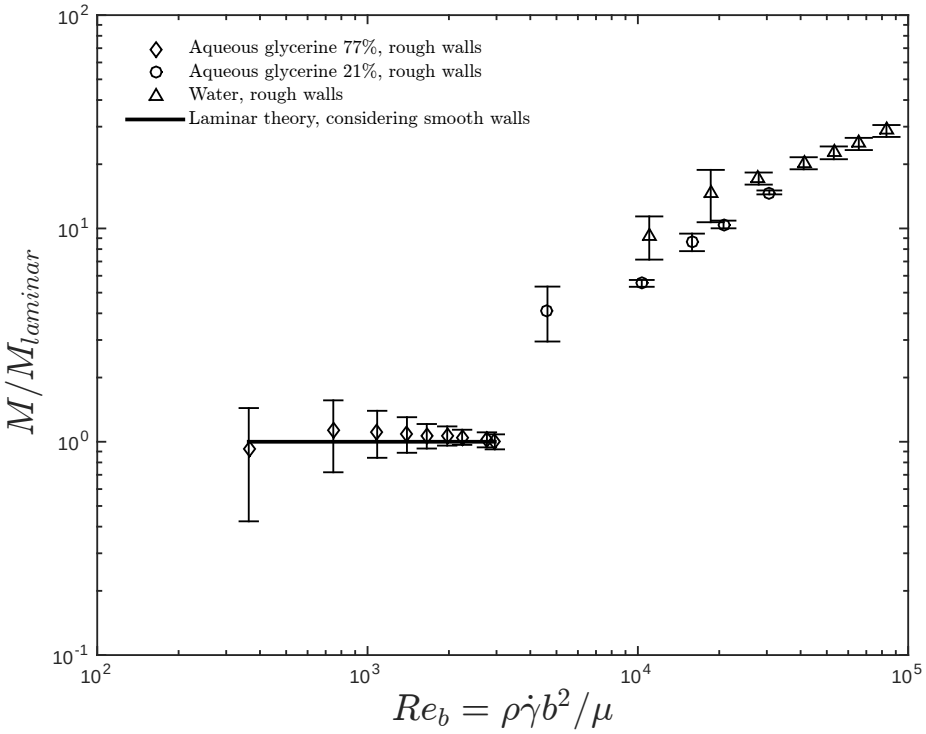

Figure 2.11: Normalized torque as a function of the gap Reynolds number for an aqueous-glycerine mixture of 77% and 21% and plain water with no particles.

To compare the current results with the work of Taylor (1936a), Figure 2.12 shows the normalized torques as a function of the modified gap Reynolds number used by Taylor, defined as

$$Re_b^* = \frac{\rho\omega r_o b}{\mu}. \tag{2.6}$$

Based on the work of Taylor (1936a,b) and considering the reduction in gap due to the rough walls, the critical gap Reynolds number at which the flow becomes unstable for the current apparatus geometry is 1.1×10^4 (for rough walls). The range of gap Reynolds number corresponding to plain water and 21% aqueous glycerine is between $4.6 \times 10^3 \leq Re \leq 8.31 \times 10^4$. Therefore, most of these experiments are above the critical Reynolds number. Figure 2.12 also shows the normalized torques from Koos (2009) performed with smooth walls. Comparing the smooth and rough walls measurements, the ratio of torques for the latter deviates from the laminar behavior at modified gap Reynolds where the smooth walls show laminar behavior. This suggests that the presence of rough walls can lower the critical Reynolds number.

Figure 2.13 shows a comparison between the current measurements and the data of Bagnold (1954); Taylor (1936a) and Wendt (1933) for pure fluid torque measurements normalized with the torque predicted from laminar theory. The normalized torques are presented as a function of the modified gap Reynolds number (Re_b^*) used by Taylor (1936a) and defined as equation 2.6. All of

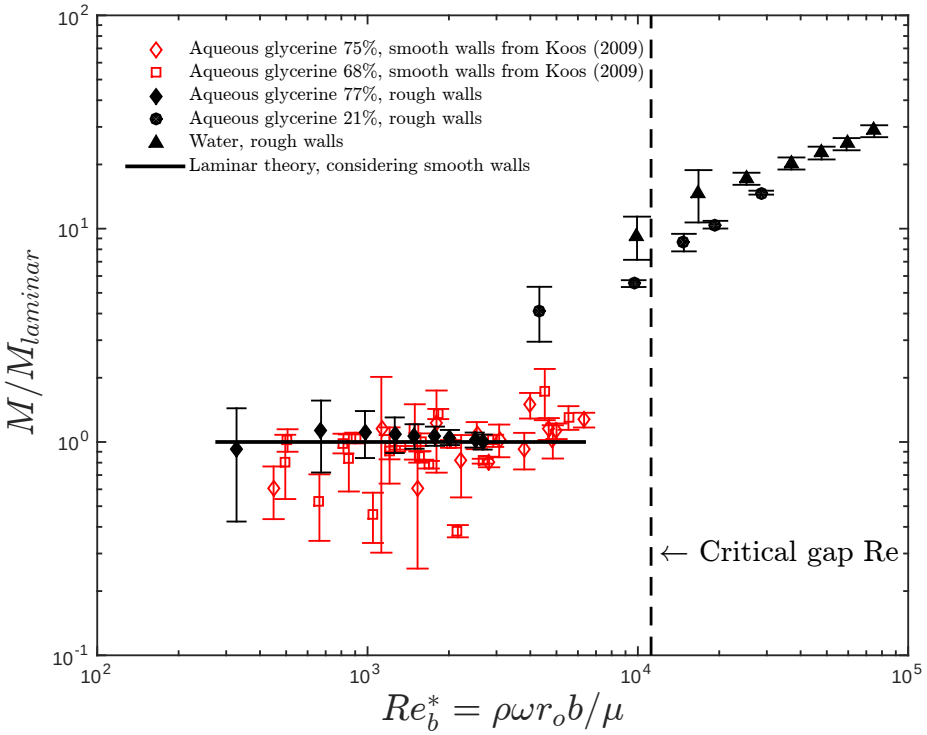

Figure 2.12: Closed symbols: normalized torques as a function of the modified gap Reynolds number for pure fluids measured with rough walls. Open symbols: normalized torques for pure fluid measured with smooth walls from Koos (2009). Vertical dashed line represents the critical modified Re based on the work of Taylor (1936a) and considers the gap width for rough walls.

these studies were performed with smooth walls. The shear gap width to outer radius ratio for the current experiments is smaller ($b/r_o = .133$) than the corresponding ratio for the data of Taylor ($b/r_o = .15$ and $b/r_o = .21$), Wendt ($b/r_o = .15$), and Bagnold (b/r_o=.19). A smaller ratio leads to lower critical gap Reynolds number. The normalized torques for the lower range of gap Re compares favorably with the current results; however, a deviation from laminar theory occurs at a lower Reynolds number than the one predicted using the data of Taylor (1936a). Cadot et al. (1997); Lee et al. (2009) and van den Berg et al. (2003) studied the effect of rough boundaries on Taylor-Couette flow, where the liquid was sheared by the rotation of the inner cylinder. These studies show that the presence of rough walls does not affect the laminar transition. A lower critical Re might be due to a smaller ratio in the annulus height to shear gap width. For the experiments of Taylor, this ratio was $h_T/b = 99$ and $h_T/b = 141$, and for the experiments of Wendt, $h_T/b = 28$, which is considerably higher than the ratio for the current experiments ($h_T/b = 14.9$). Moreover, when the flow is driven by the rotation of the outer cylinder, Taylor (1936a) observed that the transition occurred at a range of Reynolds number rather than at an specific one. Experiments on Taylor-Couette flow with rough walls and inner cylinder rotating indicate that the presence of rough walls does not affect the instability of Taylor vortex flow for low Reynolds numbers, but it does intensify the turbulent Taylor vortex flow at Reynolds numbers above the critical one (Lee et al., 2009). This rough walls effect leads to higher measured torques. The measured torque for pure fluid for the current experiments is consistent with these findings.

To verify the Newtonian behavior of the liquids used for these experiments, viscosity measurements were performed using a strain-controlled rheometer (TA instruments, ARES-RFS, Rheometrics fluid Spectrometer). The results obtained using the rheometric fluid spectrometer indicate that the liquids used are indeed Newtonian.

2.5 Particles

Two type of particles are used in these experiments: polystyrene elliptical cylinders and polyester scalene ellipsoids. The properties of these particles are summarized in table 2.2. The diameter reported in table 2.2 is the equivalent spherical particle diameter. These particles are the same particles used by Koos et al. (2012). The particles vary in size, shape, and density. These variations lead to different values for the random loose and random-close packing. The values used for these packings were obtained from the measurements done by Koos (2009).

Polystyrene: density ratio = 1 and 1.05

Figure 2.14 shows the polystyrene particles used in the current experiments, which are elliptical cylinders. The specific gravity for these particles is 1.05 and they are neutrally buoyant in an aqueous

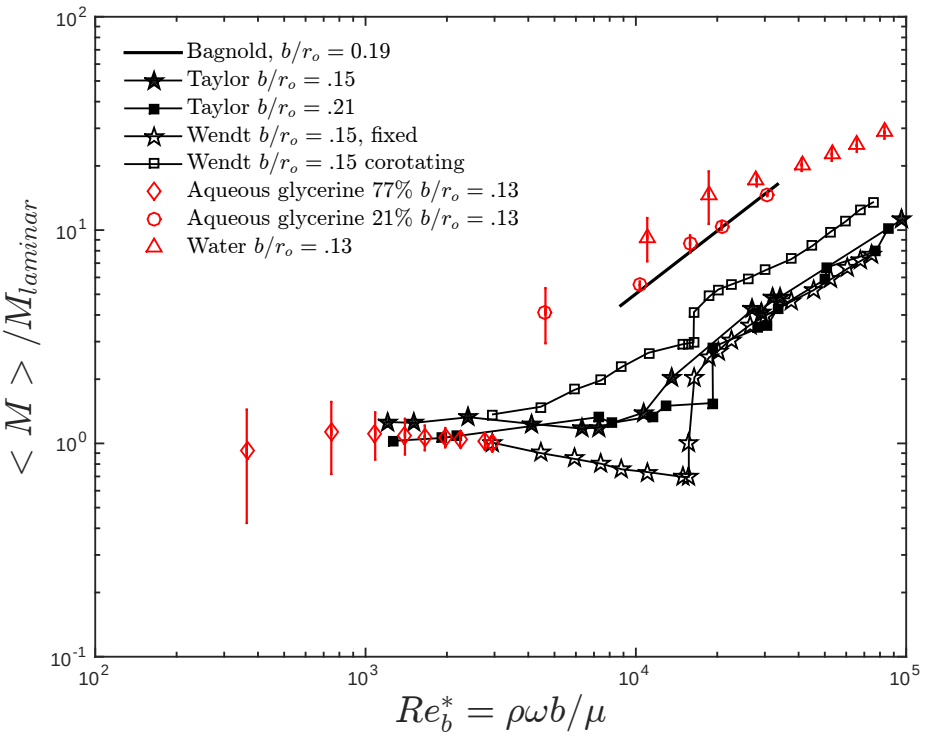

Figure 2.13: Pure fluid torque measurements normalized with laminar Couette flow as a function of modified gap Reynolds number. Comparison between pure fluid data of Bagnold (1954); Taylor (1936a) and Wendt (1933).

Property	Polystyrene	Polyester
diameter, d (mm)	3.34	2.93
$\frac{\text{gap width smooth walls}}{\text{diameter}}$, b_s/d	9.46	10.79
$\frac{\text{gap width rough walls}}{\text{diameter}}$, b/d	7.46	8.5
particle density, ρ_p (kg/m^3)	1050	1400
liquid density, ρ (kg/m^3)	1000-1050	1000-1160.5
shape	elliptical cylinders	ellipsoids
sphericity, ψ	0.7571	0.9910
RLP, ϕ_{RLP}	0.553	0.593
RCP, ϕ_{RCP}	0.663	0.65
Young's modulus, E (MPa)	3000	2800
Yield Strength, Y (MPA)	40	55
Poisson's ratio ν	0.34	0.39

Table 2.2: Particles properties

glycerine mixture of 21% glycerine. Koos (2009) measured the particle diameter and lengths of 50 particles. The sample had an average small diameter $d_{small} = 2.08$ mm, large diameter $d_{large} = 2.92$, and length $l = 3.99$ mm. The particle length was found to be bimodal, whereas the diameters were found to be unimodal. By measuring the displaced volume of 1000 particles and considering that the volume of each particle is

$$V_p = \frac{\pi}{4} d_{small} d_{large} l.$$

Koos (2009) found an equivalent sphere diameter of $d = 3.35$ mm. By weighing the same sample and considering a particle density of $\rho_p = 1050\ kg/m^3$, an equivalent sphere diameter of $d = 3.34$ was found. Both measurements were in agreement and the particles are taken to have an equivalent spherical diameter of $d = 3.34 \pm 0.02$ mm. Polystyrene particles are the ones used to roughen the

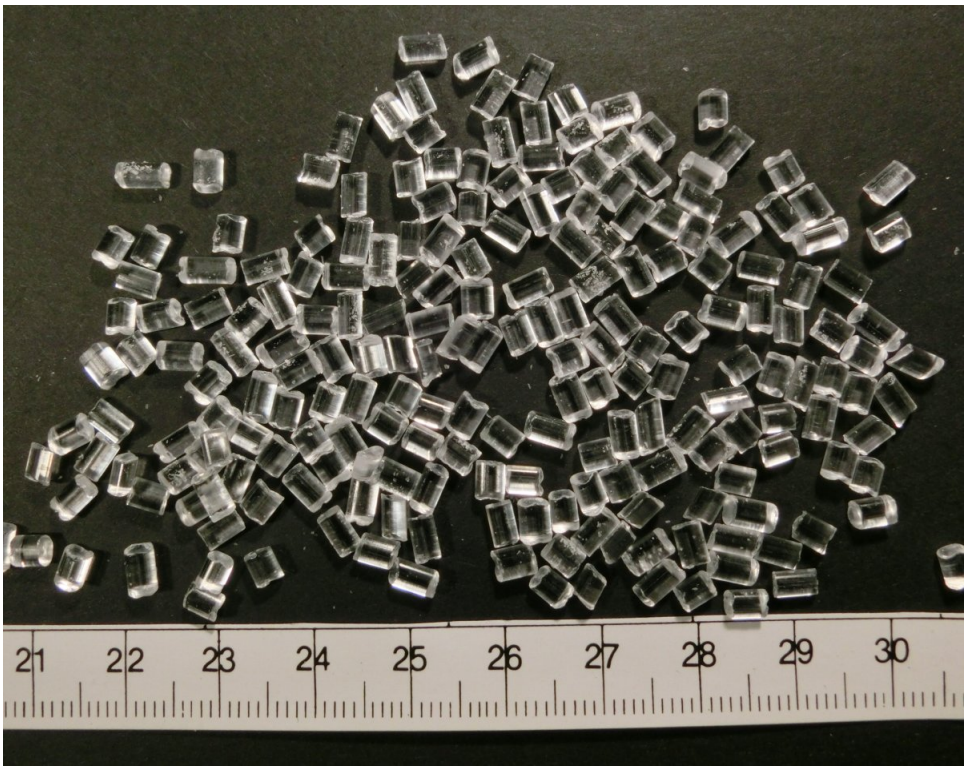

Figure 2.14: Polystyrene particles. Specific gravity of 1.05 and have an equivalent spherical particle diameter of 3.34 ± 0.02 mm. Reference shown in cm.

rheometer walls. Figure 2.15 shows a picture of the surface roughness of the walls using polystyrene particles.

Polyester: density ratio=1.2 and 1.4

The polyester particles used in the current experiments are shown in Figure 2.16. These particles have a specific gravity of 1.4 and a shape of scalene ellipsoids. Koos (2009) found an equivalent

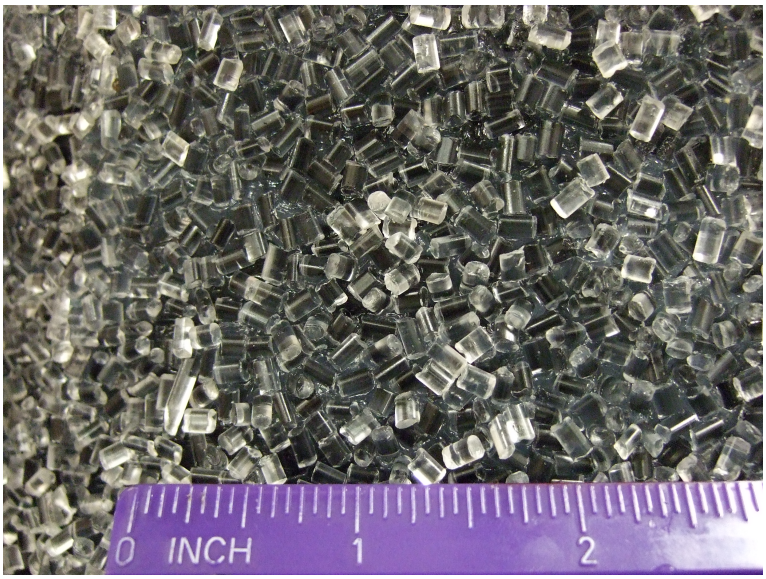

Figure 2.15: Rheometer walls surface roughness formed by polystyrene particles. The reference is in inches.

spherical diameter of $d = 2.93 \pm 0.02$ mm. The rough walls used in these experiments are the same

Figure 2.16: Polyester particles. Specific gravity of 1.4 and have an equivalent spherical particle diameter of 2.93 ± 0.02 mm. Reference shown in cm.

as the ones used for the polystyrene particles.

2.6 Visualizations

Visualizations of the flow are performed by replacing the top fixed guard and test cylinder with a transparent acrylic cylinder. This cylinder has the same radius as the inner cylinder: $r = 15.89$ cm and it is 30 cm in length. The surface of the visualization cylinder is roughened using polystyrene particles. A window of the same length of the cylinder height and 3.8 cm in width is left smooth and used for visualization purposes. Figure 2.17 shows a sketch of the visualization setup. A digital camera is located inside the visualization cylinder to record the flow. The flow is illuminated with halogen lights located on top. An acrylic ring with a width slightly smaller than the gap shear width is put on the rim of the visualization cylinder to work as an end cap. For the visualization of

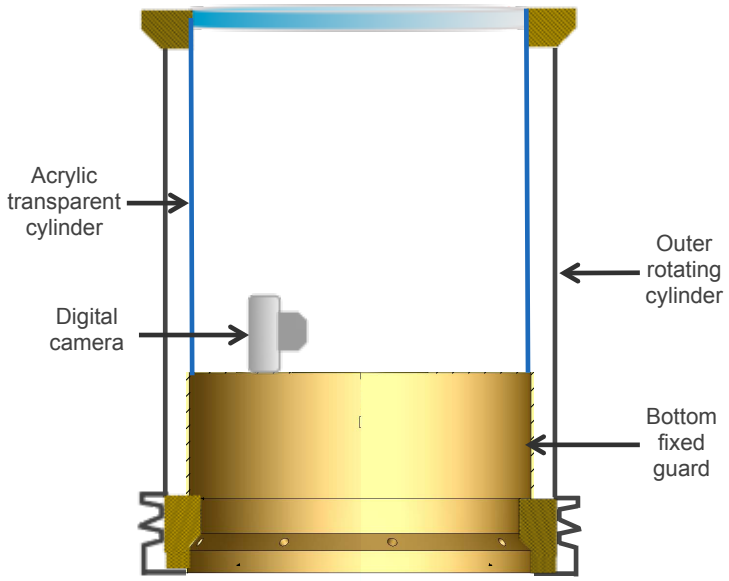

Figure 2.17: Visualization cylinder setup. The walls of the inner transparent cylinder are roughened with polystyrene particles except from the visualization window (3.8×30 cm)

the flow of polystyrene particles, 20% percent of these particles were painted on one side to better track the flow. The painted particles did not exhibit difference in density. Figure 2.18 shows a sample of painted and not painted polystyrene particles immersed in water. The mixture seems to be evenly mixed. Because of the replacement of the test cylinder with the fixed acrylic cylinder, the visualizations of the flow cannot be performed simultaneously with the torque measurements.

Figure 2.18: Sample of polystyrene particles used for visualization purposes. The particles are immersed in water. The mix of painted particles are evenly mixed with the non-painted ones, and thus the paint does not seem to have a considerable influence on particles density.

Chapter 3

Previous experiments on smooth and rough walls

The present work is a continuation of the work done by Koos (2009). A detailed analysis and revision was made to this study and the revised work was published in Koos, Linares-Guerrero, Hunt, and Brennen (2012). Further experimental work has been done since then to extend the range of Stokes and Reynolds number previously studied. This is accomplished by studying liquid-solid mixtures with particles denser than the suspending liquid. Emphasis on the effects of settling and the process of particle resuspension is explored in the current work using the same experimental setup used by Koos with minor modifications to allow the visualization of the flow as described in Chapter 2.

This chapter presents the previous experimental work done on smooth and rough walls presented in Koos et al. (2012). Differences in the calibration method between the current and previous work is explained in Section 3.1. Note that parts of this chapter are taken from the paper by Koos et al. (2012).

Most of the work done by Koos et al. (2012) involved experiments where the walls of the rheometer were left smooth and the density ratio was close to one. The range of Reynolds number tested is between 20 to 800 and Stokes numbers from 3 to 90. A set of experiments with rough walls was also presented which made it possible to quantify the effect of slip at the wall by measuring the near-wall particle velocities. The depletion layer thickness, a region next to the walls where the solid fraction decreases, was calculated based on these measurements. A relation between the relative viscosity measured with rough walls and the apparent relative viscosity measured with smooth walls was given in terms of the thickness of the depletion layer. This relation has been appropriately modified and amended from the original work of Koos (2009) and it is presented in the paper of Koos et al. (2012).

3.1 Calibration

Koos (2009) measurements involved a different calibration method than the one carried out in the current experiments. The springs were calibrated in the same way as described in Section 2.2 but only during the pure fluid calibration. The subsequent torque measurements were performed without calibrating the springs nor the optic probes, since it was thought that constraining the torque measurements through the origin would overcome any uncertainty in the torque measurements. Koos considered the liquid-solid mixture flow to be Newtonian and by using the slope between points for each experiment, the intercept of the linear fit was subtracted to the corresponding data. Constraining the torque measurements through the origin will affect the recorded torque values, but will not influence the slope of the linear fit. This slope was used by Koos (2009) to find the effective viscosity of the mixture. Therefore, any error in the y-intercept in the flow curve (shear stress versus shear rate) can affect the recorded shear stress values, but does not influence the measurement of the effective relative viscosity. Constraining the torque measurements through the origin is only valid if the torque measurements are strictly linear.

A shift in the initial optic probe target can change the voltage vs displacement curve, leading to higher measurements of the torque. For the current experiments, the spring and optic probe used for each set of experiments was calibrated before and after to account for any uncertainty in the measurement of the torque and for any non-linear behavior of the flow. Moreover, the springs were pre-loaded for each experiment to account for their initial tautness and ensure their linear response.

3.2 Previous smooth walls measurements

The smooth walls experiments performed by Koos et al. (2012) involved neutrally and slightly non-neutrally buoyant particles (ρ_p/ρ goes from 1.000 to 1.009). Most of the experiments used the same polystyrene particles used in this work. Nylon and Styrene Acrylonitrile (SAN) particles were also tested by Koos. The properties of these particles are listed in table 3.1.

These particles differed in size, shape, and density, and were suspended in an aqueous glycerine solution that had a density within 0.9% of the particle density. The nylon particles were nearly spherical and about twice the size of the polystyrene ones. The styrene acrylonitrile particles were ellipsoids with a diameter close to the polystyrene particles. The random loose packing ϕ_{RLP} and the random close packing ϕ_{RCP} of each type of particle were measured in a rectangular container with a width equal to the gap in the concentric cylinder rheometer.

Figure 3.1 shows the torque measurements results of Koos (2009) for polystyrene particles for volume fractions, from 0.077 to 0.64 with a $\rho_p/\rho = 1$ and $\rho_p/\rho = 0.991$. Each point represents the mean of at least five individually recorded measurements; the error bars represent the standard

	Nylon	Polystyrene	Styrene Acrylonitrile
diameter (mm)	6.36	3.34	3.22
diameter/ gap width	0.2013	0.1057	0.1019
density (kg/m^3)	1150	1050	1070
shape	spheres	elliptical cylinders	ellipsoids
sphericity, ψ (min./max. width)	0.9999	0.7571	0.9798
RLP, ϕ_{RLP}	0.568	0.553	0.611
RCP, ϕ_{RCP}	0.627	0.663	0.657

Table 3.1: Properties of the particles used in the smooth wall experiments performed by Koos (2009). The random loose and close packing (RLP and RCP) volume fractions were measured by Koos for each type of particle.

deviation in these measurements. Linear fits for each volume fraction are also shown. The torque increases rapidly with the volume fraction, varying by several orders of magnitude between the smallest and largest volume fraction. The dependence on the volume fraction appears to be somewhat more pronounced as the volume fraction increases. The nearly linear increase in the torque with the Stokes number (and equivalently the Reynolds number for the neutrally buoyant particles, $St = \frac{1}{9}Re$) implies that the flow in these previous experiments is close to Newtonian.

The measured torque was normalized by the corresponding torque predicted from theoretical laminar flow, $M_{laminar}$. Under the assumption that the velocity distribution of the interstitial fluid is unchanged by the presence of the particles, and that the only contribution to the torque is the result of stresses from the fluid and solid phases, the ratio of the torques, M/M_f, iFrom Koos et al. (2012).s equal to the relative apparent viscosity μ_{app}/μ. Figure 3.2 presents this ratio, which is a strong function of the volume fraction and relatively independent of the Stokes number (and equivalently the Re number), except at the two lowest volume fractions ($\phi = 0.077$ and $\phi = 0.154$) where the ratio of the torques exhibits an increase at the highest Stokes number. In Koos et al. (2012), it was shown that this increase in the deviation from the mean was likely to be due to secondary flow effects. The relative apparent viscosity for the non-neutrally buoyant experiments is lower than the neutrally buoyant experiments with the same volume fraction ($\phi = 0.30$ and $\phi = 0.40$). For the non-neutrally buoyant experiments, the particles tended to float away from the test cylinder where the measurements are taken. Therefore, the actual volume fraction in the test zone may be less than the measured one. A decrease in the volume fraction would lead to a decrease in the apparent relative viscosity, which explains why the non-neutrally buoyant experiments exhibit a lower relative apparent viscosity.

Figure 3.3 shows the apparent relative viscosity results of Koos (2009) for nylon and styrene acrylonitrile particles in aqueous glycerine mixtures that matched the density of the particles.

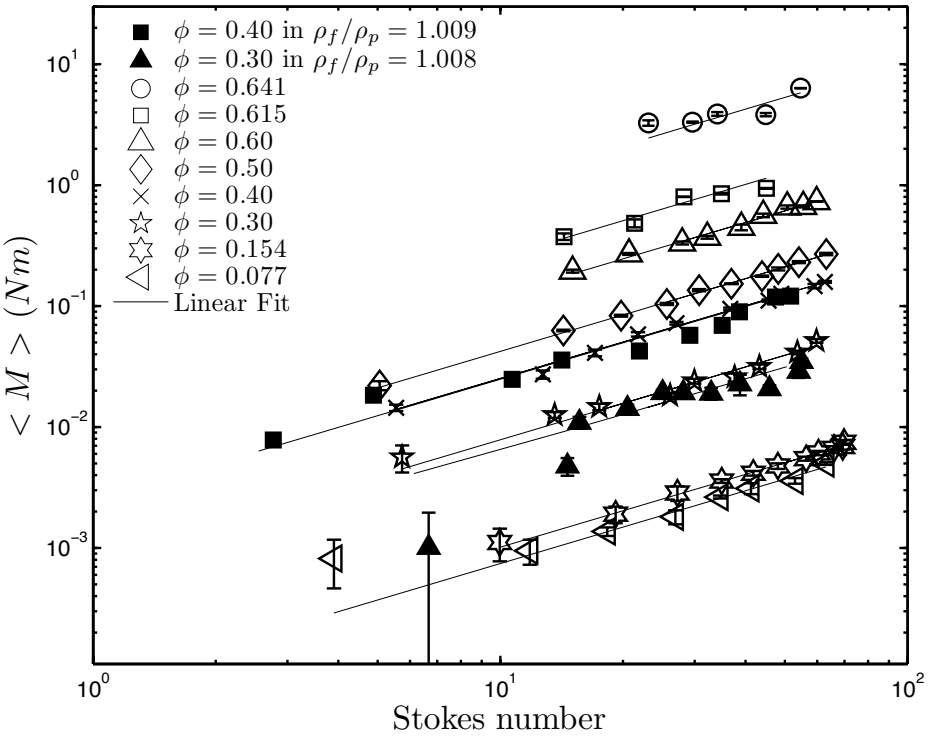

Figure 3.1: Previous torque measurements results with smooth walls. The mean measured torque ($< M >$) for suspensions of polystyrene particles in aqueous glycerine as a function of Stokes number. Closed symbols correspond to slightly non-neutrally buoyant particles. From Koos et al. (2012).

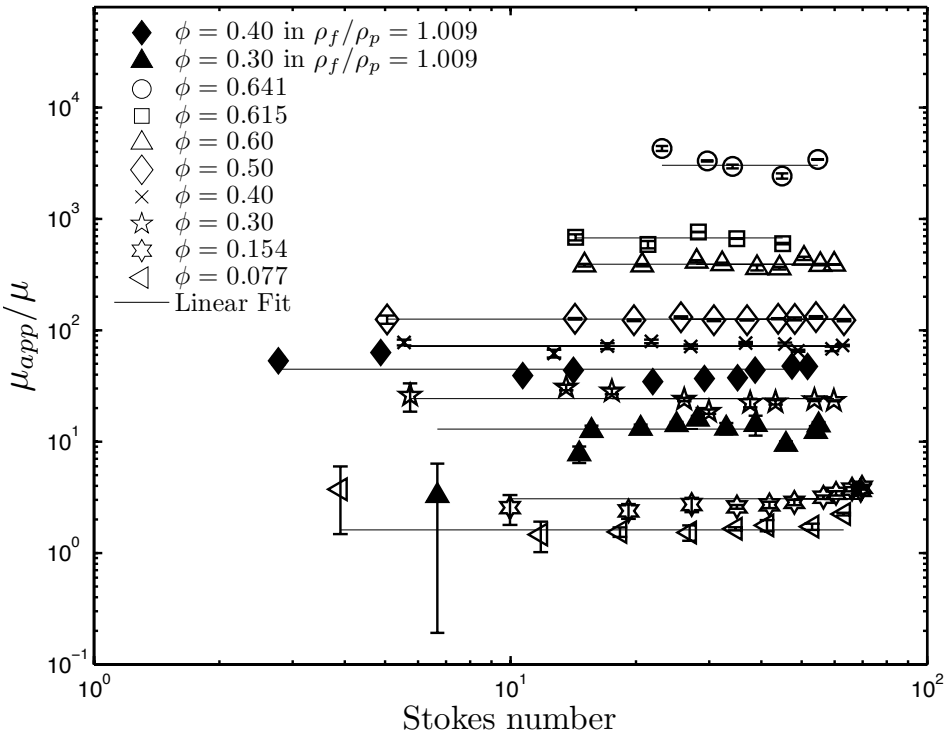

Figure 3.2: Previous normalized torques results with smooth walls. The ratio of measured to pure fluid torque (μ_{app}/μ) for suspensions of polystyrene particles in aqueous glycerine. Closed symbols correspond to non-neutrally buoyant particles. From Koos et al. (2012).

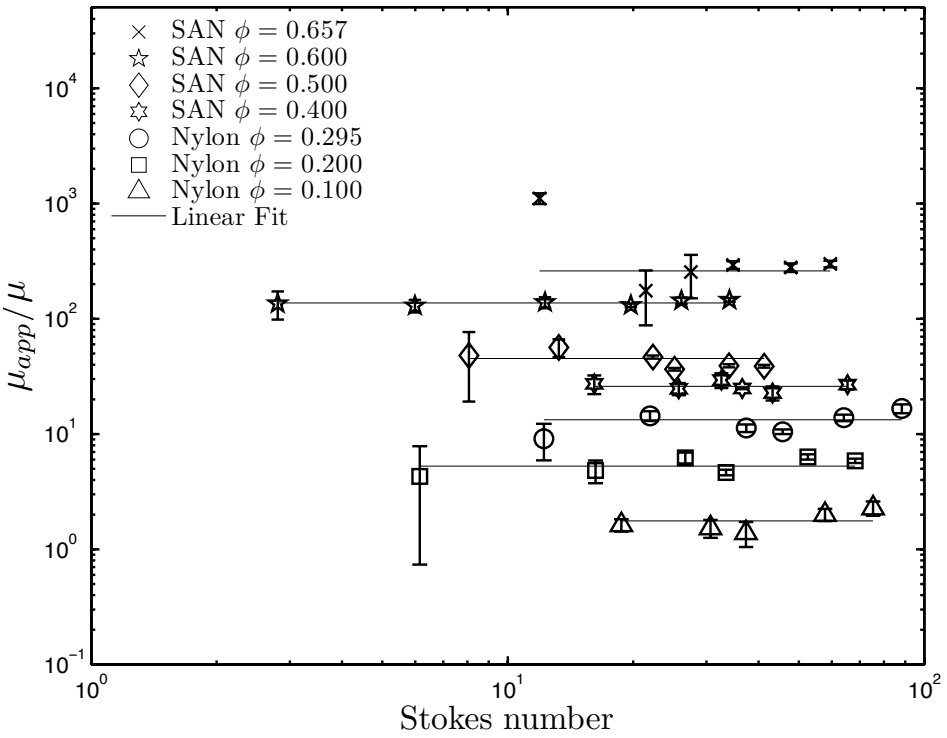

Figure 3.3: Previous results for nylon and SAN particles apparent relative viscosity (Koos et al., 2012).

The relative apparent viscosity for these experiments is also a function of the volume fraction and independent of the Stokes number except at the highest solid fraction. To compare the three experiments, the volume fraction was normalized by the random loose packing ϕ_{RLP} of each type of particles. By fitting horizontal lines to the data in Figure 3.2 and Figure 3.3 the dependence of

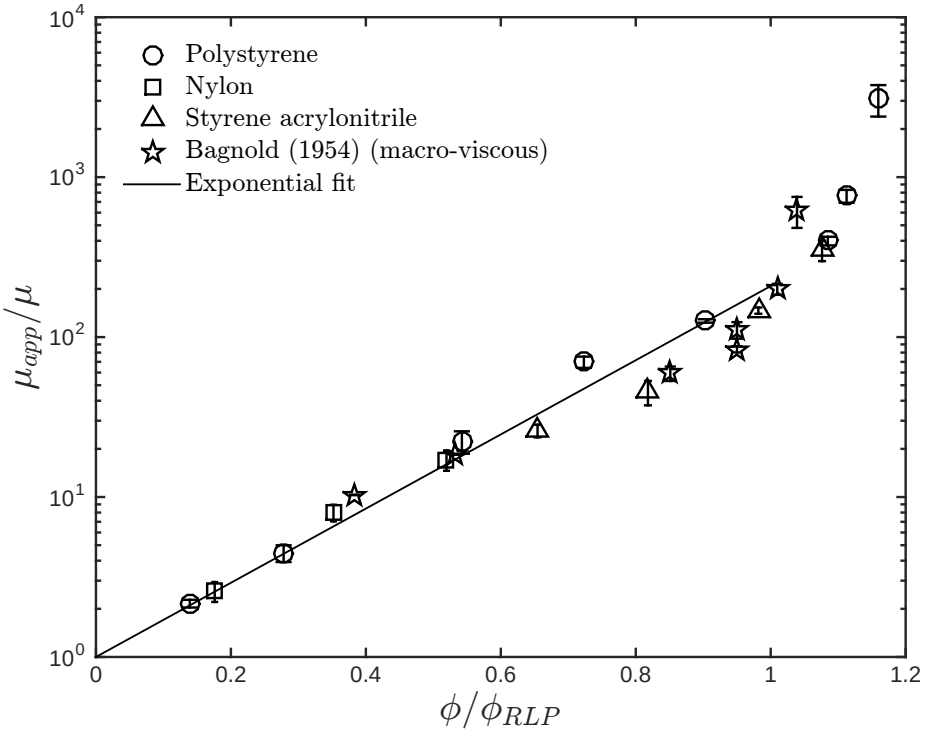

Figure 3.4: Previous results of the apparent relative viscosity for different non-settling particles in aqueous glycerine. Closed symbols correspond to non-neutrally buoyant polystyrene particles. The line is an exponential fit to the data in the region, $\phi/\phi_{RLP} < 1$. From Koos et al. (2012).

μ_{app}/μ on the volume fraction was obtained, as shown in Figure 3.4. The data in Figure 3.4 are plotted against the normalized volume fraction, ϕ/ϕ_{RLP}. Despite differences in the particle sizes and shapes, the data for all the particles tested by Koos fall along a single curve, which correlates with the volume fraction ratio.

The differences in apparent relative viscosity between $\phi > \phi_{RLP}$ and $\phi < \phi_{RLP}$ were attributed to the possible jamming of the particles. When ϕ is higher than ϕ_{RLP} the particles are not able to move past each other without deforming, which further increases the apparent viscosity. The previous smooth wall experiments show that when normalized by the size and shape dependent random loose packing fraction, ϕ_{RLP}, the relative apparent viscosity shows no dependence on the particle size or shape. Comparing the nylon to SAN particles, both have a high sphericity ($\psi = 1.00$ and 0.98), but the nylon particles are nearly twice the size of the SAN particles. Comparing the rod-shaped polystyrene particles to the nearly spherical SAN particles, there is also no difference in the measured effective viscosity. This result is different from what has been reported for low

Reynolds number suspensions, where the influence of the particles shape on the bulk viscosity has been studied (Clarke, 1967; Ward and Whitmore, 1950; Moreland, 1963). These studies showed that the more the shape of the particle deviated from that of a sphere, the greater was the bulk viscosity. Moreover, aspherical particles demonstrate increased ordering near the walls (an effect that is more pronounced for the smooth walls) (Chrzanowska et al., 2001; Börzsönyi et al., 2008).

Figure 3.4 shows the comparison between the previous smooth walls results of Koos (2009) and the previous experiments of Bagnold (1954). Only the Bagnold experiments that were free of secondary flows ($Re_b < 6,000$) are considered. The macro-viscous data from Bagnold (1954) compares favorably with the experiments of Koos (2009) and shows a similar transition at ϕ_{RLP}.

3.3 Previous rough walls experiments

Among the factors that influence the results described above is the particular structure of the liquid/solid flow at the walls of the apparatus, namely the reduction in the volume fraction near the wall and the apparent particle slip associated with that less concentrated layer. This slip is most apparent with smooth walls (Yilmazer and Kalyon, 1989; Gulmus and Yilmazer, 2007); it may lead to an erroneous mixture viscosity if a correction is not applied Barnes (2000). Experiments have shown that the slip is significantly reduced when the surface roughness is the same size as or larger than the diameter of the particles Barnes (2000). To further investigate the influence of slip on the mixture viscosity measurements, Koos performed additional experiments with rough walls using polystyrene particles. The inner and outer cylinder walls were roughened by coating them with the same polystyrene particles. The particles were glued to thin rubber sheets, which were then attached to both surfaces. The glued particles were oriented randomly and had a surface area fraction of 0.70. The decrease in gap thickness due to the rough walls was considered when calculating the shear rate for these experiments.

Figure 3.5 shows the normalized torque done by Koos (2009) with rough walls. The volume fractions tested ranged from 0.10 to 0.60. For each volume fraction, the measured torques were nearly a linear function of the Stokes number as in the case of the smooth wall data. The effective viscosity ratio increases by almost four orders of magnitude between the lowest volume fraction and the highest volume fraction. This large increase is similar to that in the smooth wall experiments.

The mean effective viscosity ratios corresponding to the horizontal lines in Figure 3.5 are plotted against the volume fraction in Figure 3.6 and compared with the smooth wall data. The large increases in the relative apparent viscosity above ϕ_{RLP} that were present in the smooth wall experiments (see Figure3.4) are not present in the rough wall data and therefore appear to be an artifact of the wall slip and depletion layers, as described in the next section. The rough wall data correlate

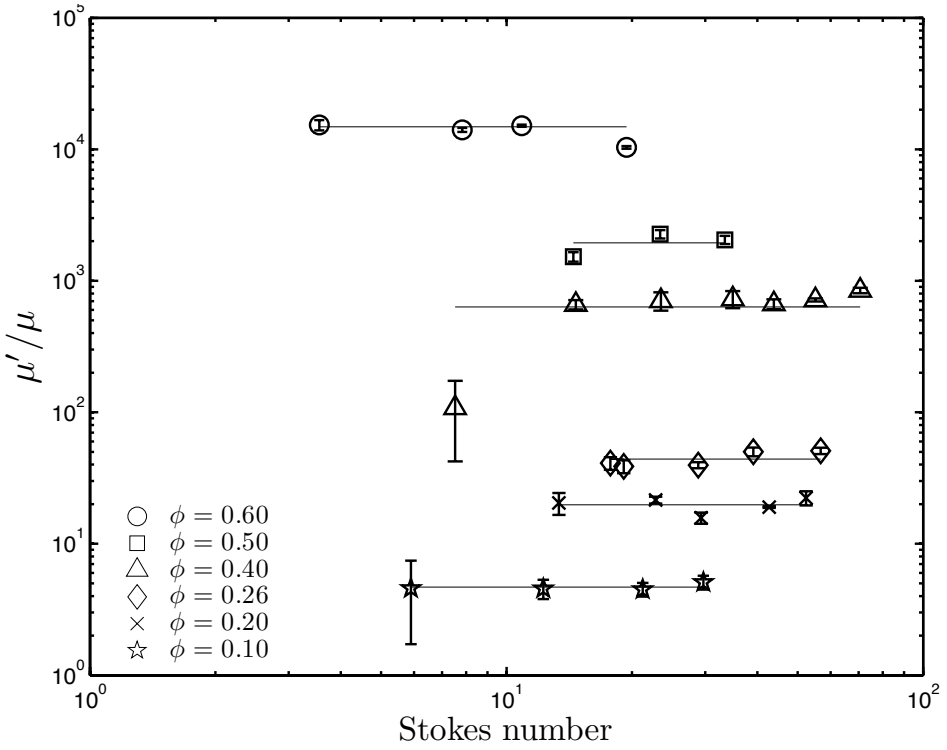

Figure 3.5: Ratio of measured torques from previous rough walls experiments. The horizontal lines are fits to the data and represent the value of the ratio of effective viscosity to pure fluid viscosity μ'/μ. From Koos et al. (2012).

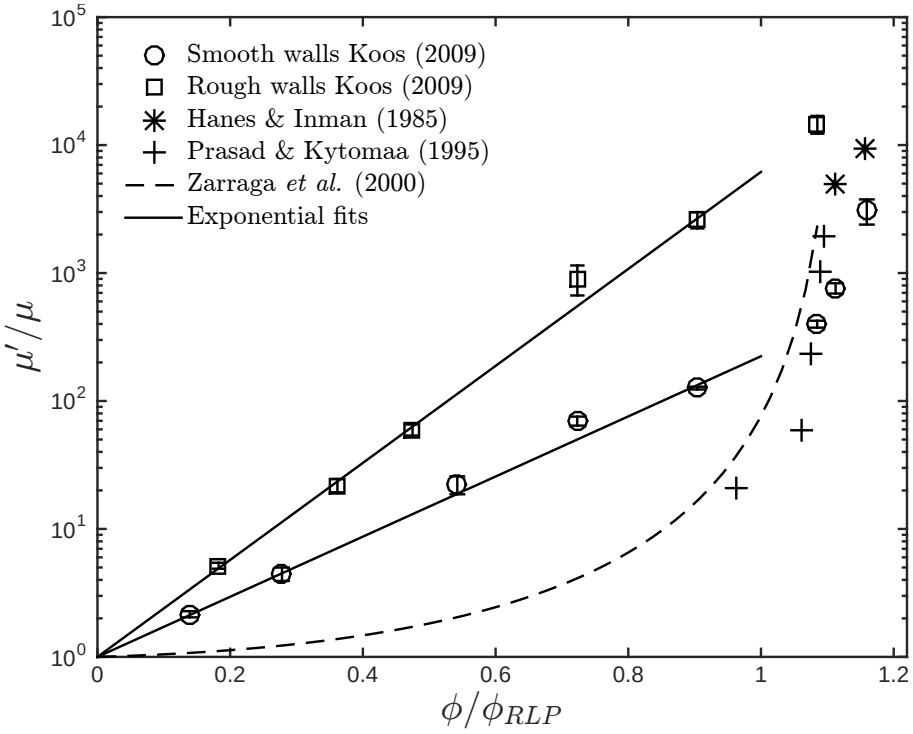

Figure 3.6: Effective viscosity ratio for neutrally buoyant polystyrene particles in aqueous glycerine solutions with rough cylinder walls. The black line is an exponential fit for the points below ϕ_{RLP}. From Koos et al. (2012).

with the volume fraction ratio and, for $\phi < \phi_{RLP}$, conform to

$$\mu'/\mu = \exp\left(8.73\frac{\phi}{\phi_{RLP}}\right), \quad \phi < \phi_{RLP}. \tag{3.1}$$

In Figure 3.4 comparison is made with the data of Hanes and Inman (1985), Prasad and Kytömaa (1995), and the empirical formula of Zarraga et al. (1999). The effective viscosities from Hanes *et al.* and Prasad *et al.* were obtained for the ratio of measured torque reported in their work and the theoretical interstitial fluid torque; their data exhibit a smaller relative effective viscosity than the current rough walls experiments. However, their experiments used settling particles; in addition, the torque was measured on the top surface of their annular gap. Hence, the torque measurements may have been affected by the migration and settling of the particles away from the top surface of the experiments. Nevertheless, the relative effective viscosities from Hanes & Inman are close to the previous data of Koos (2009). The shear rates used in their experiments were higher than those used by Prasad & Kytomaa, which may have caused a better fluidization of the suspension.

The model of Zarraga *et al.* does not fit the data of Koos. The particles used in their experiments are much smaller (of the order of microns) and therefore correspond to much lower Reynolds number ($1 \times 10^{-6} \leq Re \leq 3 \times 10^{-2}$ (Acrivos et al., 1994; Zarraga et al., 1999; Ovarlez et al., 2006; Bonnoit

et al., 2010). The apparent difference in relative effective viscosities may be due to a difference in the flow regime for this lower range of Reynolds numbers. Since particle interactions increase with Reynolds number and such interactions may cause mixing in the fluid, this could lead to an increase in the viscosity.

Depletion layer thickness

An analysis of the slip occurred with smooth walls was presented by Koos (2009). Though the interstitial fluid does not violate the no-slip condition at a solid wall, the solid particles may roll and slide, creating an effective slip (Acrivos, 1992). Slip is composed of two components. In the first component, "true slip", solid particles are able to slide over stationary walls with a non-zero velocity, creating a particle slip velocity, which is often present in granular flows (Barnes, 1995) and more marked in densely packed flows ($\phi > \phi_{RLP}$). The second component of slip, "apparent slip", is caused by the lower concentration of particles close to the walls, resulting in a lower effective local viscosity and a higher velocity gradient. Koos modeled the decrease in volume fraction near the wall by incorporating a thin depletion layer of thickness δ next to the wall in which particles are not present. This model assumes that the viscosity is uniform in both the depletion layer and the bulk core region. Amends to the model presented by Koos (2009) were done to account for algebraic mistakes. A corrected version of the model is presented in Koos et al. (2012). The model proceeds as follows. The shear stress at the inner cylinder is given by

$$\tau_i = \mu_{app} 2\omega \frac{r_o^2}{(r_o^2 - r_i^2)}, \tag{3.2}$$

where μ_{app} is the apparent viscosity of the mixture (calculated from the measured torques with smooth walls). Assuming a thin inner depletion layer devoid of particles in which the shear rate is $\dot{\gamma}_i$ it also follows that $\tau_i = \mu \dot{\gamma}_i$. Consequently, the apparent viscosity can be related to the viscosity of the two phase mixture, μ' (which is assumed to be equal to the effective viscosity measured with rough walls),

$$\mu_{app} = \frac{\mu'}{2a\left(\frac{\mu'}{\mu} - 1\right) + 1}, \tag{3.3}$$

where a is a function of the depletion layer thicknesses, δ_i and δ_o, on the inner and outer walls, respectively (see Koos et al. (2012) for derivation):

$$a = \frac{\left(\frac{\delta_i}{b} r_o^3 + \frac{\delta_o}{b} r_i^3\right)}{r_o r_i \left(r_o + r_i\right)}. \tag{3.4}$$

Previous investigations have shown that the depletion layer thickness is generally smaller than one particle diameter; its thickness increases linearly with particle diameter and, at the same volume

fraction, increases linearly with the shear stress (Soltani and Yilmazer, 1998). While these depletion layers may be smaller than a particle diameter, they can significantly change the apparent viscosity (Barnes, 2000). In addition, the radial force in a cylindrical geometry due to differences in fluid and particle densities may accentuate the depletion layer on the inner or outer cylinder surfaces. At large volume fractions, Buscall et al. (1993) and Barnes (1995) have found that the slip on the outer cylinder wall is negligible and that roughening the inner cylinder is sufficient to reduce the slip at the inner wall. Direct measurements of either the slip layer thickness or measurements of both the actual and apparent viscosities are needed to quantify this error.

Using the values of the smooth (apparent) and the rough (effective) viscosity data of Figure 3.6, the function a and the depletion layer thickness can be calculated for each volume fraction. Figure 3.7 shows the depletion layer thicknesses calculated using the smooth walls data from Koos (2009) and assuming that slip occurs either on the inner cylinder alone or that the depletion thicknesses are the same on both the inner and outer cylinders. Typical depletion layer thicknesses derived

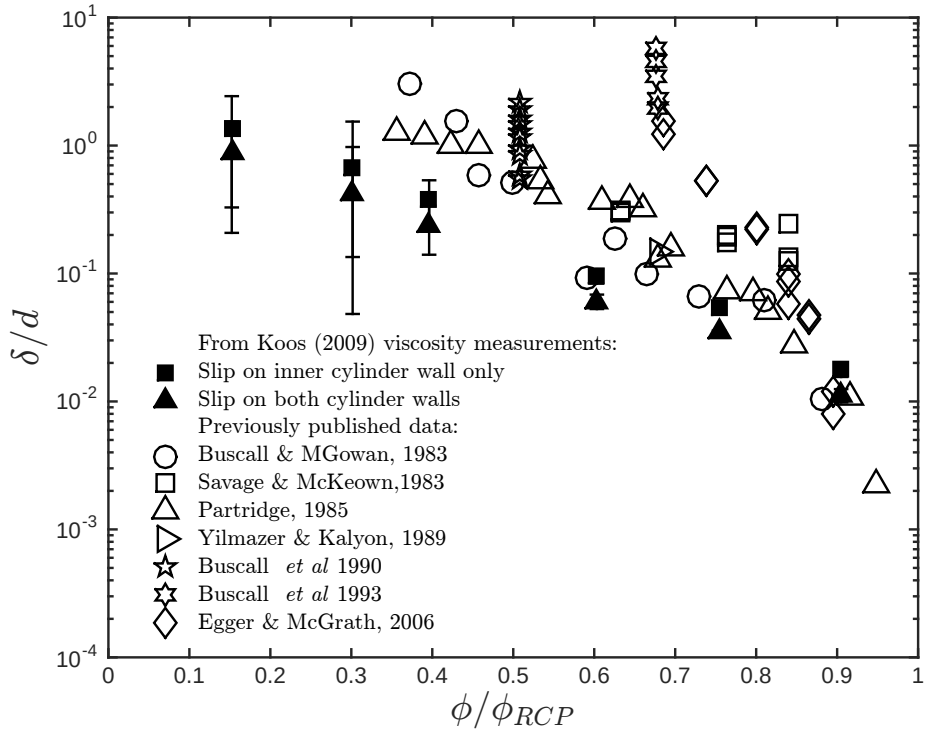

Figure 3.7: Depletion layer thicknesses (divided by the particle diameter) calculated from previous apparent and effective viscosity measurements of Koos (2009), using equation 3.3 (closed symbols) as a function of the volume fraction ratio ϕ/ϕ_{RCP}, where ϕ_{RCP} is the random close packing. The error bars account for the standard deviation in the torque measurements. Also shown are typical depletion layer thicknesses on the inner cylinder of concentric cylinder devices from references (Buscall et al. (1993); Savage and McKeown (1983); Yilmazer and Kalyon (1989); Buscall et al. (1993); Partridge (1985); Buscall et al. (1990); Egger and McGrath (2006) (open symbols).

from previously reported data are also shown in figure 3.7. The random close packing was used to

normalized the volume fraction. The Savage and McKeown shear stress measurements data with smooth and rough wall were used to calculate the depletion layer thickness by using equation 3.3 and assuming slip on the inner cylinder only. Savage and McKeown (1983) used polystyrene beads $d \approx 1$ mm particles that are approximately the same size as the ones used in the rough wall experiments of Koos. Egger and McGrath data for a $d \approx 0.5$ μm emulsion were obtained by considering slip on both cylinders and following a different approach described by the authors and discussed later in this section. The rest of the data in figure 3.7 were calculated from shear stress measurements for $d \approx 1$ μm polystyrene beads as reported in Buscall et al. (1993) and considered slip only on the inner cylinder. The calculated depletion layer thickness from the data of Koos is close to, though slightly less than, previously recorded data. This may due to the fact that Egger and McGrath (2006) and Buscall et al. (1993) considered a more idealized scenario. Egger and McGrath followed the approach made by Russel and Gran (2000) where they assumed that the applied shear stress at a given radius is uniform over the whole sample. Egger and McGrath validated this assumption by the closeness in the mapping of their rough wall data and the slip corrected data. Buscall et al. (1993) assumed that the actual viscosity (which they called true viscosity) is large enough so its inverse value can be neglected. With the data of Koos, there is little difference between the predicted values using slip on the inner wall or on both walls, though the assumption of slip in the inner wall alone results in a better match to previously recorded data.

Slip velocity measurements

The depletion layer on the inner cylinder can also be estimated from particle velocities measurements. Koos (2009) evaluated the velocities of the particles next to the inner cylinder by using a pair of MTI fiber-optic proximity probes that were installed flush with the surface of the inner cylinder at an observation port 2.86 cm below the test cylinder. These were used to both count the particles passing the probe and, by cross-correlation, to measure the velocity of those particles. The cross correlation was done over a full ten seconds to find the mean particle velocity and the measurement of individual particle velocities.

Using the velocities measurements performed by Koos, and assuming that there are no particles in the depletion layer and that the particles viewed by the optical probes are those at the depletion layer-core region interface, the interfacial velocity, u, at $r = r_i + \delta_i$ is given by

$$\frac{u}{\omega r_o} = \frac{2\delta_i r_o}{r_o^2 - r_i^2} \frac{\mu_{app}}{\mu}, \tag{3.5}$$

(see Koos et al. (2012) for derivation) and this can be used along with the measured particle velocities, u, to obtain estimates of the depletion layer thickness, δ_i. Figure 3.8 shows the calculated thicknesses as a function of Stokes number and volume fraction. Note that the thickness is relatively independent

of Stokes number but varies substantially with the volume fraction. The same data is included in Figure 3.9, where it is seen to be consistent with the values derived from the present rheological measurements. Note that the estimates for the depletion layer thickness fall slightly below previously published data for volume fractions below ϕ_{RLP}. This deviation can be explained by the ordering of particles next to the walls. Specifically, the surface area oriented towards the optic probes fluctuates as a function of the distance from the wall Chen and Louge (2008). These fluctuations can give rise to errors in the measurements of the particle velocity. In the previous experiments of Koos (2009), the orientation of the particles should result in the depletion layer thickness being underestimated.

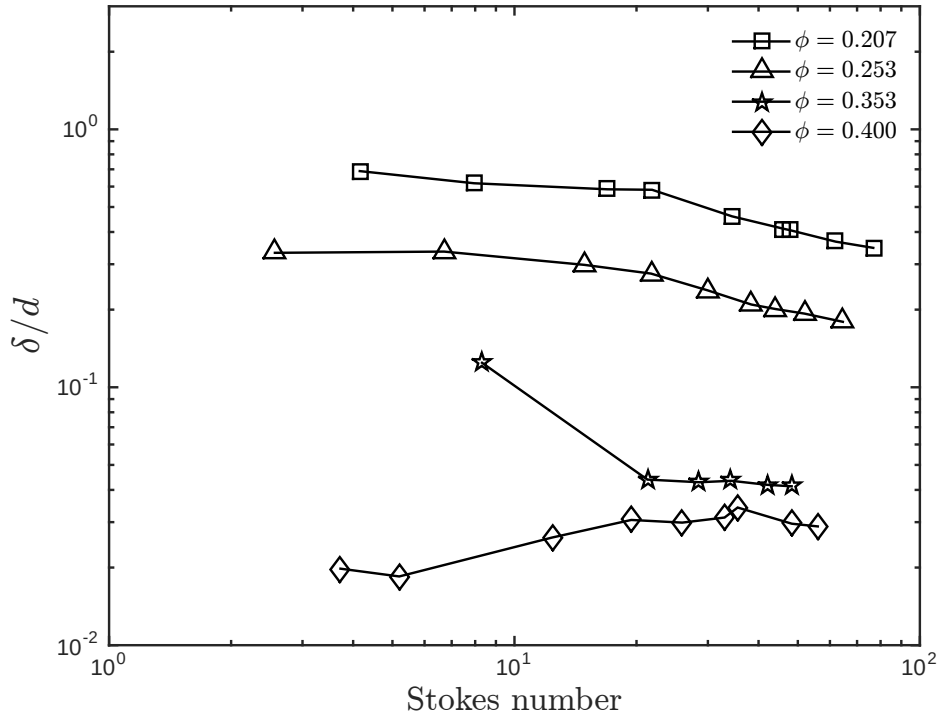

Figure 3.8: Depletion layer thicknesses (δ) calculated from Koos (2009) particle velocity measurements as a function of Stokes number for several volume fractions. From Koos et al. (2012).

3.4 Summary

The previous work covered a range of moderate Stokes number (from 3 to 90). For the smooth walls three different types of particles were tested. Despite differences in the particle materials, sizes, and shapes, the data for all tested particles correlate with the volume fraction ratio for $\phi < \phi_{RLP}$. A slight mismatch in the fluid and particle density (within 1%) does not change the dependency of the apparent viscosity on the volume fraction ratio ϕ/ϕ_{RLP}.

In the "rough wall" experiments only one type of particles was tested. These particles were glued to both the inner and outer cylinder walls. This configuration appears to result in appropriate

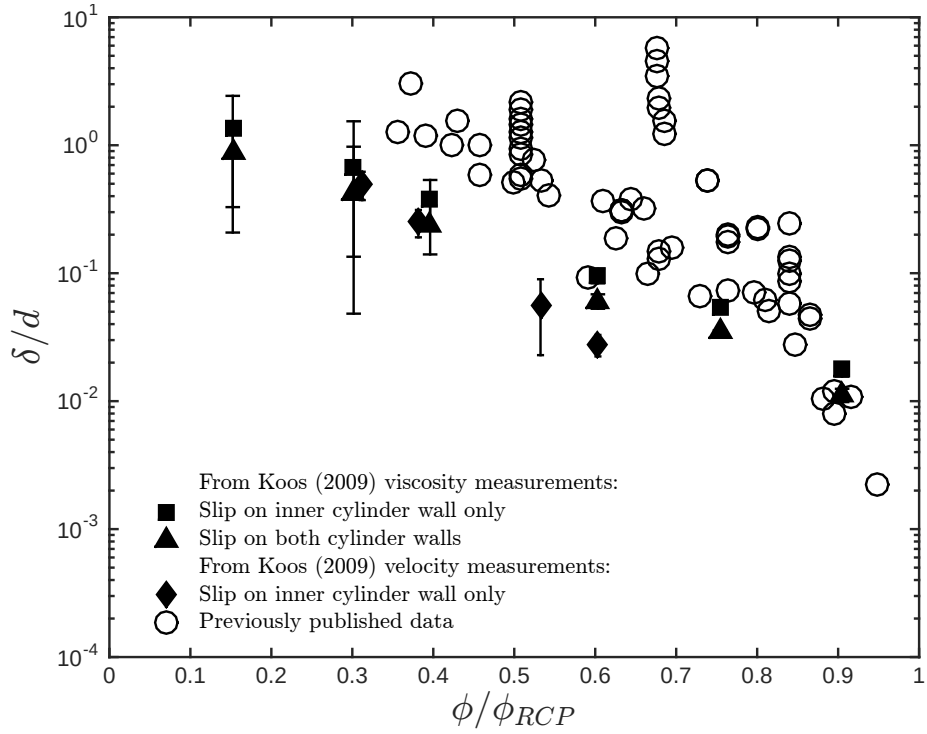

Figure 3.9: Depletion layer thicknesses calculated from previous measurements of the apparent and effective viscosity using equation 3.3 and depletion thicknesses calculated from the velocity measurements using equation 3.5. Also shown are the previously reported experimental values from figure 3.7. From Koos et al. (2012).

effective mixture viscosities that increase exponentially with the volume fraction up to the loose packed volume fraction. On the other hand, the measurements with smooth wall cylinders clearly demonstrate that wall slip substantially affects the apparent viscosity. The slip was modeled by assuming thin depletion layers on the smooth walls. The thickness of the depletion layers was estimated by measuring the particle velocities near the walls. In addition the values for the rough and smooth wall viscosities were used to evaluate the thickness of the depletion layer over the full range of volume fractions. From these two methods the resulting depletion layer thicknesses are shown to be in agreement with previous investigations. For volume fractions less than the loose packed volume fraction, ϕ_{RLP}, the slip is caused by thin depletion layers that decrease in thickness as the volume fraction is increased. For $\phi > \phi_{RLP}$, slip caused by particles sliding over the cylinder walls appears to dominate and contributes significantly to the differences between the smooth and rough wall measurements.

The previous torque measurements for rough and smooth walls scale linearly with the shear rate and only the experiments with volume fractions lower than 20% exhibited a deviation from the linear behavior at high Stokes numbers. Such deviation is likely to be due to inertial effects of the suspending liquid. In this previous study, evidence of particle interaction's effect on the scaling of the shear stress with the shear rate was not observed. However, the measured relative viscosities are higher than the previous experiments, which may result from the induced mixing of the fluid due to particle interactions.

Chapter 4

Rheological measurements with rough walls

4.1 Motivation

The previous experimental work of Koos et al. (2012) provided evidence of the presence of slip at the walls. Such slip can lead to marred conclusions if the rheological measurements are not corrected. The presence of slip can lead to measurements of lower effective relative viscosities, as was shown by Koos et al. (2012). In the case of particles denser than the liquid, the centripetal force due to the rotation of the outer cylinder would tend to push the particles away from the inner cylinder, increasing the depletion layer thickness and thus reducing the measured torques. The slip at the wall can be reduced by roughening the walls of the experiment (Barnes, 1995; Buscall et al., 1993). For this reason, all the experiments presented in this work were conducted with rough walls.

Aside from reducing the slip, rough walls are expected to enhance particle interactions. One of the aims of this work is to study the effect of such interactions on the bulk rheology of the flow.

4.2 Polystyrene particles with matched fluid density

The direct torque measurements for a volume fraction (ϕ) of 10, 20, and 30% as a function of the shear rate ($\dot{\gamma}$) are shown in Figure 4.1. Each point represents the mean of at least five individually recorded measurements; the uncertainties in measuring the torque are combined in root mean square sense (see Section 2.3) and are represented by the error bars. As mentioned in Chapter 2, the torque measurements presented here are directly measured and no correction due to contributions of friction or fluid turbulence is made. The plots also include a linear curve fit for each set of data ($R^2 = 0.993$ for 10%, $R^2 = 0.982$ for 20% and $R^2 = 0.984$). A linear relation between the torque and shear rate would correspond to a Newtonian behavior. However, the linear fit for these measurements does not intercept the origin; instead the linear fit has a negative intercept. As shown in Figure 4.1, the

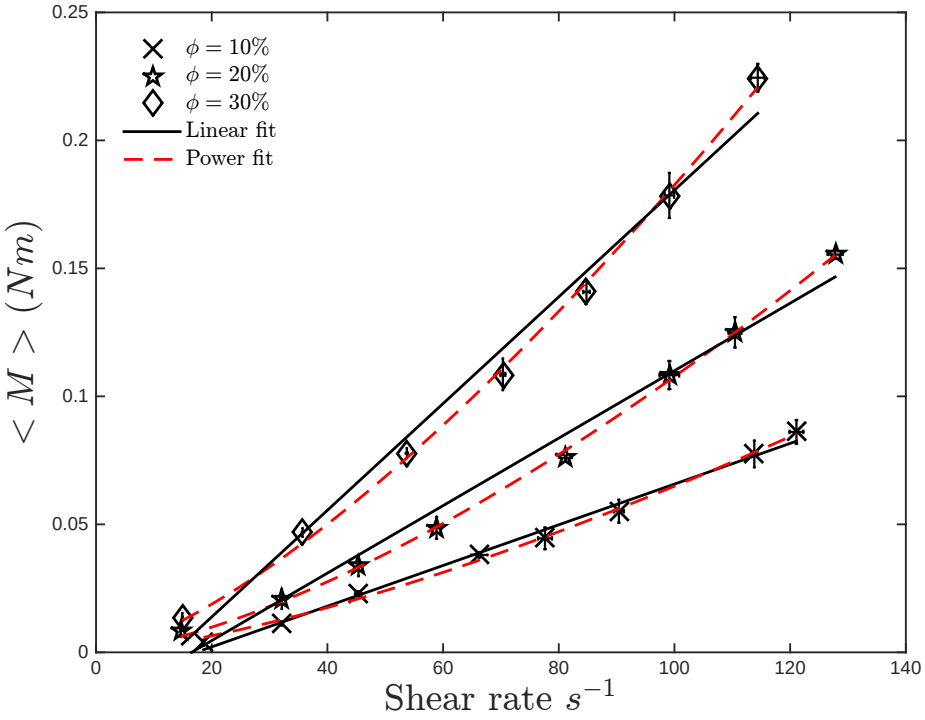

Figure 4.1: Measured torque as a function of shear rate for $\phi = 10$, 20, and 30%. $\rho_p/\rho = 1$. Solid and dashed lines are the linear and power curves fit for the present data. The error bars correspond to the combined uncertainty in the torque measurements.

trend for this set of data is not strictly linear and can also be fitted to a power law, as shown by the dashed lines. The power fit has higher R^2 values than the linear fit ($R^2 = 0.997$ for 10%, $R^2 = 0.999$ for 20% and $R^2 = 0.998$). The exponent of the power fit is around 1.4 for the three volume fractions shown.

Figure 4.2 shows the torque measurements for higher volume fractions of 40% and 50%. Unlike the lower volume fractions, these data are best fitted by a linear fit ($R^2 = 0.997$ for both volume fractions). For these higher volume fractions the intercept of the linear fit is no longer negative. A positive intercept could be a sign of the presence of a yield stress.

The torque measurements were normalized by the theoretical Couette laminar flow torque for the interstitial liquid. Figure 4.3 presents this ratio for the solid fraction of 10, 20, and 30% as a function of Stokes number. If the mixture were strictly Newtonian, this ratio would be equivalent to the relative effective viscosity, and would be independent of the Stokes number (constant viscosity). But as it can be seen in Figure 4.3, the relative viscosity increases with Stokes number. For higher volume fractions the ratio of torques does not appear to vary dramatically with the Stokes number, as shown in Figure 4.4. Only at low Stokes numbers the ratio of $M/M_{laminar}$ for these higher volume fractions exhibits a weak dependance on St, where $M/M_{laminar}$ is greater than that found at higher St.

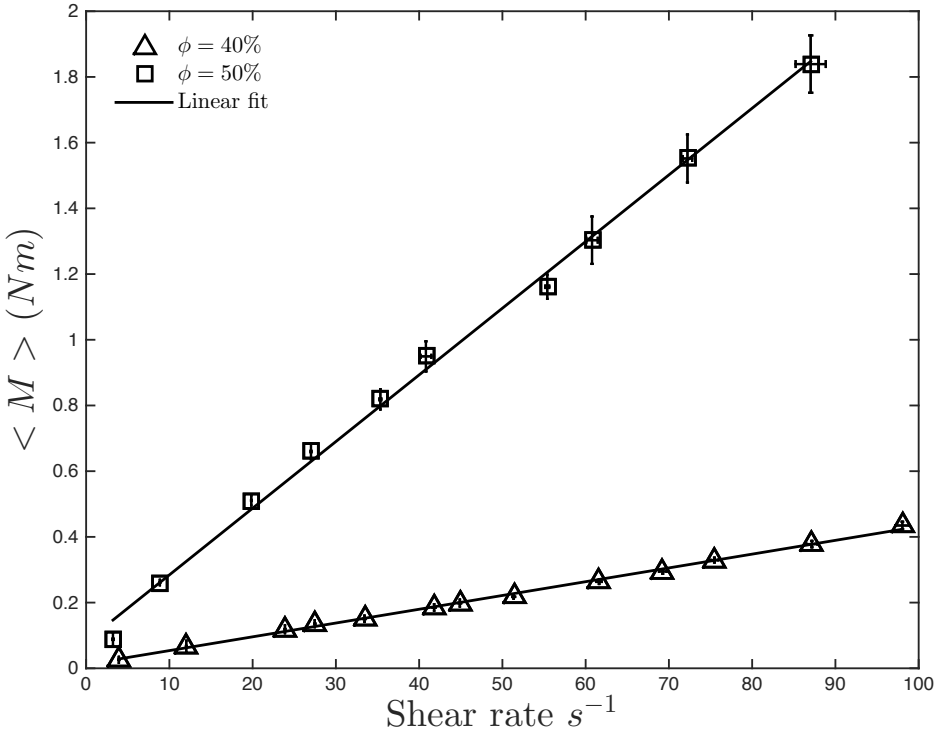

Figure 4.2: Measured torque as a function of shear rate for $\phi = 40$, and 50%. $\rho_p/\rho = 1$. Solid line is the linear curve fit for the present data. The error bars correspond to the combined uncertainty in the torque measurements.

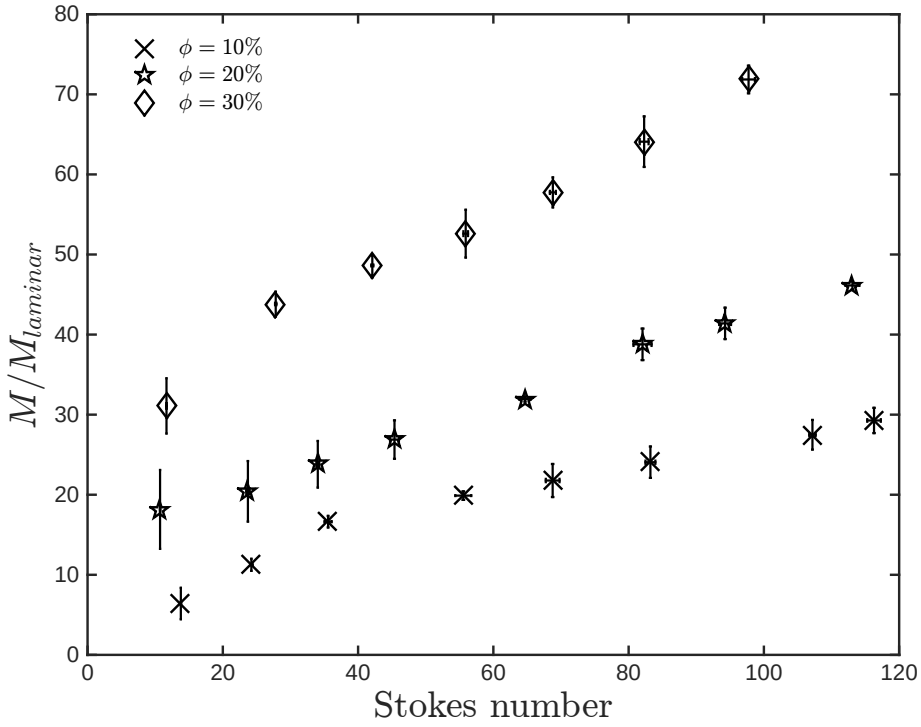

Figure 4.3: Measured torques normalized by the torque predicted from laminar theory as a function of Stokes number for $\phi = 10$, 20, and 30% with $\rho_p/\rho = 1$. The error bars correspond to the combined uncertainty in the torque measurements normalized by the corresponding $M_{laminar}$

The torques ratio exhibits a strong dependance on the volume fraction, varying approximately two orders of magnitude between the lowest and highest volume fraction, as can be observed in Figure 4.5.

In the previous work of Koos (2009) and Koos et al. (2012) it is assumed that the liquid-solid flow is Newtonian, and therefore the ratio of torques, $M/M_{laminar}$, is equal to the relative effective viscosity (μ'/μ). Figure 4.6 shows this ratio μ'/μ for all the Stokes number tested as a function of the volume fraction. The size of the symbols represents the magnitude of the corresponding Stokes number. Note that for volume fractions of 10, 20, and 30%, the ratio of toques exhibits a dependance on Stokes number (equivalently on Reynolds number), where μ'/μ increases with St. The numerical simulations of Yeo and Maxey (2013), Kulkarni and Morris (2008), and Picano et al. (2013) showed also an increase on μ'/μ with Re.

In the previous work of Koos et al. (2012), the relative viscosity for particles with $\rho_p/\rho = 1$ was shown to be an exponential function of the volume fraction normalized with the corresponding particles random loose packing (ϕ_l):

$$\frac{\mu'}{\mu} = exp\Big(8.73\frac{\phi}{\phi_l}\Big).$$

Figure 4.7 shows the relative viscosity as a function of the volume fraction for the present and

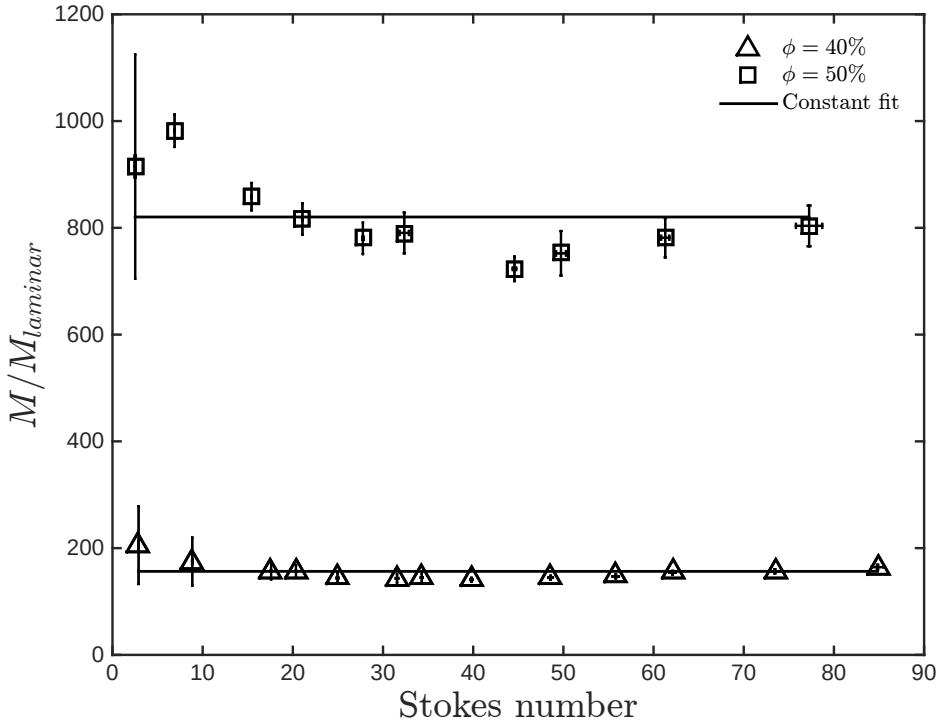

Figure 4.4: Measured torques normalized by the torque predicted from laminar theory as a function of Stokes number for $\phi = 40$ and 50% with $\rho_p/\rho = 1$. Solid lines represent the constant fit for the present data. The error bars correspond to the combined uncertainty in the torque measurements normalized by the corresponding $M_{laminar}$.

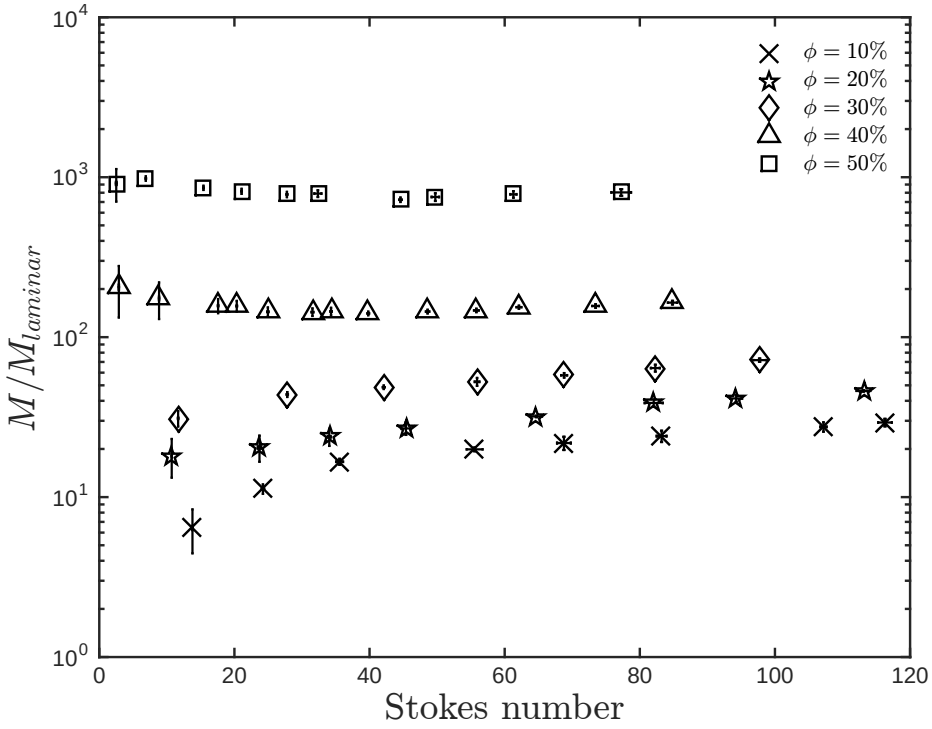

Figure 4.5: Measured torques normalized by the torque predicted from laminar theory as a function of Stokes number for all ϕ tested with $\rho_p/\rho = 1$. The error bars correspond to the combined uncertainty in the torque measurements normalized by the corresponding $M_{laminar}$.

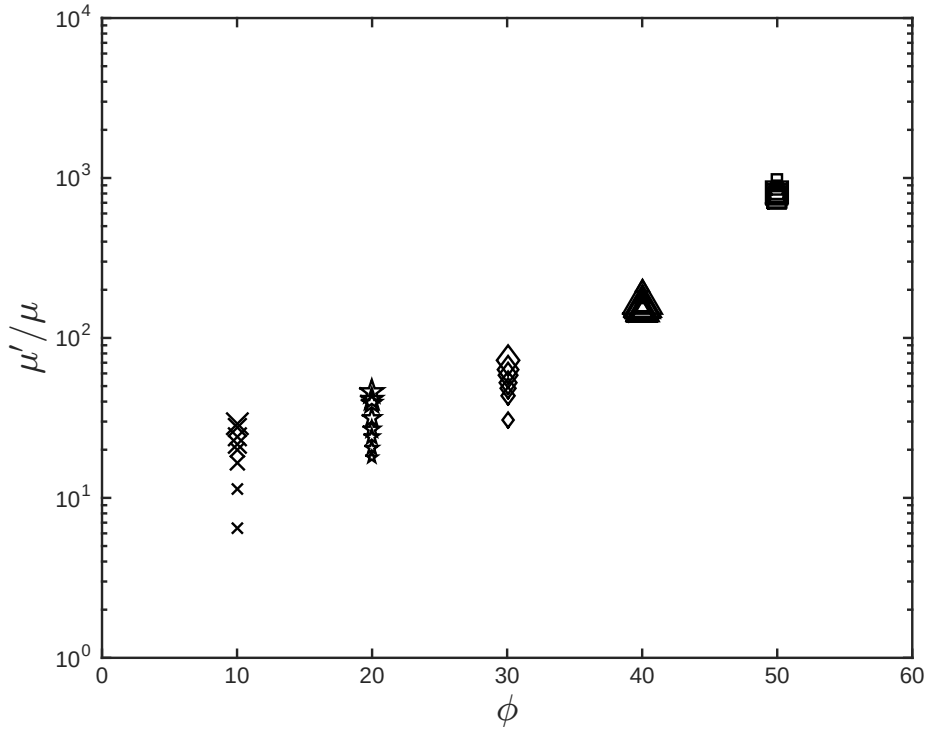

Figure 4.6: Effective relative viscosity as a function of ϕ for experiments with $\rho_p/\rho = 1$. The symbol's size denote the magnitude of the corresponding Stokes number.

previous experiments (Koos, 2009; Koos et al., 2012).

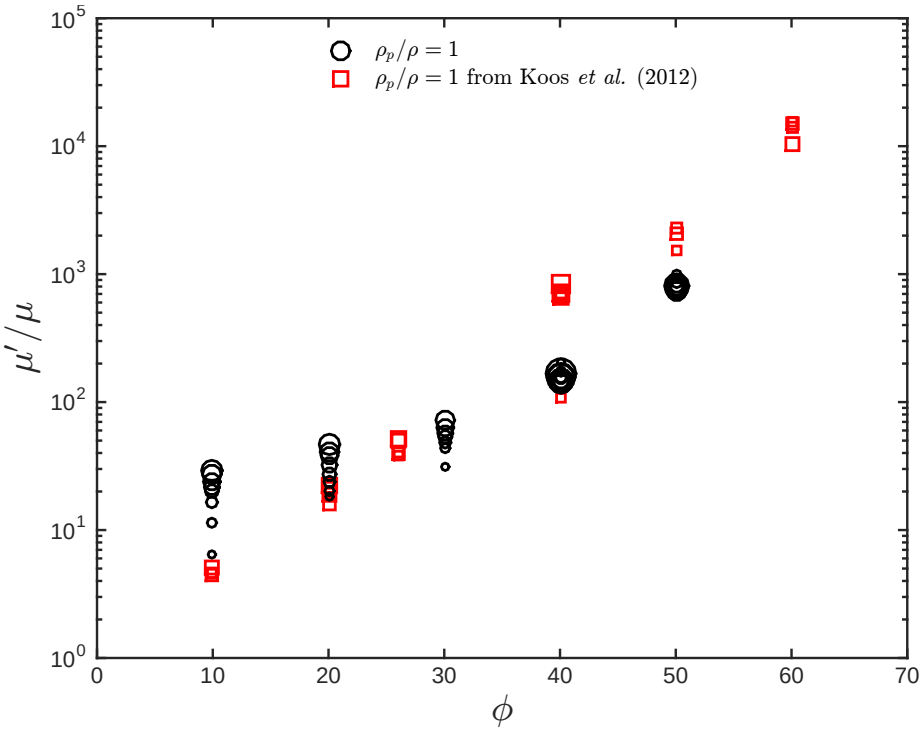

Figure 4.7: Effective relative viscosity as a function of ϕ for the current and previous experiments from Koos et al. (2012) with $\rho_p/\rho = 1$. The symbol's size denote the magnitude of the corresponding Stokes number.

The current and the previous experiments seem to agree in regards to low Stokes numbers. The Stokes numbers tested by Koos et al. (2012) are between 3 and 90, while the current experiments are slightly higher (from 2 to 116). The dependance on Stokes is higher for the current experiments for volume fractions lower than 30%.

4.3 Polystyrene particles with $\rho_p/\rho = 1.05$

To increase the Stokes number tested, experiments with polystyrene particles in water were performed. These particles are denser than water ($\rho_p/\rho = 1.05$) and settle when not sheared. Because the torque measurements are made in the middle section of the rheometer, the effective volume fraction for these experiments may differ from the overall volume fraction. That is, the particles may not be evenly distributed along the rheometer annulus height due to the liquid-solid density mismatch. For instance, at a low volume fraction of 10%, the particles settle at the bottom of the rheometer under static conditions and do not reach the middle section where the torque measurements are taken. Under shearing conditions, the particles fluidize with increasing shear rate, which leads to a presence of a gradient in the particle concentration that depends on the shear rate (an analysis of

the particle fluidization is presented in Chapter 6). For such reason the term loading fraction ($\bar{\phi}$) is used instead of volume fraction. This term denotes the ratio of volume of particles to the total rheometer annulus volume.

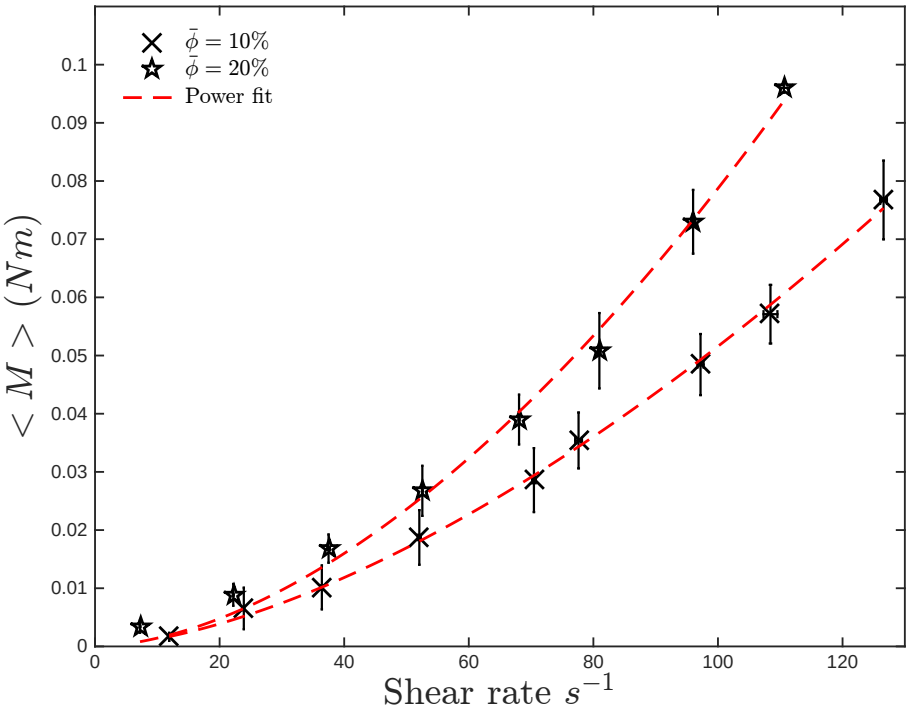

Figure 4.8: Measured torques as a function of shear rate for $\bar{\phi} = 10$ and 20% with $\rho_p/\rho = 1.05$. The dashed lines correspond to the power curve fit for the present data. The error bars correspond to the combined uncertainty in the torque measurements.

Figure 4.8 shows the torque measurements for loading fractions of 10 and 20%. The torque is best fitted by a power law. The fit exponent increases with loading fraction (1.6 for 10% and 1.7 for 20%). This dependance does not hold for higher loading fractions as it can be observed in Figure 4.9 for $\bar{\phi} = 30\%$. In this case the torque is best fitted by a polynomial of order 2. As the loading fraction increases the torque dependance on shear rate varies from a polynomial of order 2 to a polynomial of order 3, as shown in Figure 4.10 and 4.11 for $\bar{\phi} = 40\%$ and $\bar{\phi} = 50\%$.

For a loading fraction of 60% the torque is best fitted by a power law with an exponent smaller than one.

Figure 4.13 shows the results for all the loading fractions tested together with their corresponding curve fit.

Figure 4.14 shows the normalized torque results for loading fractions of 10% and 20% where the increase of $M/M_{laminar}$ with Stokes number can be observed. As the loading fraction increases, the ratio of torques exhibits an opposite behavior: instead of increasing the normalized torques decrease with St as shown in Figure 4.15. The maximum normalized torque for each loading fraction

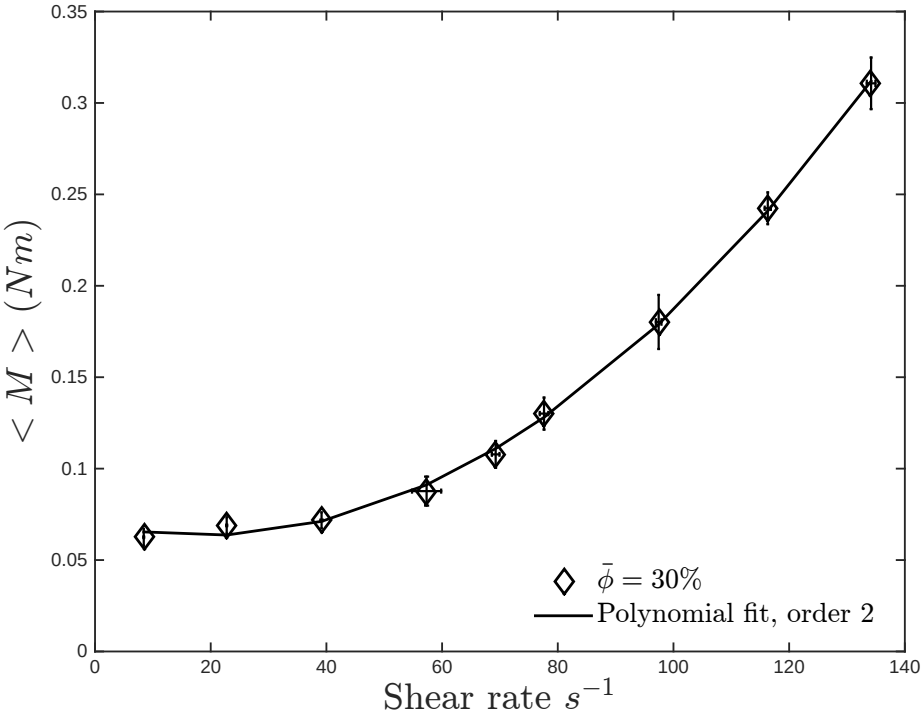

Figure 4.9: Measured torques as a function of shear rate for $\bar{\phi} = 30\%$ with $\rho_p/\rho = 1.05$. The dashed lines correspond to the polynomial curve fit of order 2 for the present data. The error bars correspond to the combined uncertainty in the torque measurements.

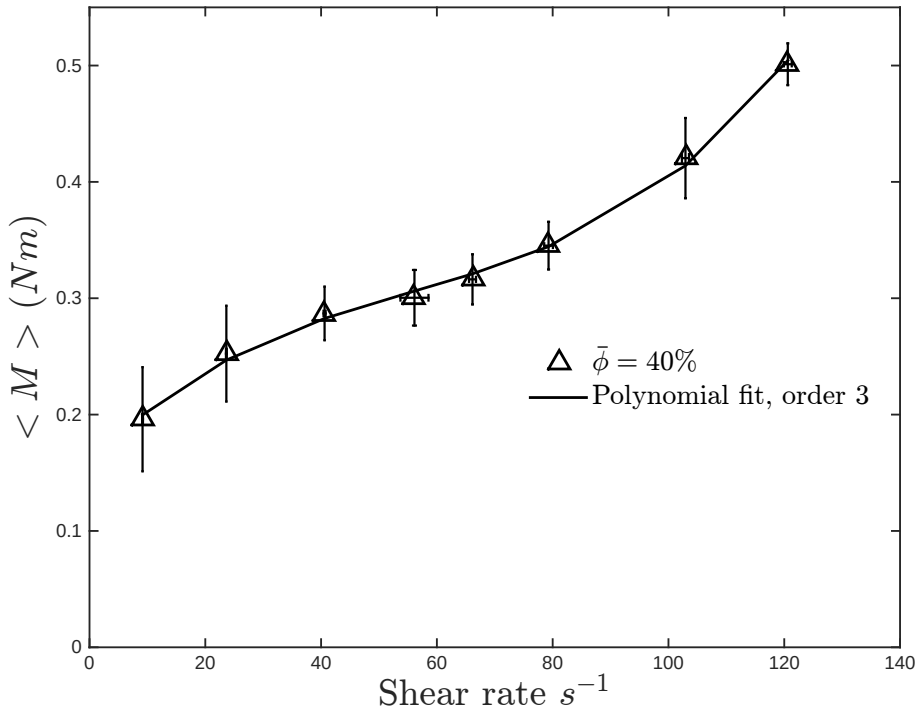

Figure 4.10: Measured torques as a function of shear rate for $\bar{\phi} = 40\%$ with $\rho_p/\rho = 1.05$. The dashed lines correspond to the polynomial curve fit of order 3 for the present data. The error bars correspond to the combined uncertainty in the torque measurements.

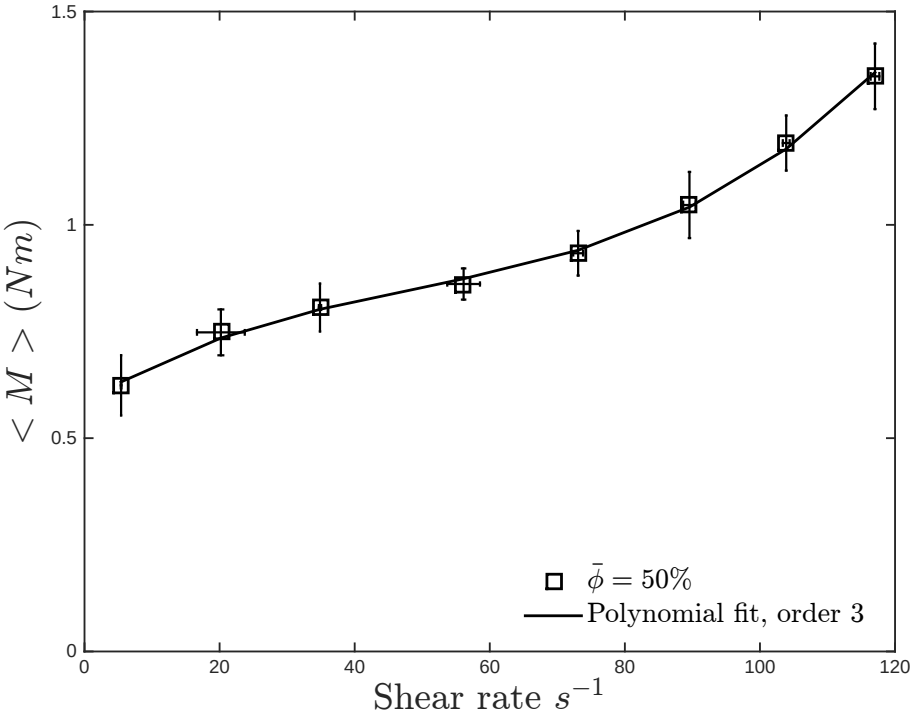

Figure 4.11: Measured torques as a function of shear rate for $\bar{\phi} = 50\%$ with $\rho_p/\rho = 1.05$. The dashed lines correspond to the polynomial curve fit of order 3 for the present data. The error bars correspond to the combined uncertainty in the torque measurements.

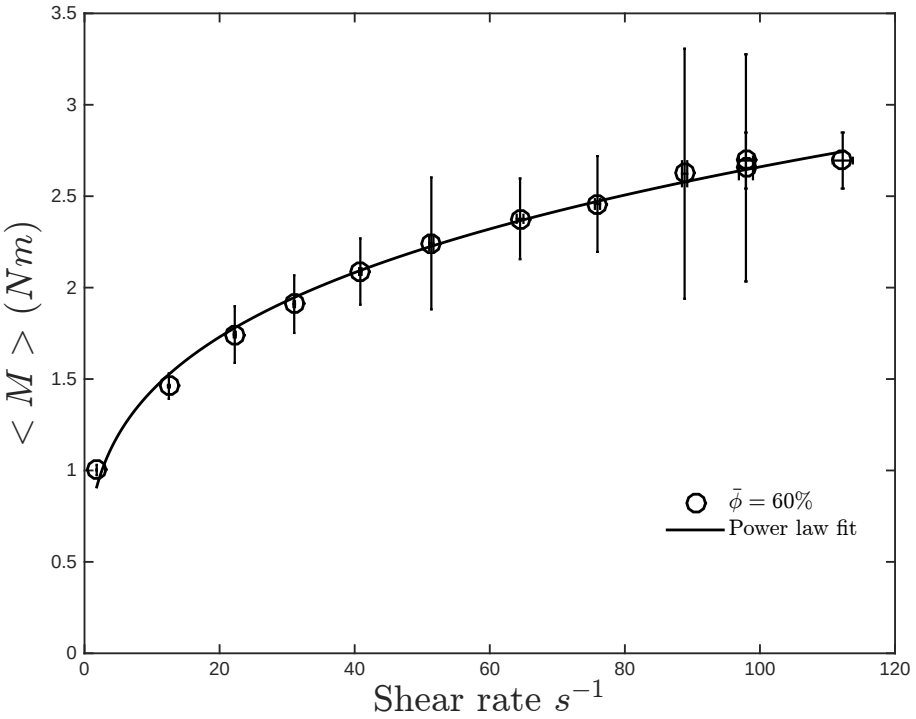

Figure 4.12: Measured torques as a function of shear rate for $\bar{\phi} = 60\%$ with $\rho_p/\rho = 1.05$. The dashed lines correspond to the power curve fit for the present data. The error bars correspond to the combined uncertainty in the torque measurements.

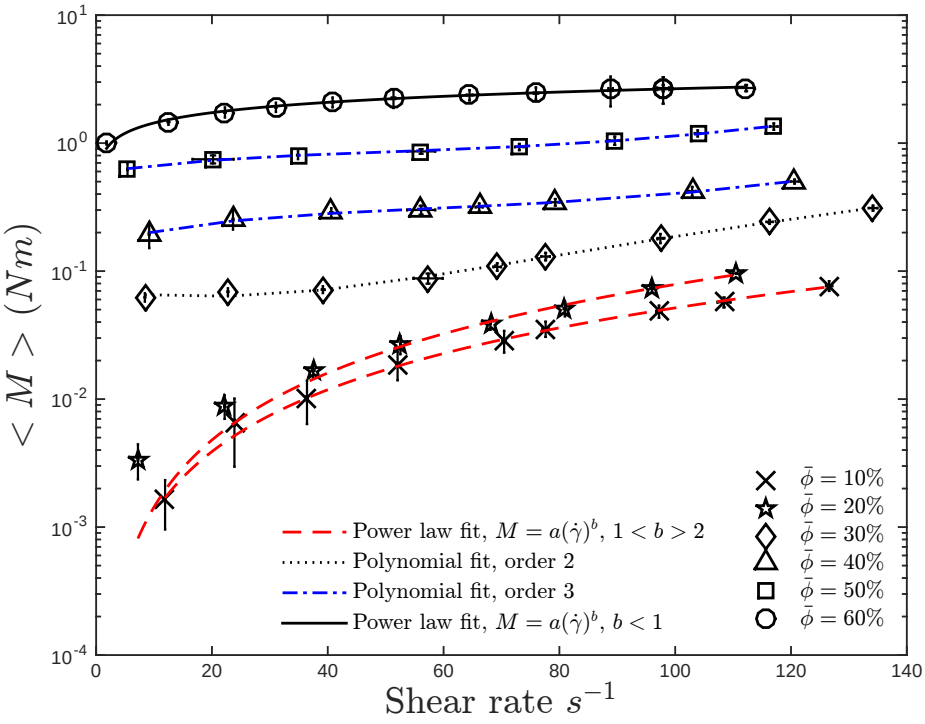

Figure 4.13: Measured torques as a function of shear rate for all $\bar{\phi}$ tested with $\rho_p/\rho = 1.05$. The different lines correspond to the curve fits for the present data. The error bars correspond to the combined uncertainty in the torque measurements.

corresponds to the lowest Stokes number for $\bar{\phi} > 20\%$. For Stokes number above 80, the normalized torques become considerably more independent of the Stokes number. These results are similar to the results found by Acrivos et al. (1994), where the relative effective viscosity of the suspension decreased with increasing shear rate. The apparent shear thinning behavior observed in their work was explained in terms of particle migration due to a slight mismatch on the particle and liquid density. This particle migration led to lower effective volume fractions. A similar mechanism occurs in the present experiments with settling particles. At low shear rates the particles are not fluidized, leading to higher effective volume fractions. A further description of the particle resuspension is given in Chapter 6 and a discussion based on the settling effect is presented in Chapter 7.

As shown in Chapter 6, the measured torques are affected by the fluidization of the particles and the change in effective volume fraction at the test section. A possible explanation for the apparent shear thinning behavior for these loading fraction is the change in effective volume fraction due to the particles resuspension.

Figure 4.16 presents the normalized torques for all the loading fractions tested.

Figure 4.17 shows the relative viscosity as a function of the loading fraction. The size of the symbols denote the magnitude of the Stokes number. For loading fractions of 10 and 20%, the ratio of μ'/μ increases with Stokes numbers. At volume fractions equal to 30% this dependance switches,

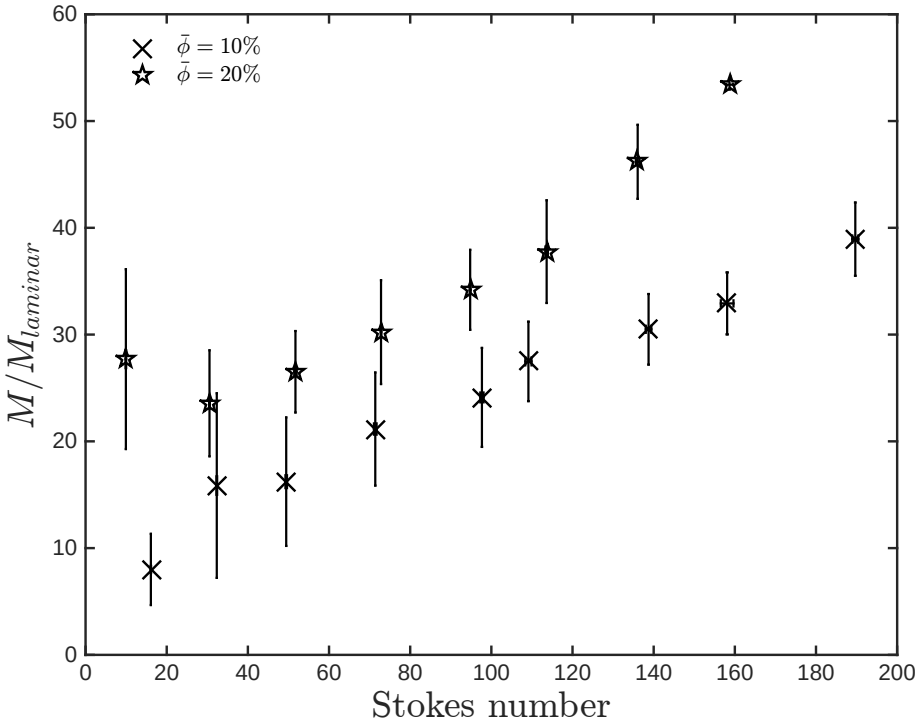

Figure 4.14: Measured torques normalized by the torque predicted from laminar theory as a function of Stokes number for $\bar{\phi} = 10$ and 20% with $\rho_p/\rho = 1.05$. The error bars correspond to the combined uncertainty in the torque measurements normalized by the corresponding $M_{laminar}$.

where the highest ratio of μ'/μ correspond to the lowest Stokes numbers. The change in dependance is discussed in Chapter 7 and it is attributed to the change in effective volume fraction at the test cylinder due to the settling and fluidization of the particles.

4.4 Summary

The results from direct measurements of the torque for $\rho_p/\rho = 1$ and $\rho_p/\rho = 1.05$ are presented. For the case with matched densities, the measured torques exhibit a non-linear dependance on the shear rate for volume fractions below 40%. For $\phi = 40$ and 50%, the dependance of the measured torque on the $\dot{\gamma}$ is linear. The ratio of $M/M_{laminar}$ increases with St for volume fractions of 10, 20, and 30% and become approximately constant for $\phi = 40$ and 50%. At low Stokes number, the $M/M_{laminar}$ for these high volume fractions show some deviation from the constant fit. Comparisons between the current experiments and the previous work of Koos et al. (2012) show that the effective relative viscosity for low Stokes numbers coincides with the previous results (this is assuming that the ratio $M/M_{laminar}$ is equal to μ'/μ). The current results exhibit a higher dependance on the Stokes numbers than the one found by Koos et al. (2012) and for volume fractions higher than 30%, the ratio of μ'/μ is lower than the results of Koos et al. (2012).

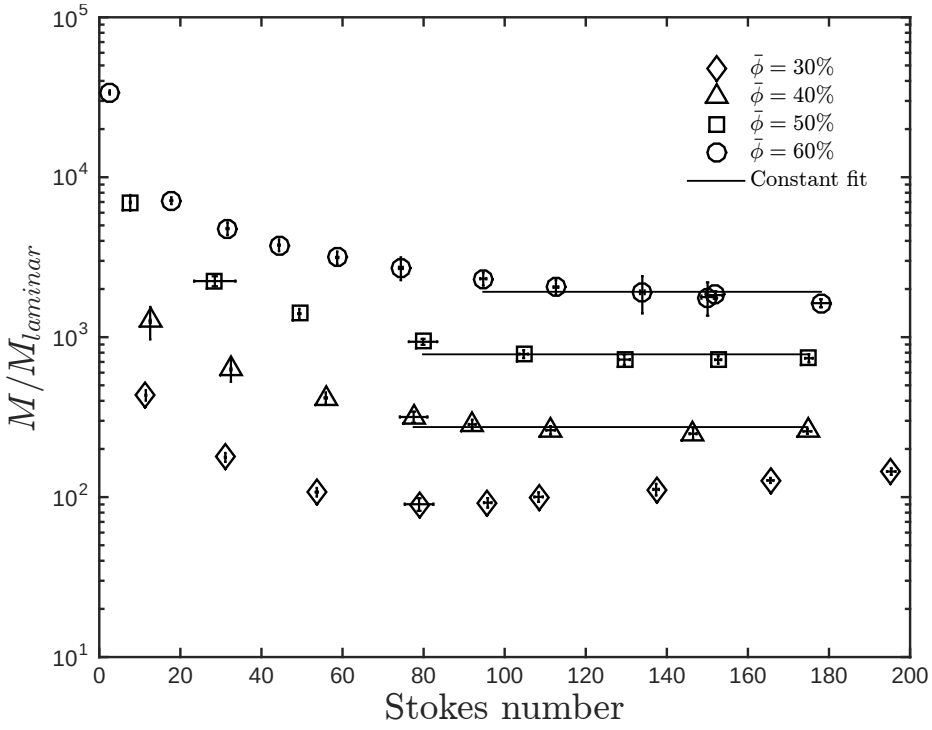

Figure 4.15: Measured torques normalized by the torque predicted from laminar theory as a function of Stokes number for $\bar{\phi} = 10$ and 20% with $\rho_p/\rho = 1.05$. Solid lines correspond to the constant fits for the present data.The error bars correspond to the combined uncertainty in the torque measurements normalized by the corresponding $M_{laminar}$.

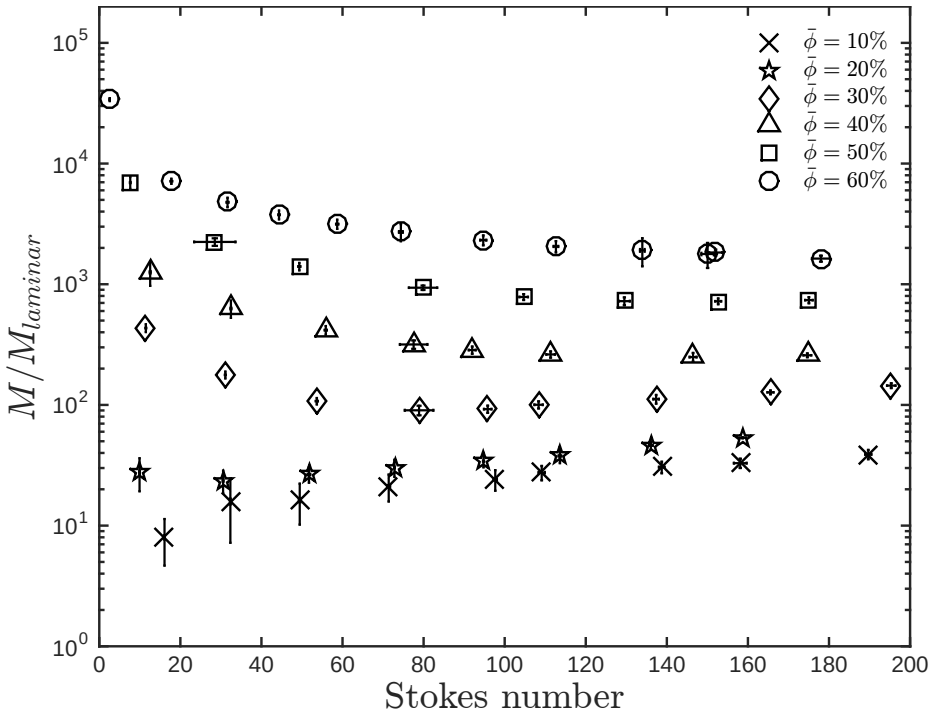

Figure 4.16: Measured torques normalized by the torque predicted from laminar theory as a function of Stokes number for all $\bar{\phi}$ tested with $\rho_p/\rho = 1.05$. The error bars correspond to the combined uncertainty in the torque measurements normalized by the corresponding $M_{laminar}$.

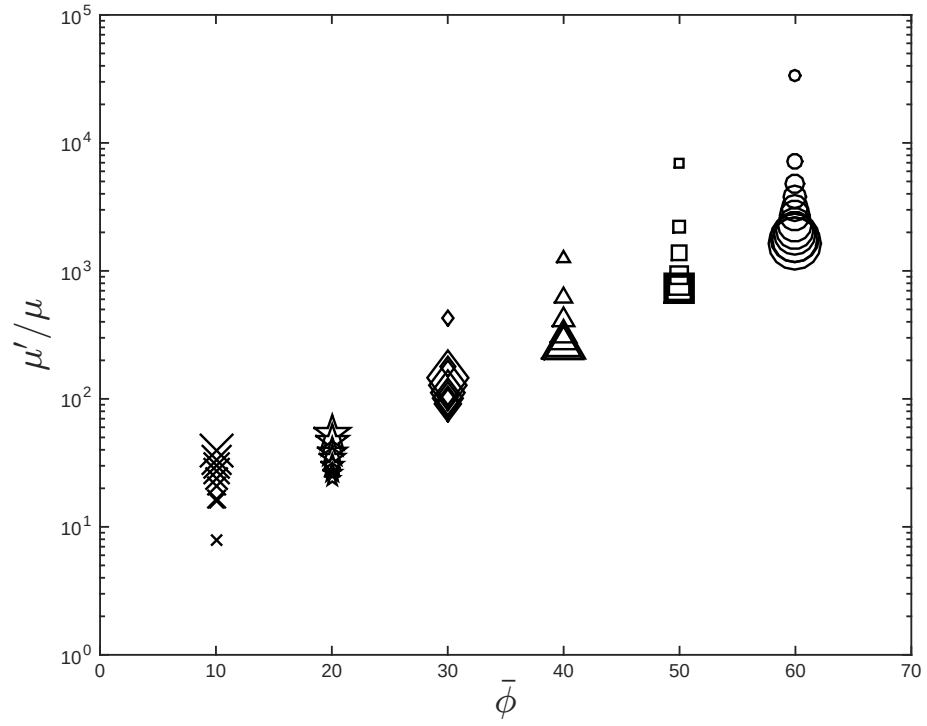

Figure 4.17: Effective relative viscosity as a function of $\bar{\phi}$ for experiments with $\rho_p/\rho = 1.05$. The symbols size denote the magnitude of the corresponding Stokes number.

For the case with settling particles, the measured torques did not show a linear dependance on the shear rate for any of the volume fractions tested. Similarly to the case with matched density, the ratio of torques for loading fractions of 10 and 20% increases with $\dot{\gamma}$ but for higher $\bar{\phi}$, the normalized torques decreases with shear rates. For the particular case of $\bar{\phi} = 30\%$, the ratio of torques decreases with St, and above Stokes number of 80 it starts increasing. For higher volume fractions the normalized torques reaches a plateau above St=80. When plotting the normalized torques as a function of volume fraction a change in Stokes dependance is observed, where for $\bar{\phi} < 30\%$ the ratio of $M/M_{laminar}$ increases with St and for $\bar{\phi} < 30\%$ the dependance is reversed.

Findings from different numerical simulations that considered Reynolds numbers equal or higher than one predict a dependance of the effective relative viscosity with Re (Yeo and Maxey, 2013; Kulkarni and Morris, 2008; Picano et al., 2013). The normalized torques for the case with matched densities and volume fractions lower than 40 exhibit the same trend. However, the Stokes and Reynolds numbers tested in this work are considerably larger than the ones considered in these simulations.

For the case with settling particles the decrease on effective relative viscosity with Stokes numbers for $\bar{\phi} > 20\%$ is similar to the one observed by Acrivos et al. (1994) where particle migration due to a mismatch in densities decreased the effective volume fraction. The same mechanism is presented in this work and it is further analyzed in Chapter 6 and 7.

Chapter 5

Rheological measurements with rough walls over a porous medium

5.1 Motivation

As mentioned in Chapter 2, the rheometer was designed to reduce the effect of secondary flows. This was achieved by increasing the ratio between height and shearing gap, rotating the outer cylinder, fixing the top and bottom boundaries, and also by making the torque measurements in the middle section (away from the top and bottom boundaries, where the secondary flows are present). While this design might help to reduce the effect of secondary flows, it limits the study of settling particles with low loading fraction. When the loading fraction is less than 20% and the particles are denser than the suspending liquid, the height of the settled particles's column is less than the height of the test cylinder. Therefore the particles may not reach the measurement zone until the shear rate is high enough to fluidize them (see Chapter 6 for particle resuspension analysis). To study the rheology of low loading fractions, the experimental setup was modified by adding a layer of glass beads at the bottom of the rheometer. These glass beads form a porous medium at the lower part of the rheometer, approximately 2 cm below the test cylinder. The polystyrene particles are placed over the glass beads, guaranteeing the presence of particles in the middle section for all the loading fractions tested. This enables the study of loading fractions of 10 and 20% at low shear rates. The presence of a porous medium also adds roughness to the lower boundary , which can affect the behavior of the suspending liquid.

5.2 Modification of the experiment and porous medium configuration

The porous medium was formed using spherical glass beads with a density of 2520 (kg/m^3) and 4 (mm) in diameter size. Glass beads (2.36 l) were poured into the rheometer and filled the bottom

region. Once the glass beads were poured and evenly distributed along the rheometer annulus, they were sheared at different speeds to account for any change of particle packing. To avoid excessive shearing of the porous medium, the walls at the bottom of the rheometer were left smooth. The height of the glass beads layer was then measured with the help of a vernier to determine the packing of the porous medium. These measurements were made dry and it is assumed that the effect of water on the packing of glass beads is negligible due to the high density of the glass beads. The glass beads packing was calculated as 0.63. Koos (2009) measured the random close packing (RCP) of spherical glass beads of 3 mm diameter with the same density and found that RCP=0.626. Using the fit found by Zou and Yu (1996) and considering the model of O'Hern et al. (2002) to calculate the random close packing of 4 mm glass beads, a value of 0.637 is obtained, which is very close to the one calculated based on the glass beads height measurements.

The volume of glass beads ensures that the maximum height reached by the porous medium after being sheared is no higher than the bottom cylinder height. Based on the glass beads height measurements, the porous medium is 1.9 cm below the test cylinder. After shearing the glass beads a change in the shape of the top surface is observed. The glass beads move slightly towards the inner cylinder, forming an angle where the porous height is slightly shorter next to the outer wall. After this re-arrangement of the glass beads, the porous medium is still approximately 1.9 cm in average below the test section. Because this re-accommodation of the beads did not seem to change the average height of the porous medium, the packing of the glass beads is considered to remain the same. If further dilatancy were to occur during the run of an experiment, and the porous medium packing went from close to loose, the maximum height reached by the particles would be 1.3 cm below the test cylinder (this is based on the random loose packing measured by Koos (2009)). Thus the glass beads do not reach the middle section. A scheme of the modified experimental setup is shown in Figure 5.1.

Once the porous medium was prepared, polystyrene particles were poured on top. For these experiments the total volume considered when calculating the loading fraction does not include the volume occupied by the glass beads. With this configuration the volume of particles needed to obtain a loading fraction of 10% is lower than for the case without a porous medium.

5.3 Torque measurements of polystyrene particles over a porous medium with $\rho_p/\rho = 1.05$

Figure 5.2 shows the torque measurements as a function of shear rate for $\bar{\phi} = 10\%$. For shear rates lower than 60 s^{-1}, the torque shows a linear dependance on the shear rate. There appears to be a change in the torque dependance for shear rates higher than 60 s^{-1}. The torque increases more rapidly and its dependance on shear rate is no longer linear. The torques for these higher shear rates

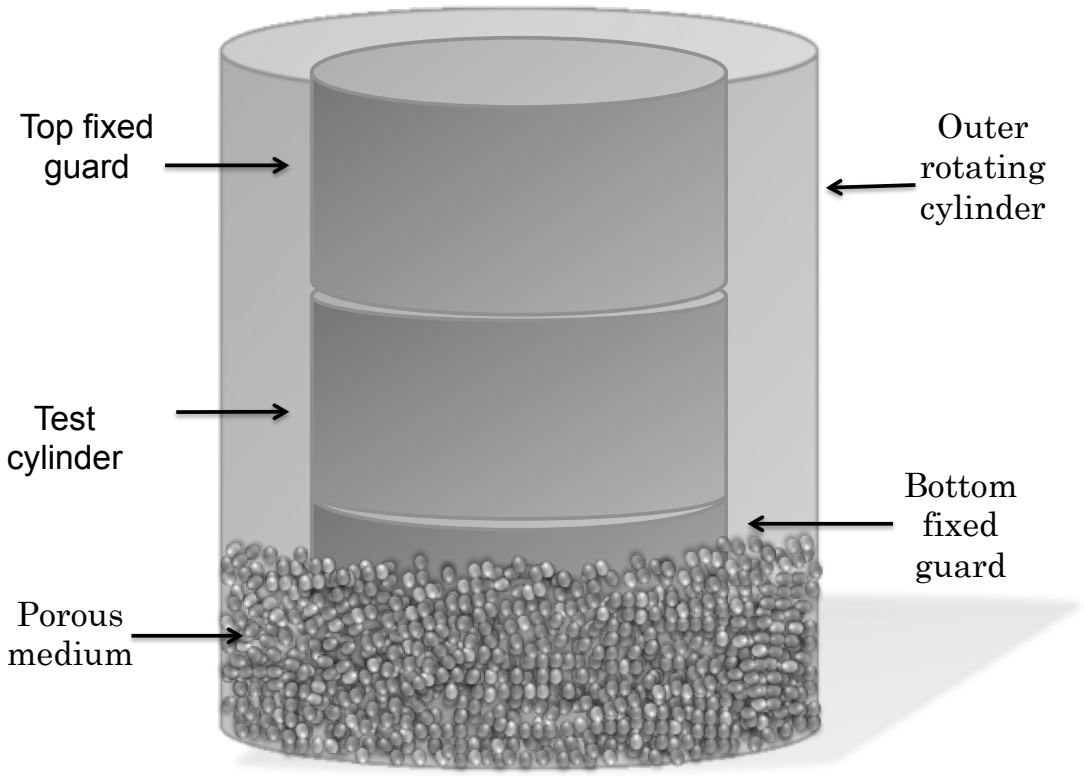

Figure 5.1: Scheme of the apparatus configuration for the experiments with flow over a porous medium.

are best fitted by a power law.

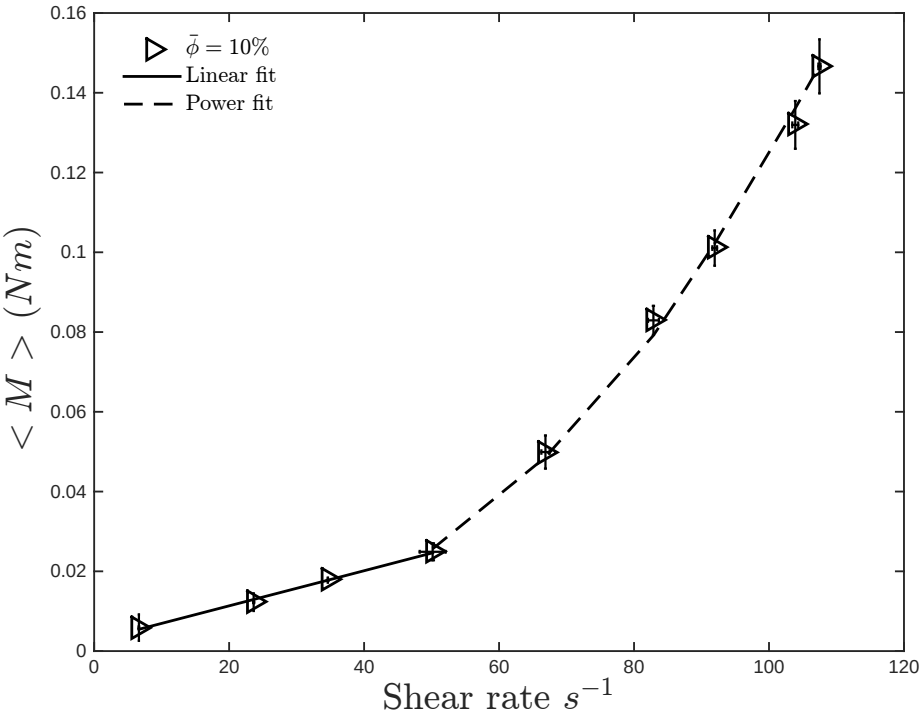

Figure 5.2: Measured torques as a function of the shear rate for flow over a porous medium for $\bar{\phi} = 10\%$ and $\rho_p/\rho = 1.05$. The error bars correspond to the combined uncertainty in the torque measurements.

Figure 5.3 presents the torque measurements for a loading fraction of 20%. Unlike the results for $\bar{\phi} = 10\%$, the torque measurements for shear rates lower than 60 s^{-1} do not seem to depend linearly on the shear rate. For shear rates higher than 60 s^{-1}, a sudden drop in the torque is observed. The torque decreases almost by half between $\dot{\gamma} = 36$ s^{-1} and $\dot{\gamma} = 68$ s^{-1}. Such decrease in the torque is not observed for $\bar{\phi} = 10\%$, nor it is observed for the previous experiments with no glass beads at the bottom. After the torque drops, it starts increasing with the shear rate and it exhibits a linear dependance. Different from what is observed for the experiments with no glass beads, the minimum torque measured for this loading fraction does not correspond to the lowest shear rates. The variation in the torque with the shear rate can be attributed to the presence of the porous medium and depends on the expansion of the polystyrene particles with shear rate. The drop in torque might be caused by the complete fluidization of the settling particles. An analysis of the resuspension of particles is presented in the following chapter.

Figure 5.4 shows the torque measurements for a $\bar{\phi} = 30\%$. For $\dot{\gamma} < 40$ s^{-1}, the torque increases with the shear rate and for shear rates between 40 and 50 s^{-1}, the torque remains constant. For shear rates higher than 50 s^{-1}, the torque starts decreasing until it increases again for shear rates higher than 90 s^{-1}. There is no sudden drop on the torque measurements for this loading fraction.

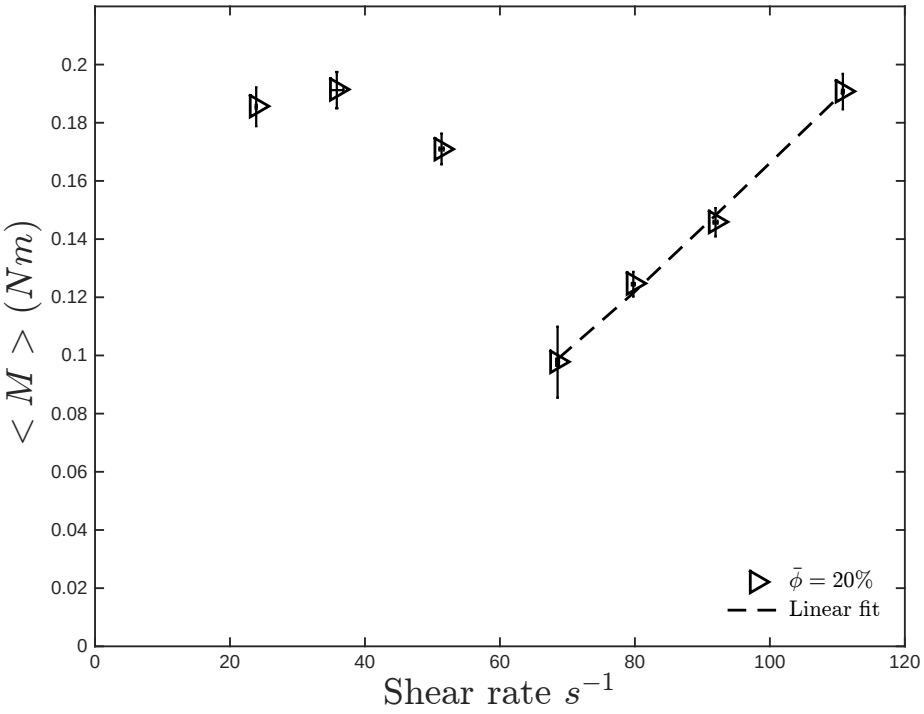

Figure 5.3: Measured torques as a function of the shear rate for flow over a porous medium for $\bar{\phi} = 20\%$ and $\rho_p/\rho = 1.05$. The error bars correspond to the combined uncertainty in the torque measurements.

However, the torque does decrease and similarly to what is found for a loading fraction of 20 %, the lowest torque measured does not correspond to the lowest shear rate.

A similar behavior is observed for higher loading fractions of 40 and 50 %, as shown in Figure 5.5. For low shear rates, the torque increases in a linear way. For shear rates higher than 60 s^{-1}, the torque dependance starts shifting. The torque starts to decrease for shear rates higher than 70 s^{-1}. For a loading fraction of 40 % and for shear rates higher than 100, the torque starts to increase again, while for $\bar{\phi} = 50\%$ the increase on torque starts at a lower shear rate of 91 s^{-1}. The decrease in the torque measured for a loading fraction of 50% is less pronounced than for lower loading fractions. For this loading fraction in particular, the minimum torque measured corresponds to the second lowest shear rates, while for the case of $\bar{\phi} = 40\%$, the lowest torque measured does not correspond to the lowest shear rate. As pointed out previously, this behavior is observed for the other loading fractions. If the decrease in torque is governed by the expansion of the particles, then for a high loading fraction this drop in the torque is less pronounced, since there is less space available for the particles to expand. Further discussion on the expansion of particles is presented in Chapter 6

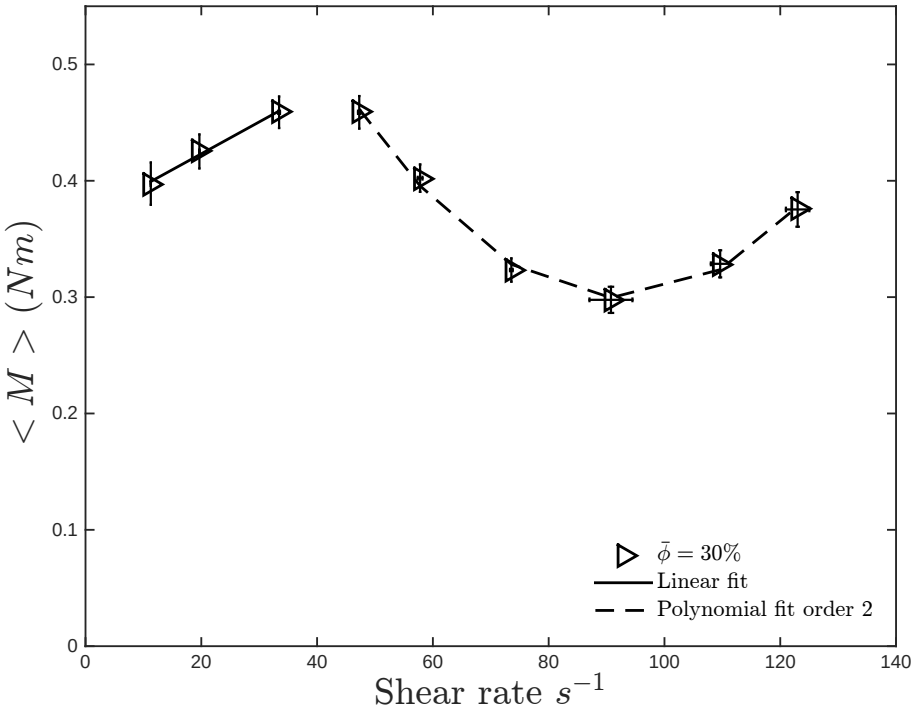

Figure 5.4: Measured torques as a function of the shear rate for flow over a porous medium for $\bar{\phi} = 30\%$ and $\rho_p/\rho = 1.05$. The error bars correspond to the combined uncertainty in the torque measurements.

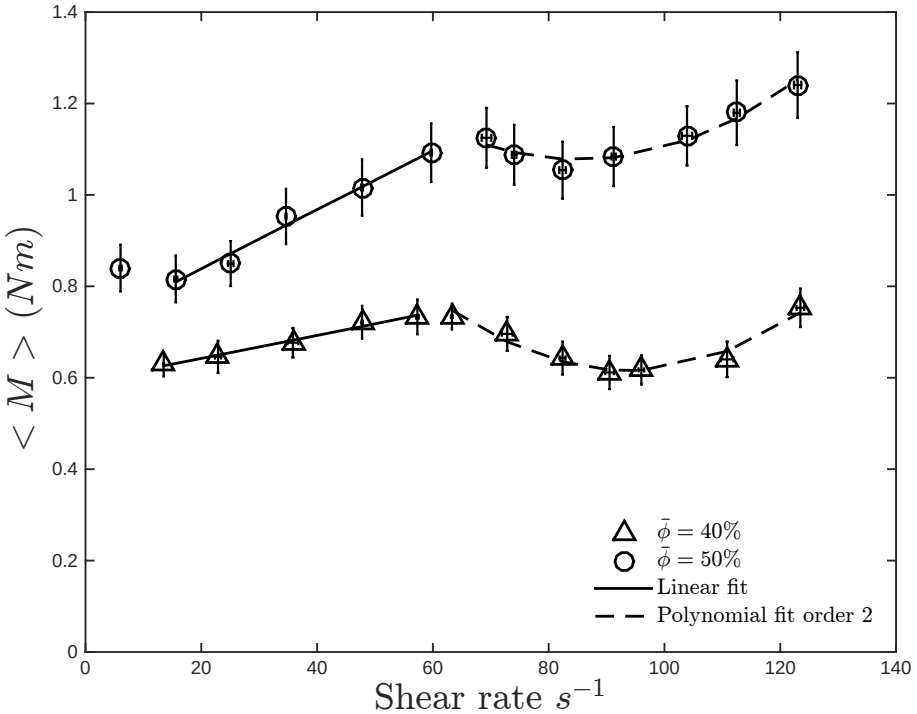

Figure 5.5: Measured torques as a function of the shear rate for flow over a porous medium for $\bar{\phi} = 40$ and 50% and $\rho_p/\rho = 1.05$. The error bars correspond to the combined uncertainty in the torque measurements.

Hysteresis

To study if there is a dependance on the shearing history of the mixture, torque measurements were made from high to low shear rates. These measurements were made right after the measurements from low to high shear rates were taken. Figure 5.6 shows the torque as a function of the shear rate for $\bar{\phi} = 10\%$, for both cases: from low to high and from high to low shear rates. For shear rates higher than 60 s^{-1}, the torque for both cases coincides. For lower shear rates, the torques corresponding to decreasing shear rates are higher.

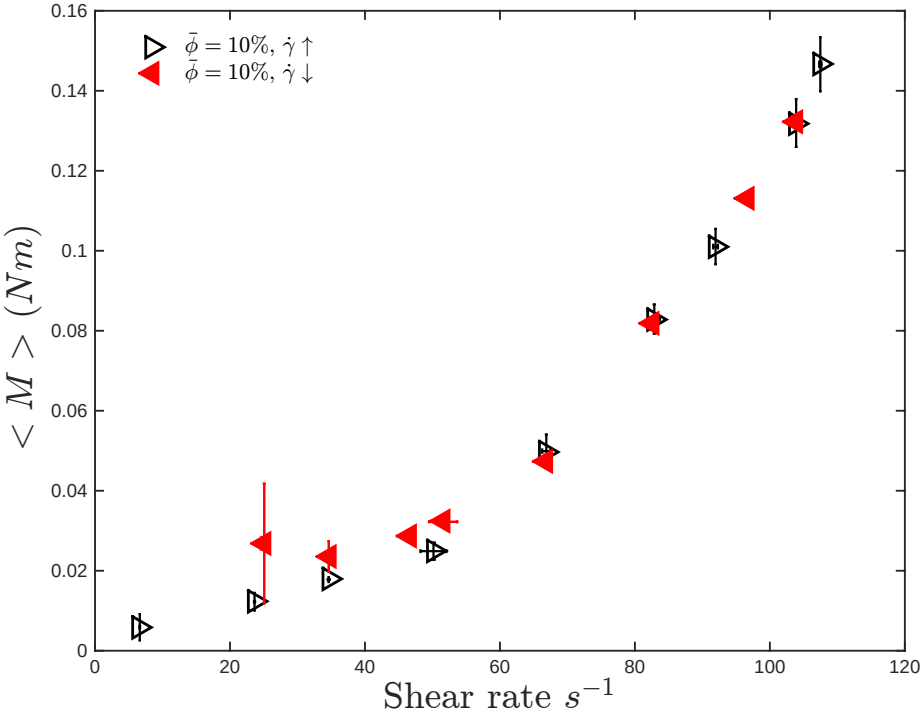

Figure 5.6: Measured torques for $\uparrow \dot{\gamma}$ and $\downarrow \dot{\gamma}$ for flow of settling particles over a porous medium with $\bar{\phi} = 10\%$ and $\rho_p/\rho = 1.05$. The error bars correspond to the combined uncertainty in the torque measurements.

For a loading fraction of 20%, the presence of hysteresis seems to be less pronounced, as shown in Figure 5.7. However, for low shear rates the torque measurements for the case with decreasing shear rate are slightly higher than the torque measurements with increasing shear rate.

Similarly, the hysteresis present for a loading fraction of 30% occurs for shear rates lower than 60 s^{-1}. But unlike $\bar{\phi} = 10$ and $\bar{\phi} = 20$, the torques measured for decreasing shear rates are lower than the ones measured for increasing shear rates, as shown in Figure 5.8. In the following section, it is shown that the apparent hysteresis found for $\bar{\phi} = 30\%$ is due to a change in the suspending liquid temperature.

As shown in Figure 5.9 for higher loading fractions of 40 and 50% the torque measurements for increasing and decreasing shear rate seem to match for all the shear rates tested.

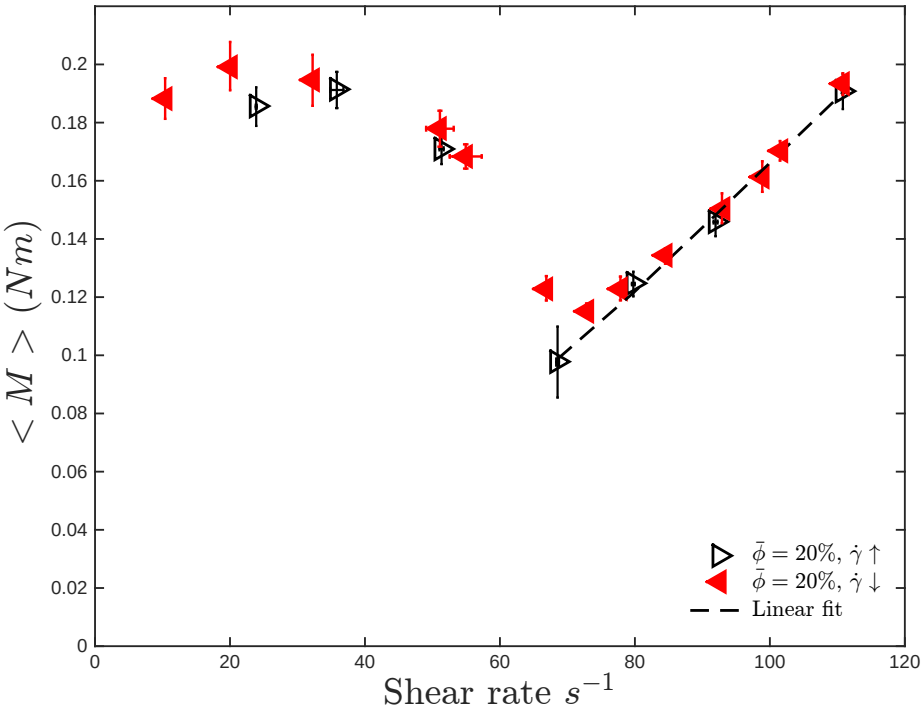

Figure 5.7: Measured torques for $\uparrow \dot{\gamma}$ and $\downarrow \dot{\gamma}$ for flow of settling particles over a porous medium with $\bar{\phi} = 20\%$ and $\rho_p/\rho = 1.05$. The error bars correspond to the combined uncertainty in the torque measurements.

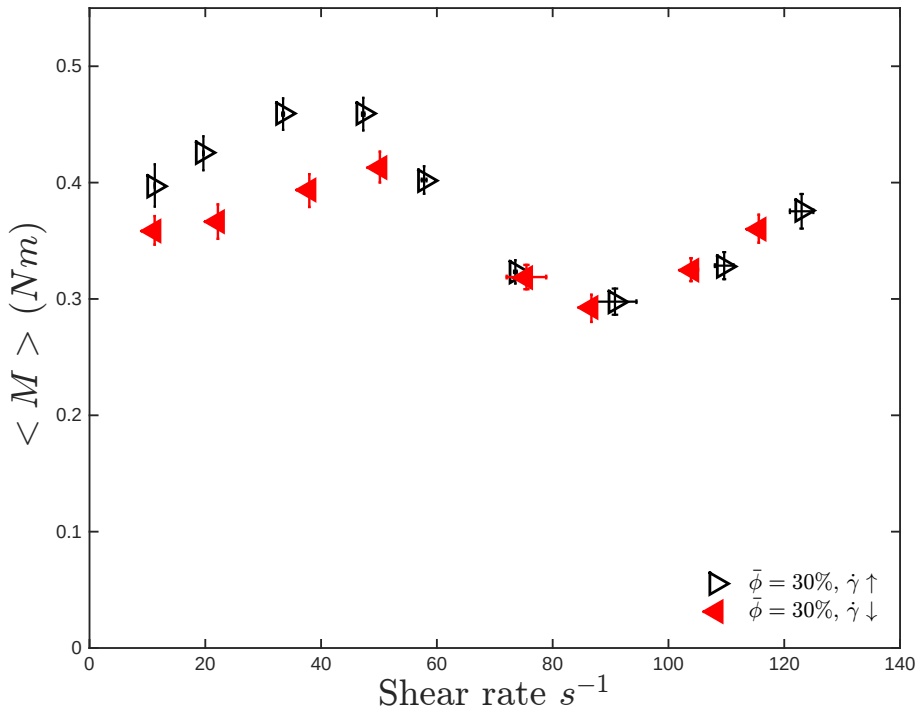

Figure 5.8: Measured torques for $\uparrow \dot{\gamma}$ and $\downarrow \dot{\gamma}$ for flow of settling particles over a porous medium with $\bar{\phi} = 30\%$ and $\rho_p/\rho = 1.05$. The error bars correspond to the combined uncertainty in the torque measurements.

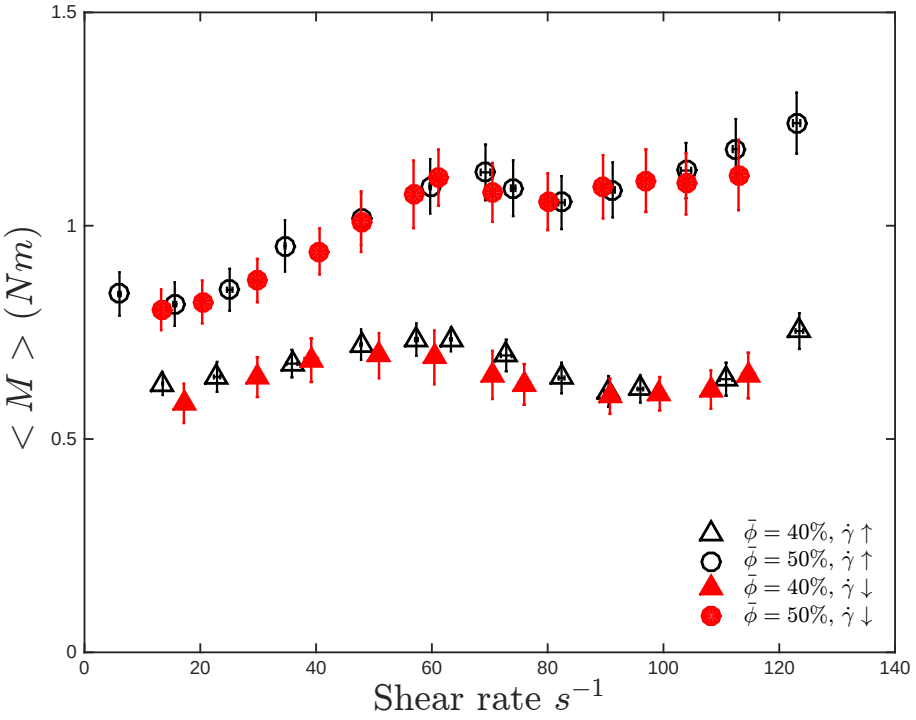

Figure 5.9: Measured torques for $\uparrow \dot{\gamma}$ and $\downarrow \dot{\gamma}$ for flow of settling particles over a porous medium with $\bar{\phi} = 40$ and 50% and $\rho_p/\rho = 1.05$. The error bars correspond to the combined uncertainty in the torque measurements.

5.4 Normalized torque for polystyrene particles over a porous medium with $\rho_p/\rho = 1.05$

Figure 5.10 shows the normalized torques for a loading fraction of 10%. Considering the case where the torque measurements were taken for increasing shear rates, the normalized torques are fairly constant for Stokes number between 25 and 80. The ratio of torques then increases with the Stokes number. A similar behavior is observed for the normalized torques measured with decreasing shear rates. For Stokes number lower than 100, the normalized torques seem to have a dependance on the shearing history of the mixture. The range of Stokes number at which the ratio of torques drops and remains constant also depends on the shearing history of the mixture.

Figure 5.11 presents the normalized torques for a loading fraction of 20%. The ratio of torques decreases with Stokes number for both increasing and decreasing shear rates. For the case with decreasing shear rate, the normalized torques are slightly higher. For Stokes number higher than 100, the normalized torques exhibit a fairly constant behavior and no hysteresis is observed in the torque measurements.

For a loading fraction of 30%, the normalized torques become constant for Stokes number higher than 120, as shown in Figure 5.12. For all the Stokes number tested, the ratio of torques seems to

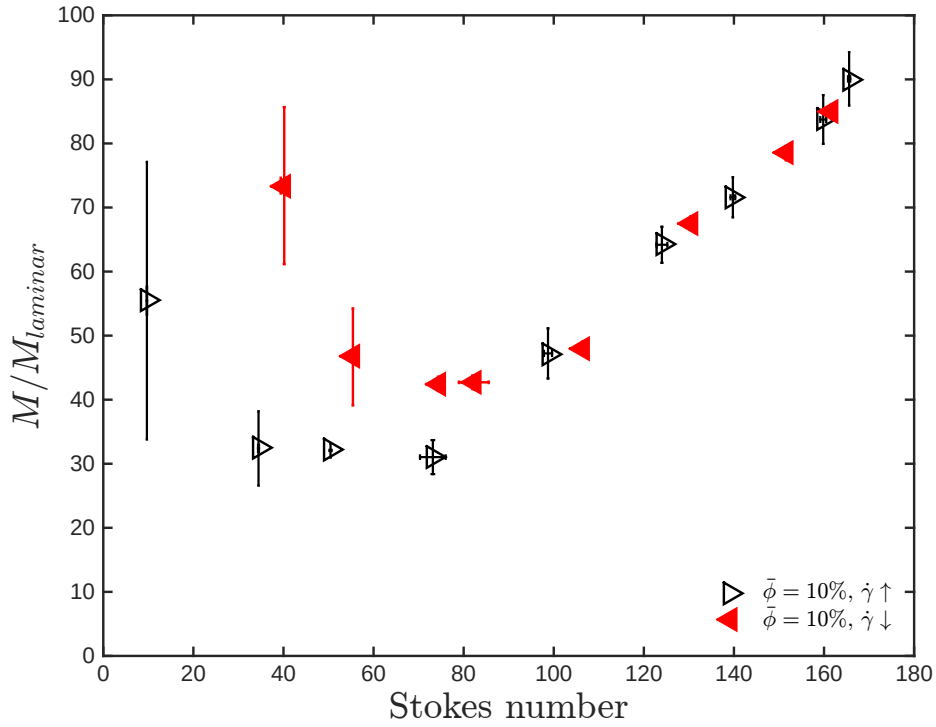

Figure 5.10: Normalized torques as a function of Stokes number for flows over a porous medium and $\phi = 10\%$ with $\rho_p/\rho = 1.05$. The error bars correspond to the combined uncertainty in the torque measurements normalized by the corresponding $M_{laminar}$.

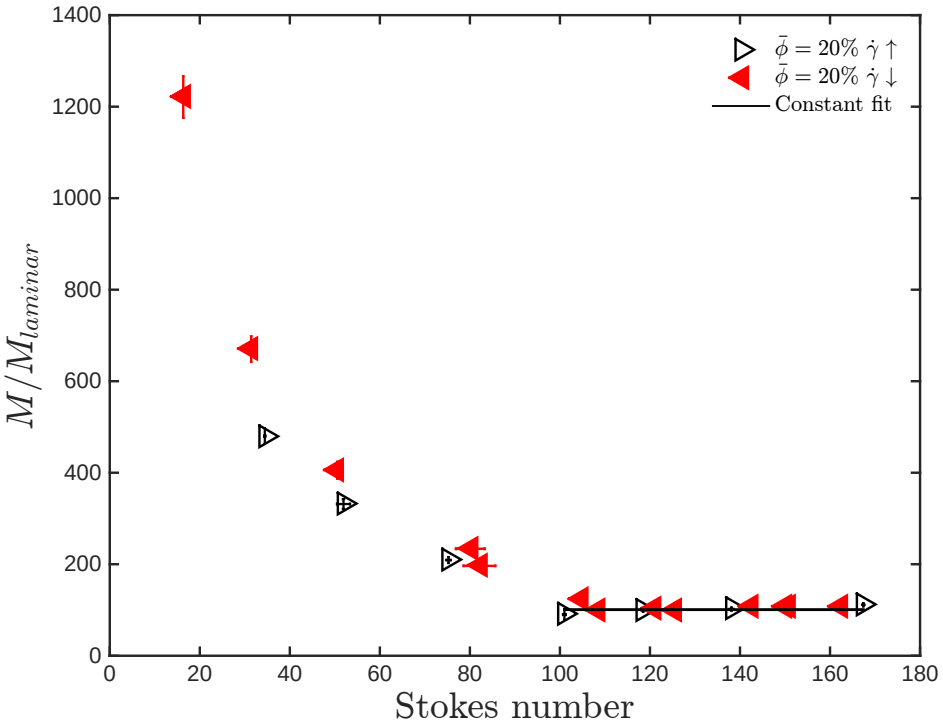

Figure 5.11: Normalized torques as a function of Stokes number for flows over a porous medium and $\phi = 20\%$ with $\rho_p/\rho = 1.05$. The error bars correspond to the combined uncertainty in the torque measurements normalized by the corresponding $M_{laminar}$.

show no hysteresis. This is different from what was observed in the previous section in Figure 5.4, where the measured torques show hysteresis. Hysteresis is not observed in Figure 5.12 because by normalizing the torque, the difference in the liquid viscosity due to an increase in temperature is considered.

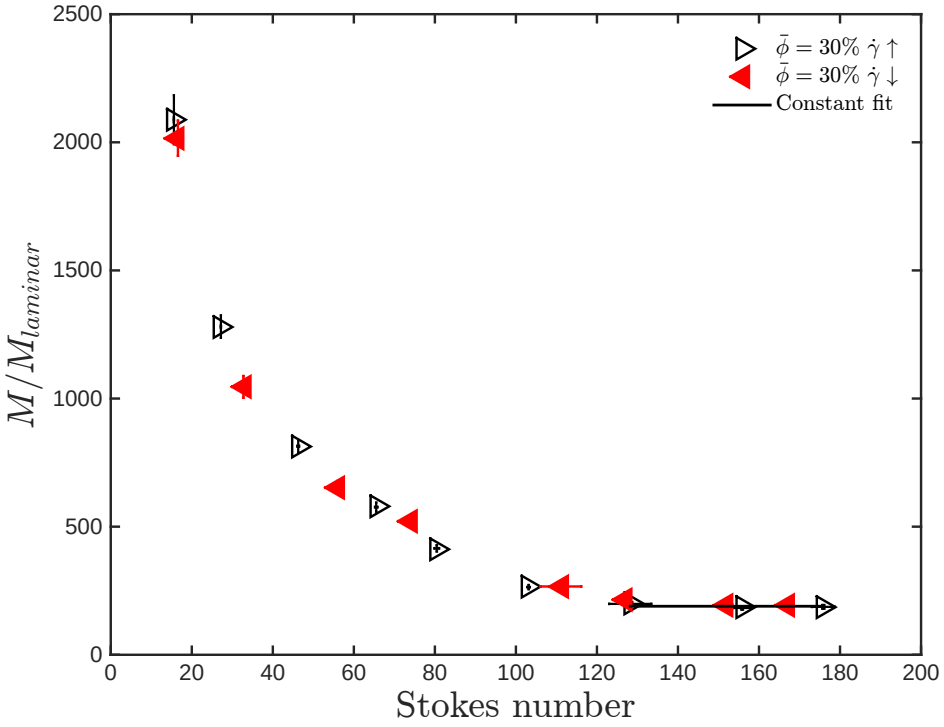

Figure 5.12: Normalized torques as a function of Stokes number for flows over a porous medium and $\phi = 30\%$ with $\rho_p/\rho = 1.05$. The error bars correspond to the combined uncertainty in the torque measurements normalized by the corresponding $M_{laminar}$.

Figure 5.13 shows the normalized torques for a loading fraction of 40 %. The ratio of torques corresponding to decreasing shear rates is slightly higher than for the case with increasing shear rates for Stokes numbers lower than 100. For Stokes number higher than 150, the normalized torques appear to be constant.

Figure 5.14 shows the normalized torques for the highest loading fraction tested for this type of experiments $\bar{\phi} = 50\%$. There seems to be no hysteresis for the whole range of Stokes numbers tested. The normalized torques decrease with Stokes number but unlike the lower loading fractions it did not become constant. This is better observed in a semi-log plot. Figure 5.15 shows the normalized torques for all the loading fractions tested. For $\bar{\phi} = 50\%$, the ratio of torques at the highest Stokes numbers suggests that $M/M_{laminar}$ may reach a constant.

As shown in Figure 5.15, for Stokes number lower than 100, the normalized torques decrease with Stokes number for all the loading fraction tested. For loading fractions higher than 10%, the normalized torques continue to decrease until they become constant, with the exception of $\bar{\phi} = 50\%$,

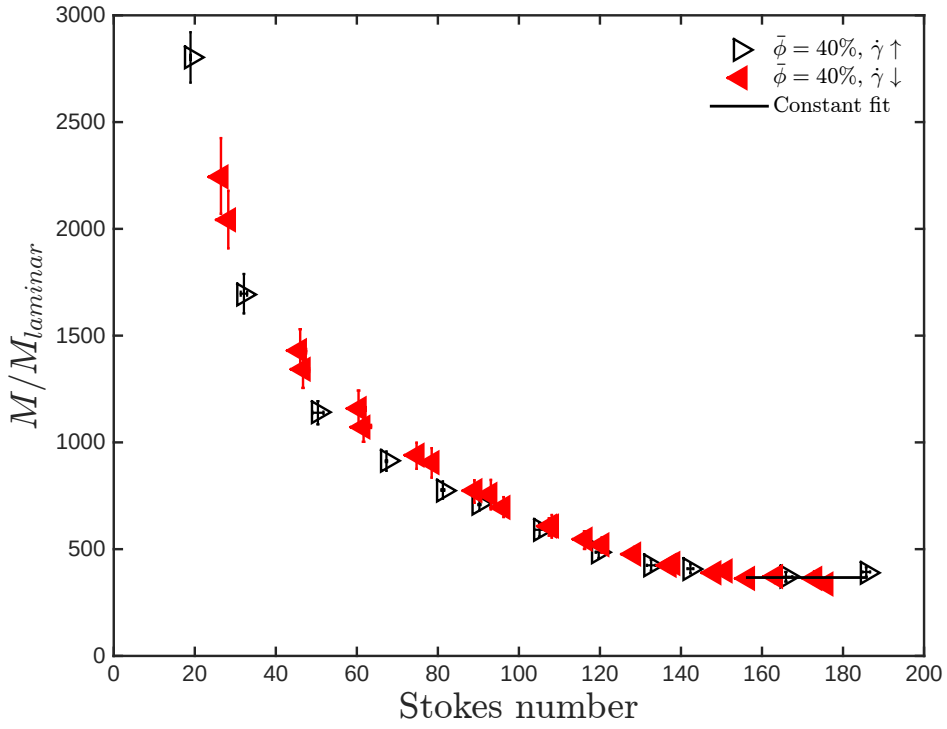

Figure 5.13: Normalized torques as a function of Stokes number for flows over a porous medium and $\phi = 40\%$ with $\rho_p/\rho = 1.05$. The error bars correspond to the combined uncertainty in the torque measurements normalized by the corresponding $M_{laminar}$.

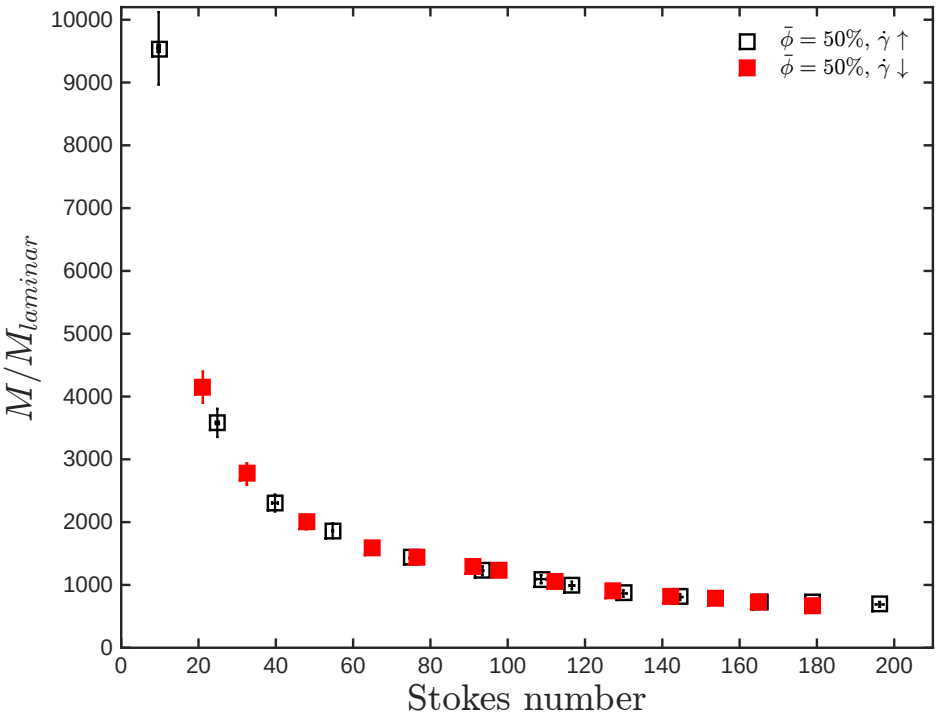

Figure 5.14: Normalized torques as a function of Stokes number for flows over a porous medium and $\phi = 50\%$ with $\rho_p/\rho = 1.05$. The error bars correspond to the combined uncertainty in the torque measurements normalized by the corresponding $M_{laminar}$.

where the normalized torque does not reach a plateau. For $\bar{\phi} = 10\%$, the normalized torques start increasing for $St > 80$. For this particular loading fraction, the maximum value for the normalized torque occurs at the lowest and the highest Stokes number.

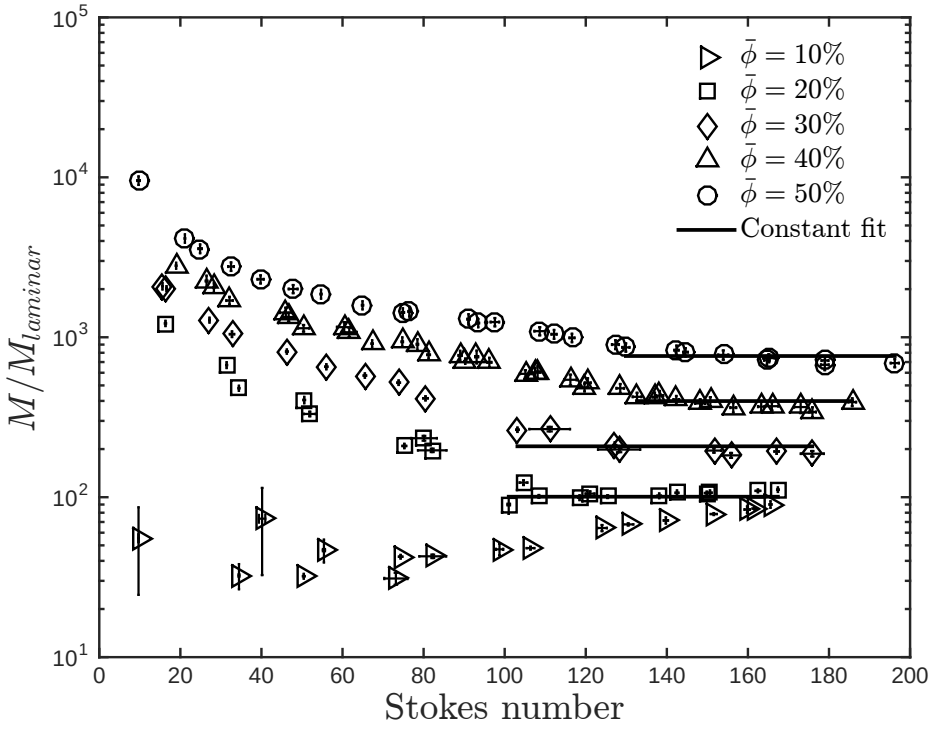

Figure 5.15: Normalized torques as a function of Stokes number for flows over a porous medium for all $\bar{\phi}$ tested with $\rho_p/\rho = 1.05$. The error bars correspond to the combined uncertainty in the torque measurements normalized by the corresponding $M_{laminar}$.

5.5 Summary

Results from experiments where the liquid-solid mixtures are sheared over a porous medium were presented. The torque measurements corresponding to shear rates lower than 60 s^{-1} increase with shear rate. For higher shear rates there is a change in the torque trend. For $\bar{\phi} = 10\%$, the torque dependance on shear rate became different: from linear to non linear (power law fit). For the rest of the loading fractions, the torque exhibits a drop where the torque decreases and then increases again with the shear rate. These marked changes in the dependance of the torque on shear rate are not observed in the experiments with no porous medium. The presence of hysteresis is studied and it is found that with the exception of $\bar{\phi} = 10\%$, once the torque is normalized there is no significant presence of hysteresis for all the loading fraction tested. In general, for Stokes number lower than 100, the normalized torques decrease with St. For a loading fraction of 10%, the normalized torques start to increase for $St > 80$. This increase is only observed for this particular loading fraction. For

the other loading fractions, the normalized torques decrease and for $\bar{\phi} < 50\%$ it becomes constant. The Stokes number at which the normalized torques reach a plateau increases with the loading fraction. For $\bar{\phi} = 10\%$, μ'/μ starts increasing for $St > 80$. For $\bar{\phi} = 20$, $\bar{\phi} = 30$, and $\bar{\phi} = 40$, μ'/μ becomes constant at $St > 120$, $St > 125$, and $St > 155$, respectively.

Chapter 6

Particle resuspension

6.1 Motivation

In previous chapters, the relative effective viscosity of a flow with particles denser than the interstitial liquid was discussed. Such results show that these flows exhibit a shear thickening behavior when the amount of particles loaded is less than 30% in volume, while for flows with particle loading higher than 30% the behavior exhibited was shear thinning. In this chapter, the results of the visualization of such flows are presented to understand the mechanism behind such behaviors and to further explore the resuspension of flows consisting of settling polystyrene particles.

6.2 Particle settling

The visualizations are made by using the visualization setup described in Chapter 2, where the test cylinder and top fixed guard are replaced by a transparent acrylic cylinder. As described in Chapter 2, the acrylic cylinder wall is roughened in the same manner as for the torque measurements, leaving only a portion of the wall smooth and which serves as a visualization window. A percentage of approximately 20% in volume of particles is painted on one face to make the visualization process easier. The interstitial liquid for all the cases describe in this chapter is water and the particles are all polystyrene; thus the density ratio between the particles and the liquid is $\rho_p/\rho = 1.05$. For each set of experiments, a known volume of particles is loaded into the annulus. The volume of the particles is obtained by carefully adding the particles to a known volume of water until they all sink, and then measuring the volume of water displaced. The loading volume fraction ($\bar{\phi}$) is the ratio between the volume of particles loaded and the total annulus volume. Each experiment is prepared by running the rheometer for 30 minutes at a shear rate of, $\dot{\gamma} = 50\ s^{-1}$, with the objective to remove air bubbles from the mixture and guarantee a homogeneous distribution of the particles. Once the mixture has been sheared for 30 minutes, the rheometer is brought to a complete stopped and the particles are allowed to come to rest in a loose, random orientation. Observations through

the visualization window show that the particles settled and stop moving in less than a minute. However, pictures of the apparent settle column of particles taken several minutes later show that the minimum settling height of the column is not reached once the particles stop moving but some time after that. An image sequence of the particles settling is shown in Figure 6.1.

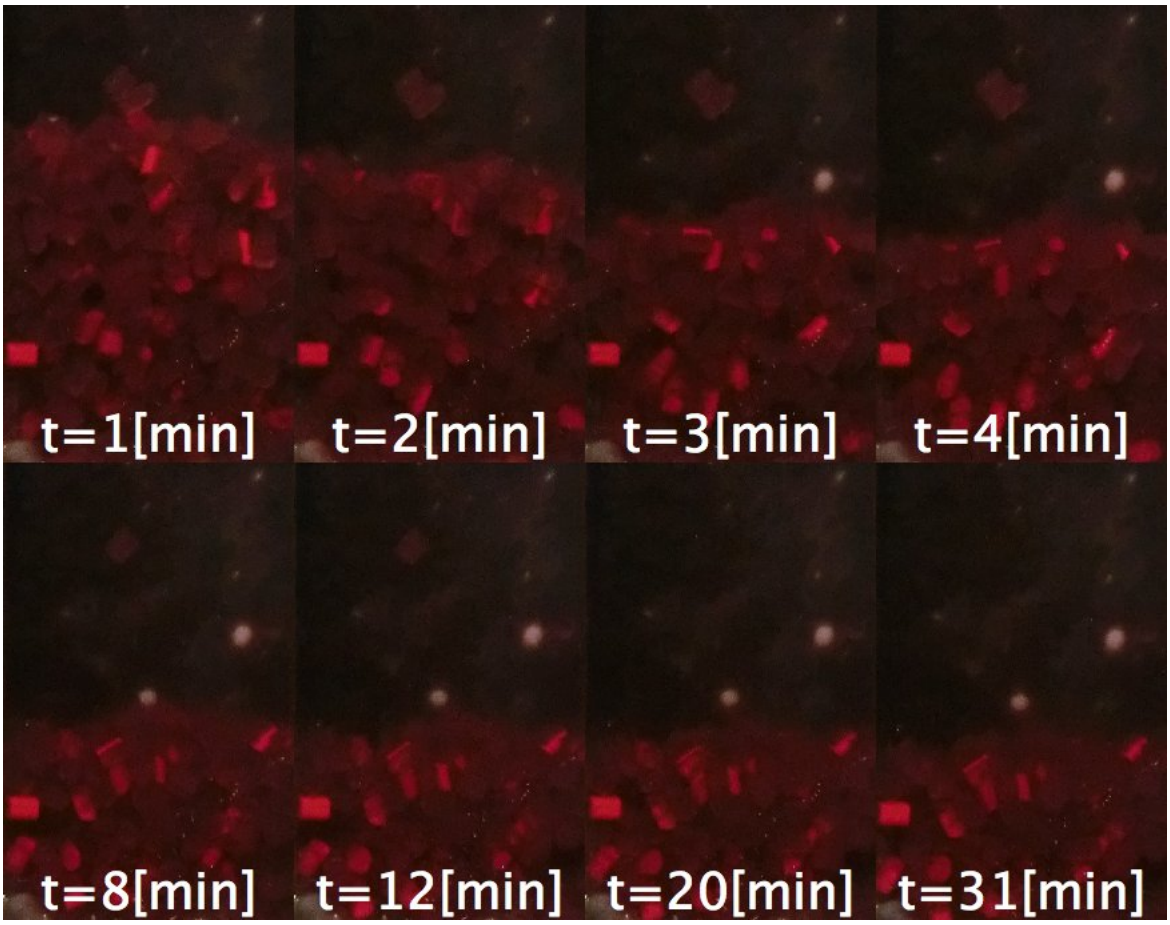

Figure 6.1: Settling process after the rheometer is brought to a complete stop for a loading volume fraction of 25%. Polystyrene particles, $\rho_p/\rho = 1.05$. Pictures taken from inside the inner cylinder. Each window has a width of approximately 3.8 (cm) and the bottom of each picture corresponds to the top of the lower fixed guard.

The height of the settled particles is measured by drawing a line that follows the top contour of the particles. The vertical coordinates along the contour are considered and averaged to obtain the particle's mean height. An example of the contour used to measure the settled particle's height is shown in Figure 6.2

The minimum loading volume fraction that could be studied is 20%. For lower loading volume fractions the particles are below the visualization window. In Figure 6.3 the ratio of the height of the settled particles (h_s) and the total annulus height (h_t) of the rheometer for a loading volume fraction of 25% is shown. The particle's packing decreases approximately 2.54 cm and reach a

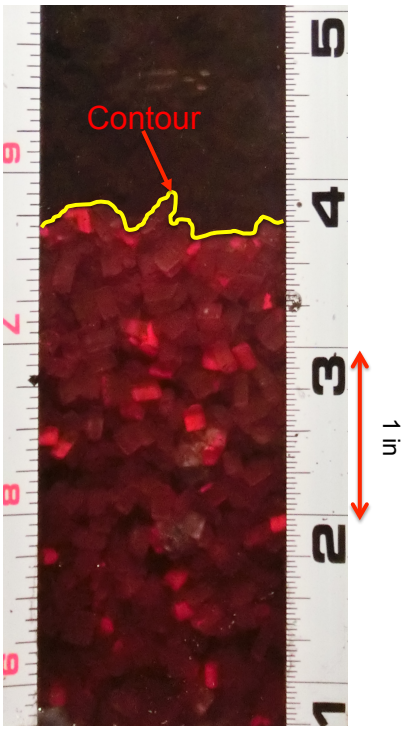

Figure 6.2: Settled particles and their contour marked by the yellow line. The case shown corresponds to a loading volume fraction of 30%. The ruler shown is in inches. The ratio between particles and fluid density is $\rho_p/\rho = 1.05$.

minimum constant height in 20 minutes. The height of the settled particles decreases by a total of 10.6% of its initial length.

To compare the settling process between different loading volume fractions, the minimum height was subtracted from the measured heights for each loading volume fraction and normalized by the total annulus height. Figure 6.4 shows how much the settled particles compact with time. An average of 15 minutes is the time it takes for the particles to reach a minimum height. From Figure 6.4 it can be seen that the height difference $(h - h_{min})$ increases with the loading volume fraction; that is, the higher the amount of particles there is, the more the particles compact.

Figure 6.5 shows the height of the settled particles normalized with the annulus total height as a function of the loading volume fraction. The normalized height exhibits a linear relation with the loading volume fraction. The linear fit does not intercept the origin and therefore cannot be used to predict the height for lower loading volume fractions. For very low loading volume fractions the particle's height may show a different dependance with the loading volume fraction. This could be better seen by considering a very low loading volume fraction where the number of particles is not enough to completely cover the base of the annulus. For such a case the presence of a few extra particles strongly influences the measured height; meanwhile, for higher loading volume fractions the mean measured height is not be affected by the presence of a few extra particles. Note that

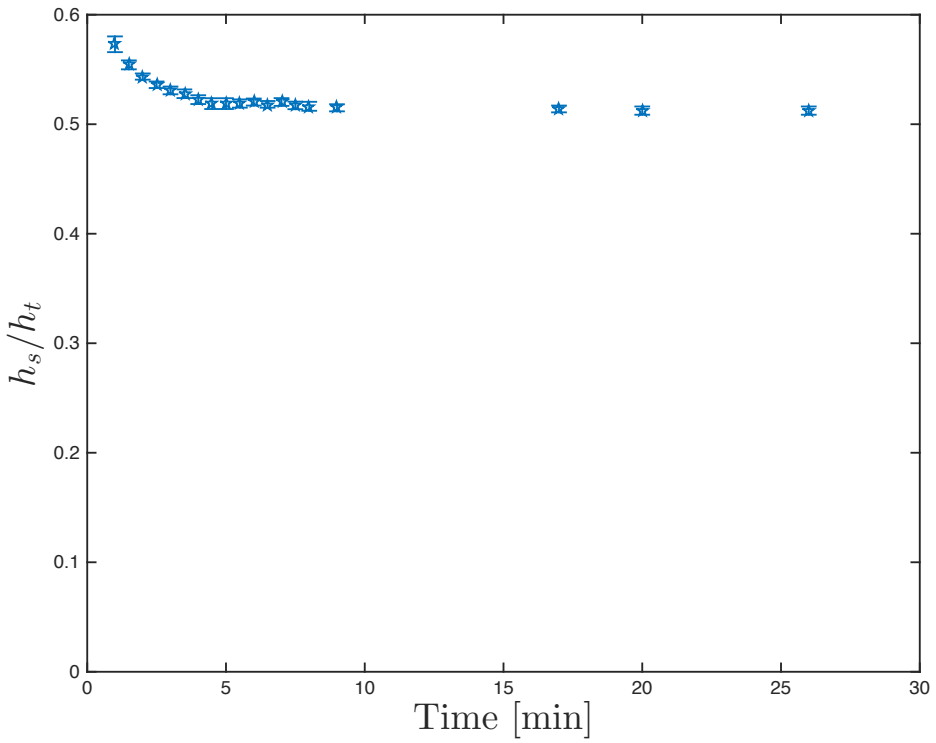

Figure 6.3: Settled particles height (h_s) normalized with the total annulus height (h_t) as a function of time for a loading fraction of 25%. The ratio between particles and fluid density is $\rho_p/\rho = 1.05$. The vertical error bars correspond to the standard deviation of the height measurements, while the horizontal error bars represent the uncertainty in the time at which the corresponding picture was taken.

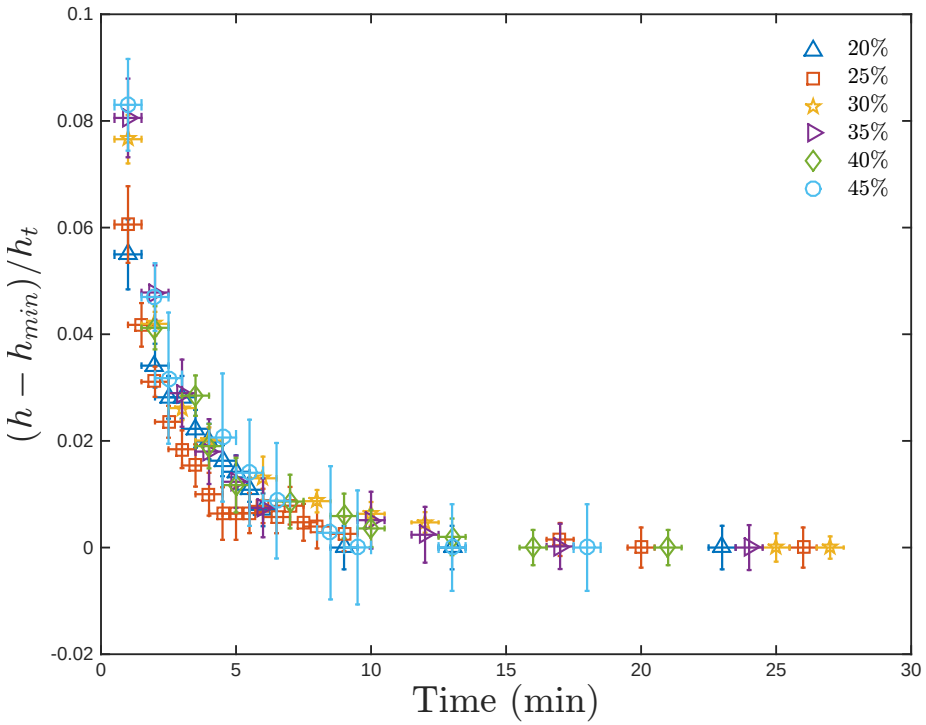

Figure 6.4: Difference of settled particles height and its minimum (h_{min}) normalized with total annulus height (h_t) as a function of time for different loading volume fractions for polystyrene particles. The ratio between particles and fluid density is $\rho_p/\rho = 1.05$. The vertical error bars correspond to the standard deviation of the height measurements, while the horizontal error bars represent the uncertainty in the time at which each picture was taken.

if the linear fit in Figure 6.5 is extrapolated to $h_s/h_t = 1$, the loading fraction is 55.8, which is approximately equal to the random loose packing measured by Koos (2009).

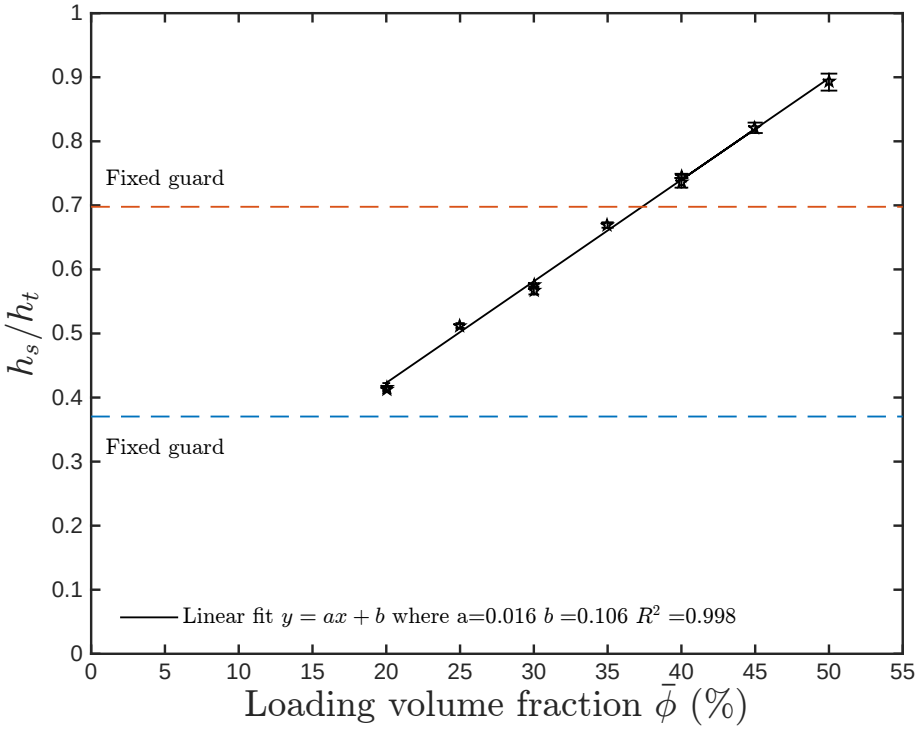

Figure 6.5: Settled particle's height (h_s) normalized with the total height of the rheometer annulus (h_t) as a function of the loading volume fraction. Dashed lines correspond to the relative position of the low and top fixed guards. The ratio between particles and fluid density is $\rho_p/\rho = 1.05$. Error bars correspond to the height measurements standard deviation.

Particle settling over a porous medium

Visualizations are also made for the case of a flow over a porous medium where the rheometer is filled with spherical glass beads (diameter of 4 (mm) and density of 2520 (kg/m^3)) up to approximately 6/7 of the bottom fixed guard. Polystyrene particles are placed on top of this layer of glass beads, as described in Chapter 5. The density ratio between the polystyrene particles and the interstitial liquid (water) for the experiments described in this section is $\rho_p/\rho = 1.05$. The volume of the annulus considered for these experiments does not take into account the volume occupied by the glass beads. Therefore, the volume of polystyrene particles needed to obtain a loading volume fraction of 10% is less than for the case with no glass beads on the bottom (approximately 33% less in particles volume). To account for the volume occupied by the porous medium, measurements of its height are conducted, and from this the packing of the porous medium is calculated. As described in Chapter 2, the porous medium is prepared by first measuring the volume of the glass beads. This is done by pouring them into a known volume of water and measuring the volume of liquid displaced. Then,

the known volume of glass beads is poured into the bottom part of the annulus and it is evenly distributed along the perimeter of the rheometer. Once the entire volume of glass beads is poured and evenly distributed, the porous medium is sheared to account for any change in packing due to shearing (to prevent excessive shearing on the porous medium, the walls of the bottom part of the rheometer are not roughened). The height between the top of the lower fixed guard and the porous medium is measured with the help of a vernier. These measurements are made dry and it is considered that the effect of water on the packing of glass beads is negligible due to the high density of the glass beads. A packing of 0.62 is found, which is what Koos (2009) measured for the random loose packing of spherical glass beads of 3 mm in diameter and with the same density.

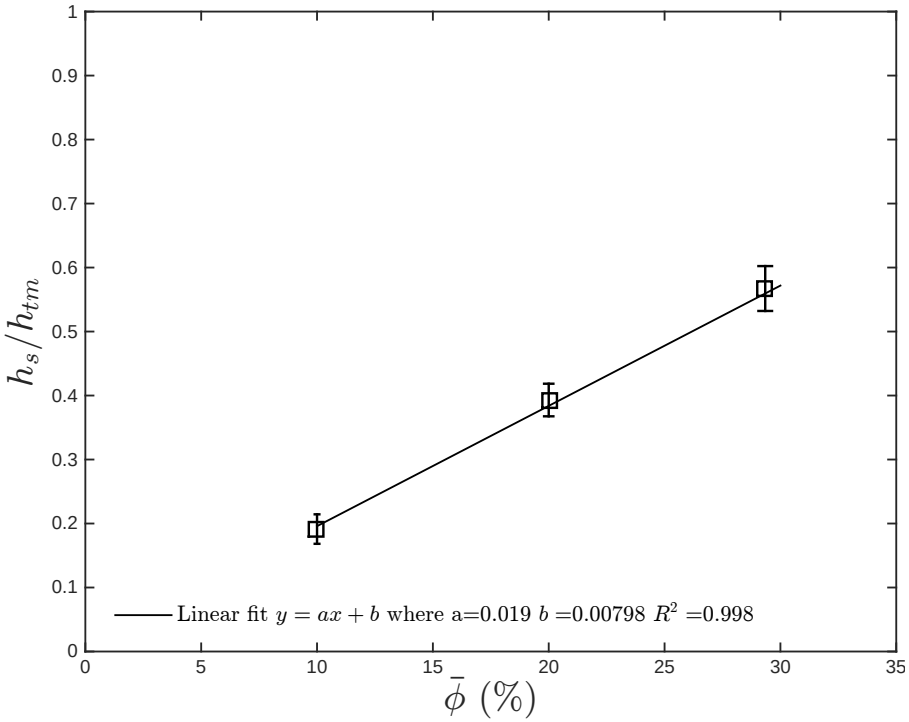

Figure 6.6: Settled particles height (h_s) normalized with the total height of the annulus modified for the presence of porous medium (h_{tm}). The ratio between particles and fluid density is $\rho_p/\rho = 1.05$. Error bars correspond to the height measurements standard deviation.

Figure 6.6 shows the settled particles height normalized by the height between the top of the glass beads' bottom layer and the top of the rheometer annulus (h_{tm}). As with the previous measurements for the height of settled particles, the relation between the loading volume fraction and h_s is linear and the fit does not intercept at the origin. Figure 6.7 shows the settling height normalized by the annulus total height (h_t) for the experiments with and without porous medium. The difference in normalized height for the same loading fraction between experiments is due to the presence of the porous medium. With a porous medium, even for a low loading fraction of 10%, the particles' height is always above the bottom fixed guard. Figure 6.8 shows the settling heights for the experiments

with porous medium normalized by the modified annulus height (without considering the layer of glass beads) and the non-porous medium heights normalized by the total annulus height. For the experiments with porous medium, the particles height is slightly lower than for the case with no porous medium. The little difference between the normalized heights has a more pronounced effect when the random loose packing is measured, as discussed in the next section.

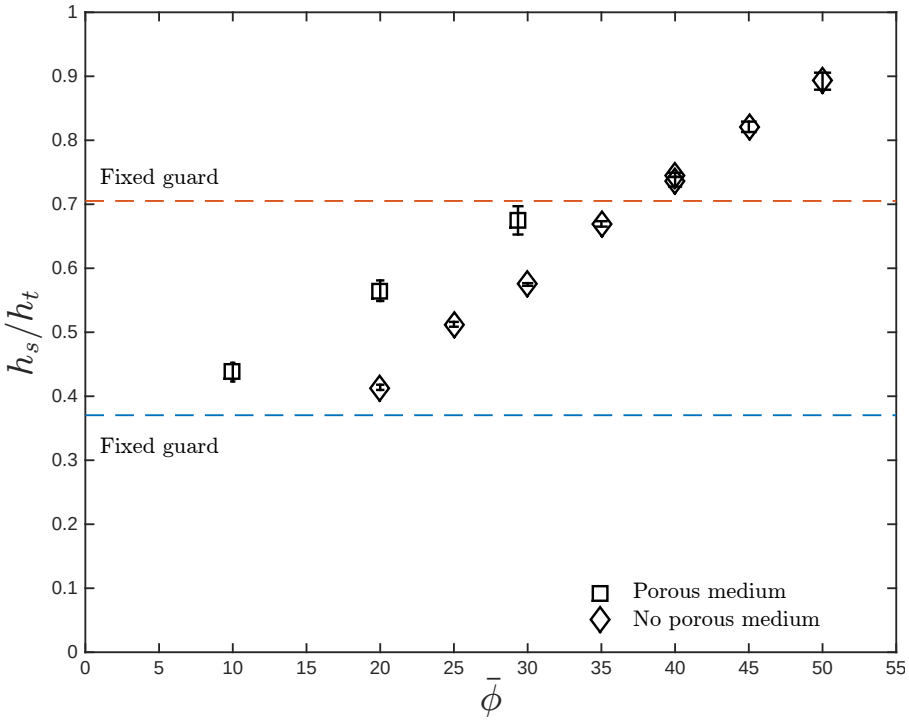

Figure 6.7: Settled particles height (h_s) normalized with the total height of the annulus (h_t) for experiments with and without porous medium. The ratio between particles and fluid density is $\rho_p/\rho = 1.05$. Error bars correspond to the height measurements standard deviation.

6.3 Random loose packing

The random loose packing, ϕ_{RLP}, can be calculated from these height measurements by considering that the total volume occupied by the particles is equal to the measured settled height times the area of the base of the rheometer annulus. The height measured through the visualization window is considered to be the same along the perimeter and in the radial direction of the rheometer. The reduction in the annulus base area due to the rough surface is considered when calculating this area. The random loose packing is then be given by

$$\phi_{RLP} = \frac{\text{Volume of particles}}{\text{Volume occupied by particles}} = \frac{\text{Volume of particles}}{\text{Annulus base area} \times h_s}, \tag{6.1}$$

where h_s is the minimum settling height reached by the settled particles after 15 minutes or

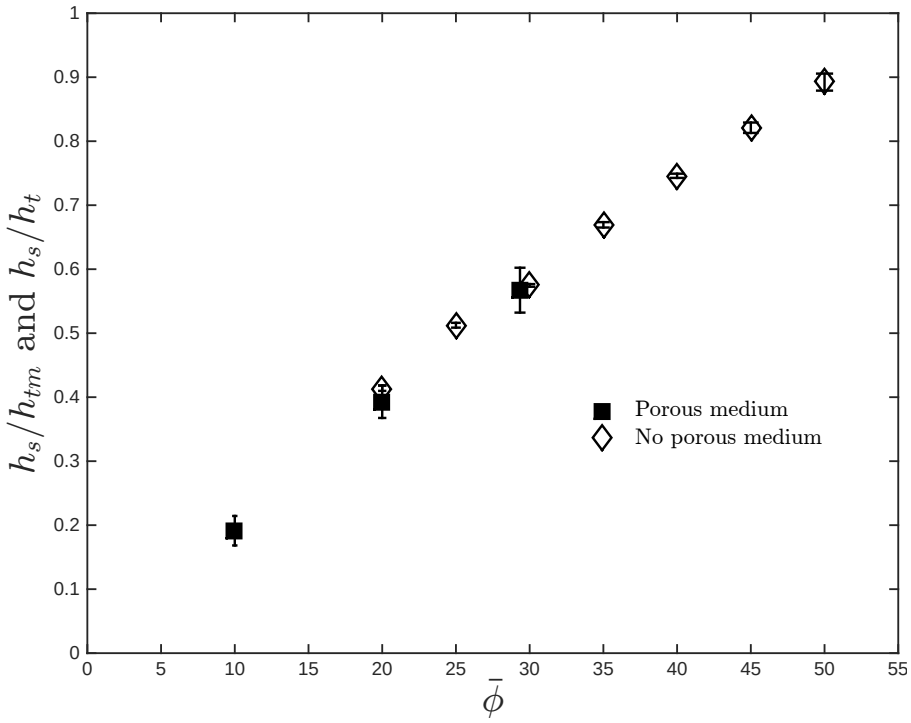

Figure 6.8: Settled particles height (h_s) normalized with the total height of the annulus (h_t). For the experiments with porous medium, the settling height is normalized by the modified total height annulus (h_{tm}). The ratio between particles and fluid density is $\rho_p/\rho = 1.05$. Error bars correspond to the height measurements standard deviation.

more have passed. Figure 6.9 shows the random loose packing as a function of the loading volume fraction. As seen in Figure 6.4, the higher the loading volume fraction, the more the particles are compacted, which leads to a higher random loose packing. One of the sources of uncertainty for the random loose packing calculation is the area considered for the annulus base. To verify that the annulus base area is constant along the vertical axis, measurements of the height of a known volume column of water are performed. These measurements show that the column water height increases linearly with the water volume. Hence, the annulus base area seems to be constant along the annulus height. The annulus base area can be measured from these measurements; however, the area occupied by the water is larger than the area that can be occupied by the particles, since the water can enter cavities in the rough surface that the particles can not. For this reason, the annulus base area is considered to be equal to $\pi \times ((r_o - d)^2 - (r_i + d)^2)$, where r_o and r_i are the outer and inner cylinder radius with smooth walls and d is the particle diameter.

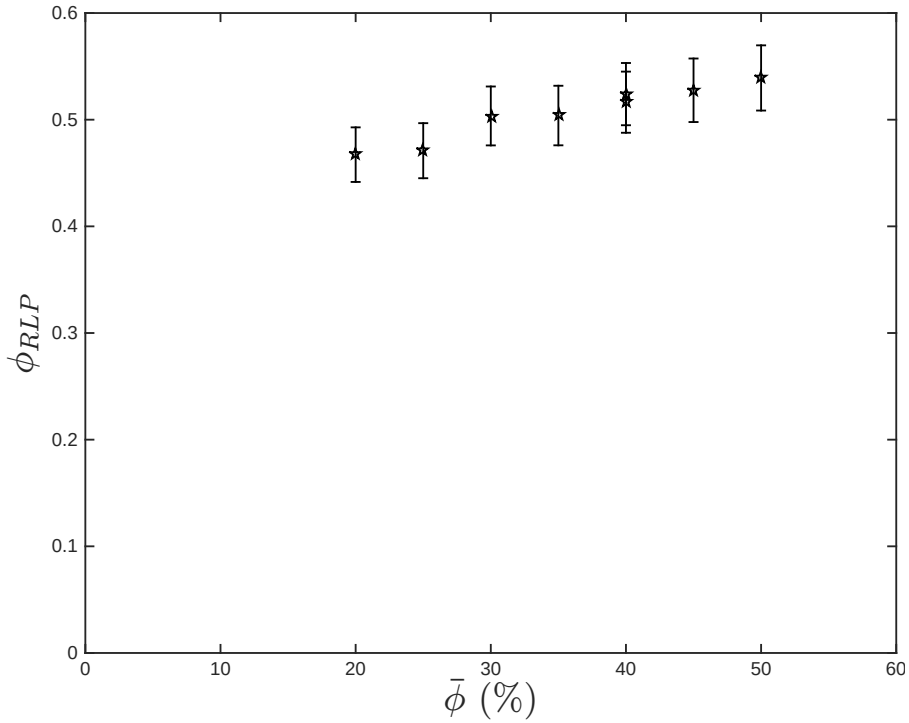

Figure 6.9: Measured random loose packing from the settling height measurements as a function of the loading volume fraction. The ratio between particles and fluid density is $\rho_p/\rho = 1.05$. Error bars correspond to the uncertainty involved in these measurements.

The reason why the random loose packing is not constant is still not completely understood, but one explanation could be the effect that the extra weight due to the increase in particles has on further compacting the column of particles. Moreover, it is likely that some particles have a lighter density, leading to higher measurements of the particle column height and thus a decrease in the random loose packing calculated. The ratio between the random loose packing for the highest and

lowest loading volume fraction is 1.16; thus the random loose packing varies up to 16% for different loading volume fractions.

Random loose packing of polystyrene particles over a porous medium

The random loose packing is calculated for the loading volume fractions of 10, 20 and 30 percent. Higher loading volume fractions are not measured because the view window only covered the height of the test cylinder, which is lower than the height of the particles. As mentioned before, the volume of the annulus considered when there is a porous medium on the bottom of the rheometer depends on the packing of such medium.

The polystyrene particles' column height is measured in the same way as for the previous cases, where the mixture is sheared for several minutes to ensure a homogeneous distribution of the particles and then brought to rest. Figure 6.10 shows the random loose packing calculated for the settled particles over a porous medium. As with the previous random loose packing measurements, the

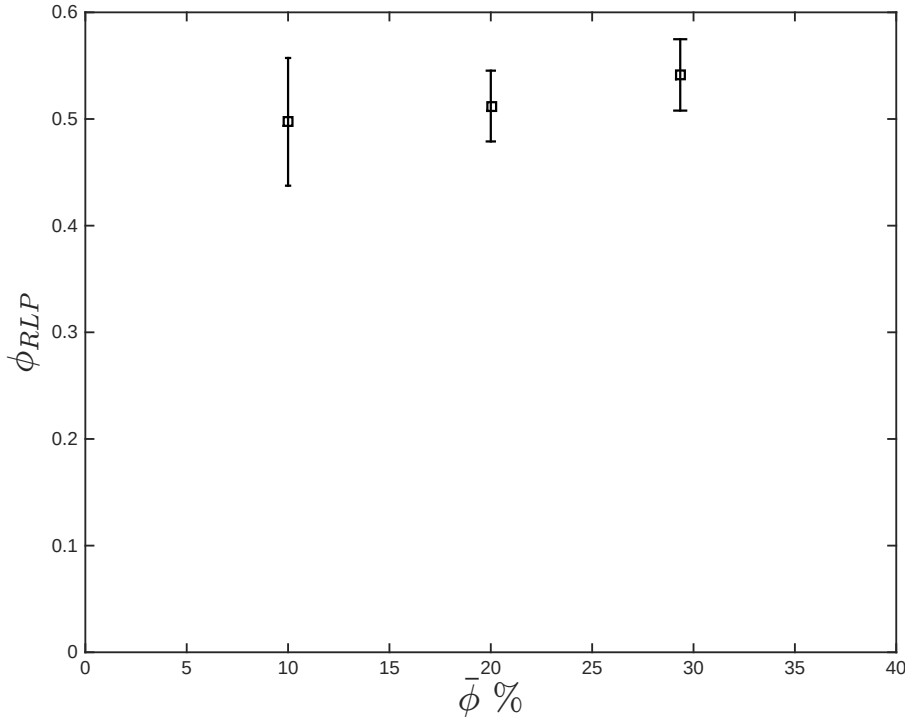

Figure 6.10: Measured random loose packing from the settling height measurements of polystyrene particles over a porous medium as a function of the loading volume fraction. The ratio between particles and fluid density is $\rho_p/\rho = 1.05$. Error bars correspond to the uncertainty involved in these measurements.

ϕ_{RLP} increases with loading volume fraction. The random loose packing for polystyrene particles over a porous medium can be compared to the one measured without porous medium on the bottom. Figure 6.11 shows this comparison. For all the loading volume fractions, the random loose packing

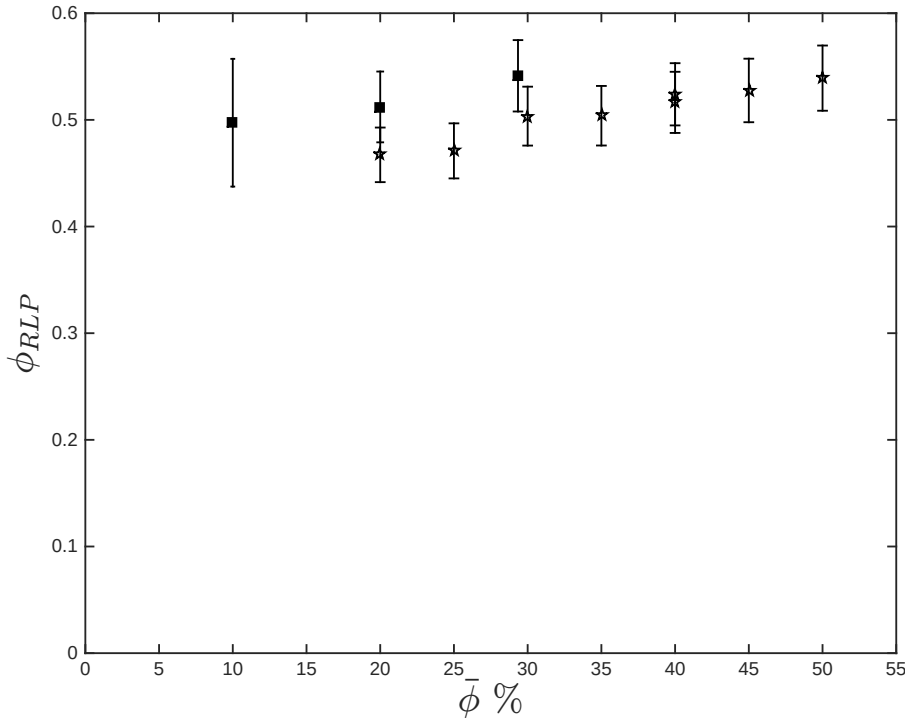

Figure 6.11: Comparison between measured random loose packing of polystyrene particles with and without a porous medium on the bottom as a function of the loading volume fraction. The ratio between particles and fluid density is $\rho_p/\rho = 1.05$. Error bars correspond to the uncertainty involved in these measurements.

for the cases with glass beads on the bottom is higher than for the case without glass beads. However, the random loose packing for the case without porous medium is within the lower error bar for the ϕ_{RLP} with a porous base. Besides the porous medium, these two cases differ in the amount of particles necessary to reach the same loading volume fraction. There are less particles for the case with porous medium, which makes the topology of the particles' top surface a source of greater uncertainty.

6.4 Particle resuspension for $\rho_p/\rho = 1.05$

The characteristics of settled polystyrene particles immersed in water are discussed in the previous section. For all the cases presented in the previous section the Stokes and Reynolds numbers were equal to zero. In this section, the resuspension of the particles due to an increase in the shear rate and consequently an increase on the Stokes and Reynolds numbers is studied. The case without porous medium on the bottom is analyzed first. For all the experiments studied in this section the interstitial liquid of the flow is water and the density ratio between the particles and the liquid is $\rho_p/\rho = 1.05$.

Figure 6.12 shows an image sequence of the resuspension for a loading volume fraction of 25 %. Each picture is taken after several minutes of shearing the liquid-solid mixture at the shear rate corresponding for each Stokes number. As Stokes number increases, the particles start fluidizing until they reach a steady state where the level reached by the particles remains constant with time. The level reached by the particles for each Stokes number is measured in the same way as the height of the column of settled particles (described in the previous section). A minimum of 9 pictures for each Stokes number is taken and used to measure the resuspension height. Figure 6.13 shows the resuspension height normalized by the total height of the rheometer annulus.

The change in height occurs abruptly as the Stokes number is increased from zero, as shown in Figure 6.12 and 6.13 . The height normalized by the annulus height, as shown in both figures, for $St = 0$ corresponds to the settled particles' height after the particles have been at rest for more than 15 minutes. The further packing of the particles while at rest described in Section 6.1 contributes for this sudden change in height. A similar profile is observed for different loading volume fractions, as shown in Figure 6.14.

The normalized resuspension heights increase with loading volume fraction but exhibit a similar dependance on Stokes number. This suggest that the data could be collapsed into one curve, and such a parameter can be the particles packing. For St=0, the random loose packing is measured and described in detail in Section 6.3. A volume fraction for non-zero Stokes numbers is given by:

$$\phi = \frac{\text{Volume of particles}}{h \times \text{Annulus base area}} = \phi_{RLP}\frac{h_s}{h}, \tag{6.2}$$

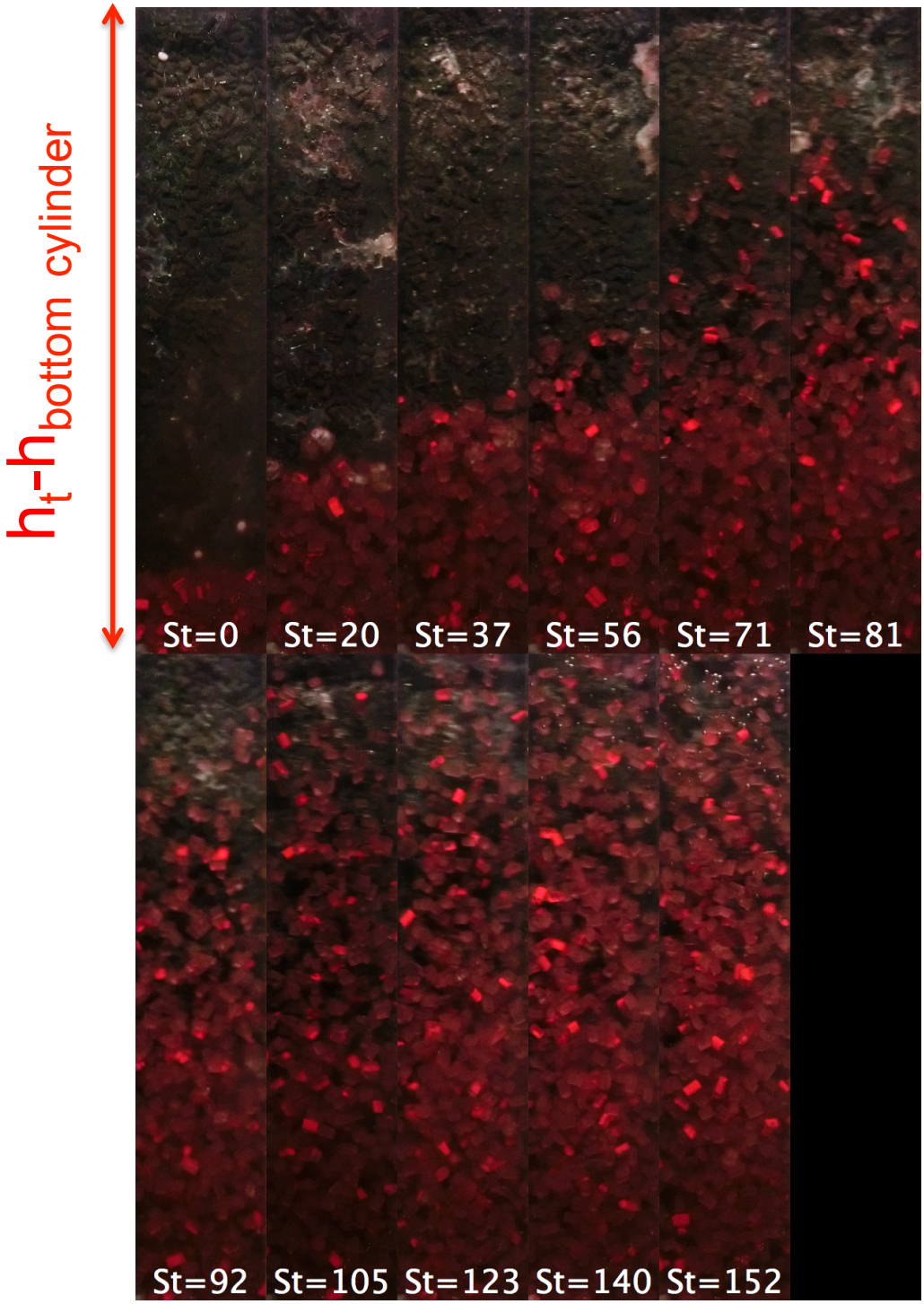

Figure 6.12: Particles resuspension for a loading volume fraction of 25% for different Stokes numbers. Pictures taken from inside the inner cylinder. Each window has a width of approximately 3.8 (cm) and a height equal to the total rheometer annulus height minus the lower fixed guard height. The bottom of each picture corresponds to the bottom of the test cylinder.

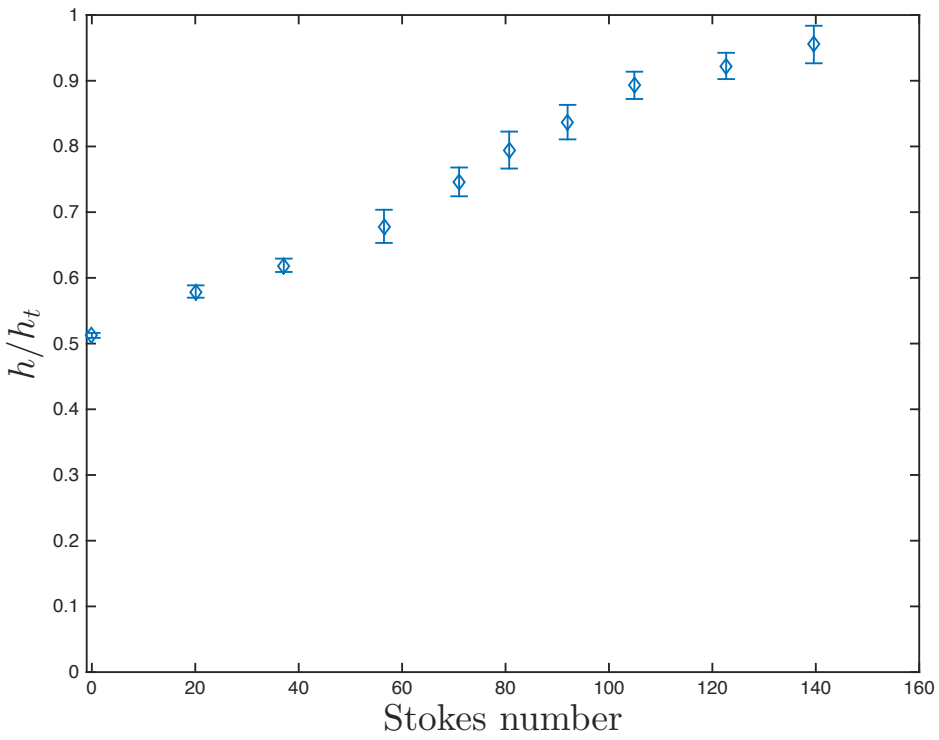

Figure 6.13: Resuspension height (h) normalized by the total rheometer annulus height (h_t) as a function of Stokes numbers for a loading volume fraction of 25%. Error bars correspond to the standard deviation in the resuspension height measurements.

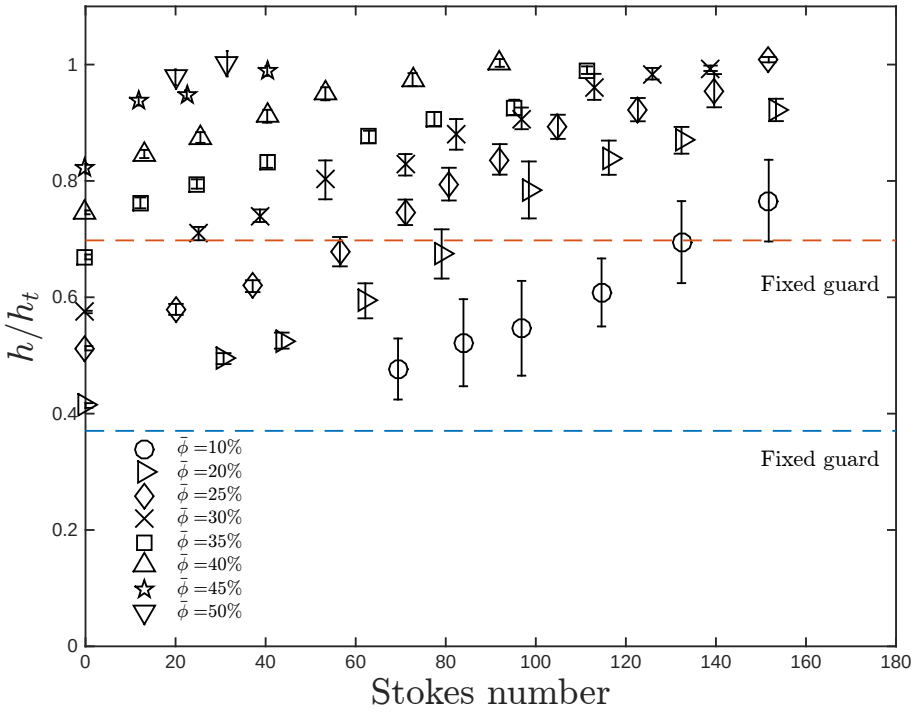

Figure 6.14: Resuspension height (h) normalized by the total rheometer annulus height (h_t) as a function of Stokes numbers. Error bars correspond to the standard deviation in the resuspension height measurements.

where h_s is the settled particles' height and h is the resuspension height. Figure 6.15 shows the particles packing's strong dependance on Stokes number. There is some dependance on the loading volume fraction but this can be further minimized if the particles packing is normalized by the measured random loose packing for each loading volume fraction as shown in Figure 6.16. Predictions of how much the particles would expand given a certain Stokes number can be done using this relation. Such predictions are used in the next chapter to predict the effective volume fraction of the torque measurements.

Particle resuspension over a porous medium ($\rho_p/\rho = 1.05$).

The analysis of the resuspension of settling particles over a layer of glass beads (porous medium) is done in a similar way as discussed in the previous section. Only the total rheometer annulus height is reduced to take into account the bottom layer of glass beads. The height for this type of experiments is measured from the top surface of the porous medium. Figure 6.17 shows the resuspension height normalized by the modified total annulus height (h_{tm}). As with the previous experiments, the normalized height increases with the Stokes number and with the loading volume fraction. To study the effect of the bottom glass beads layer on the resuspension, the heights are normalized by the modified total height and compared with the normalized measured heights for the

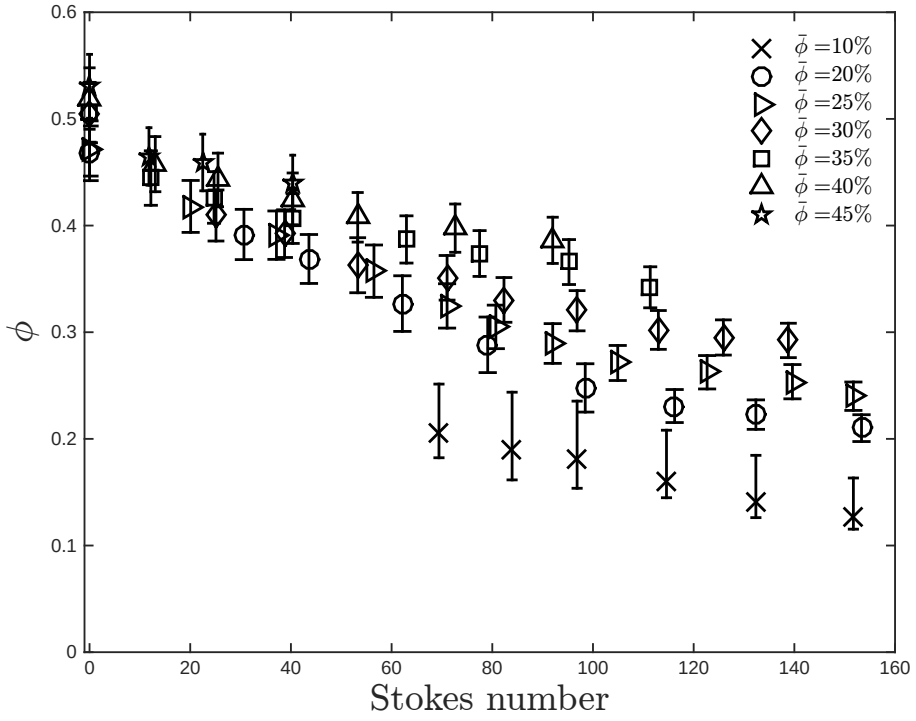

Figure 6.15: Particle packing for different loading volume fractions as a function of Stokes numbers. The uncertainties in measuring the particles packing are combined in root mean square sense and are represented by the error bars.

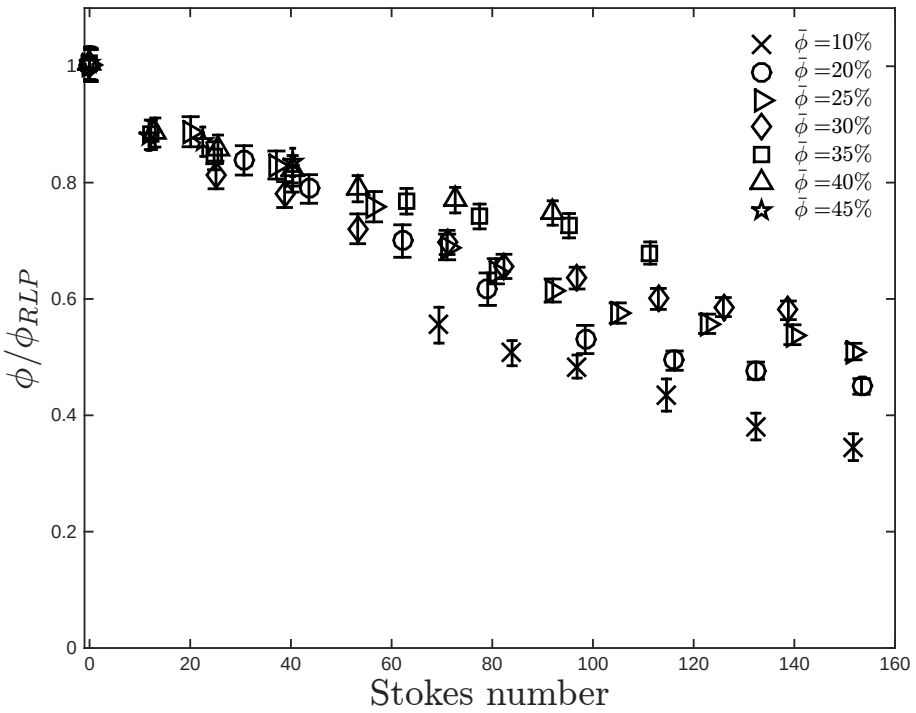

Figure 6.16: Particle packing for different loading volume fractions normalized by the random loose packing as a function of Stokes numbers. The uncertainties in measuring the particle packing are combined in root mean square sense and are represented by the error bars.

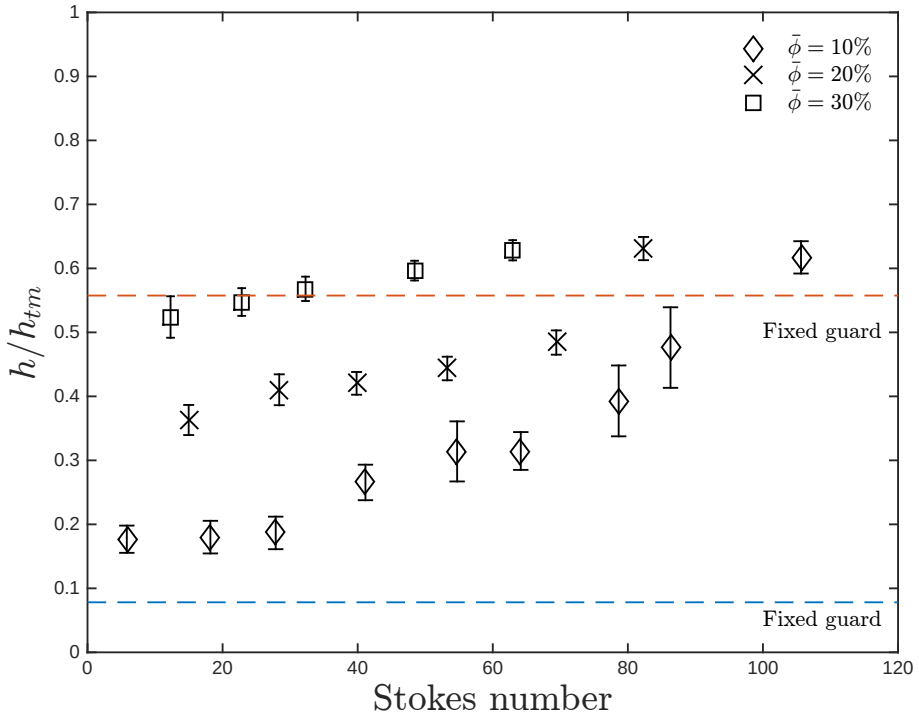

Figure 6.17: Resuspension height normalized by the modified annulus height (h_{tm}) as a function of Stokes numbers. The height of the particles column is measured from the surface of the porous medium. The error bars correspond to the standard deviation of the height measurements.

experiments without a porous medium. Figure 6.18 shows this comparison. The normalized heights for the experiments with porous medium do not seem to follow the same expansion exhibited for the experiments with the same loading fraction but without porous medium . For the case with flow with no porous medium, the expansion at low loading fractions occurs in a more pronounced way than the expansion for the same loading fraction but with porous medium at the bottom. Figure 6.19 shows the heights for the experiments with porous medium measured from the bottom of the annulus normalized by the total annulus height (h_t). These normalized heights are plotted together with the normalized heights for the case without a porous medium on the bottom. In this way, the portion of the test cylinder that is covered by the particles can be observed as a function of the Stokes numbers. The differences in the expansion of a column with the same height but a different amount of particles can be also analyzed with Figure 6.19. The expansion of the column of particles for the case with porous medium on the bottom and $\bar{\phi} = 10\%$ coincides with the expansion measured for a $\bar{\phi} = 20\%$ and no porous medium. Similarly, the expansion of $\bar{\phi} = 20$ and 30% for flow over porous medium compares favorably with the expansion of $\bar{\phi} = 25$ and 30% without porous medium, respectively. This suggests that the expansion of the particles is determined by the distance from the surface of the column of particles to the top boundary rather than the loading fraction. If the same loading volume fraction is considered, the normalized heights for the case with a porous medium

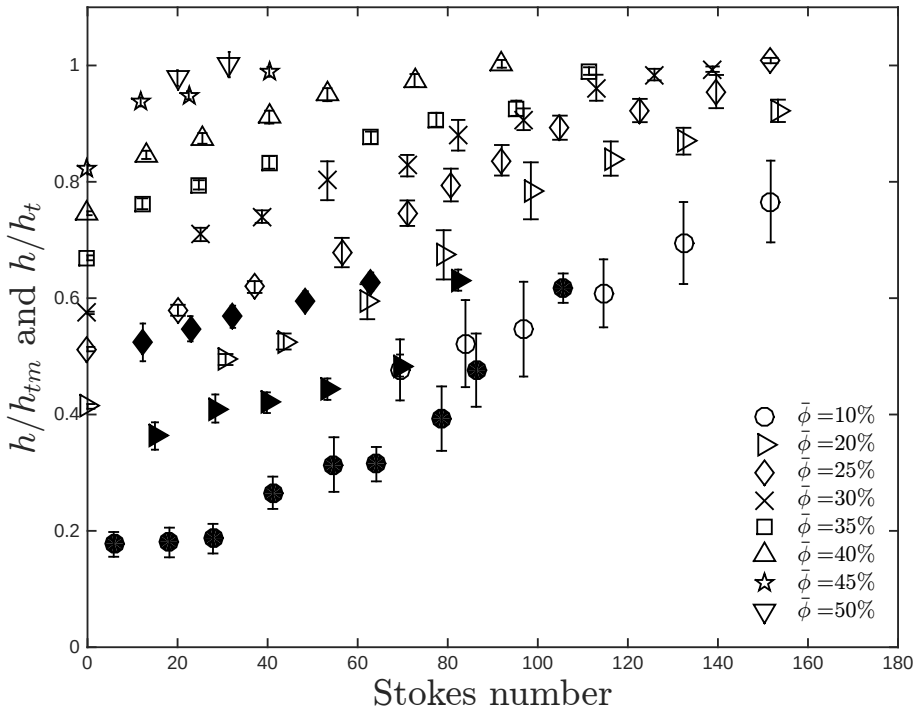

Figure 6.18: Resuspension height normalized by the total modified annulus height (h_{tm} and h_t) for the case with and without porous medium as a function of Stokes numbers. Open symbols correspond to the case with no porous medium on the bottom and close symbols correspond to the case with a porous medium. The heights for the latter case are measured from the top of the porous medium. The error bars correspond to the standard deviation of the height measurements.

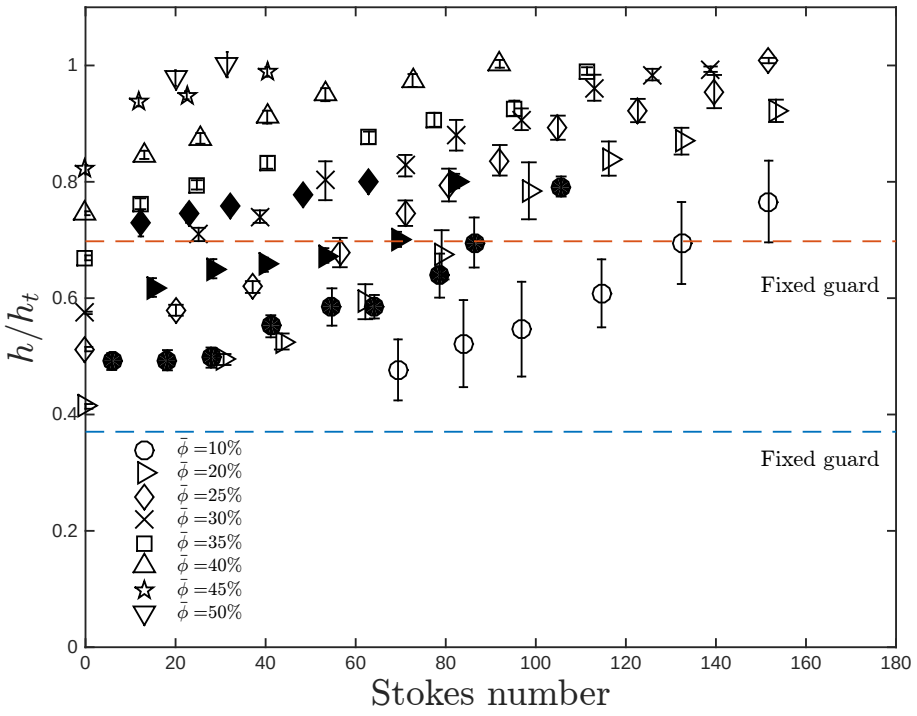

Figure 6.19: Resuspension height normalized by the total annulus height (h_t) as a function of Stokes numbers. Open symbols correspond to the case with no porous medium on the bottom and close symbols correspond to the case with a porous medium on the bottom . For the latter case, the heights shown considered the height of the glass beads layer. The error bars correspond to the standard deviation of the height measurements.

on the bottom coincide with the experiments without the porous medium. Figure 6.20 shows the dependance of the particles packing on the Stokes number for the case of particles fluidized over a porous medium. The dependance on the loading volume fraction is relatively weak compared to the dependance on Stokes number observed for the experiments with no porous medium. The particles' packing data collapses when normalized by the measured random loose packing, as shown in Figure 6.21. The normalized particle packing seems to collapse better than for the case with no porous medium; however, the resuspension of the particles could only be measured for Stokes numbers lower than 100 because of limits on the viewing window.

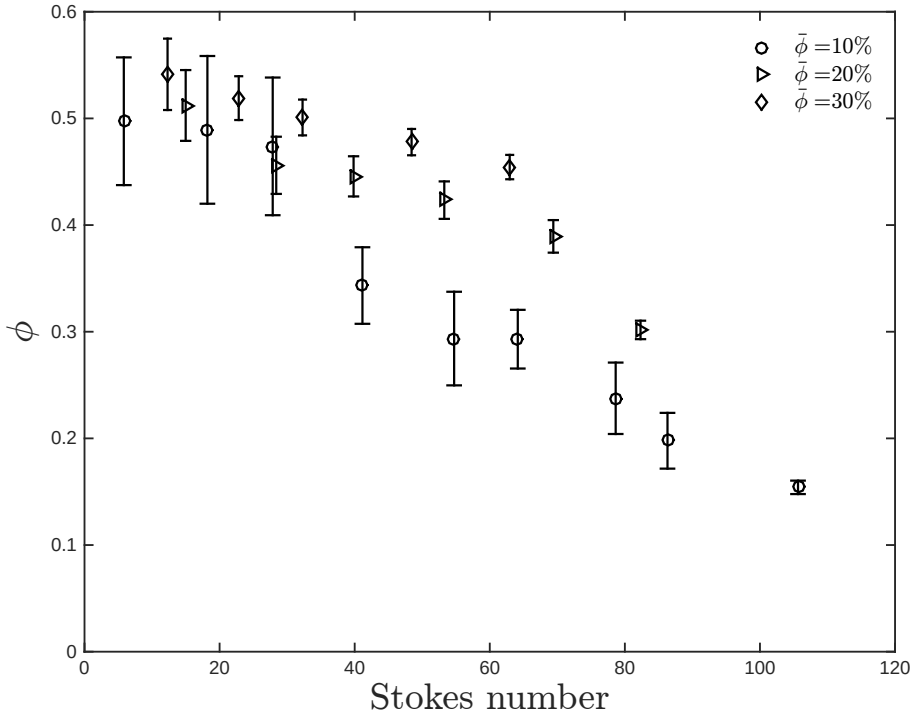

Figure 6.20: Particles packing for different loading volume fractions as a function of Stokes numbers for the case of flow over a porous medium. The uncertainties in measuring the particle packing are combined in root mean square sense and are represented by the error bars.

The packing for porous medium is compared against the packing without a porous medium in Figure 6.22. The normalized particle packing and its dependance on Stokes number for the case of porous and no porous medium on the bottom are shown in Figure 6.23. The particles over a porous medium fluidized less readily as compare with experiments without porous medium on the bottom. However, these differences are not big and both cases seem to follow a similar dependance on the Stokes number.

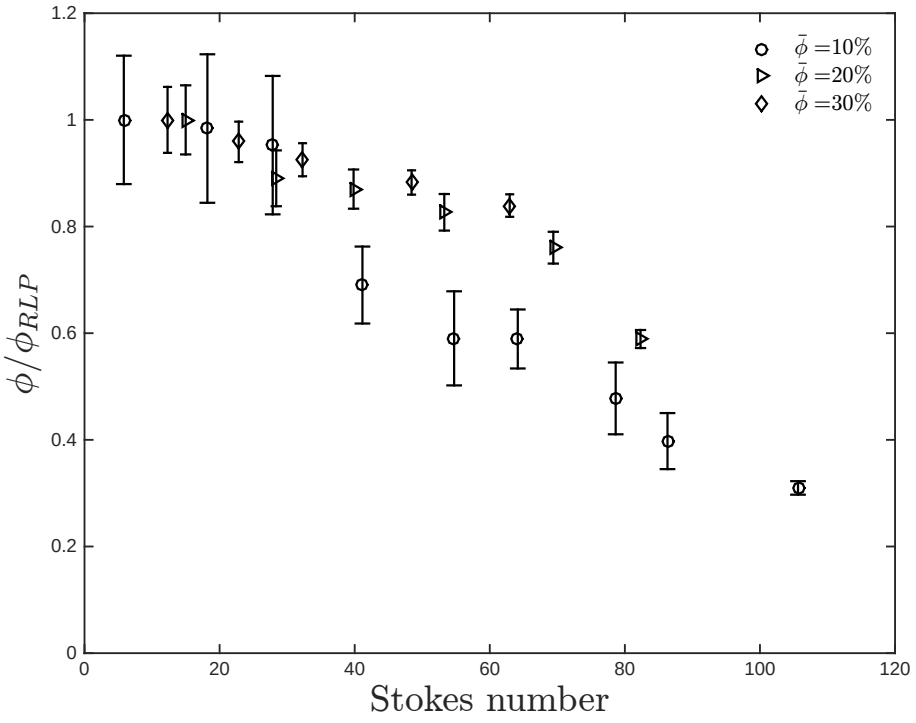

Figure 6.21: Particles packing for different loading volume fractions normalized with the measured random loose packing as a function of Stokes numbers for the case of flow over a porous medium. The uncertainties in measuring the particle packing are combined in root mean square sense and are represented by the error bars.

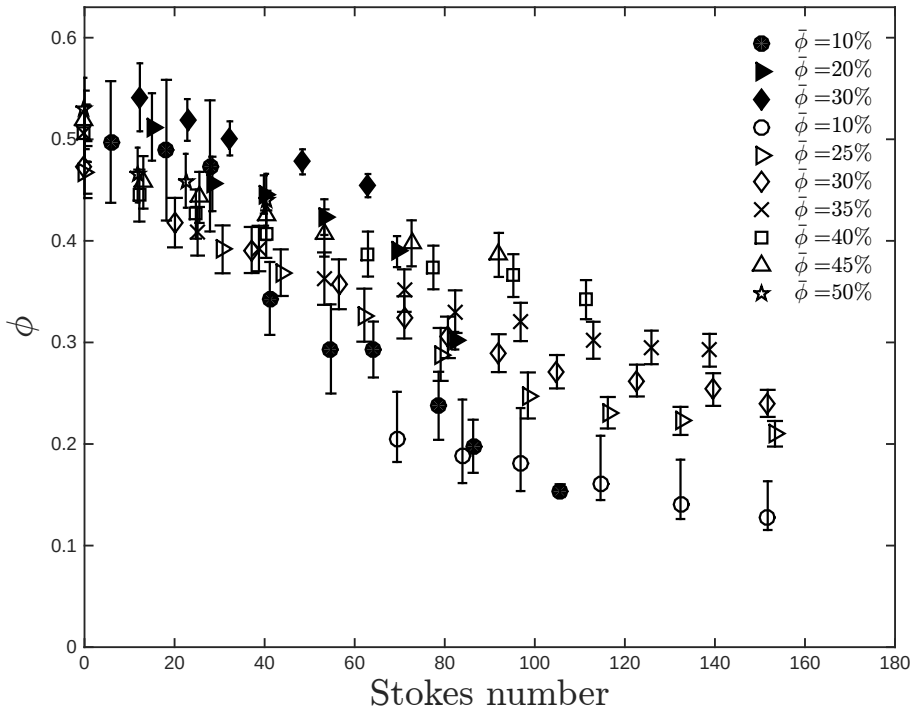

Figure 6.22: Particles packing for different loading volume fractions as a function of Stokes numbers for the case with and without porous medium. Close symbols corresponds to the flow over a porous medium. The uncertainties in measuring the particle packing are combined in root mean square sense and are represented by the error bars.

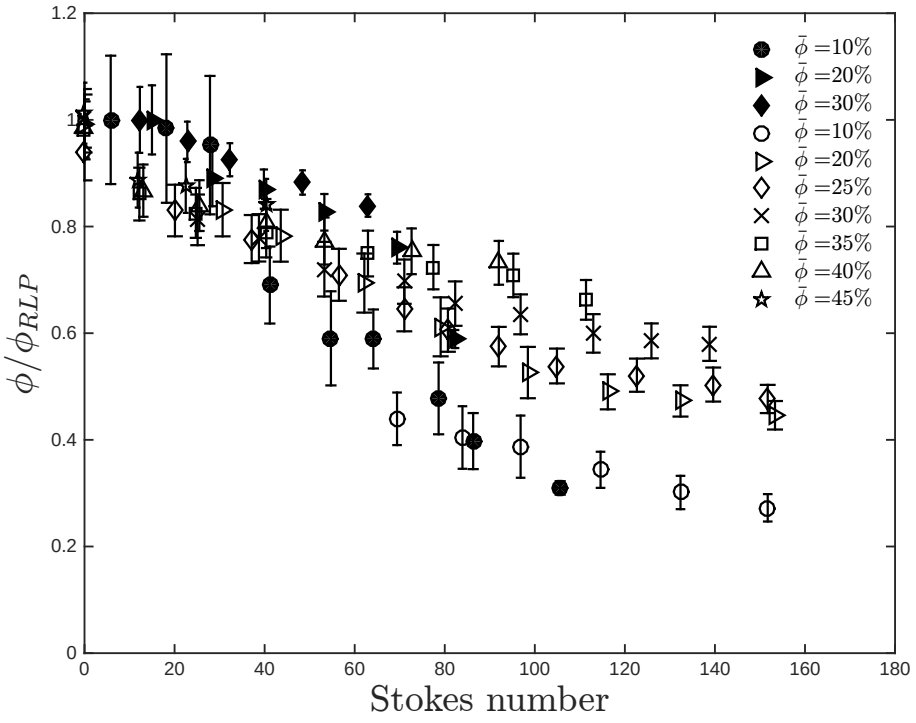

Figure 6.23: Particles packing for different loading volume fractions normalized with the measured random loose packing as a function of Stokes numbers for the case of flow over a porous and no porous medium. The uncertainties in measuring the particle packing are combined in root mean square sense and are represented by the error bars.

6.5 Summary

The particle settling process for non neutrally buoyant particles with a density ratio of $\rho_p/\rho = 1.05$ is presented in the first section of this chapter for the case of no porous medium on the bottom. A gradual compaction of the settled particles is found, where the initial height of the settled particles decreases over a period of 15 minutes once the rheometer is brought to a complete stop. The reason for this further packing of the particles is not completely understood but one explanation could be the gradual release of trapped air in the mixture.

Using the measurements of the particles settled height, the random loose packing is calculated and found to depend on the loading volume fraction for the experiments without a porous medium. The reason why the random loose packing is not constant might have to do with the presence of slightly buoyant particles. Lighter particles would cause the column of particles to further expand, leading to a decrease in the random loose packing.

Finally, the resuspension of the particles due to shearing is presented. When the measured heights for the experiments with a flow over a porous medium is normalized with the modified total annulus height, it does not strictly coincide with the experiments without porous medium with the same loading fraction. However, when the height of the column of particles over a porous medium is measured from the bottom of the annulus and normalized with the total annulus height, it coincides with the normalized measured height for the experiments without porous medium but higher loading fractions. This suggests that the fluidization of the column of particles depend on the position of the particle column or equivalently on the length of the column of liquid on top of that column. The particles resuspension is characterized by measuring the packing of the particles for different Stokes numbers. The particles' packing decreases with the Stokes number for both cases of porous and non-porous medium on the bottom, and if normalized with the measured random loose packing, the resuspension data collapses and follows a single trend where the largest scatter occurs for the highest Stokes number.

Chapter 7

Discussion

This chapter is a discussion of inertial and particle concentration effects for the experiments with a matched density, followed by direct comparisons of the torque measurements with different density ratios. In the previous chapter the effective volume fraction was measured with the help of the flow visualization. Such measurements are used to predict the effective volume fraction of mixtures with a density ratio of $\rho_p/\rho = 1.05$. It is hypothesized that the effective relative viscosity for flows with a mismatch density is equal to the effective relative viscosity for flows with a match density as long as both cases have the same effective volume fraction. This hypothesis is based on the results for mixtures with a matched density, where for $\phi > 30$ the effective relative viscosity does not appear to vary dramatically with the Stokes number but it strongly depends on the volume fraction.

7.1 Inertial and particle concentration effects on mixtures with $\rho_p/\rho = 1$

In Section 4.2 it was shown that the effective relative viscosity for experiments with a liquid with matched density and volume fractions of 10, 20, and 30% exhibit a dependance on Stokes number, (see Figure 4.3). To study if this dependance can be attributed to the presence of particles or to the hydrodynamic inertial effects, a comparison between the normalized torques for the mixture and for the suspending liquid is made as a function of the gap Reynolds number as defined in equation 2.5. Figure 7.1 shows the measured torques normalized by the theoretical laminar torque for volume fractions of 10, 20, and 30%, and for pure fluid. Both normalized torques increase with the gap Reynolds number. The normalized torque for the mixture is higher than the normalized torque for pure liquid. If the dependance of the normalized torque with Reynolds number is due to the suspending liquid inertial effects, the effect of the presence of particles would be to only increase the viscosity of the mixture. To account for the increase in flow viscosity due to the presence of particles, an effective gap Reynolds number ($Re_{b,\,eff}$) is considered. In this modified Reynolds number, the

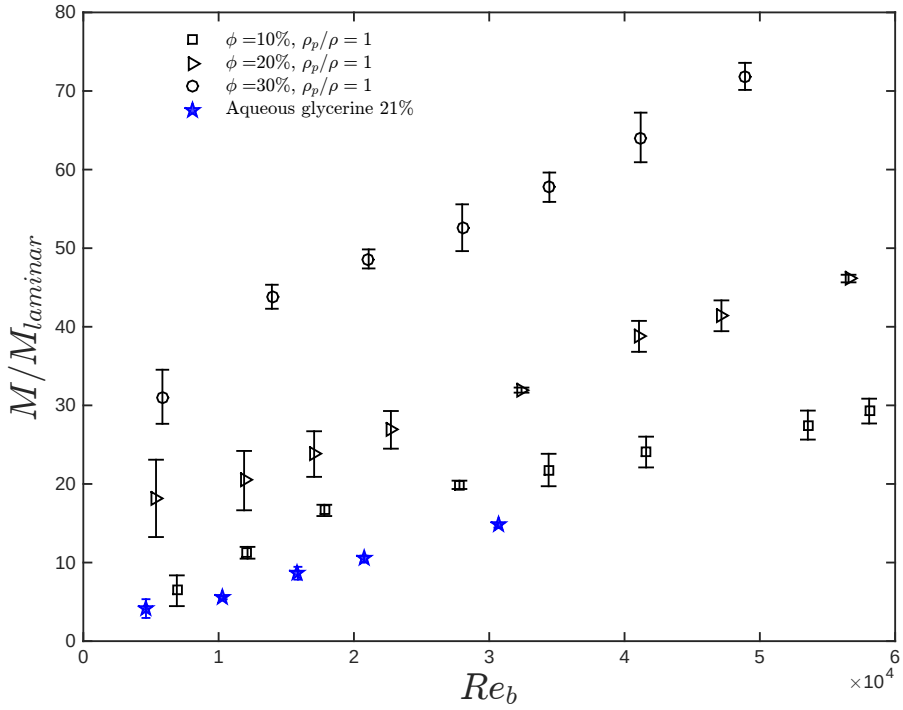

Figure 7.1: Normalized measured torques as a function of gap Reynolds numbers defined in equation 2.5 for pure fluid and mixtures with $\phi = 10$, 20 and 30% and $\rho_p/\rho = 1$.

effective viscosity of the mixture is used instead of the suspending liquid viscosity,

$$Re_{b,\,eff} = \frac{\rho \omega r_o b}{\mu'}.$$

The next step is to determine the effective viscosity of the mixture. Under no hydrodynamic effects, this effective viscosity would be independent of the Reynolds number and be only a function of volume fraction. Figure 7.2 shows the normalized torques for the experiments with $\rho_p/\rho = 1$ as a function of the loading fraction from the rough walls experiments of Koos et al. (2012) and the current experiments. For volume fractions lower than 40%, the data for the lowest Stokes numbers tested appear to coincide with the data from Koos (2012). As mentioned in Chapter 3, the range of Stokes numbers tested by Koos is slightly lower than the present experiments with $\rho_p/\rho = 1$ (Stokes number from $3 \leq St \leq 90$). Therefore, it is likely that hydrodynamics effects on the lowest Stokes numbers are negligible and the effective viscosity of the mixture can be inferred from these low St measurements. Figure 7.3 shows the effective relative viscosity of the mixture for the lowest Stokes numbers (μ'_{min}/μ) as a function of volume fraction compared with the effective relative viscosity from Koos et al. (2012). This effective viscosity is used to define the effective gap Reynolds number and it is considered to be only a function of volume fraction. To study the contribution from the hydrodynamic effects on the measured torques, it is instructive to normalize them by an "effective

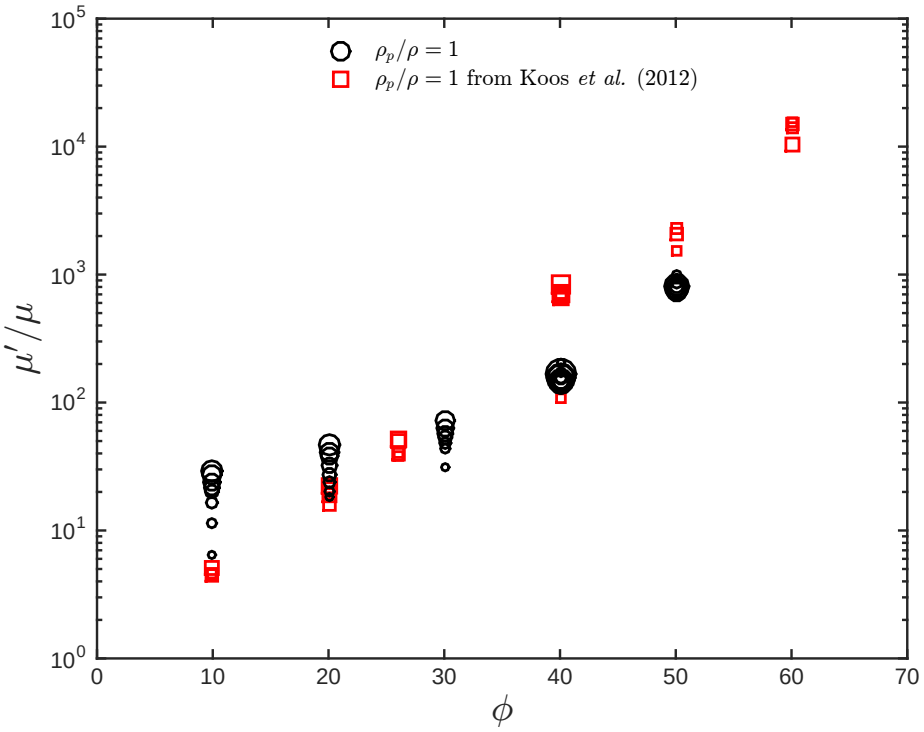

Figure 7.2: Effective relative viscosity as function of ϕ for current and previous work of Koos et al. (2012) with $\rho_p/\rho = 1$.

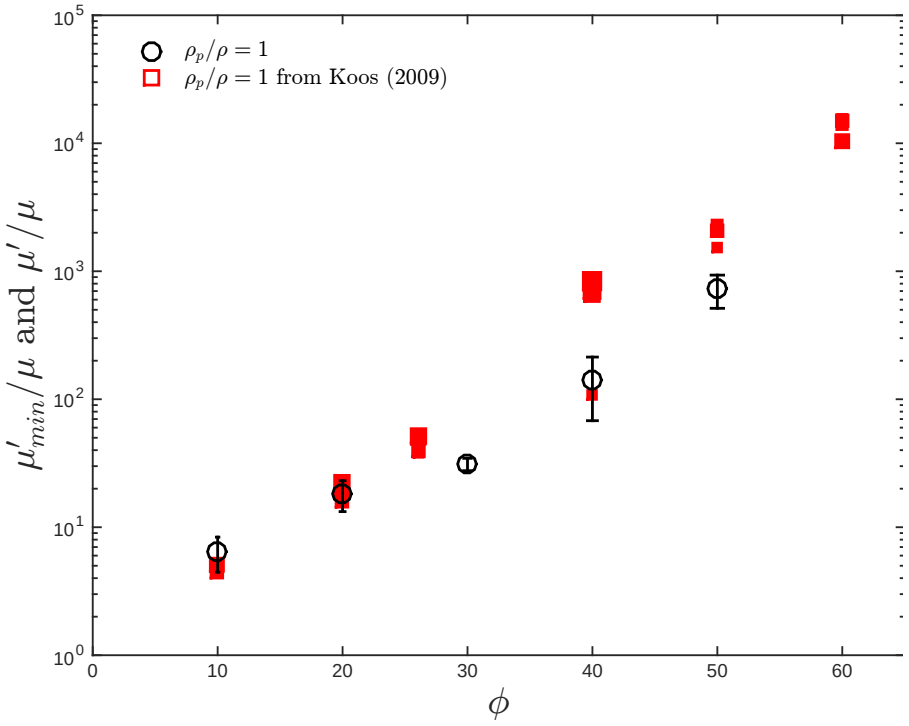

Figure 7.3: Minimum effective relative viscosity as function of ϕ for current experiments (μ'_{min}/μ) compared with the effective relative viscosity from Koos et al. (2012) with $\rho_p/\rho = 1$.

laminar torque", which is defined as a the corresponding torque for a Newtonian liquid with a viscosity equal to $\mu'_{min}(\phi)$,

$$M_{eff,\,laminar} = 2\pi r_i^2 H \dot{\gamma} \mu'_{min}(\phi).$$

If the effect of the presence of particles is to only increase the effective viscosity of the flow, the ratio between the measured torques and $M_{eff,\,laminar}$ would be independent of the effective gap Reynolds number when $Re_{b,\,eff}$ is below a critical value or regime, where the hydrodynamic effects are negligible.

Figure 7.4 shows the ratio between the measured torques and the effective laminar torque for all the volume fractions tested as a function of the effective gap Reynolds number based on μ'_{min}. The range of effective gap Reynolds number goes from $1 \leq Re_{b,\,eff} \leq 10 \times 10^4$. If the results of Taylor (1936a) can be applied to the liquid-solid mixture, the critical Reynolds number for the onset of Taylor-Couette vortices is expected to occur about $Re_{b,\,eff} \approx 1.1 \times 10^4$ for the current geometry of the apparatus. From Figure 7.4 it can be seen that the normalized torque increases for effective Reynolds numbers in a lower range. However, pure fluid torque measurements showed that the measured torques deviate from the laminar theory at a similar gap Reynolds number range (see Figure 2.13). Figure 7.5 shows the pure fluid and mixture measurements as a function of

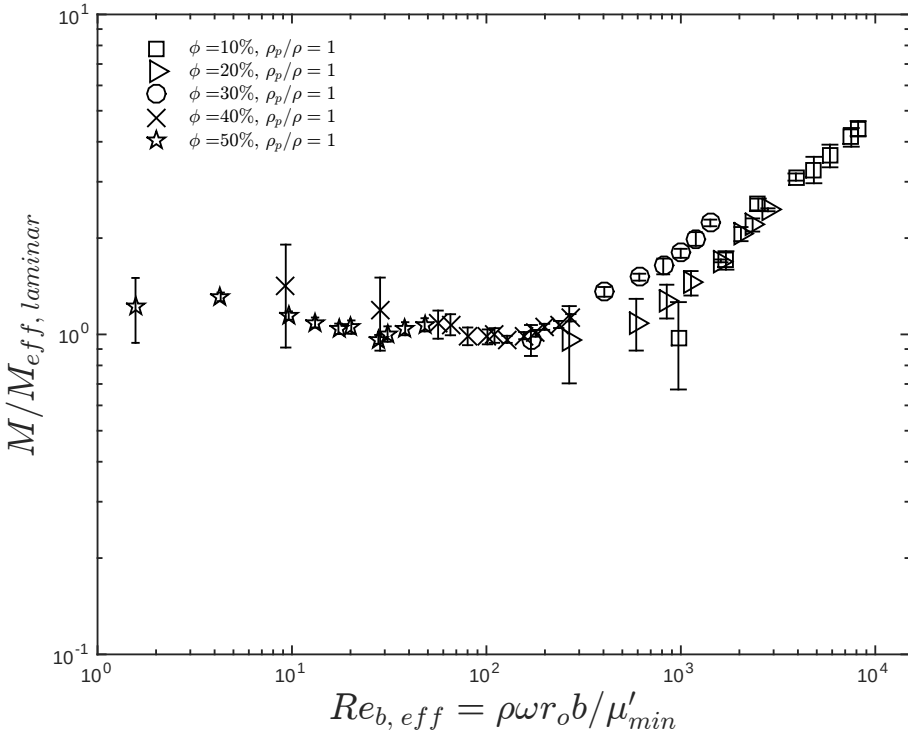

Figure 7.4: Measure toques normalized by effective laminar torque as a function of effective Reynolds number defined by the minimum value of μ'/μ for each volume fraction.

gap and effective gap Reynolds number. The deviation from laminar theory occurs at an effective

Reynolds number range where the pure fluid measurements exhibit a non-laminar behavior. The mixture normalized torques start deviating from the laminar theory at lower effective Reynolds number range. In the Couette-Taylor flow studies from Taylor (1936a), it was shown that when the flow is sheared by the rotation of the outer cylinder, the flow transition did not occur at a specific critical gap Reynolds number but within a range. Based on this, it is likely that the hydrodynamic effects are present in a range of Reynolds number rather than above a critical value. Therefore, the deviation from the laminar behavior of the mixture at effective gap Reynolds number is more likely to be due to hydrodynamics effects rather than an effect of particle interactions.

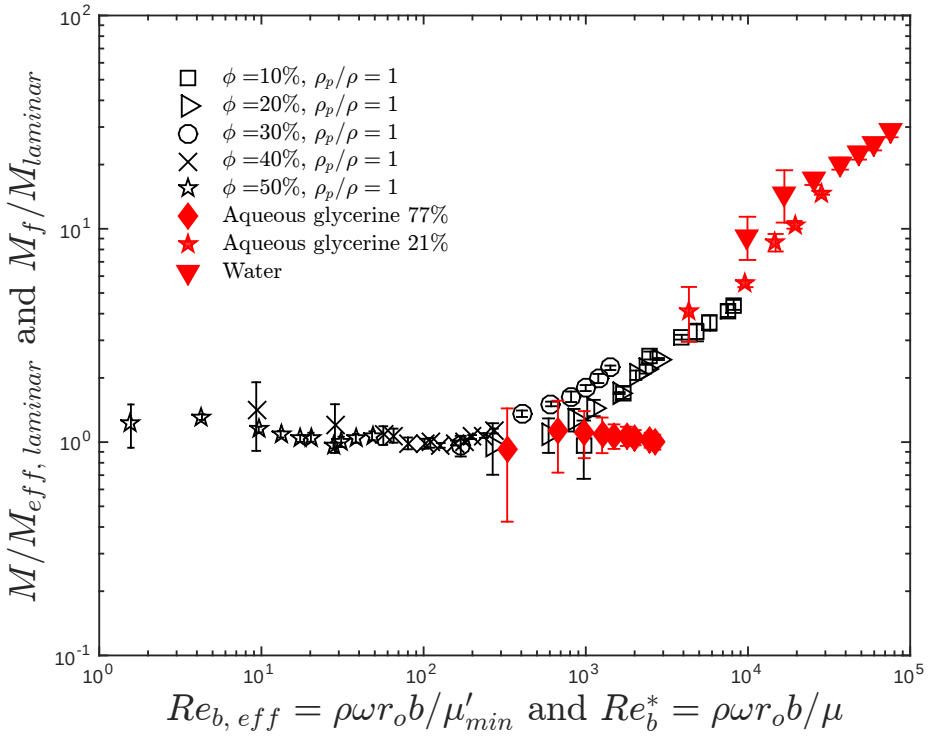

Figure 7.5: Measure toques normalized by $M_{eff,\,laminar}$ as a function of $Re_{b,\,eff}$ compared with normalized pure fluid torque measurements. For pure fluid, the normalized torques are plotted against Re_b^*.

In an ideal scenario where secondary flow effects are not present, the transition from "viscous" to "inertial" regime in liquid-solid flows would be governed by particle interactions. These interactions are controlled by the Stokes number, which is based on the particle size and the fluid viscosity rather than the effective viscosity of the mixture. Therefore, it is not possible to determine what the Stokes number regime at which the transition occurs due to merely particle inertia is.

For larger volume fractions the relative effective viscosity exhibited a weaker dependance on the Stokes number (see Figure 4.4), suggesting that for these experiments the inertial effects from the fluid and particles are not present. From Figure 7.5 it can be seen that for $\phi = 40$ and 50%, the corresponding $Re_{b,\,eff}$ is lower and possibly below the critical Reynolds number.

7.2 Direct comparisons between $\rho_p/\rho = 1$ and $\rho_p/\rho = 1.05$

Figure 7.6 shows the ratio of torques as a function of the Stokes number for the lowest loading fraction (10%) for the case with settling and non settling particles. Above Stokes number higher than 60, the normalized torques for both cases seem to match . Visualizations of the flow (a detailed analysis of this is presented in Chapter 6) for the case of settling particles at $\bar{\phi} = 10\%$ show that for Stokes numbers lower than 60, the height of the column of particles is lower than the bottom fixed guard height. Therefore, for $St < 60$ the particles do not reach the test cylinder. For this reason the torque measurements for these shear rates are not considered.

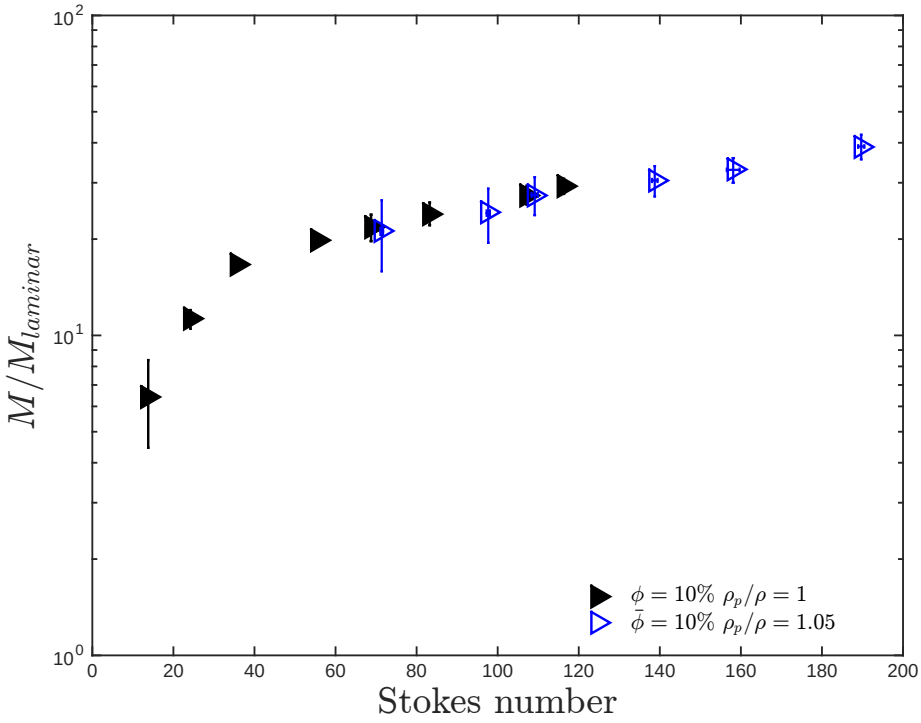

Figure 7.6: Normalized torques for 10% loading fractions as a function of St for $\rho_p/\rho = 1$ and 1.05.

Figure 7.7 shows the comparison between the normalized torques for a loading fraction of 10% with settling particles and the normalized torque measurements for just the liquid (plain water with no particles). These torques were normalized with the torque corresponding to a laminar flow. The normalized torques for a loading fraction of 10 % match the values for the torque measurements for just the fluid when the gap Reynolds number is lower than 5×10^4. For higher Re_b, the mixture exhibit higher normalized torques than the pure fluid. Above $Re = 3 \times 10^4$, the visualization of the flow starts showing the presence of particles in the middle test section.

The reason why the normalized torques for non-settling particles matches the normalized torques for the settling ones at $St < 135$ might be coincidental. In the case with settling particles, below

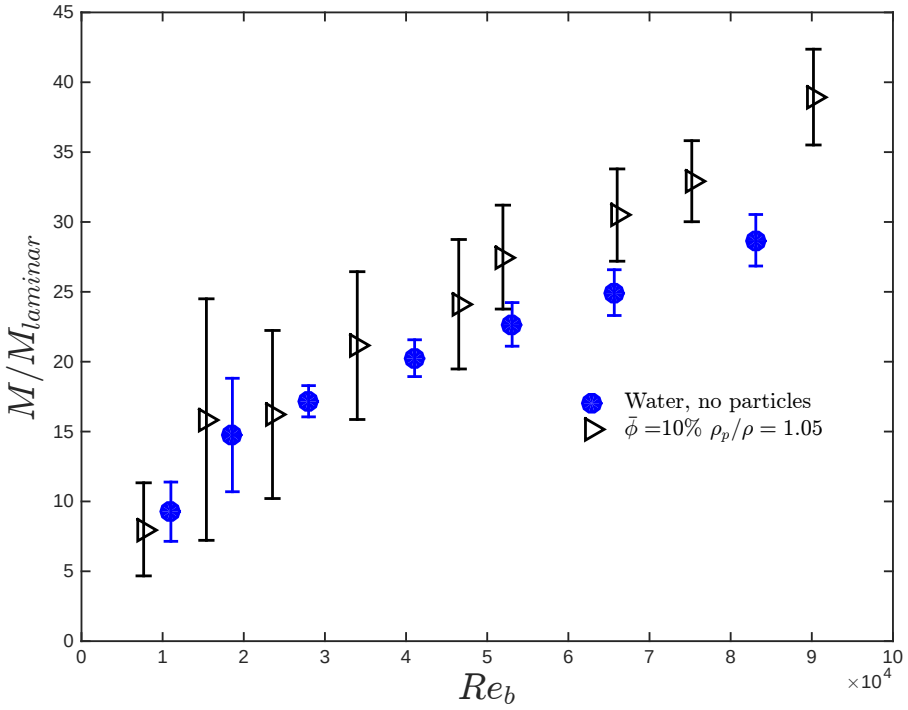

Figure 7.7: Comparison between normalized torques as a function of gap Reynolds number for pure fluid and $\bar{\phi} = 10\%$ with $\rho_p/\rho = 1.05$.

$St = 80$, the solid phase contribution to the torque at low shear rates is null, while for the case with neutrally buoyant particles the solid phase is always present (see Figure 7.8 for a comparison on the flow visualization between these two cases). Therefore at about $St = 80$, the measured torque includes a contribution from the pure fluid and a contribution from the particles.

For a higher loading fraction of 20%, the normalized torques for $\rho_p/\rho = 1$ are higher than for the case with $\rho_p/\rho = 1.05$ for $St > 60$, as seen in Figure 7.9. For the particular case of these low loading fractions, it is possible that the torque contribution from the suspending liquid is higher than the torque predicted from laminar theory. As presented in Section 2.4, the measured torques for plain water and 21% aqueous glycerine mixture are 4 to 28 times higher than the torques predicted by laminar theory. For the case of $\rho_p/\rho = 1.05$ and $\bar{\phi} = 10\%$, the visualization of the flow shows that the test cylinder is fully covered by the particles only for $St > 135$ (see Figure 6.14 or table 7.1). This means that for lower Stokes numbers, the measured torque does not correspond solely to the liquid-solid mixture and thus it is not representative of the suspension. A comparison of these loading fractions is given later in Section 7.6.

Figure 7.10 shows the normalized torques for a loading fraction of 30% for the case with settling and non-settling particles. For the case with settling particles, only the normalized torques corresponding to Stokes numbers where the particles are closed to be completely fluidized are considered (based on the settling particles heights and visualizations) so the settling effect on the measured

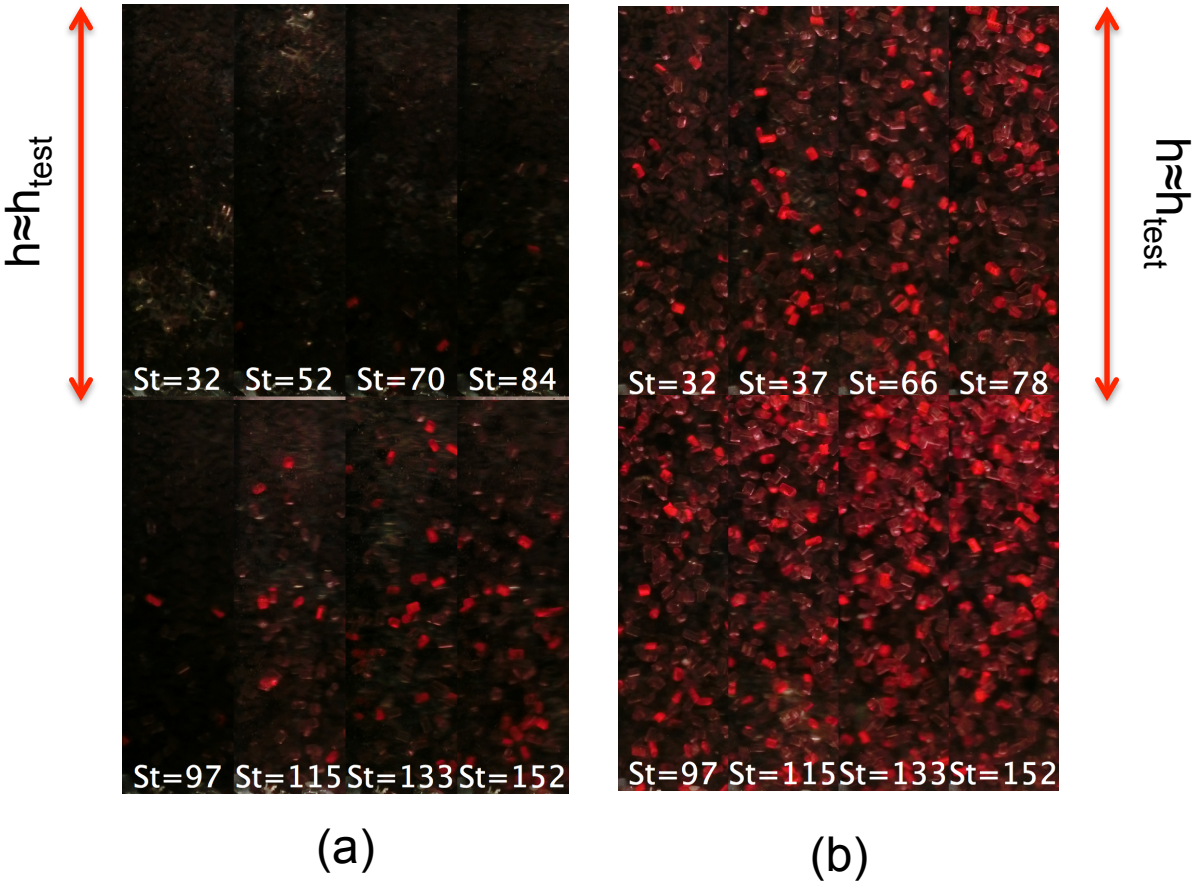

Figure 7.8: (a) Image sequence of the flow for $\bar{\phi} = 10\%$ and $\rho_p/\rho = 1.05$ for different Stokes numbers. (b) Same as (a) but for $\rho_p/\rho = 1$. The height of the visualization window is slightly higher than the test section.

	No porous medium		Porous medium	
$\bar{\phi}$	St fully covered	St fluidized	St fully covered	St fluidized
10	135	NA	80	80
20	80	NA	65	100
30	NA	80	NA	120
40	NA	95	NA	140
50	NA	100	NA	180
60	NA	100	NA	NA

Table 7.1: Critical Stokes numbers for fluidization. *St fully covered* denotes the Stokes number above which the test cylinder is fully covered by particles based on Figure 6.19. *St fluidized* denotes the Stokes number above which the ratio of torques exhibits a change in slope based on Figures 4.16 and 5.15.

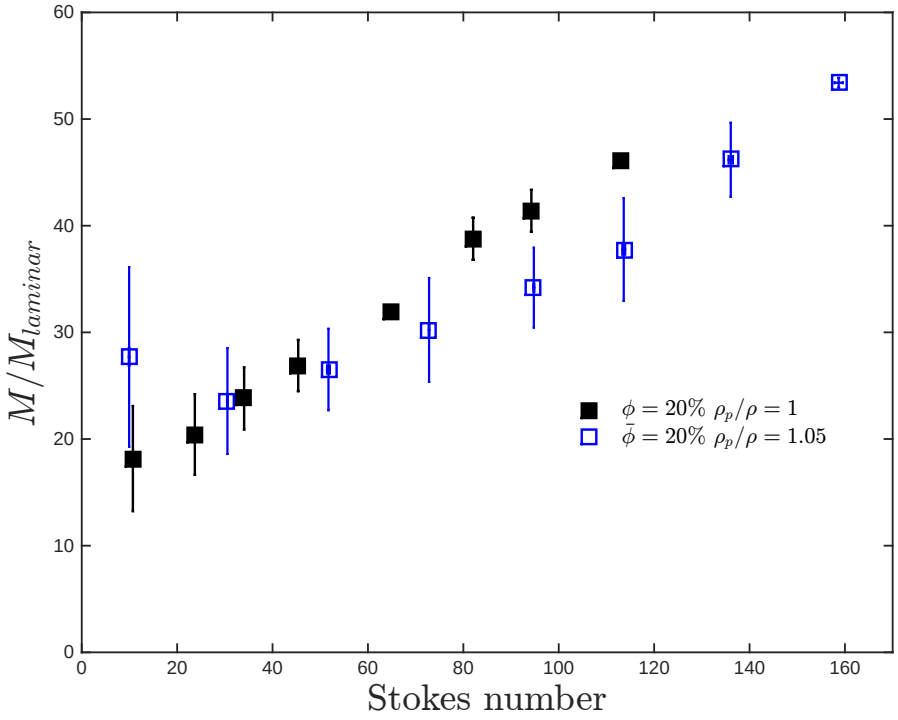

Figure 7.9: Comparison between normalized torques as a function of Stokes numbers for $\rho_p/\rho = 1$ and $\rho_p/\rho = 1.05$ with $\bar{\phi} = 20\%$.

torques is weaker. For both cases, the normalized torques increase with Stokes number and exhibit a linear dependance with similar slopes. The normalized torques for the settling particles at the two similar Stokes numbers are higher than for the non settling ones. A possible explanation for these differences is that the effective volume fraction for the settling particles is slightly higher. The Stokes number at which the particles reach the top of the rheometer (see table 7.1) is around 113, but even when the particles have reached the top, it does not imply an homogeneous distribution of the particles. A gradient on the volume fraction may exist, leading to effective volume fractions higher than the loading fractions and therefore higher normalized torques. An analysis of the effective volume fraction is presented in Section 7.3.

Based on the particles height measurements, the test cylinder is fully covered at most Stokes numbers for a loading fraction higher than 30% (see Figure 6.14 or table 7.1). The torque contribution from the suspending liquid might be less than in the more dilute cases since the concentration of particles is high enough to decrease the effective Reynolds number of the flow, making the suspending liquid contributions closer to the torque predicted from laminar theory. Figure 7.11 shows the normalized torques for the higher loading fractions and for $\rho_p/\rho = 1$ and $\rho_p/\rho = 1.05$. Only the Stokes numbers at which the particles reached the top are considered. Predictions of the effective volume fraction based on the flow visualizations are presented later in Section 7.3. For the case with matched densities, there is a slight decrease in the effective relative viscosity for $\phi = 40$ and 50%

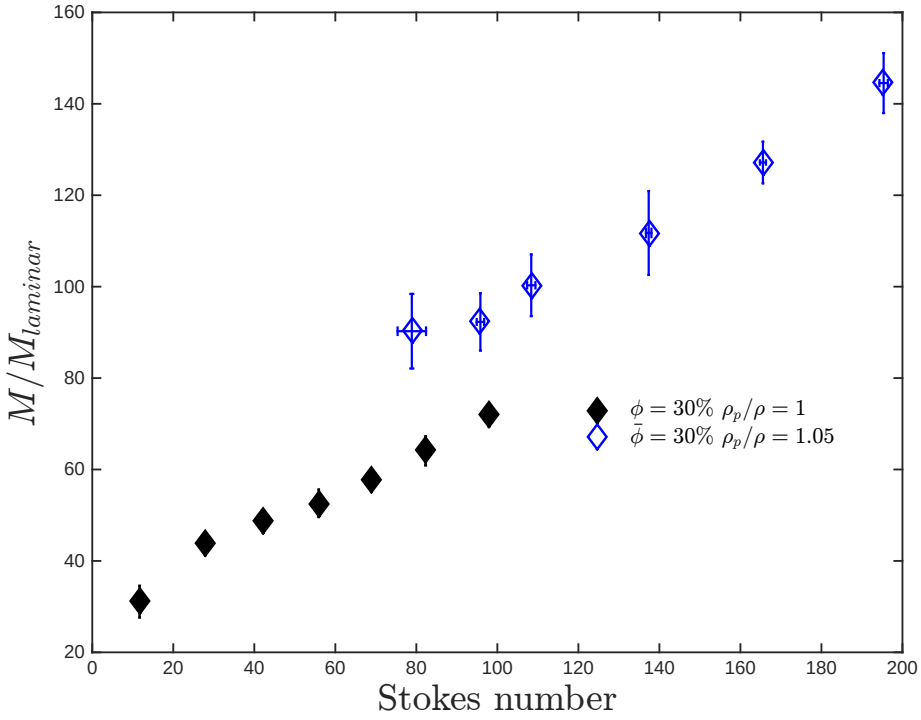

Figure 7.10: Comparison between normalized torques for $\rho_p/\rho = 1$ and $\rho_p/\rho = 1.05$ as a function of Stokes numbers with $\bar{\phi} = 30\%$. For the case of $\rho_p/\rho = 1.05$, only the data without settling is shown.

at the lowest Stokes number, and this decrease might be due to slight settling of the particles, but it is considerably less dramatic than the one observed for settling particles at low Stokes numbers (see Figure 4.15). The normalized torques for $\phi = 50\%$ for $\rho_p/\rho = 1$ are almost the same as for $\rho_p/\rho = 1.05$. At this high loading fraction the effective volume fraction after fluidization matches the effective volume fraction for $\rho_p/\rho = 1$. For $\phi = 40\%$ and $\rho_p/\rho = 1$ the normalized torques have lower values than for $\rho_p/\rho = 1.05$, and it is possible that there exists differences in effective volume fraction due to settling.

For all the cases shown in Figure 7.11, the normalized torques exhibit a weak dependance on the Stokes number. In the absent of strong hydrodynamics effects, the normalized torques would depend on the concentration and possible interaction of particles. If the latter is not present or if it is weak, the normalized torques would be independent of Stokes number and would exhibit a strong dependance on volume fraction. Therefore, for these loading fractions, the effects of fluid and particle inertia are not strong. An analysis of the inertial effects for the case with $\rho_p/\rho = 1.05$ is presented in Section 7.4.

The normalized torques for Stokes numbers where the particles are completely fluidized and for loading fractions higher than 20% seem to coincide with the normalized torques for the case with $\rho_p/\rho = 1$ as can be observed in Figure 7.12.

Assuming that the normalized torques are equal to the effective relative viscosity, Figure 7.13

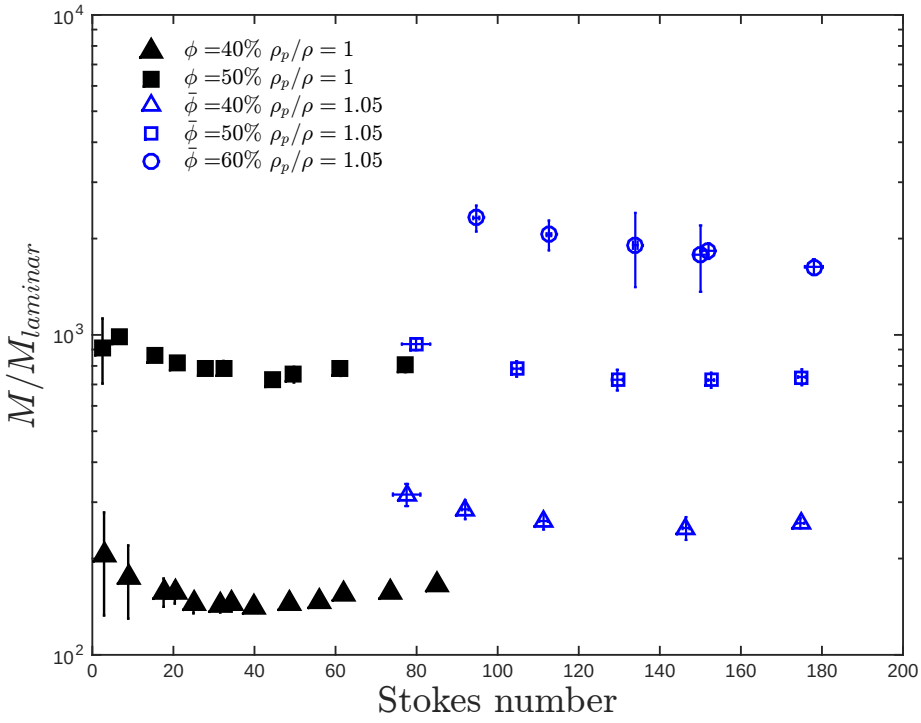

Figure 7.11: Normalized torques as a function of Stokes numbers with $\bar{\phi} = 40$, 50, and 60% for $\rho_p/\rho = 1$ and $\rho_p/\rho = 1.05$. For the case of $\rho_p/\rho = 1.05$, only the data without settling is shown.

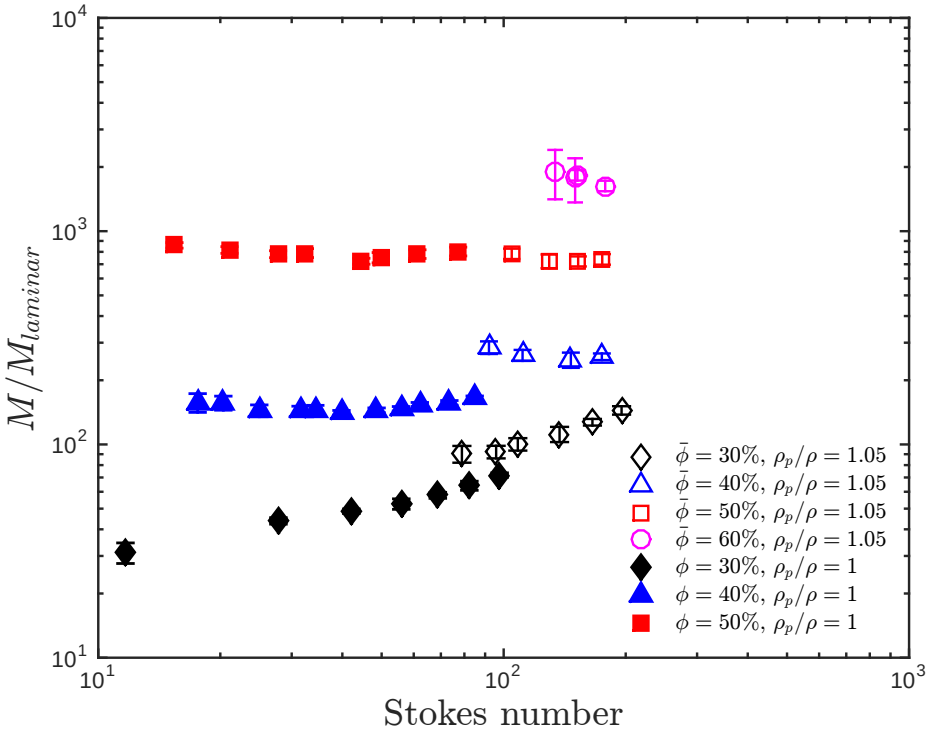

Figure 7.12: Normalized torques as a function of Stokes number for $\rho_p/\rho = 1$ and $\rho_p/\rho = 1.05$. For the case with settling particles, only the normalized torques corresponding to Stokes number where the particles are fully fluidized are shown.

shows the effective relative viscosity for all the volume fraction tested and for $\rho_p/\rho = 1$ and $\rho_p/\rho = 1.05$. For the case with settling particles, the data corresponding to Stokes numbers below the fluidization threshold are not included. The Stokes number magnitude is denoted by the size of the symbol. The effect of Stokes number is the same for both density ratios. For loading fractions lower than 40%, the effective relative viscosity increases with St. At higher loading fractions the effect of Stokes is not very noticeable for the both density ratios studied as long as the data with settling effects are not considered. Figure 7.14 shows the ratio of μ'/μ for all the Stokes number tested, including the data where the particles are settling. It can be seen from Figure 7.14 that for loading fractions higher than 20%, the ratio of μ'/μ decreases with St for $\rho_p/\rho = 1.05$. This is linked to the settling effects and it is similar to what was observed by Acrivos et al. (1994). It is expected that these two curves would collapse when the effective volume fraction is used instead of the loading fraction. The prediction of the effective volume fraction is studied in the next section.

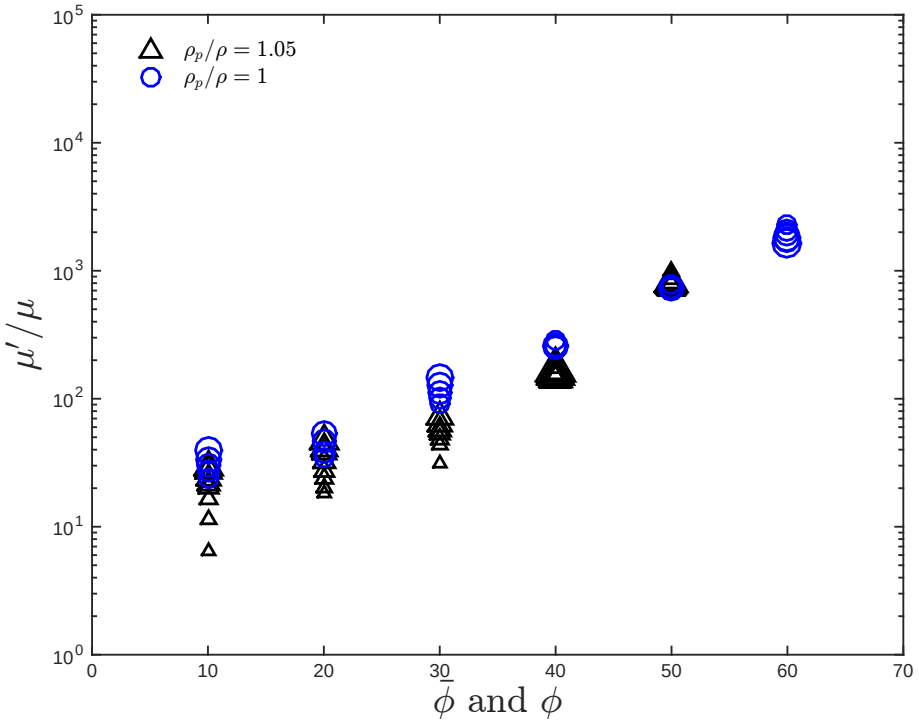

Figure 7.13: Relative effective viscosity as a function of ϕ and $\bar{\phi}$ for $\rho_p/\rho = 1$ and $\rho_p/\rho = 1.05$. For the case of $\rho_p/\rho = 1.05$, only the data without settling is shown.

A comparison between the two sets of data for the current experiments and the rough walls experiments from Koos et al. (2012) is presented in Figure 7.15.

The effect of Stokes number is considerably less for the previous experiments of Koos (2009) at lower volume fractions.

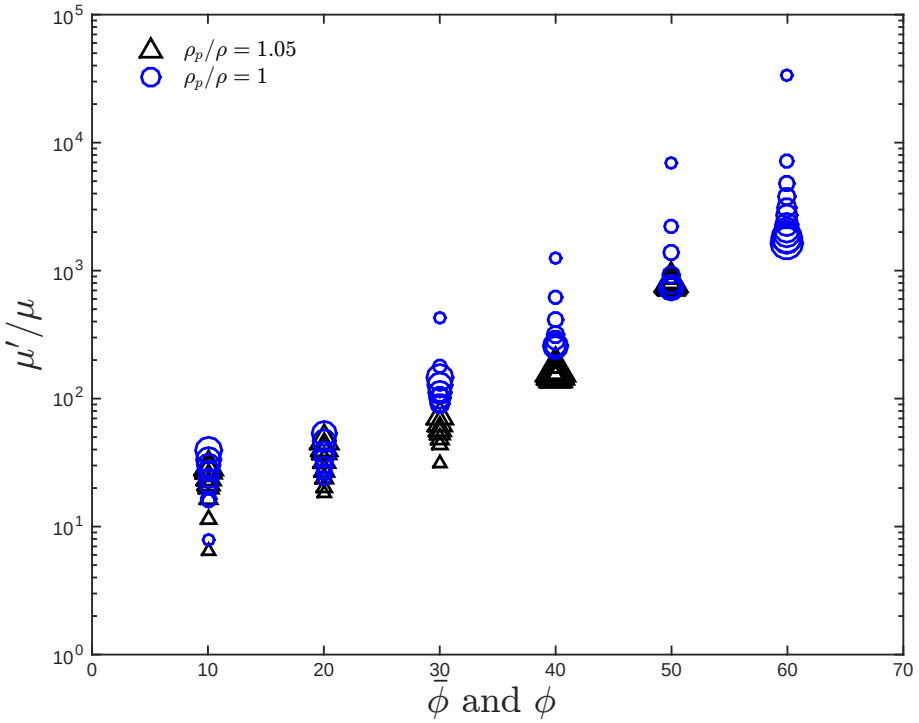

Figure 7.14: Relative effective viscosity as a function of ϕ and $\bar{\phi}$ for $\rho_p/\rho = 1$ and $\rho_p/\rho = 1.05$. All the Stokes number tested are shown, including the ones with settling effects.

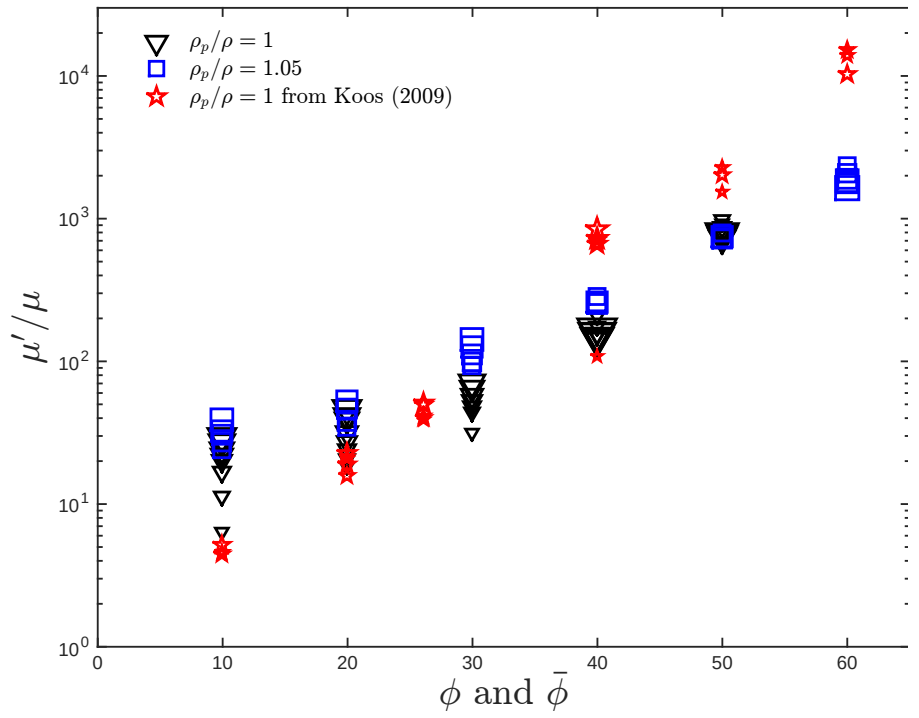

Figure 7.15: Relative effective viscosity as a function of ϕ and $\bar{\phi}$ for $\rho_p/\rho = 1$ and $\rho_p/\rho = 1.05$ compared with the effective relative viscosity from Koos et al. (2012). For the case of $\rho_p/\rho = 1.05$, only the data without settling is shown.

7.3 Prediction of the effective volume fraction

As mentioned before in Section 7.2, for settling particles at low loading fractions and below a certain Stokes number, the particles do not entirely cover the test cylinder. To compare these low loading fractions and the low loading fractions with $\rho_p/\rho = 1$, only the measurements where the test cylinder is fully covered are considered.

Figure 7.16 shows the effective relative viscosity as a function of the Stokes numbers for $\phi = 10$ and 20%, and for $\rho_p/\rho = 1$ and $\rho_p/\rho = 1.05$. For the lowest volume fraction the effective relative viscosity for the settling particles appears to coincide with the trend observed for $\rho_p/\rho = 1$. However, the St numbers at which the particles fully covered the test cylinder are higher than the tested St for $\rho_p/\rho = 1$ but they seem to follow the same trend. This suggests that the difference in density is less important when the particles are completely fluidized for this dilute case.

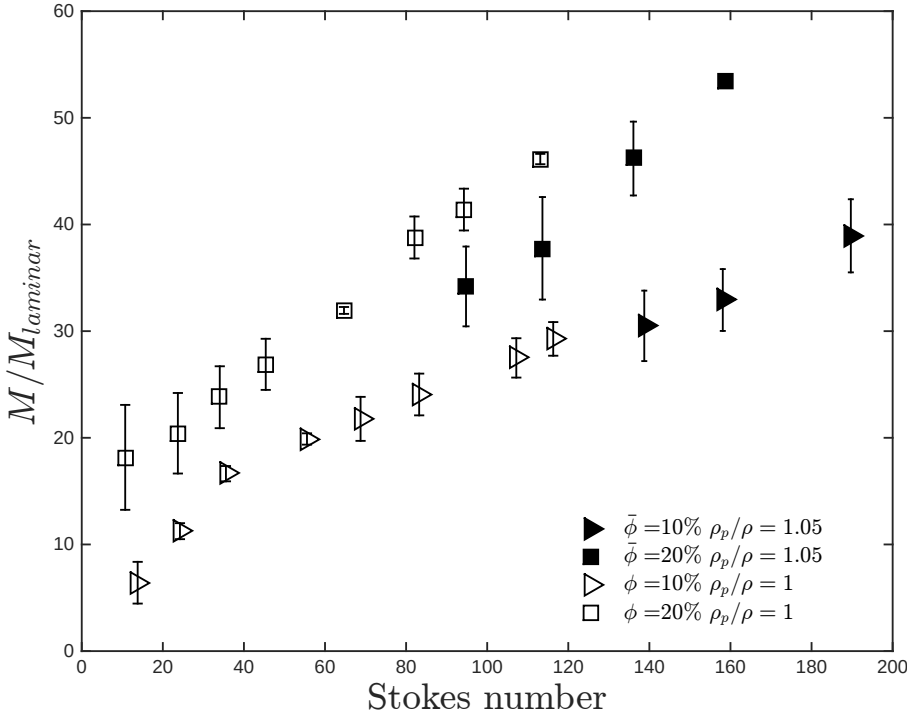

Figure 7.16: Relative effective viscosity as a function of Stokes numbers with $\bar{\phi} = 10$ and 20% for $\rho_p/\rho = 1$ and $\rho_p/\rho = 1.05$. For the case of $\rho_p/\rho = 1.05$, only the data without settling is shown.

For the higher loading fraction of 20%, the effective relative viscosity for the settling particles is slightly lower than for the density matched experiments with same loading fraction. This difference is an indication of the particles' effect since the suspending liquid for the case with settling particles has a lower viscosity than for the case with $\rho_p/\rho = 1$. Thus, an increase in the effective relative viscosity must be due to an increase in the particle concentration. In Figure 7.17, visualization of the flow is shown for a loading fraction of 20%, where it can be seen in the difference in particle

concentration.

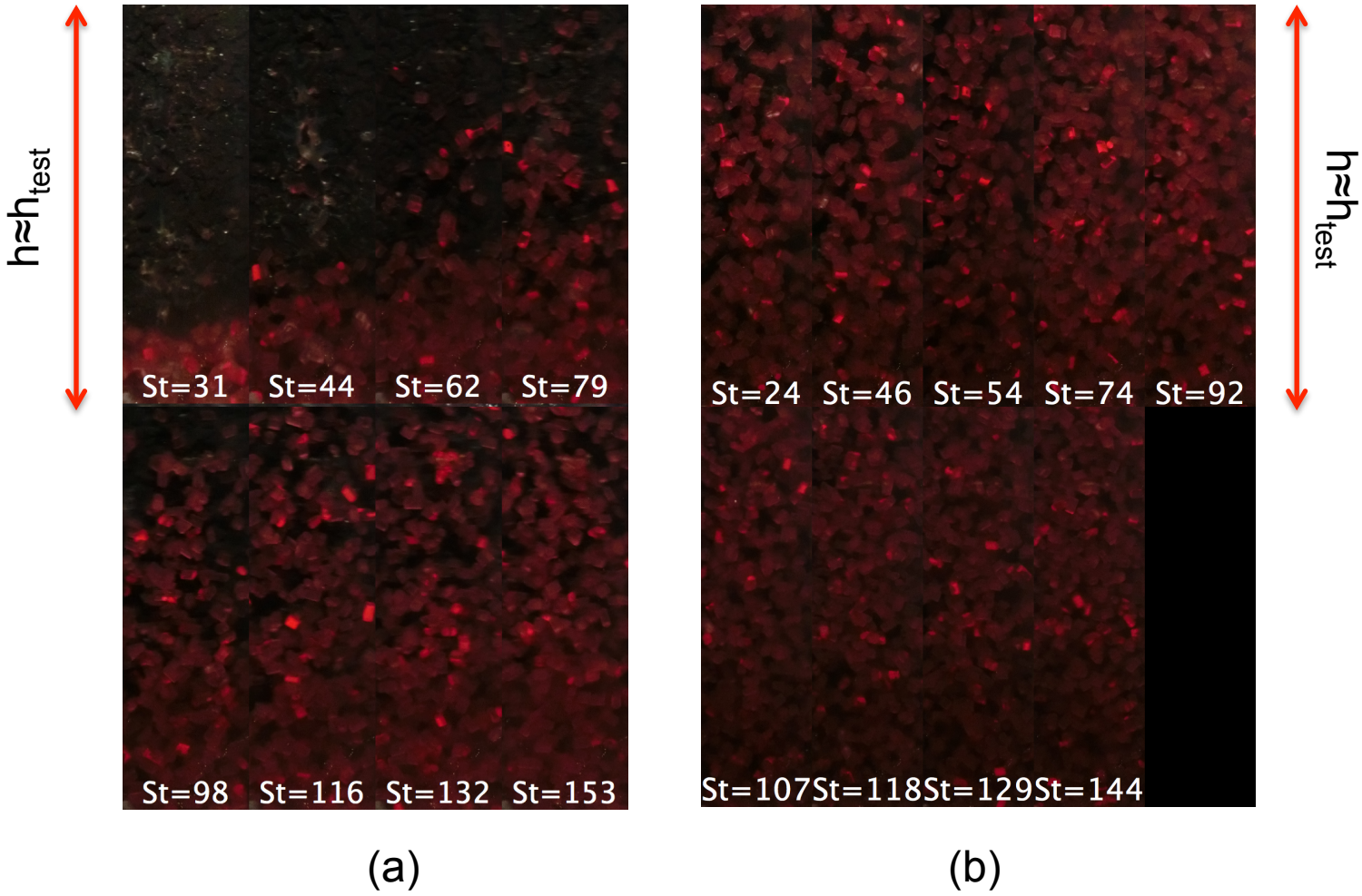

Figure 7.17: (a) Image sequence of the flow for $\bar{\phi} = 20\%$ and $\rho_p/\rho = 1.05$ for different Stokes numbers. (b) Same as (a) but for $\rho_p/\rho = 1$. The height of the visualization window is slightly higher than the test cylinder.

To account for the effect of solid concentration, the effective volume fraction for the settling particles is inferred from the particle resuspension measurements. Using a linear interpolation, the effective volume fraction at specific query Stokes number can be inferred from the volume fraction calculated using the particles height measurements presented in Chapter 6. Figure 7.18 shows the effective relative viscosity as a function of the effective volume fraction for different Stokes numbers tested for $\rho_p/\rho = 1.05$. Here only the cases where the test cylinder is fully covered are considered. The magnitude of the Stokes numbers is represented with different size symbols (the larger the Stokes number, the larger the symbol). As the Stokes number increases, the effective volume fraction decreases. The highest relative viscosity corresponds to the highest volume fraction and the lowest

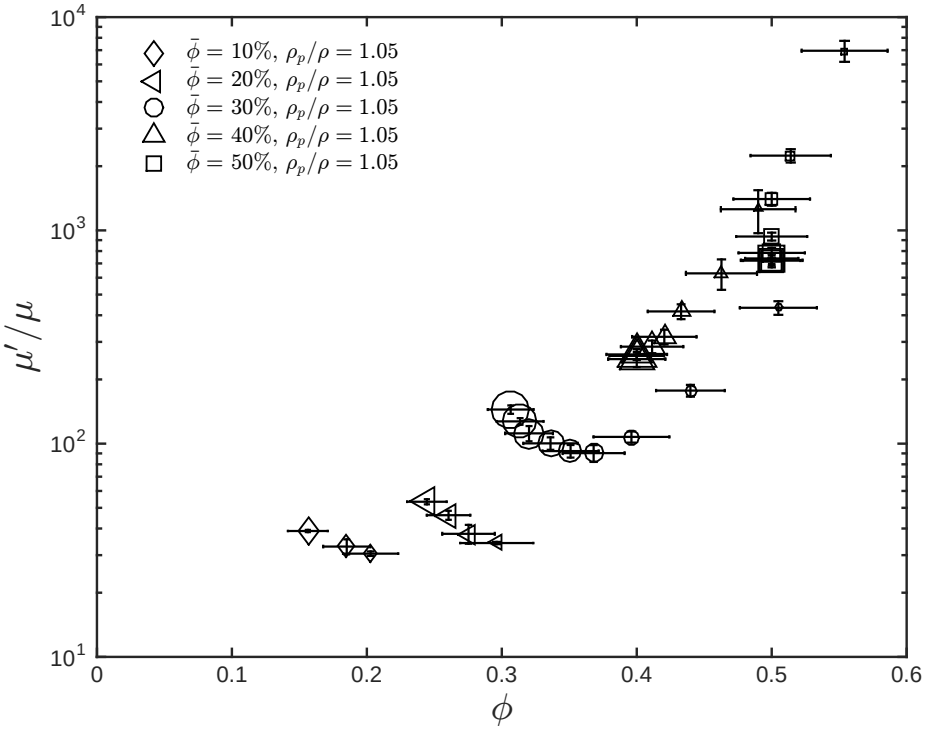

Figure 7.18: Effective relative viscosity as a function of the predicted volume fraction. The size of the symbols denotes the magnitude of the Stokes numbers, where the largest symbols correspond to the largest Stokes numbers. Only the cases where the mixture cover the test cylinder are presented.

Stokes number. For loading fractions higher than 30%, the data seem to collapse. For the cases with lower $\bar{\phi}$, the data seem to scatter more.

To study the effect on differences in density, the effective relative viscosity and volume fraction are compared with the case with $\rho_p/\rho = 1.$. Figure 7.19 shows this comparison.

The effective relative viscosity for the two sets of data seems to coincide and follow the same trend. This suggests that there are no strong effects on different density ratios. Figure 7.20 shows the comparison between the current experiments and the previous experiments from Koos (2009).

The data seem to coincide for most volume fractions. The loading fractions that deviate more are the loading fraction of 10 and 40% from Koos (2009).

7.4 Inertial and particle concentration effects on mixtures with $\rho_p/\rho = 1$

The predicted effective volume fraction is used to estimate the effective viscosity of the mixture. Based on Figure 7.3, the effective viscosity of the mixture for a $\rho_p/\rho = 1.5$ is assumed to be independent of the density ratio. This assumption is validated with the results presented in the previous section, where the effect of differences in density was weak (it should be noted that the

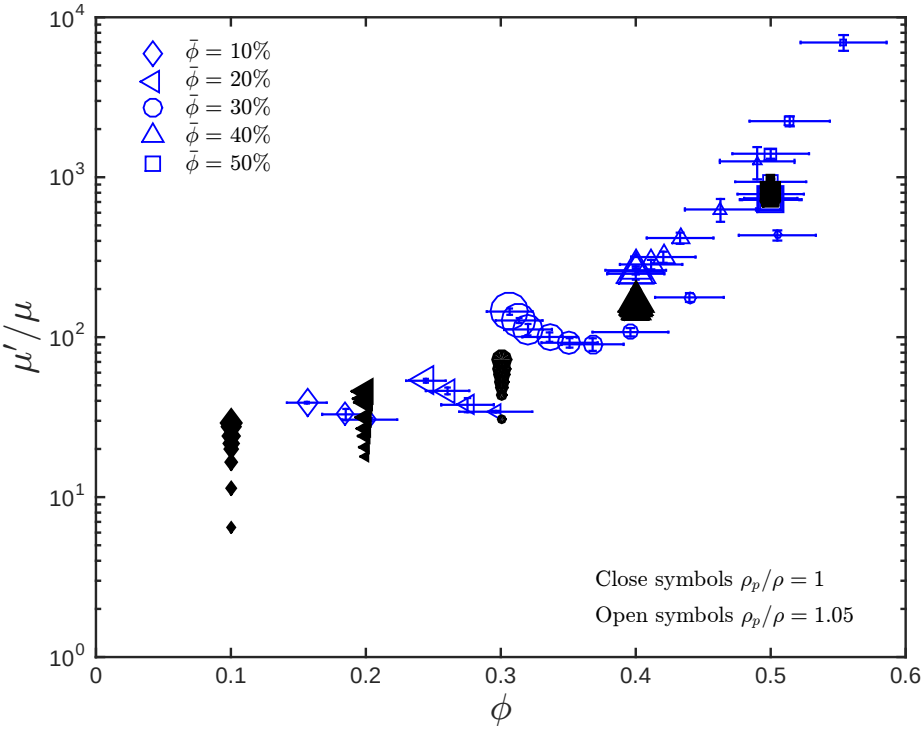

Figure 7.19: Effective relative viscosity as a function of the loading and predicted volume fraction for $\rho_p/\rho = 1$ and $\rho_p/\rho = 1.05$.The size of the symbols denotes the magnitude of the Stokes numbers, where the largest symbols correspond to the largest Stokes numbers. Only the cases where the mixture cover the test cylinder are presented.

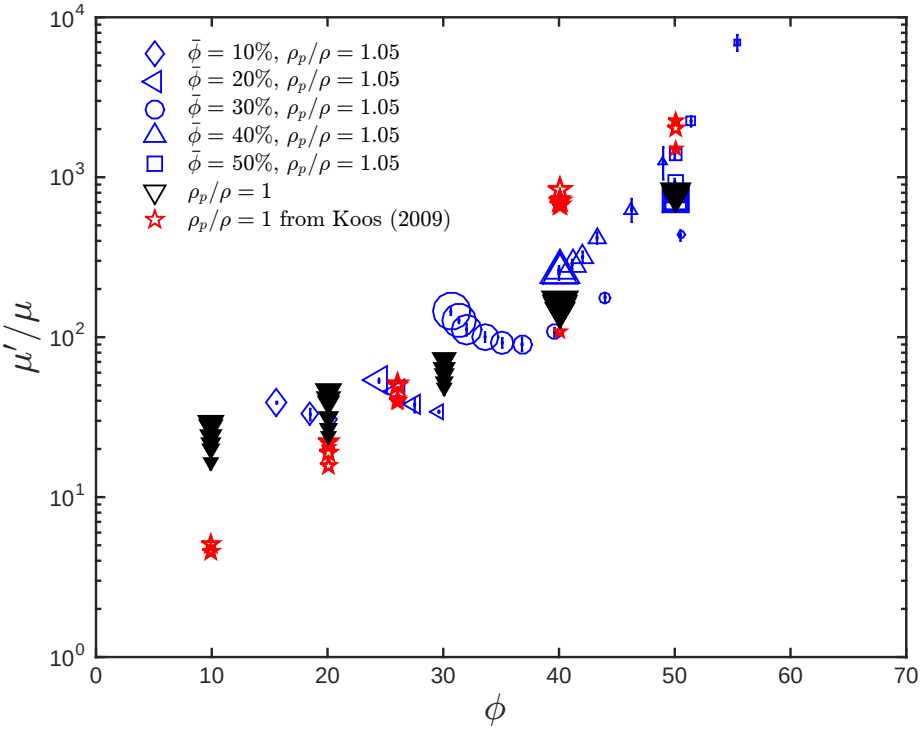

Figure 7.20: Effective relative viscosity as a function of the loading and predicted volume fraction for $\rho_p/\rho = 1$ and $\rho_p/\rho = 1.05$, compared with the data from rough walls of Koos (2012). The size of the symbols denotes the magnitude of the Stokes numbers, where the largest symbols correspond to the largest Stokes numbers. Only the cases where the mixture cover the test cylinder are presented.

differences in density is only 5%). It follows then that the normalized torque corresponding to the same volume fraction would be the same as long as no hydrodynamics effects are present. Based on this, the effective relative viscosity between two mixtures with different suspending liquid but same volume fraction is

$$\frac{\mu'_{min,\ 21\%\ glycerine}}{\mu_{21\%\ glycerine}} = \frac{\mu'_{min,\ H_2O}}{\mu_{H_2O}}.$$

Using this relation the effective viscosity is found for the experiments with settling particles. The effective Reynolds number is calculated in the same way as before. Figure 7.21 shows the measured torques normalized with the corresponding laminar torque for a effective mixture viscosity. Only the data with fluidized particles is considered to isolate the effect of settling.

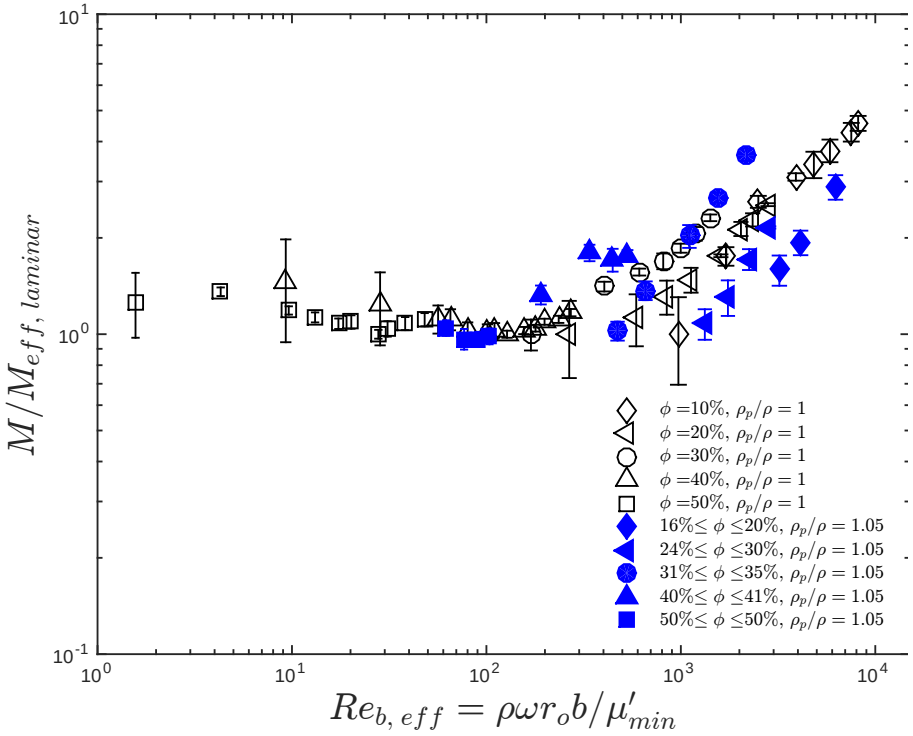

Figure 7.21: Measured torques normalized with effective laminar torque as a function of $Re_{b,\ eff}$ for $\rho_p/\rho = 1.05$. The effective viscosity of the mixture is inferred from the effective volume fraction and Figure 7.3.

The settling particles show a wider scatter than the data with density ratio equal to one. This is due to the uncertainties introduced when estimating the effective viscosity of the mixture (μ'_{min}). The accumulative uncertainty would involve the uncertainty on predicting the effective volume fraction and the uncertainty involved inferring μ'_{min} from the data with $\rho_p/\rho = 1$. If the mixture effective viscosity is considered to be equal to the effective viscosity for the lowest values of Stokes number found for $\rho_p/\rho = 1.05$, then the source of uncertainties reduces. In such case the modified

effective Reynolds number is defined as

$$Re^*_{b,\,eff} = \frac{\rho\omega b}{\mu'^*_{min}},$$

where μ'^*_{min} corresponds to the minimum value of μ'/μ found for each loading fraction. For the case with $\rho_p/\rho = 1.05$, this corresponds to the highest Stokes numbers where the particles are fully fluidized. Figure 7.22 shows the measured torques normalized by the effective laminar torque considering μ'^*_{min} ($M^*_{eff,\,laminar}$). The scattered in this plot is considerably less.

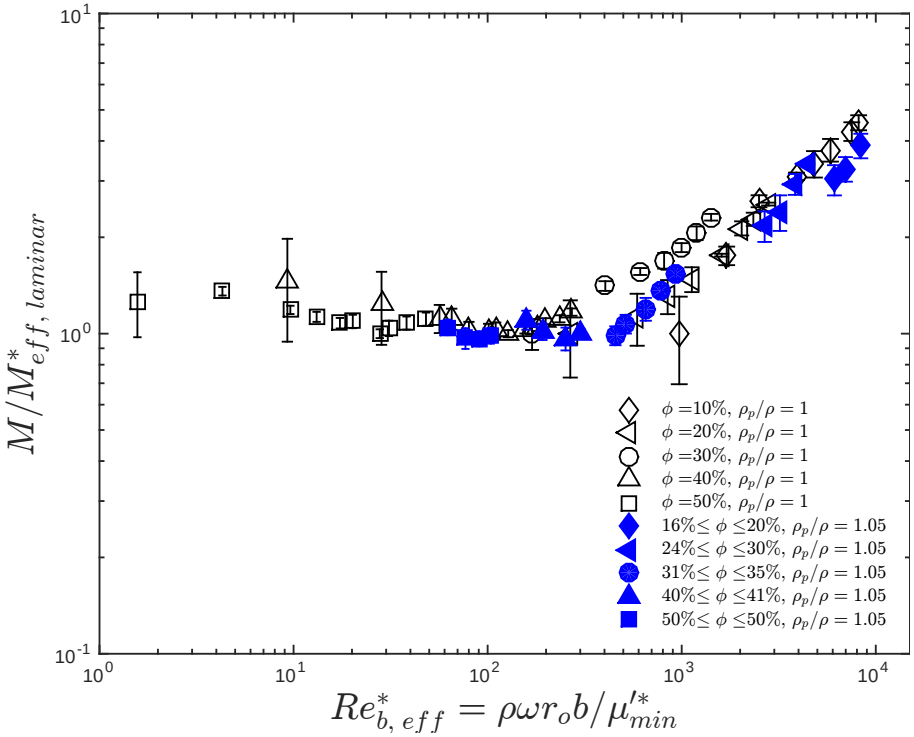

Figure 7.22: Measured torques normalized with effective laminar torque as a function of $Re^*_{b,\,eff}$ for $\rho_p/\rho = 1.05$. The effective viscosity of the mixture used for $Re^*_{b,\,eff}$ corresponds to the minimum μ'/μ for each loading fraction.

In both figures the range of effective Reynolds number at which the normalized torques deviate from a laminar behavior coincides with the region found for the case with $\rho_p/\rho = 1$. Based on these results, any dependance of the Stokes or Reynolds number is due to hydrodynamics effects.

7.5 Flow over a porous medium $\rho_p/\rho = 1.05$

In an attempt to study low loading fractions, experiments of the mixture flow over a porous medium were performed. For all the loading fractions, the normalized torques decrease with Stokes numbers, with the exemption of $\bar{\phi} = 10\%$. One of the main differences found between these experiments and

the ones without a porous bed is that the measured torque decreases at a certain Stokes number. This is observed at all loading fractions and it was independent of the shearing history of the flow (no hysteresis). This drop on the measured torque is likely to be linked to a settling (or equivalently to a resuspension effect). This drop in torque is observed as a change in slope on the normalized torques. A comparison between the visualization of the flow and the relative viscosity is presented in the next section.

Effect of resuspension on flow over a porous medium

Figure 7.23 (a) shows the flow visualization for a 10% loading fraction at different Stokes numbers. Each image was taken after several minutes of shearing the flow at a constant shear rate for each St. As mentioned in the previous chapter, the height of the visualization window for these experiments is approximately one inch higher than the test cylinder. Therefore, only the flow in this region, which is the same region where the torque measurements take place, is visualized. The corresponding St for each image increases from left to right, starting at the upper left corner with a $St = 0$. The height reached by the particles increases considerably when the St goes from 0 to 18 and it remains almost constant between St from 18 to 55 (see Figure 6.17 to see the actual height measurements). There is a bigger increase in height when the St goes from 67 to 81, and when $St = 109$ the particles appeared to be completely resuspended and covered the whole test cylinder. These observations can be compared with the effective relative viscosity measurements. In Figure 7.23 (b) it can be observed that μ'/μ corresponding to the measurements that were taken from low to high shear rates (closed symbols), decreases abruptly when St increases from 10 to 34. This abrupt change in μ'/μ coincides with the abrupt increase in the height reached by the particles between $0 \leq St \leq 18$. This means that the mixture requires higher shear stress in order to initiate the flow of settled particles, and as soon as the particles became re-suspended the needed shear stress decreased. For St larger than 20, μ'/μ remains almost constant. When the St is higher than 80, μ'/μ starts increasing. As pointed out previously in Chapter 5, this increase was only observed for this particular loading fraction. It is possible that this behavior is due to settling effects. By simply comparing the top and bottom row of the image sequence in Figure 7.23 (a), the big difference between the area covered by particles for St lower than 91 (top row) and the area covered for St higher than 100 can be noticed. The ratio between the highest and the lowest normalized height for this loading fraction (see Figure 6.17) is 2.06, while the ratio for a loading fraction of 20% is 1.51. Even when the particles are more packed at low Stokes numbers, they don't cover a significant region of the area where the torque measurements are taken. When the particles fluidized, they are more diluted but they cover a bigger region of the test area. In the following section, an analysis about the possible hydrodynamics effects present in this set of experiments is presented. Because of the limitation of the short visualization window used for these experiments, measurements of the total height reached by the particles when

fluidized are not available. The ratio μ'/μ keeps increasing for St higher than 120. It is possible that this increase on μ'/μ is due to inertial effects.

When the experiments are performed from high to low shear rates (Figure 7.23 open symbols), and for St higher than 80; the effective relative viscosity exhibited the same behavior as for the case where the shear rate went from low to high. For St lower than 80, the μ'/μ for high to low shear rate experiments is higher. These differences were only observed for this loading fraction and the reason why is not completely clear. The glass beads that formed the porous media and the settling polystyrene particles re-arranged themselves after being sheared at high shear rates, which increased the settling height of the particles and the effective volume fraction.

Figure 7.24 shows the visualization for flow over a porous media with a loading fraction of 20%. Similar to what is observed in Figure 7.23 (a), the height reached by the particles for Stokes numbers lower than 80 increases gradually but not abruptly. For $St = 82$ there is an abrupt increase in height and the particles covered the whole visualization window. As St increases, the images for the visualization look very similar to each other. In Figure 7.24 (b) the μ'/μ as a function of St is presented. Unlike the case for a loading fraction of 10%, the effective relative viscosity decreased considerably for St lower than 82 (the ratio between the μ'/μ for the lowest St and the minimum μ'/μ for a loading fraction of 20% is 13, meanwhile for a 10% loading fraction that ratio is 2.9). For St higher than 82, μ'/μ remains fairly constant. Since there was not a significant variation between the images corresponding to such St, the reason why μ'/μ appears to be independent of the St could be that the effective volume fraction remained constant.

For the case with a 30% loading fraction presented in Figure 7.25 (a), the particles covered almost the entire visualization window. It can be seen that the particles start rising gradually for St lower than 74. Due to the visualization window size it is not possible to see if there was an abrupt change in the height reached by the particles. However, the μ'/μ measurements (Figure 7.25 (b)) show a change in slope for St higher than 120. It is possible that the particles' full resuspension occurs at a higher St than for the lower loading fraction cases.

For larger loading fractions, the area where the torque measurements take place was completely covered by the particles, as shown in Figure 7.26. Based on these images it is not possible to identify when the particles are fully fluidized because of the size of the visualization window. However, as described in Chapter 5, the effective relative viscosity does exhibit a change in slope at Stokes numbers between 120 and 130 (see Figure 7.27). These findings suggest that the effective volume fraction became constant for St higher than 130.

Direct comparisons between flow with and without a porous medium base

Figure 7.28 shows the normalized torques for loading fractions of 20% for the case with different density ratios for $\bar{\phi} = 10\%$ over a porous medium. For the case with settling particles, only the

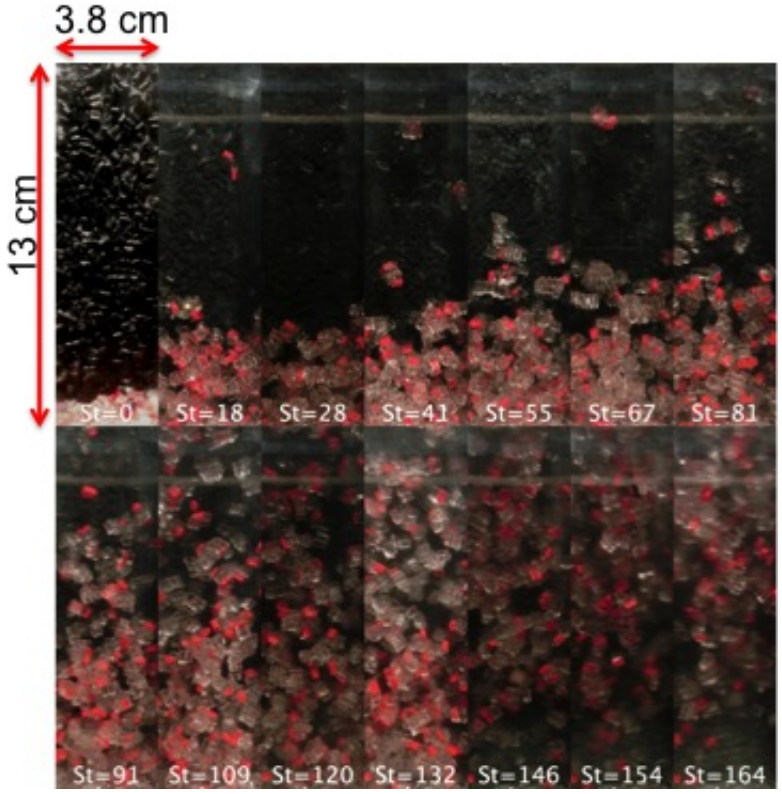

(a)

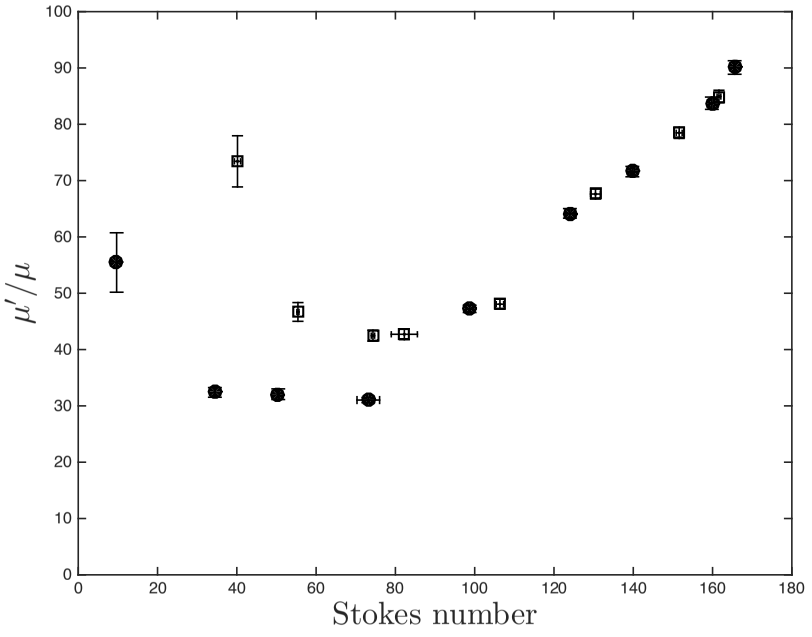

(b)

Figure 7.23: (a) Image sequence of flow over porous media with a loading fraction of 10% for different Stokes numbers. The height of the visualization window is the same as the height of the inner middle cylinder where the torque measurements are taken. (b) Effective relative viscosity as a function of Stokes number for loading fraction of 10% over a porous media. Closed symbols correspond to measurements taken with increasing shear rate. Open symbols correspond to measurements taken from high to low shear rates. $\rho_p/\rho = 1.03$.

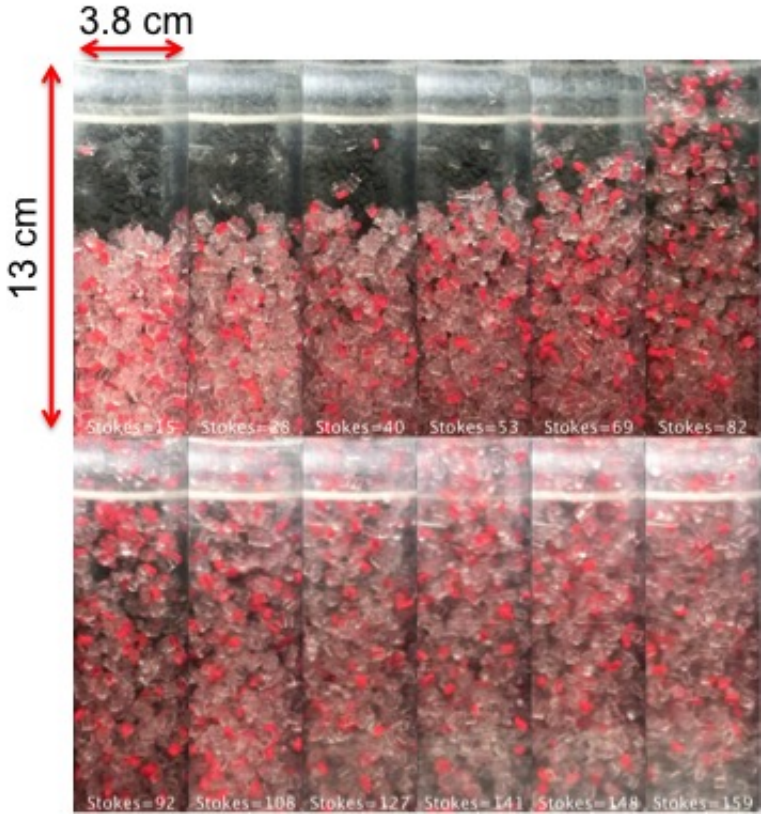

(a)

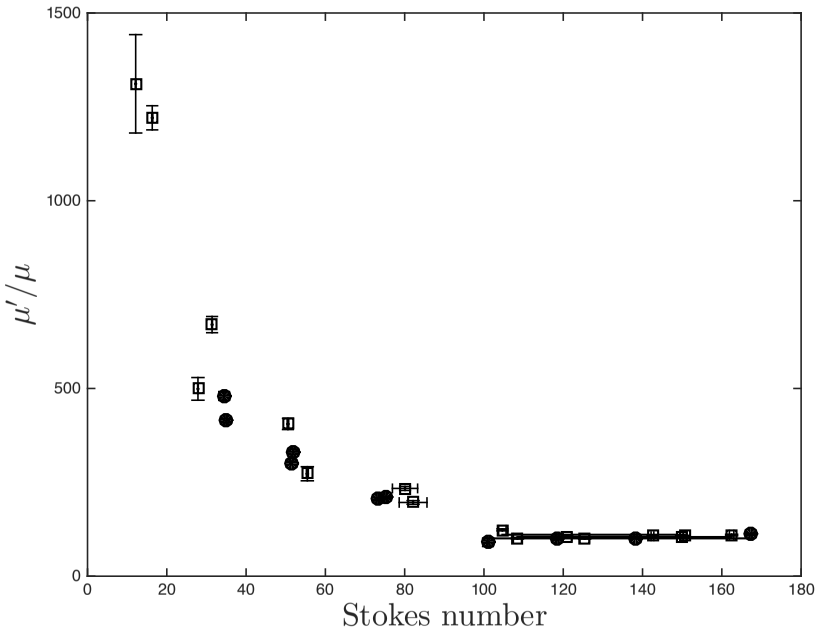

(b)

Figure 7.24: (a) Image sequence of flow over porous media with a loading fraction of 20% for different Stokes numbers. The height of the visualization window is the same as the height of the inner middle cylinder where the torque measurements are taken. (b) Effective relative viscosity as a function of Stokes number for loading fraction of 20% over a porous media. Closed symbols correspond to measurements taken with increasing shear rate. Open symbols correspond to measurements taken from high to low shear rates. $\rho_p/\rho = 1.03$.

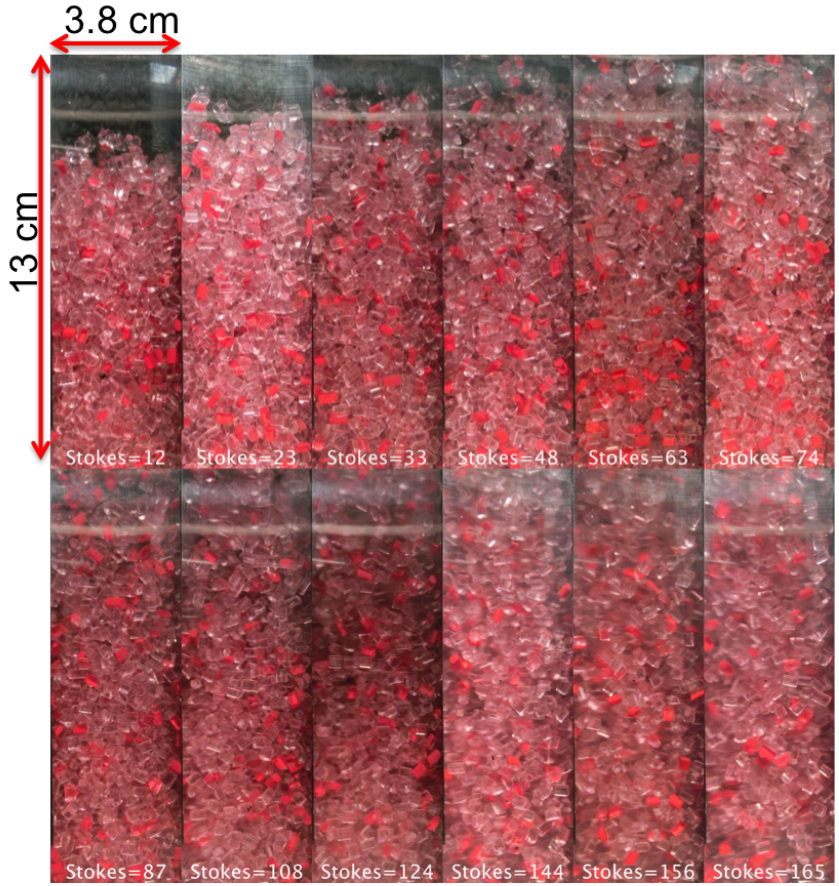

(a)

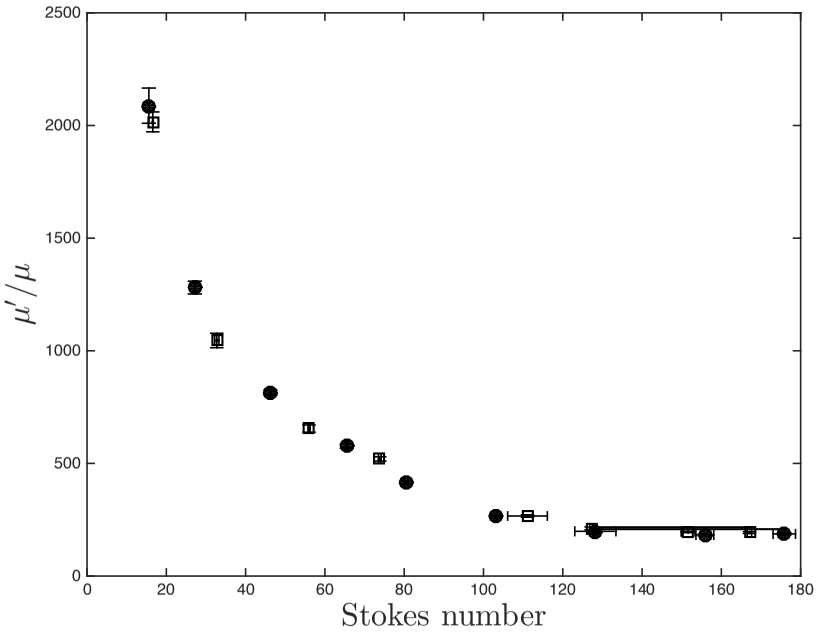

(b)

Figure 7.25: (a) Image sequence of flow over porous media with a loading fraction of 30% for different Stokes numbers. The height of the visualization window is the same as the height of the inner middle cylinder where the torque measurements are taken. (b) Effective relative viscosity as a function of Stokes number for loading fraction of 30% over a porous media. Closed symbols correspond to measurements taken with increasing shear rate. Open symbols correspond to measurements taken from high to low shear rates. $\rho_p/\rho = 1.03$.

(a)

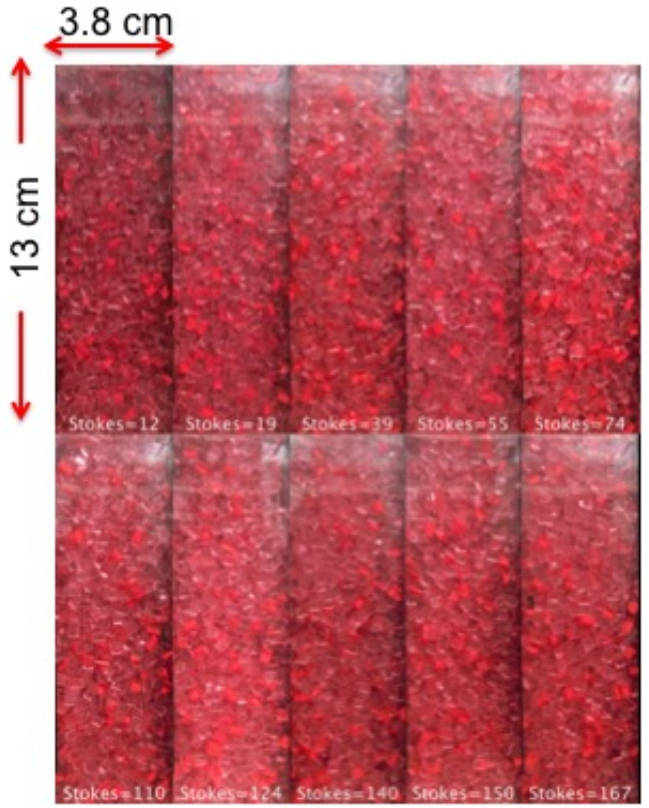

(b)

Figure 7.26: Image sequence of flow over porous media for different Stokes numbers. The height of the visualization window is the same as the height of the inner middle cylinder where the torque measurements are taken. (a) Loading fraction of 40%. (b) Loading fraction of 50%.

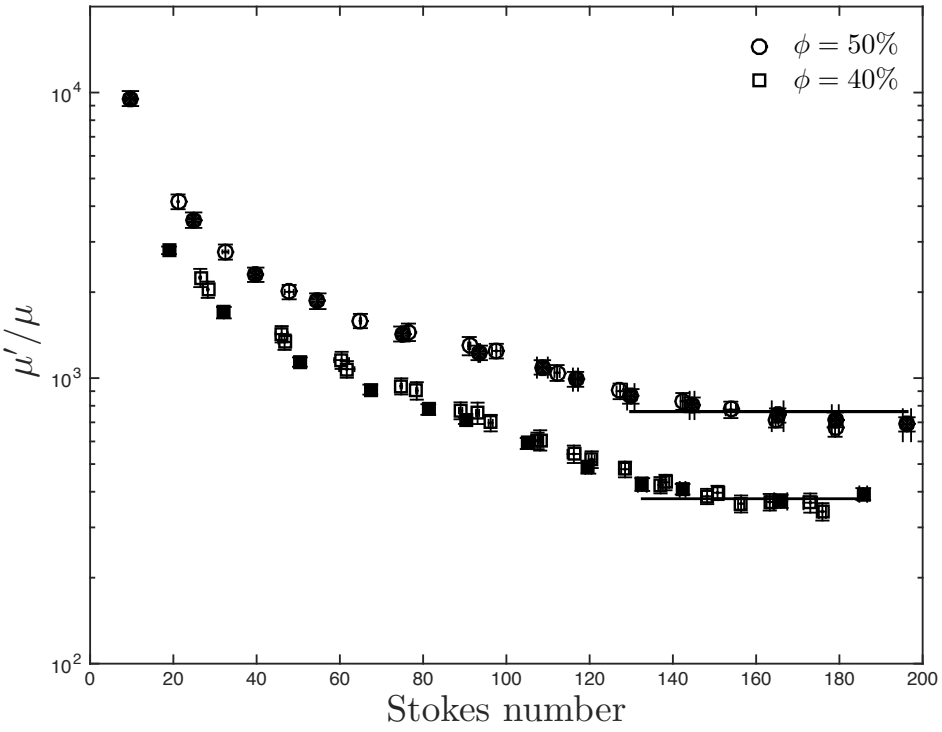

Figure 7.27: Effective relative viscosity for flow over porous media. Closed symbols correspond to measurements taken with increasing shear rate. Open symbols correspond to measurements taken from high to low shear rates. $\rho_p/\rho = 1.05$.

Stokes number corresponding to the cases where the particles cover the test cylinder completely are considered. The normalized torques for the flow over a porous media are higher than for the cases without a porous medium base. Figure 7.29 shows the normalized torques for the 3 cases studied:

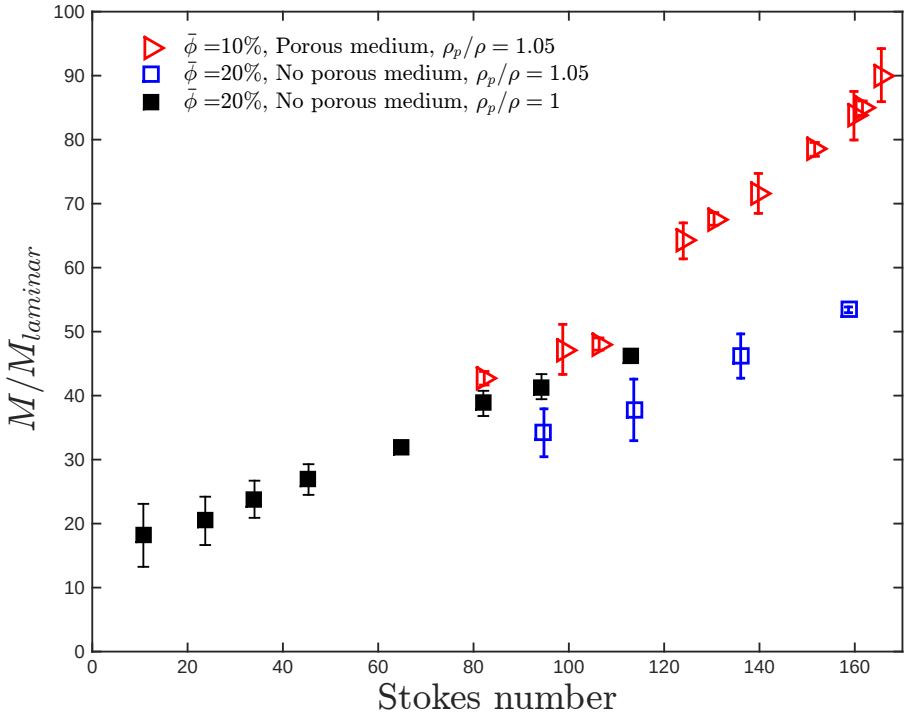

Figure 7.28: Flow over porous medium normalized torques as a function of St for $\bar{\phi} = 10$ compared with no porous medium with $\bar{\phi} = 20\%$ and $\rho_p/\rho = 1.05$ and $\rho_p/\rho = 1$. Only the data with no settling effects are considered.

$\rho_p/\rho = 1.05$, with and without bottom porous medium, and $\rho_p/\rho = 1$. The loading fraction for the flow over porous medium is 20% while the loading fraction for no porous medium is 30%. Only the case where the settling particles have reached the top of the annulus are considered. For the case with porous medium, this is considered to be at Stokes numbers where the normalized torques change in slope (see Figure 7.24). The cases without porous medium show a stronger dependance on the Stokes numbers than the case for the flow over a porous medium. However, the trend for these 3 cases is very similar. Figure 7.30 shows the normalized torques for a loading fraction of 30% with a porous medium and for a loading fraction of 40% for the case without it. The normalized torques for the flow over porous medium lie between the normalized torques for a $\bar{\phi} = 40\%$ with $\rho_p/\rho = 1.05$ and $\rho_p/\rho = 1$. The change in normalized torques dependance on Stokes number for the case with settling particles is considered to be linked to the fluidization of the particles. In the absent of hydrodynamics and particle interactions effects, a constant behavior of the normalized torques with the Stokes number would indicate a constant volume fraction. The results shown in Figure 7.30 suggest that the effective volume fraction for the case with a porous medium and $\bar{\phi} = 30\%$ is

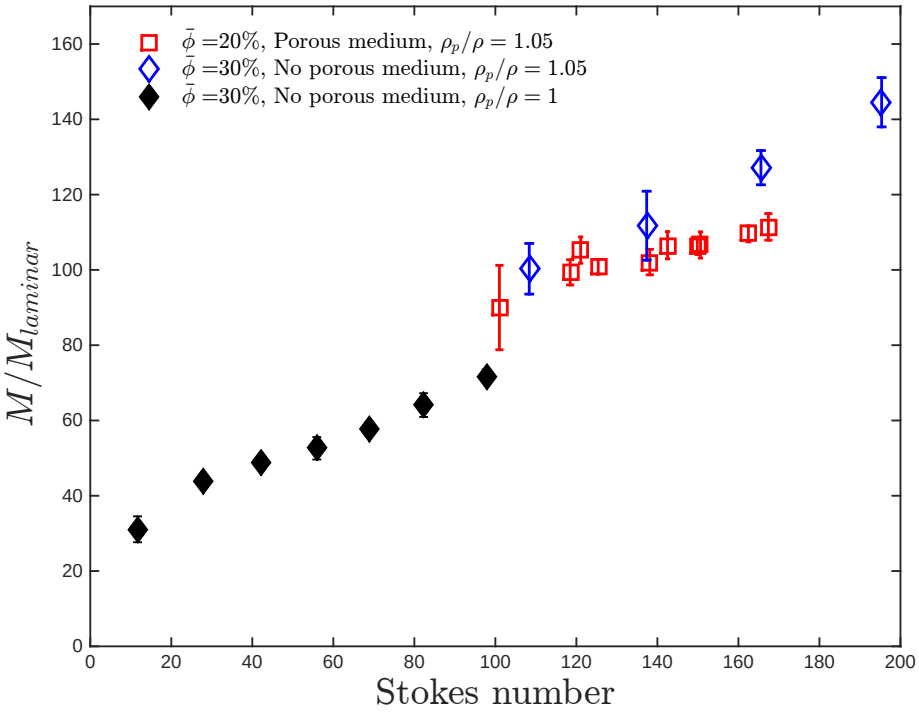

Figure 7.29: Flow over porous medium normalized torques as a function of St for $\bar{\phi} = 20$ compared with no porous medium with $\bar{\phi} = 30\%$ and $\rho_p/\rho = 1.05$ and $\rho_p/\rho = 1$. Only the data with no settling effects are considered.

higher than 40% (considering that the loading fraction for the case with matched densities is equal to the effective volume fraction), and that is less than the effective volume fraction for the case with settling particles and a loading fraction of 40%. In the next section a study of the effective volume fraction is presented to correct for the differences in loading and effective volume fraction. Lastly, Figure 7.31 shows the normalized torques for the three cases considered above with the normalized torques for a loading fraction of 40 and 50% for the flow over porous media, and 50% for the flow without it. As mentioned before, the normalized torques for the loading fraction of 50% decreases with Stokes number and did not become constant. However, by inspecting the measured torques, (see Figure 5.5), a drop occurs at shear rates around 60 s^{-1}, which corresponds to Stokes numbers around 100. In Figure 7.31 it is observed that the normalized torques for flow without the porous medium are more or less independent of the Stokes numbers. For the case with porous medium, the normalized torques continue to decrease with Stokes number. This indicates that the effects of settling (decreasing of the normalized torques with Stokes number) are more pronounced than for the case with porous medium. Therefore, even when the top particles have resuspended and touch the top section of the rheometer, the middle section of the column of particles have not been effectively fluidized. This suggests that the presence of the porous medium enhances the effects of a volume fraction gradient in the vertical direction. It is possible that in the absent of porous media,

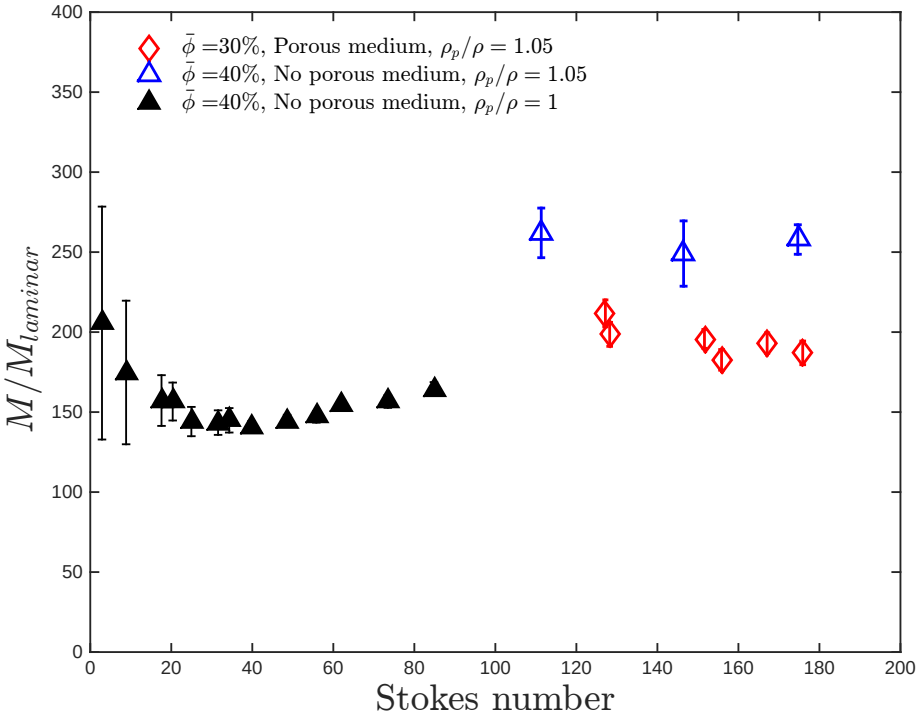

Figure 7.30: Flow over porous medium normalized torques as a function of St for $\bar{\phi} = 30$ compared with no porous medium with $\bar{\phi} = 40\%$ and $\rho_p/\rho = 1.05$ and $\rho_p/\rho = 1$. Only the data with no settling effects are considered.

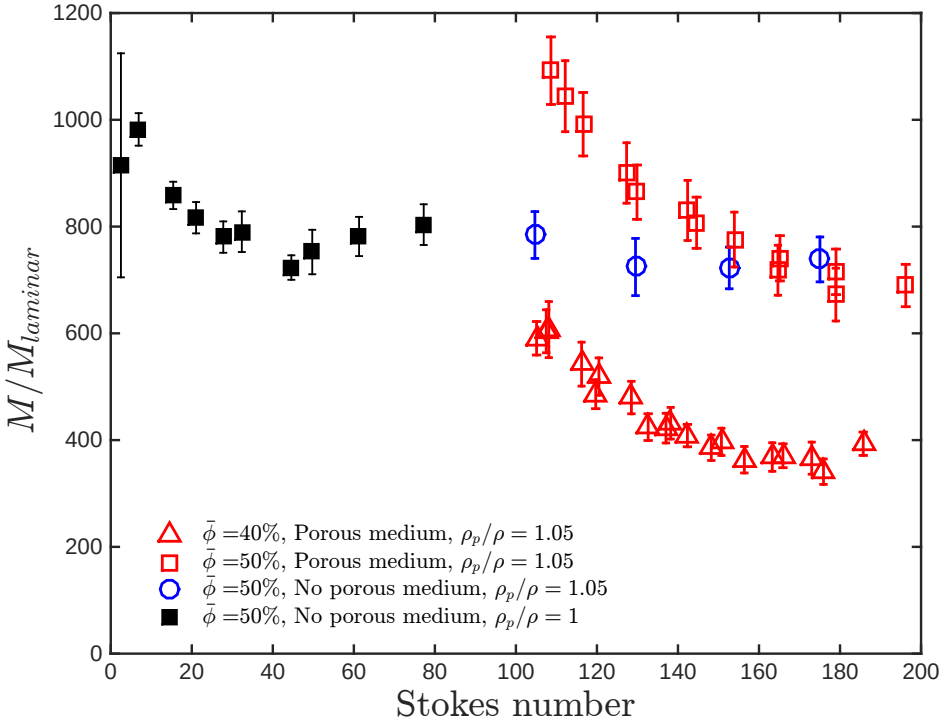

Figure 7.31: Flow over porous medium normalized torques as a function of St for $\bar{\phi} = 40$ and 50% compared with no porous medium with $\bar{\phi} = 50\%$ and $\rho_p/\rho = 1.05$ and $\rho_p/\rho = 1$. Only the data with no settling effects are considered.

the formation of secondary flows at the bottom helps fluidized the settling particles; meanwhile, the presence of porous media might weaker this effect.

Effective volume fraction prediction for flow over a porous medium with $\rho_p/\rho = 1.05$

The effective volume fraction for the settling particles is inferred from the particle resuspension measurements that are described in Chapter 6. Using the same method described in Section 7.3, the effective volume fraction is estimated from the expansion results. However, due to the limited view of the visualization window used for these experiments, measurements of the height at high Stokes number are not possible. By comparing the measure heights normalized with the total height for the cases with and without a porous medium, similarities between certain loading fractions are found. Figure 7.32 shows the normalized measure heights for the case without porous medium and loading fractions of 20, 25, and 30 % compared with the normalized measure heights for flow over porous medium with loading fractions of 10, 20, and 30%. The normalized measure heights for the case

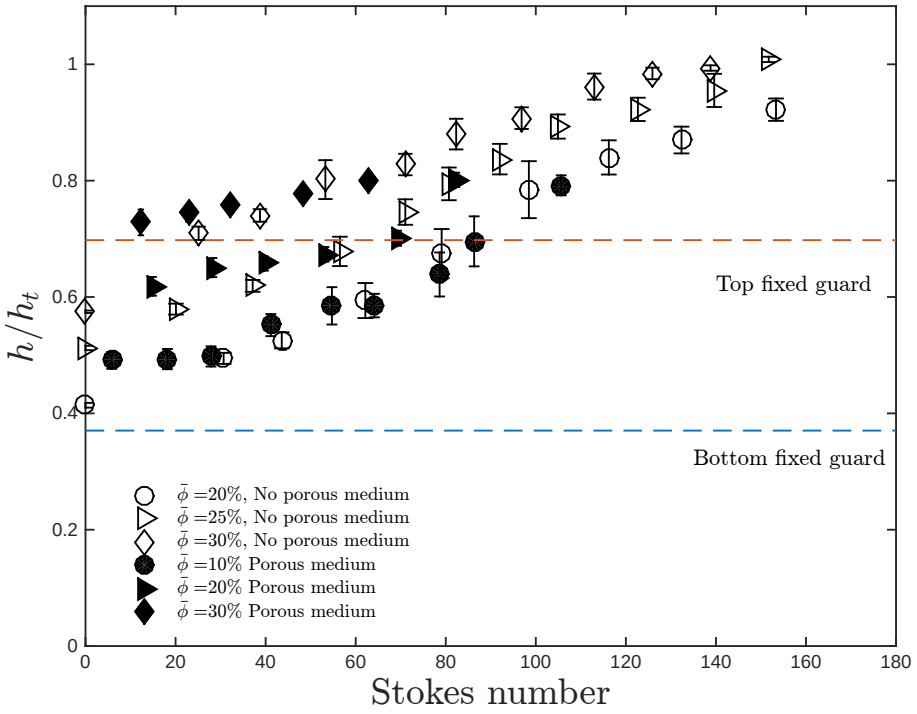

Figure 7.32: Particles normalized heights for flow with and without porous medium. The height is measured from the bottom of the annulus and normalized by the annulus total height.

with glass beads at the bottom seem to coincide with the heights corresponding to a higher loading fraction when no porous medium is placed. The effective volume fraction can then be inferred for a wider range of Stokes numbers by using the expansion for which the measured normal heights

seem to coincide. To test this method, the effective volume fraction is also predicted using linear extrapolation from the height measured for the limited Stokes numbers. Both methods lead to similar effective volume fractions. Figure 7.33 shows the effective relative viscosity as a function of the effective volume fraction for different Stokes numbers tested for $\rho_p/\rho = 1.05$. In here only the cases where the test cylinder is fully covered are considered. The magnitude of the Stokes numbers is represented with different sized symbols (the larger the Stokes number, the larger the symbol). The effective relative viscosity increases with volume fraction and for a loading fraction of 10% an

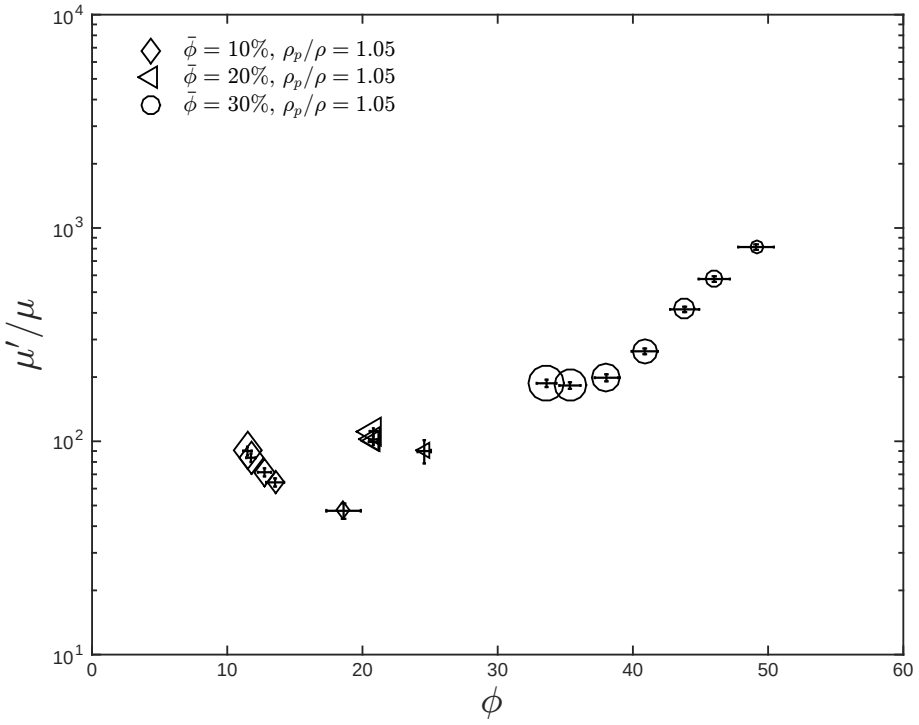

Figure 7.33: Effective relative viscosity for flow over porous media as a function of the effective volume fraction. Only the data where the test cylinder is fully covered are considered.

effect on the Stokes number is observed. For this particular case, the larger the St, the higher the effective relative viscosity and the lower the effective volume fraction is.

Comparisons between the case with settling particles but no porous medium are shown in Figure 7.34. The effective relative viscosity is higher for the case with a porous medium for volume fractions lower than 30%. For higher volume fractions the effective relative viscosity appears to coincide for both cases presented. Figure 7.35 shows the comparison between the three cases studied. With the exemption of the low volume fractions with a porous medium, the effective relative viscosity for all the other scenarios considered seem to coincide and follow the same trend. The differences in effective relative viscosity for low volume fractions seem to indicate the presence of a gradient in the volume fraction in the vertical direction. This gradient is more evident for the case with flow over a porous medium.

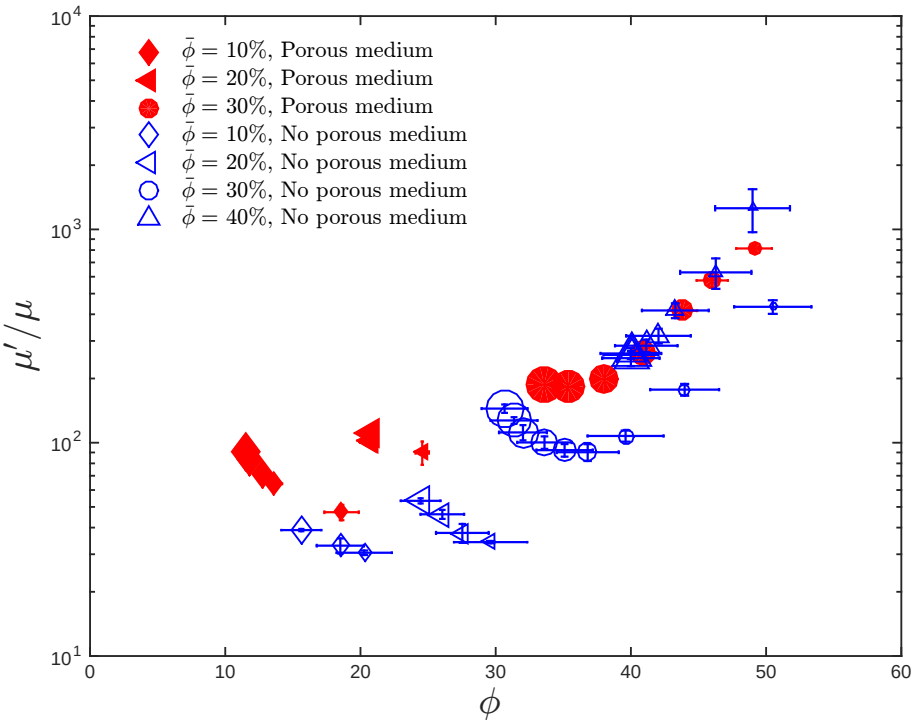

Figure 7.34: Effective relative viscosity as a function of the effective volume fraction for flow with and without porous medium. Only the data where the test cylinder is fully covered are considered.

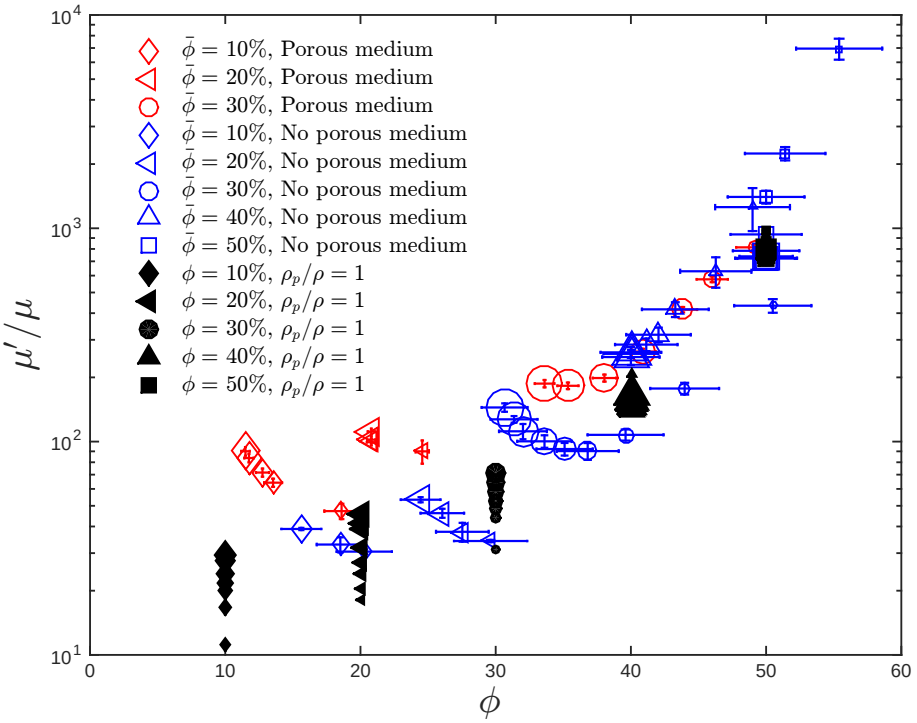

Figure 7.35: Effective relative viscosity as a function of the effective volume fraction for flow with and without porous medium with different density ratios. Only the data where the test cylinder is fully covered are considered.

Inertial and particle concentration effects on flow over a porous medium with $\rho_p/\rho = 1.05$

Similar to the analysis done in Section 7.4 and 7.1, the effective viscosity of the mixture (μ'_{min}) is inferred using the predicted effective volume fraction and Figure 7.3. The values of μ'_{min} are used to calculate the effective laminar torque ($M_{effe,\,laminar}$) and the effective gap Reynolds number ($Re_{b,\,effe}$). The measured torques normalized with the effective laminar torque as a function of the effective gap Reynolds number are presented in Figure 7.36 and compared with the different density ratio cases without porous medium. As considered for the cases without porous medium, only the data for Stokes number without settling effects are considered.

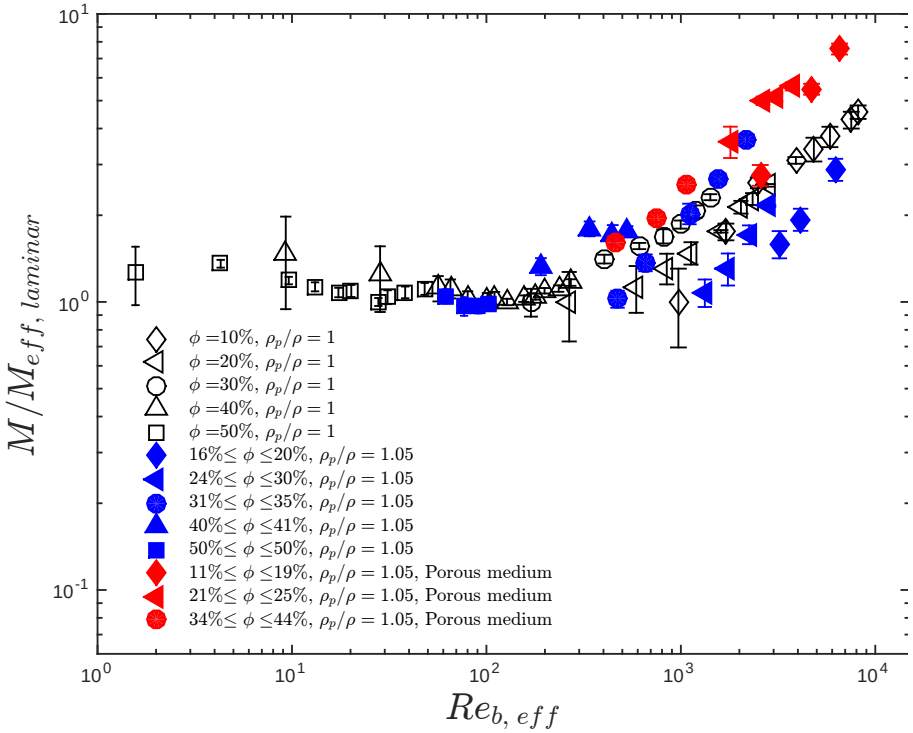

Figure 7.36: Measured toques normalized by the effective laminar torques as a function of the effective Reynolds numbers for $\rho_p/\rho = 1$ and $\rho_p/\rho = 1.05$ with and without porous medium. The effective viscosity of the suspension is inferred from the predicted effective volume fraction and Figure 7.3.

The normalized torques using the predicted effective viscosity are higher for the flow over a porous medium. As mentioned before, using Figure 7.3 to infer the value of the effective viscosity μ'_{min} introduces the uncertainties involved in estimating the effective volume fraction. If μ'_{min} is instead considered to be equal to the minimum value of μ'/μ found for each loading fraction, then the scatter found in Figure 7.36 is reduced, as shown in Figure 7.37. For all the cases shown, the deviation from the laminar behavior occurs at the range of effective Reynolds number where the

pure fluid torque measurements are higher than the ones predicted from laminar theory.

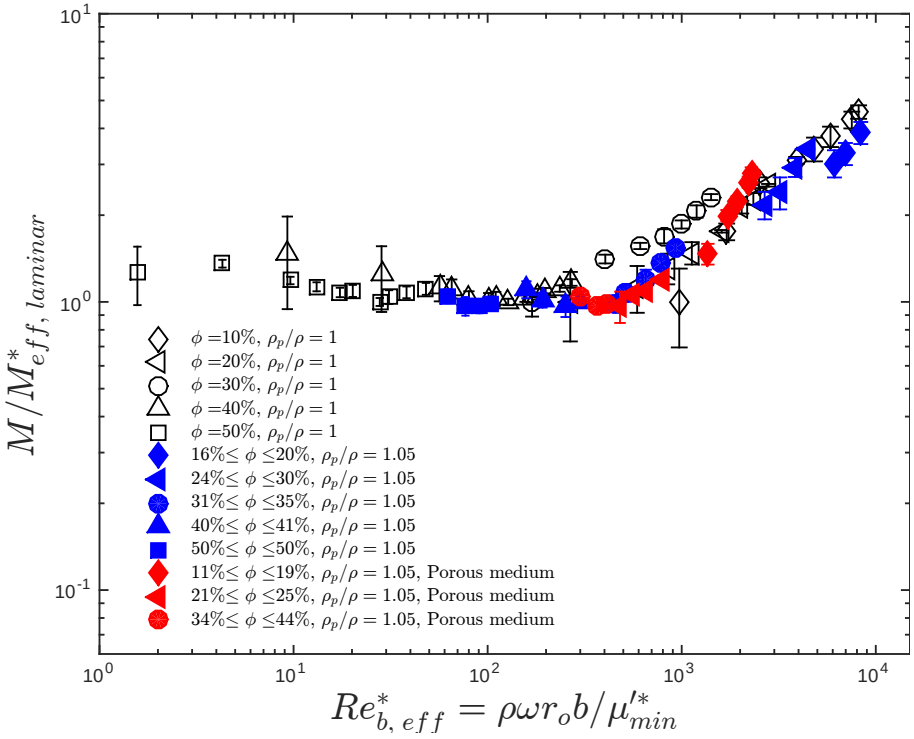

Figure 7.37: Measured toques normalized by the effective laminar torques as a function of $Re^*_{b,\ eff}$ for $\rho_p/\rho = 1$ and $\rho_p/\rho = 1.05$ with and without porous medium. The effective viscosity of the suspension is considered to be the minimum of the ratio μ'/μ for each loading fraction.

7.6 Corrected torque for partial filling

As mentioned before in Section 7.2, for settling particles at low loading fractions and below a certain Stokes number, the particles do not cover entirely the test cylinder. To compare between these low loading fractions and the low loading fractions with $\rho_p\rho = 1$, a correction of the measured torques is needed. Such correction should take into account just the area covered by the liquid-solid mixture. This can be achieved by formulating that the measured torque is the sum of the contribution of the mixture and the contribution of the fluid, which leads to the following relation:

$$M = \tau 2\pi r_i^2 h_f + \tau_{mix} 2\pi r_i^2 h,$$

where M is the measured torque, τ is the fluid shear stress , τ_{mix} is considered to be the shear stress applied by the liquid-solid mixture, and h_f and h are the height from the test cylinder covered by just the fluid and the mixture, respectively. The torque corresponding for just the mixture can be

obtained from equation 7.39 by considering that the fluid shear stress is equal to

$$\tau = \frac{M_f}{2\pi r_i^2 h_{test}},$$

where M_f is the measured torque for just the fluid and h_{test} is the height of the test cylinder. Since M_f was measured for a limited range of gap Reynolds number, a curve fit from these measurements is used to infer the corresponding values of M_f for higher Reynolds numbers. Figure 7.38 shows in a log log scale the pure fluid measured torque together with the curve fit used to infer the values of M_f for plain water and the aqueous glycerine mixture of 21% used for the case with matched liquid density.

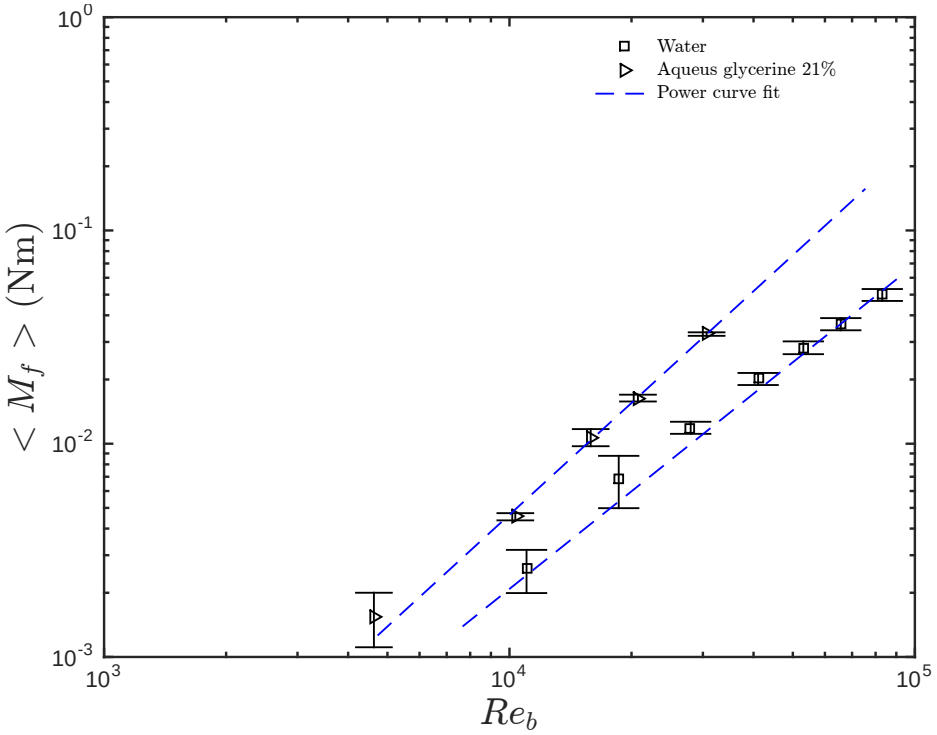

Figure 7.38: Measured torque for pure fluid as a function of gap Reynolds number and its curve fit presented in a log-log scale.

By substituting equation 7.6 into 7.39, the corrected torque for the mixture is

$$M_{mix} = M - M_f \frac{h_f}{h_{test}}, \tag{7.1}$$

where h_f is equal to $h_{test} - h$. Figure 7.39 shows the corrected measured torque for volume fractions of 10 and 20% with $\rho_p/\rho = 1.05$. The correction applies only to the shear rates for which the liquid-solid mixture is only partially covering the test cylinder. For shear rates where the height predicted using the particles height measurements (discussed in Chapter 6) is above the test cylinder height,

M_{mix} is considered to be equal to the measured torque (M). The torques for the shear rates where the test cylinder is partially covered, ($\dot{\gamma} < 80\ s^{-1}$ for $\bar{\phi} = 10$ and $\dot{\gamma} < 60\ s^{-1}$) does not show a strictly linear dependance with the shear rate, although there are not a significant number of measurements to determine the trend (for $\bar{\phi}$=10%, only 3 points were measured and for $\bar{\phi} = 20\%$ only 4). There is a jump between the corrected torques and the corresponding measured torque for the case where the particles fully cover the test cylinder. This might suggest that the contribution from the fluid to the measured torque is over-estimated during the correction or that the full resuspension of the particles increases the torque abruptly.

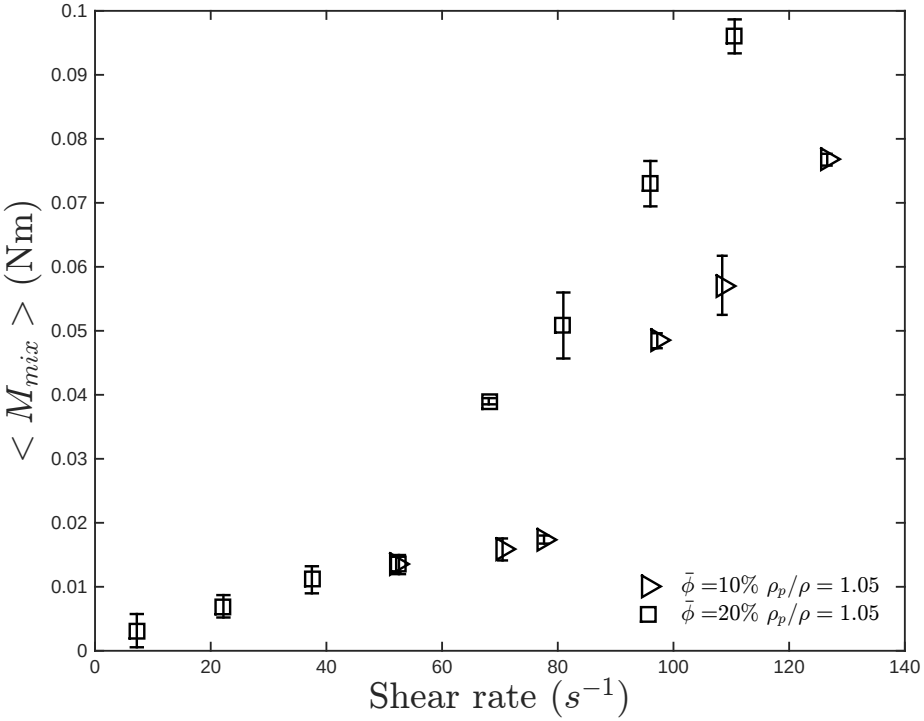

Figure 7.39: Corrected torque as a function of shear rate for partially covered test cylinder.

As mentioned before, it is possible that for these diluted mixtures, the contribution of the liquid might be stronger than for higher solid fractions. The presence of particles might not be strong enough to reduce the effective Reynolds number of the suspension. In such case, the contribution to the torque from the suspending liquid might be closer to the value measured for just the fluid. Figure 7.40 shows the corrected torque normalized by the theoretical laminar torque as a function of the Stokes number. The normalized torques for the Stokes for which the particles are partially covered are more scattered. When the test cylinder is fully covered, the normalized torques fluctuate less. For a loading volume fraction of 10% and 20% , the normalized torques increase with Stokes numbers when the test cylinder is fully covered.

Figure 7.41 shows a comparison between the normalized torques for $\rho_p/\rho = 1.0$ and $\rho_p/\rho = 1.05$. For the case with settling particles, the torques have been corrected to account when the test cylinder

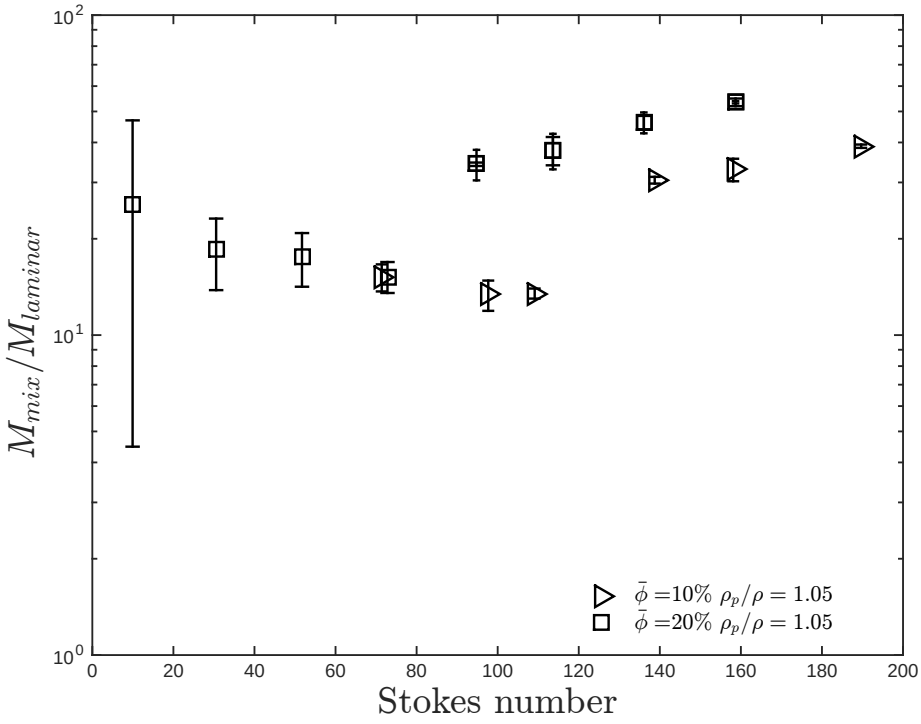

Figure 7.40: Corrected torque normalized by $M_{laminar}$ as a function of Stokes numbers.

is partially covered ($M_{mix}/M_{laminar}$).

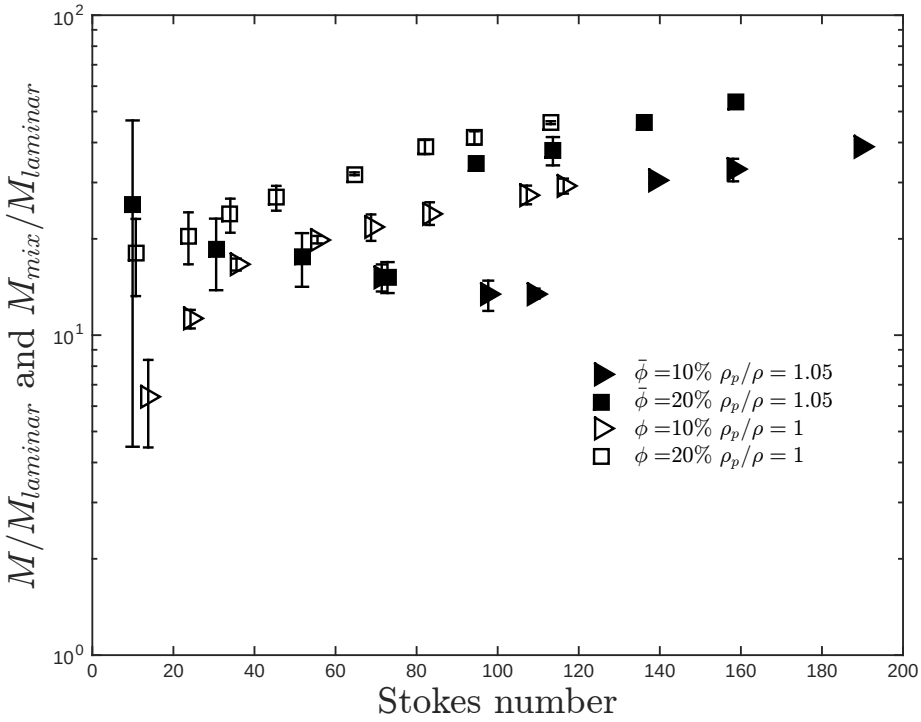

Figure 7.41: Corrected torque normalized by $M_{laminar}$ as a function of Stokes numbers compared with the data for $\rho_p/\rho = 1$.

For the case with $\rho_p/\rho = 1.05$, the normalized corrected torques for a loading fraction of 20% decrease with Stokes number, and once the particles fully covered the cylinder the corrected normalized torque increases. A similar behavior is found for a loading fraction of 10%. For this loading fraction only the data corresponding to the Stokes number where particles were present in the test section are considered. The correction of the torque when the test cylinder is partially covered does not seem to coincide with the measured torques for fully covered. This suggests that either the predicted height or the predicted pure fluid torque considered is not completely adequate.

7.7 Comparison between current and previous experimental and numerical results

The effective relative viscosity for the current and previous experiments of inertial suspensions is shown in Figure 7.42. For the current experiments with settling particles, the relative effective viscosity is plotted against the predicted volume fraction normalized by the particles random loose packing measured by Koos et al. (2012) ($\phi_{RLP} = 55.3\%$). Only the previous experiments with rough walls and Stokes numbers higher than 10^{-1} are compared. The empirical model used by Zarraga et al. (1999) is also shown in Figure 7.42 to compare the non-inertial results. The current experiments exhibit higher effective relative viscosities than the previous experimental work. Most of the experimental work of Prasad and Kytömaa (1995) correspond to Stokes numbers lower than the present study ($3.2 \times 10^{-2} \leq St \leq 3.2$) and their measurements involved settling particles with higher density ratio ($1.12 \leq \rho_p/\rho \leq 2.09$). Their torque measurements were made on the top of their annular shell and the suspension was sheared at the bottom at low shear rates. Such conditions could lead to lower effective volume fractions since the suspension is not sheared fast enough for the particles to fluidize. Similarly to Prasad and Kytömaa (1995), the density ratios for the experiments of Hanes and Inman (1985) are higher than for the present study ($2.48 \leq \rho_p/\rho \leq 2.78$) and the torques were also measured on the top surface. Unlike the work of Prasad and Kytömaa (1995), Hanes and Inman (1985) considered high shear rates. However, even when these experiments consider high shear rates, the complete fluidization of the particles may have not be achieved due to the higher density ratio which could lead to lower effective volume fraction than the one reported, and therefore lower effective relative viscosities.

As shown in Section 7.2, the effective relative viscosity for volume fractions higher than 30% showed no dependance on Stokes numbers as long as the particles are completely fluidized. Moreover, at these higher volume fractions, the hydrodynamic inertial effects were not present according to the analysis done in Sections 7.1 and 7.4. It is not clear then why the relative effective viscosity for these experiments is approximately one order of magnitude higher than the effective relative viscosity for the non-inertial suspensions. One possible explanation could be that at higher Reynolds numbers

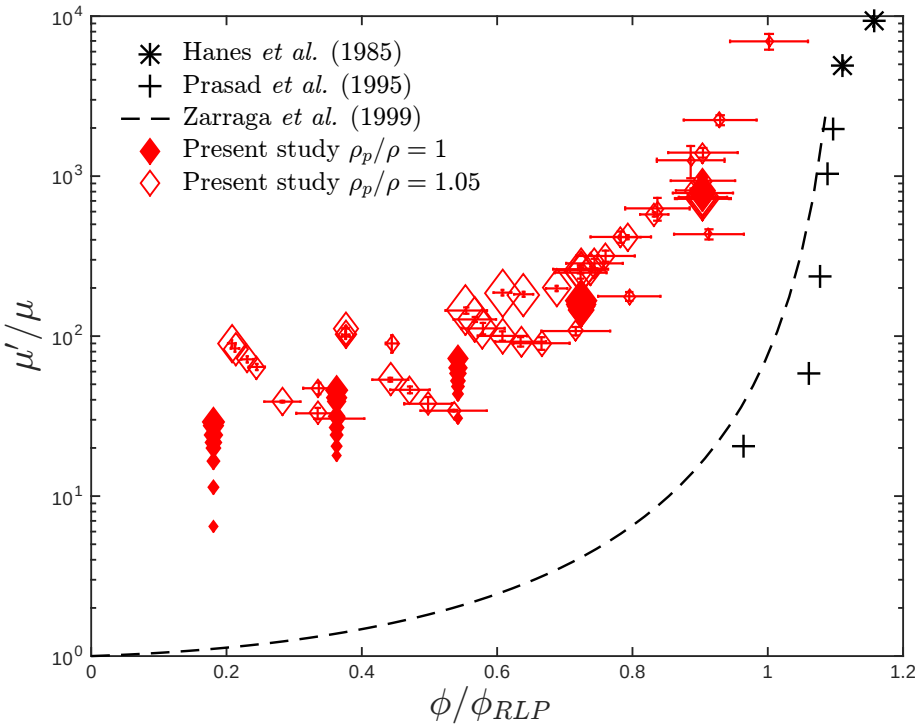

Figure 7.42: Effective relative viscosity as a function of volume fraction normalized by random loose packing for the present and previous experimental work. Only the previous experimental work with rough walls and Stokes numbers higher than one are presented. Dashed line corresponds to the empirical model proposed by Zarraga et al. (1999) to represent the results for non inertial suspensions. For the current results the size of the symbol represents the Stokes number magnitude.

the particle interactions increase and thus the velocity fluctuation of the flow. Velocity fluctuations lead to the presence of Reynolds stresses that are not present at low Reynolds number regimes. However, these Reynolds stresses increase with Reynolds number, leading to an increasing effective relative viscosity; however, the effective relative viscosity for these experiments show no dependance on Reynolds number. If Reynolds stresses are present for these experiments, then there must be a competing mechanism that balances the effect of increasing velocity fluctuations. It is not clear which mechanism could that be.

Figure 7.43 shows a comparison between the present study and the numerical results for suspensions with moderate Reynolds number. Only the current experiments with the lowest Reynolds numbers for each volume fraction is presented. The relative effective viscosity is plotted against the volume fraction normalized by the random loose packing. Since all the simulations considered spherical particles, the random loose packing used to normalized the volume fraction is calculated for monodisperse spherical particles using the fit of Zou and Yu (1996). Similarly to the comparison with previous experimental work, the present results show higher effective relative viscosities. For volume fractions lower than 30% the Reynolds number for the current experiments is approximately an order of magnitude higher than the Reynolds number considered in the simulations. The simulations of Kulkarni and Morris (2008) consider a Reynolds number range of $0.05 \leq Re \leq 16$, while the simulations of Picano et al. (2013) range the Reynolds number from $4 \leq Re \leq 40$ and the simulations of Yeo and Maxey (2013) consider lower Reynolds range of $0.02 \leq Re \leq 8$. The latest show the lowest relative effective viscosity even for the cases with the same volume fraction and Reynolds number. This discrepancy might be due to differences in their assumptions. Aside from using a different numerical method, Yeo and Maxey (2013) considered the Reynolds stress to be negligible. The later work of Haddadi and Morris (2014) showed that the contribution of the Reynolds stress to the bulk and particle-phase stresses is significant, therefore neglecting it would lead to lower effective relative viscosities which is consistent with the results showed in Figure 7.43.

Figure 7.44 shows the comparison between the effective relative viscosity as a function of Reynolds number for the present and numerical work of Picano et al. (2013) and Kulkarni and Morris (2008). Good agreement between the numerical simulations is shown. However, the present experimental work shows higher effective relative viscosities. A possible reason for this is the presence of slip at the wall observed in the work of Picano et al. (2013), where the ratio of particle velocity next to the wall and the wall velocity in their simulations is approximately 0.6. Similar velocity ratio was found in the smooth walls experiments of Koos (2009) for Reynolds numbers smaller than 100 and volume fractions below 40%. Such velocity ratio indicates the presence of slip and as shown by Barnes (2000) and Koos et al. (2012) it leads to lower effective viscosities. The relative effective viscosity for the current experiments for the lowest Reynolds number tested ($\mathcal{O}(100)$) are between 3 to 5 times higher than the numerical results of Picano et al. (2013) for Reynolds number equal to 40.

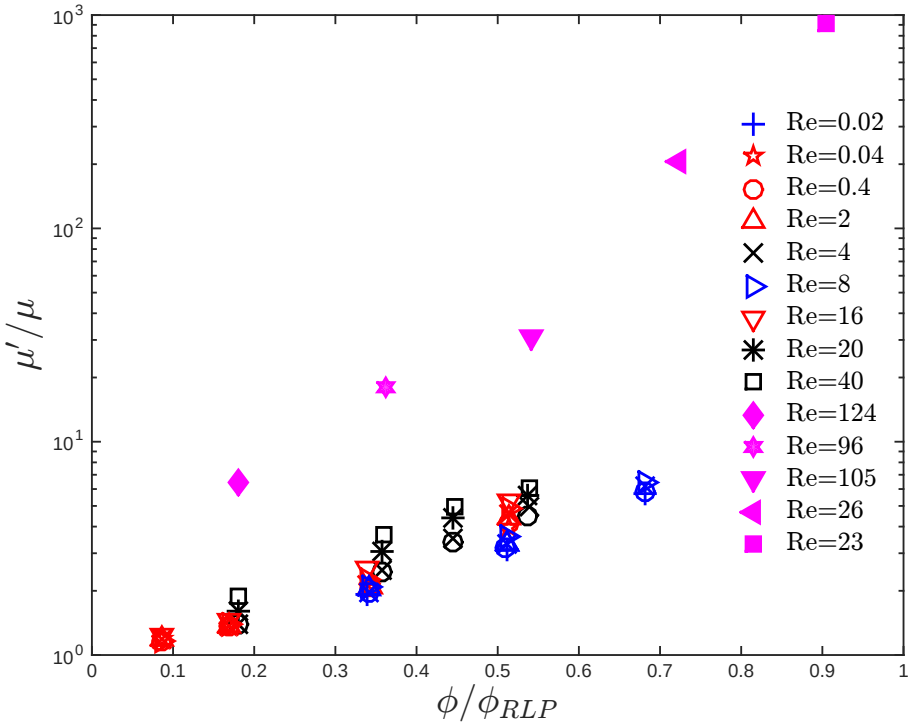

Figure 7.43: Effective relative viscosity as a function of volume fraction normalized by random loose packing for the present and previous numerical work. Solid symbols correspond to the present data. Blue symbols correspond to Yeo and Maxey (2013), red symbols correspond to Kulkarni and Morris (2008) and black symbols correspond to Picano et al. (2013).

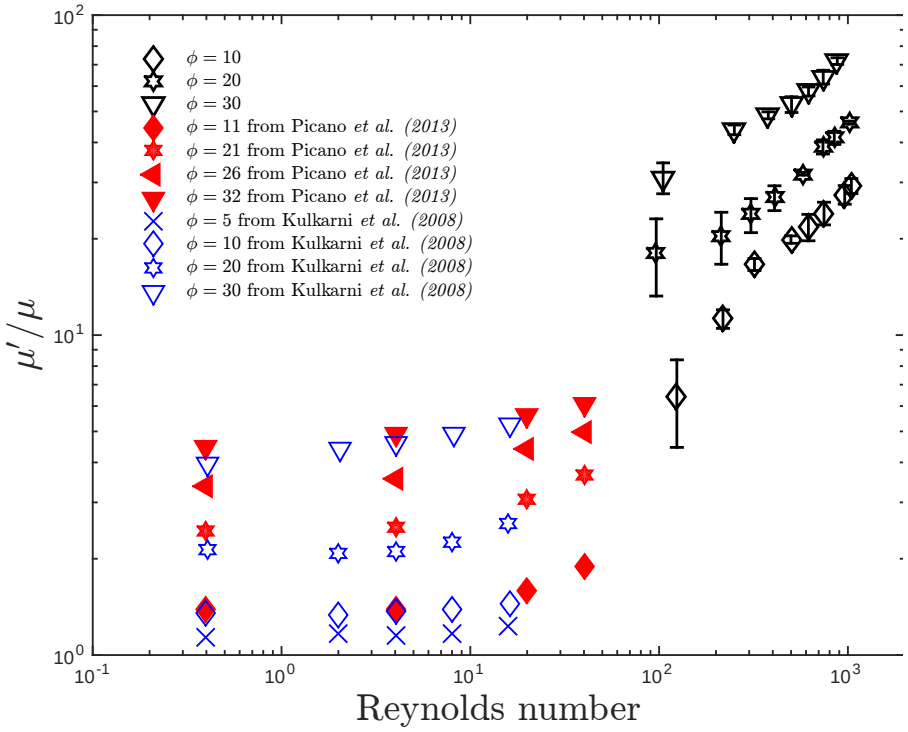

Figure 7.44: Effective relative viscosity as a function of Reynolds number for the present and previous numerical work. Black symbols correspond to the present data. Closed symbols correspond to Picano et al. (2013), red symbols correspond to Kulkarni and Morris (2008).

Based on the results of Koos et al. (2012), the effective viscosity can be up to 4 times higher than the apparent viscosity corresponding to experiments affected by slip at the wall for volume fractions lower than 40%.

A different mechanism occurs in the numerical work of Kulkarni and Morris (2008) where the particles tend to concentrate at the walls. The opposite behavior is observed experimentally, where the particles tend to move away from the wall. Kulkarni and Morris (2008) calculated the bulk stress and the stress at the wall, with the latest higher than the former. Because the particles are concentrating at the walls, there are less particles at the bulk, which would decrease the amount of particle interactions leading to lower effective relative viscosities.

7.8 Summary

Comparison between the cases of matched density and settling particles with and without a porous medium are presented.

Based on Figures 7.5, 7.22, and 7.37, the hydrodynamic inertial effects from the liquid seem only to be present for the dilute and moderately dilute liquid-solid mixtures. In the transition from laminar to turbulent flow in liquids, an increase in the liquid viscosity leads to a delay in

the transition regime because of the decrease in Reynolds number. It is unlikely that liquid-solid flows with low and moderate volume fractions would be an exception to this rule. As the volume fraction increases, the effective relative viscosity of the suspension increases considerably, leading to a decrease in effective Reynolds number of the mixture. For the three cases studied, the deviation from the laminar behavior occurs at an effective Reynolds number range that coincides with the region where the pure fluid measurements show a deviation from the laminar theory. This analysis is done by considering the data where the particles have been fluidized and where the effects of settling are weaker.

The effective volume fraction for the experiments with settling particles is predicted based on the results from the particle resuspension analysis (Chapter 6). When the effective volume fraction is considered, the relative effective viscosity for the case with $\rho_p/\rho = 1$ and $\rho_p/\rho = 1.05$ seems to coincide. This indicates that the effective relative viscosity is independent of the differences in density as long as the effective volume fraction is considered to correct for the presence of settling.

The experiments with a porous medium show higher relative viscosity at similar effective volume fraction. This suggests the presence of gradient in the volume fraction in the vertical direction. The presence of a lower base of heavier glass beads seems to affect the relative effective viscosity. The mechanism for this is still not clear.

Corrections to the measured torques for low loading fraction cases where the particles do not fully cover the test cylinder are presented considering that the contribution from the mixture and the suspending fluid can be obtained by inferring the height covered by the particles. The corrections do not seem to recover the shape of the normalized torques once the test cylinder is fully covered.

Comparison between the present and previous experimental and numerical work show that the effective relative viscosity for the current experiments are higher even for the cases where the inertial hydrodynamic effects are not present. The reason for this is not completely clear but possible reasons include a change in the effective volume fraction considered by the previous experimental work and presence of slip in the numerical simulations.

Chapter 8

Conclusions

This thesis presents rheological measurements of liquid-solid flows at Stokes and Reynolds numbers where inertial effects are important. The results for the case with $\rho_p/\rho = 1$ are summarized in the following section followed by a summary of the hydrodynamic instability effects. The effect of particle settling is summarized in section 8.2 . A discussion about the differences between the current work and the experimental results found for inertial and non-inertial suspensions is presented in Section 7.7. Comparisons with numerical results for inertial suspensions are discussed as well and emphasis has been focused on the possible reasons for the discrepancies observed. Finally, topics of possible future interest are discussed in Section 8.4.

8.1 Particles with matched density

Experiments with $\rho_p/\rho = 1$ were performed for a volume fraction range of $10\% \leq \phi \leq 50\%$ using polystyrene particles immersed in an aqueous glycerin solution. The range of Stokes numbers tested for this case is $2.5 \leq St \leq 116.3$ (equivalently, the Reynolds number range is $22.6 \leq Re \leq 1.04 \times 10^3$). For $\phi \geq 40\%$, the measured torque exhibits a linear dependance on the shear rate. When normalizing the measured torque by the fluid torque predicted by laminar theory, the dependance on Stokes number is negligible. This indicates that for $\phi \geq 40\%$ the flow exhibits a Newtonian behavior where the effective relative viscosity is given by the normalized torques and it increases with volume fraction but remains constant with the Stokes number and equivalently with the Reynolds number:

$$\frac{M}{M_{laminar}} = f(\phi) \quad \text{for} \quad \phi \geq 40\% \quad \text{and} \quad \rho_p/\rho = 1.$$

For $\phi \leq 30\%$ the measured torques exhibit a non-linear dependance on the shear rate. The normalized torques for these lower volume fractions increase not only with ϕ but also with Stokes and

equivalently Reynolds number:

$$\frac{M}{M_{laminar}} = g(\phi, St) \quad \text{for} \quad \phi \leq 30\% \quad \text{and} \quad \rho_p/\rho = 1.$$

To study if this dependance is a result of an increase in the particle interactions or the presence of hydrodynamics instabilities, an analysis of fluid and particle inertia was done. The torque measurements for pure fluid indicate the presence of hydrodynamic instabilities for modified gap Reynolds higher than 3×10^3. If the liquid-solid mixture is considered to be a Newtonian fluid and its effective viscosity is used to define the modified gap Reynolds number, it is possible to determine if the range of Reynolds number tested lie within the range of Reynolds number where hydrodynamic instabilities are present.

In this hypothetical scenario the viscosity of the liquid-solid mixture is considered to be independent of the shear rate and it only depends on the particle volume fraction. The effective relative viscosity of the mixture is then considered to be equal to the normalized torques corresponding to the lowest Stokes number:

$$\frac{\mu'_{min}}{\mu}(\phi) = \frac{M}{M_{laminar}}(St_{min})$$

where St_{min} is the lowest Stokes number tested for the corresponding loading fraction and μ'_{min}/μ is the hypothesized effective relative viscosity. This is based under the assumption that at the lowest Stokes number, the measurements are not affected by hydrodynamics instabilities. The measured torques are then normalized by a laminar torque that considers the effective viscosity of the mixture instead of the fluid viscosity. Similarly, an effective Reynolds number is defined where the effective viscosity of the mixture is considered instead of the fluid viscosity.

The measured torques normalized with the effective laminar torque for $\phi \geq 40\%$ are close to one and the corresponding effective Reynolds number range for these experiments are within the modified gap Reynolds number region where the pure fluid exhibits a laminar behavior. For $\phi \leq 30\%$, the normalized torques deviates from unity and their corresponding effective Reynolds number is within the region where hydrodynamic instabilities were observed.

Based on this analysis the inertial effects are present for effective Reynolds numbers ($Re^*_{b,\,eff}$) higher than 400:

$$\frac{M}{M_{laminar}} = g(\phi, St) \quad \text{for} \quad Re^*_{b,\,eff} > 400 \Rightarrow \text{hydrodynamic instabilities effects}$$

and for effective Reynolds numbers lower than 400, the effects of hydrodynamics instabilities are negligible:

$$\frac{M}{M_{laminar}} = f(\phi) \quad \text{for} \quad Re^*_{b,\,eff} < 400$$

8.2 Effect of particle settling

Experiments with particles denser than the suspending liquid were performed where $\rho_p/\rho = 1.05$. The range of Stokes number tested for this case is $2.6 \leq St \leq 195$ and the range of Reynolds number is $22 \leq Re \leq 1.7 \times 10^3$. In this set of experiments, the particles used were the same polystyrene particles, but water was used as the suspending liquid. For this case the particle distribution is no longer homogeneous and depending on the shear condition the particles settle ($\dot{\gamma} = 0$) or re-suspend. Therefore, the volume fraction at the test section is no longer equal to the loading fraction ($\bar{\phi}$)

$$\bar{\phi} = \frac{\text{Volume of particles}}{\text{Volume of annulus}} \neq \phi \quad \text{for} \quad \rho_p/\rho = 1.05.$$

To determine the effective volume fraction for these experiments, visualizations of the flow were performed. The particle resuspension was characterized by measuring the height reached by the particles for different loading fractions and at different Stokes numbers. Based on these measurements the volume fraction could be inferred. When the inferred volume fraction is plotted as a function of Stokes number, it collapses into one curve for all the loading fractions tested. This indicates that the resuspension process is independent of the loading fraction.

The results from the flow visualization were used to analyze the torque measurements for the experiments with $\rho_p/\rho = 1.05$. The range of loading fraction tested is $10\% \leq \bar{\phi} \leq 60\%$. For $\bar{\phi} \geq 30\%$, the normalized torques decrease with Stokes number and for $\phi \geq 40\%$, the normalized torques reach a plateau for Stokes numbers above a critical value. The value for this critical Stokes number increases with the loading fraction. The visualization of the flow for these experiments show that this dependance is a settling effect. At low Stokes numbers the particles settle, which leads to an increase in the effective volume fraction. As the Stokes numbers increase, the particles start fluidizing and thus decreasing the effective volume fraction. A decrease in the effective volume fraction leads to a decrease in the normalized torques. The normalized torques for $\bar{\phi} = 30\%$ stop decreasing at the Stokes number where the complete fluidization of the particles occurs and start increasing with Stokes numbers above the fluidization threshold. A different dependance is observed for $\bar{\phi} \leq 20\%$, where the normalized torques increase with the Stokes number instead of decreasing. At these low loading fractions the particles settle at the bottom of the rheometer and do not reach the test section. As the Stokes number increases, the particles fluidize and start covering the test cylinder, which leads to an increase in the effective volume fraction and thus an increase in the normalized torques. Comparisons between the normalized torques for pure fluid and $\bar{\phi} = 10\%$ show that for gap Reynolds numbers lower than 5×10^4, the normalized torques for pure fluid and $\bar{\phi} = 10\%$ are the same. This indicates that there is no presence of particles in the test section for these gap Reynolds numbers. The visualization of the flow confirms this hypothesis. Measurements

of the height reached by the particles allow to determine the Stokes numbers at which the particles are partially covering the test section. Corrections to the measured torque for the case where the particles are partially covering the test section were done. Such corrections do not seem to coincide with the measured torques for the case where the test section is fully covered. This suggests that the contribution from the fluid considered in the correction might be over-estimated.

The effective volume fraction of the torque experiments is predicted using the particle resuspension analysis. When the effective volume fraction is considered, the normalized torques for both cases with different density ratio coincide indicating that the normalized torques are independent of the density ratio.

When only the cases where the particles are completely fluidized are considered, a similar behavior to the case with $\rho_p/\rho = 1$ is observed. The normalized torques for $\phi \leq 30\%$ exhibit a dependance on the Stokes number. The effective Reynolds number for these experiments is higher than 400, indicating that such dependance is due to the presence of hydrodynamic instabilities.

Flow over a porous medium

As mentioned earlier in this section, when the loading fraction is lower than 30%, the particles settle and do not reach the test section. To further study these low loading fractions, experiments with settling particles over a porous medium were performed. The lower section of the rheometer was filled with glass beads up to a height of approximately 11 cm ($\approx$ 2 cm below the test cylinder) and the polystyrene particles were placed on top. In this way, the polystyrene particles are brought up and their presence in the test section is guaranteed even for a loading fraction of 10%. The measured torque for these experiments increases with the shear rate and exhibits a drop for shear rates above a critical value. This drop is not observed for the case without porous medium. The torque was measured with increasing and decreasing shear rates to study the dependance on the shear rate history. The torques measured with increasing shear rates coincide with the torques measured with decreasing shear rates. This indicates that these flows exhibit no hysteresis.

In the same way as for the case without porous medium, visualizations of the flow over a porous medium were performed and used to analyze the torque measurements for this set of experiments. The drop in the measured torque observed for the case with porous medium occurs at the same Stokes number where the particles are fully fluidized. The normalized torques decrease with Stokes number and reach a plateau when the particles are fully fluidized. This behavior was observed for all the loading fractions tested with the exception of $\bar{\phi} = 10\%$. For this particular loading fraction and when the particles are fully fluidized, the normalized torques increase instead of becoming constant.

The effect of settling for these experiments is more marked than for the case without porous medium. The reason for this might be the presence of a vertical gradient in the particle concentration, where the particles located at the bottom are more packed than at the top. By having a porous

medium, the particles bottom layer is brought in closer proximity to the test section making the change in effective volume fraction more pronounced.

When the effective volume fraction is considered, the normalized torques for the case with a porous medium are slightly higher than for the case without porous medium. The reason for these differences might be due to the presence of a vertical gradient in the volume fraction. It is also possible that the presence of the porous medium affects the normalized torque but the reason for this effect is not clear.

8.3 Comparison with previous results

The effective viscosity for the current experiments is higher than the effective viscosity found in previous experimental work for inertial suspensions (Hanes and Inman, 1985; Prasad and Kytömaa, 1995). A possible reason for these differences is that the effective volume fraction in their measurements might be lower than the one reported due to settling. For both experimental studies, the torque was measured on the top of the annular shell and the particles were denser than the suspending liquid. Additionally, the work of Prasad and Kytömaa (1995) considers a lower Stokes regime which would increase the effect of settling in their measurements.

The effective viscosity for non-inertial suspensions is lower than the one found in the present work even for the cases where the normalized torques show no dependance on Stokes and Reynolds number. The reason for this is still not clear.

The numerical simulations for inertial suspensions show a dependance on Reynolds for volume fractions equal or higher than 10% (Kulkarni and Morris, 2008; Yeo and Maxey, 2013; Picano et al., 2013). This result agrees with the current experimental work; however, the effective viscosity found in these simulations is lower than the one found in the present experiments. Depending on the numerical work, a possible reason was proposed that include the neglecting of Reynolds stresses in the work of Yeo and Maxey (2013) and the presence of slip at the wall in the work of Picano et al. (2013).

8.4 General comments and future work

The main objective of the work presented in this thesis is to expand the Stokes and Reynolds number regime studied experimentally in liquid-solid flows where the inertia of both: the solid and liquid phase is important. A characterization of the particle settling and resuspension was presented through visualizations of the flow which allow to infer the effective volume fraction. Two density ratios: $\rho_p/\rho = 1$ and $\rho_p/\rho = 1.05$ were studied and when the effective volume fraction is considered, the difference in density ratio does not seem to affect the effective relative viscosity of the mixture;

however, this thesis considered only a 5% variation in density.

The characterization of the particle resuspension can have important implications in the modeling of systems involving settling and resuspension particles. Such systems are frequently found in many industrial processes (drilling muds, mixing of nuclear waste, handling of oil sands, mining processes, etc) and natural phenomena (debris-flows, lava flows, rock transport by rivers, etc). In the presence of settling, the materials are no longer homogeneous which can strongly affect their mechanical properties as shown by the results of the present work. *Viscous resuspension* has been previously examined by Leighton and Acrivos (1986). However, in most industrial processes involving sediments the inertia of the flow is significant and viscous resuspension is negligible (Wallner and Schaflinger, 1998). A model to predict the particle resuspension in inertial liquid-solid flows remains to be developed. This could be achieved by modifying the particle terminal velocity (v_{ter}) in the model develop by Leighton and Acrivos (1986) . For higher Reynolds numbers, the terminal velocity can be found from a balance of drag, gravitational and buoyancy forces. Additional modification to the diffusion coefficient might be also necessary to obtain more accurate results.

The presence of hydrodynamic instabilities seem to affect the current torque measurements for $\phi \leq 30\%$. The presence and effect of particle interactions that are not a result of secondary flows is still not resolved. An experimental setup with longer test apparatus might allow the study of liquid-solid flows that are not affected by hydrodynamics instabilities. Alternatively, experiments in a gravity free field would allow the study of moderate Stokes and Reynolds numbers regime for a wide range of volume fractions without having the effects of settling.

A more accurate measurement of the effective volume fraction can be achieved by analyzing the particle concentration gradient. Measurements of the particle velocity can confirm the existence of secondary flows in the test cylinder region and evidence the presence or absence of shear bands for the case with settling particles. Measurements of the particle collisions and its frequency can provide information of the effect of particle agitation in the bulk behavior of the mixture. Experiments with fluidized beds performed by Aguilar-Corona (2008) show that the frequency of collisions reaches a maximum for a volume fraction of approximately 30%. It is of interest to determine if similar results are found for the current experiments. Such findings can help to develop theoretical models or computer simulations.

Zenit et al. (1997) measured the collisional particle pressure for a vertical gravity-driven and fluidized bed, and similar to the findings of Aguilar-Corona (2008), the maximum particle pressure occurs at solid fractions of 30%. Measurements of the particle pressure in the current experiments can be made if pressure transducers are placed at the rheometer walls. Such measurements can shed a light into the relation between the normal and shear stress for liquid-solid flows with inertial effects.

In Appendix A, the results for experiments with polyester particles with $\rho_p/\rho = 1.2$ and $\rho_p/\rho =$

1.4 are presented. The visualization for these flows exhibit a particle concentration gradient in the radial direction. The particle resuspension analysis for these experiments is limited due to this radial migration of the particles. Experiments with particles of different size, shape and material where the centrifugal effects do not affect the radial migration of particles remain to be performed. It would be of interest to know if higher density ratios affect the effective viscosity of the mixture. Visualization of the flow for such experiments would allow to study the effects of particle shape and size in the particle resuspension process.

Appendix A

Inferred torque for zero shear rate

Depending on the loading fraction and density ratio, the best curve fit for the measured torques as a function of shear rate does not always go through the origin. Figure A.1 shows the inferred value of the liquid-solid flow's torque at $\dot{\gamma} = 0$ for density ratio of 1 and 1.05. The value was inferred considering the best fit for the lowest Stokes numbers measurements. For the case of $\rho_p/\rho = 1$, the curve fit considers all the points and for $\phi \leq 30\%$, the intercept torque is zero since the data is best fitted by a power law. For the case of $\rho_p/\rho = 1.05$, a linear fit is considered for the first three points. The intercept torque increases with loading fraction for the case with settling particles, indicating a presence of a yield stress for these flows. For the case with density ratio equal to one the intercept torque is equal or close to zero for all the loading fractions tested.

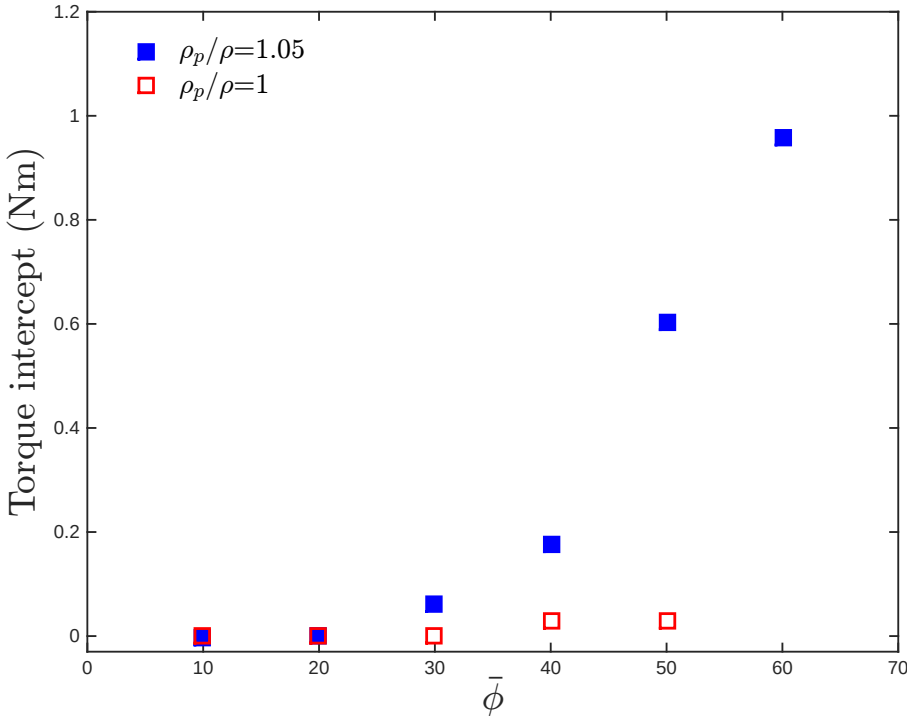

Figure A.1: inferred torque at the origin for $\rho_p/\rho = 1$ and $\rho_p/\rho = 1.05$.

For the experiments with flow over a porous medium, a linear fit for the first three points was considered. Figure A.2 shows the intercept torques for this case. There is more than one intercept torque for each loading fraction and it corresponds to the experiments with increasing and decreasing shear rates. The intercept torques exhibits a linear behavior with respect of the loading fraction, which is different from the behavior observed for the case without porous medium.

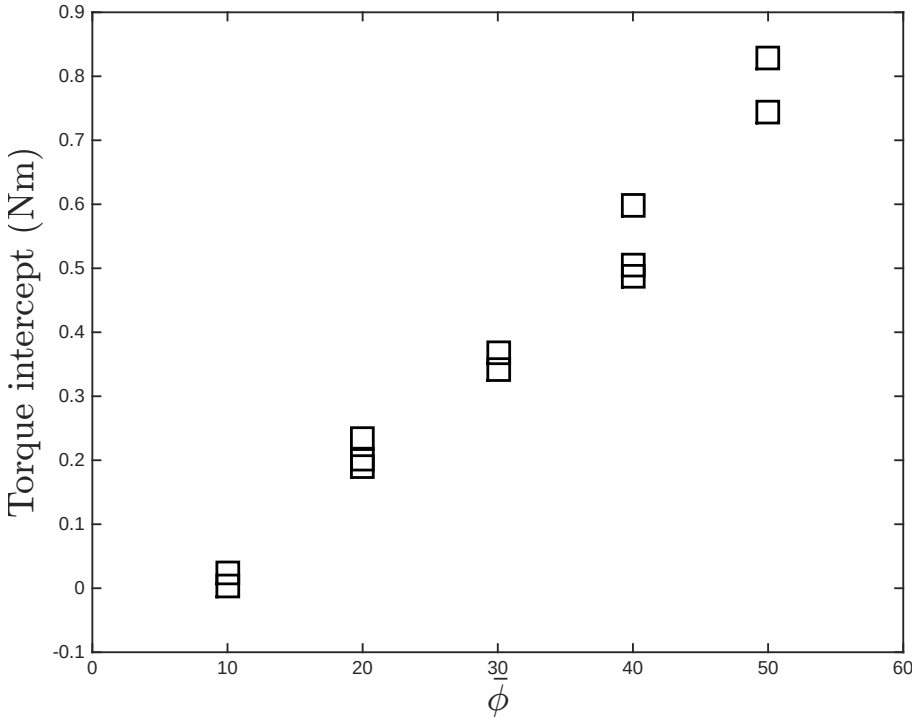

Figure A.2: inferred torque at the origin for flow over porous medium as a function of the loading fraction.$\rho_p/\rho = 1.05$.

Comparison between the intercept torques corresponding to flow with and without porous medium is presented in Figure A.3 as a function of the loading fraction. The intercept torque increases with loading fraction for the cases with settling particles. However, the intercept torque dependance on loading fraction is different for the case with a porous medium. The effective volume fraction for the two cases is significantly different than the loading fraction and these differences lead to differences in the intercept torque, which seems to depend on the particles' column height. For this reason the intercept torques are plotted against the normalized particles' column height in Figure A.4. The intercept torques for the experiments without a porous medium are closer to the intercept torques with a porous medium; however it does not exactly coincide for normalized heights. The reason for this discrepancy might be due to the topology of the particles' top surface. For the case with h_s/h_t between 0.5 and 0.8, the intercept torques show the largest differences. This seems to indicate that the presence of a porous medium increases the yield stress of the flow. The reason for this is not clear.

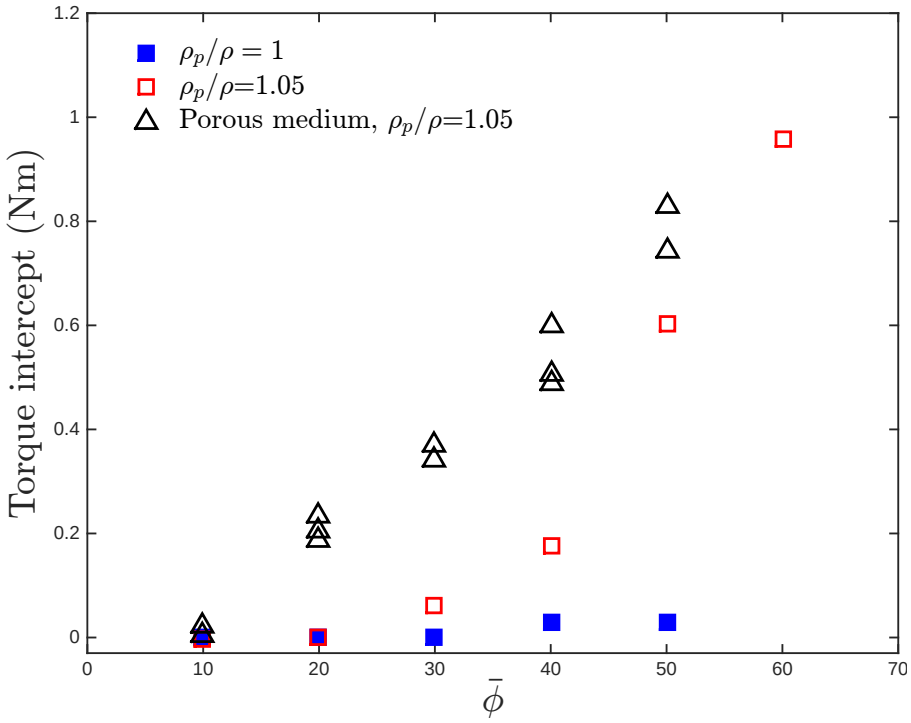

Figure A.3: inferred torque at the origin for flow with and without porous medium and $\rho_p/\rho = 1.05$, and $\rho_p/\rho = 1.05$ as a function of $\bar{\phi}$.

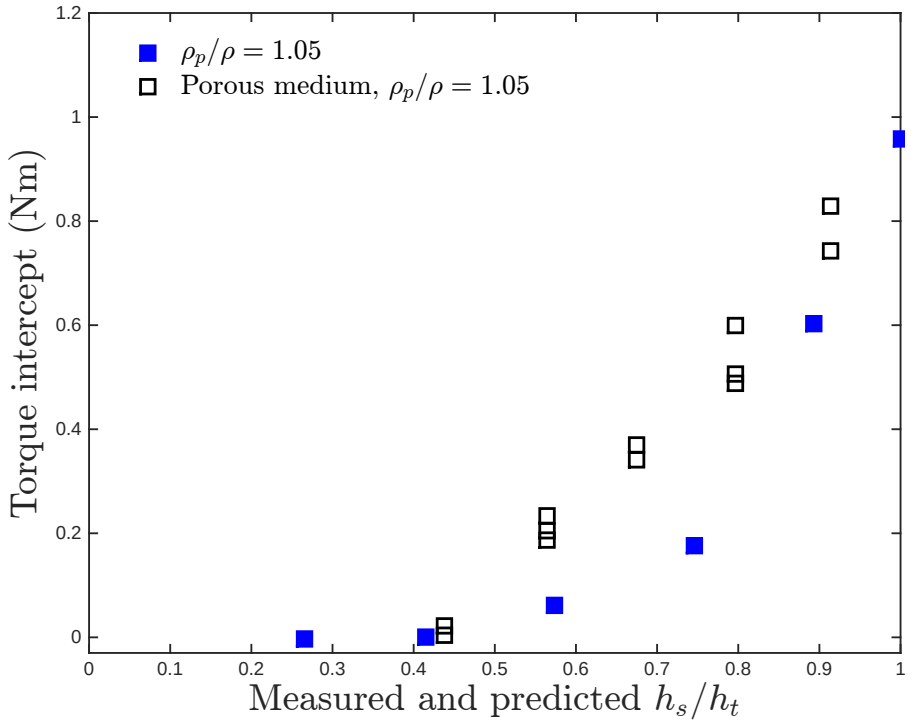

Figure A.4: inferred torque at the origin for flow with and without porous medium as a function of normalized settling height. $\rho_p/\rho = 1.05$.

Appendix B

Particles projected area as a way to infer the effective volume fraction

One of the limitations of measuring the volume fraction with the height reached by the particles is the lack of information about the concentration gradient. For this reason measurements of the particles projected area are made. In this way, differences in concentration along the vertical axes are taken into account. The problem with this method is that it gives no information regarding the volume fraction. One way to infer the volume fraction from the projected area is to use the projected area fraction of a known volume fraction to calibrate the measurements. Considering that the particles are homogeneously distributed for the experiments with a density ratio equal to 1, their projected area can be used to calibrate the measurements for settling particles. The methodology for measuring the projected area is described next.

The images from the visualization of the flow are first filtered by a FFT bandpass filter to correct for differences in lighting, then by an unsharp mask to filter the blur parts of the image. It is considered that only the sharp parts of the picture correspond to the particles next to the test section wall. The weight of the mask is chosen manually, and therefore this is a source of uncertainty. Once the image is processed, sixteen different automatic thresholds are applied. Each method segments the image into black and white and measures the area fraction. Then the method that best segments the image is considered. Note that this is another source of uncertainty since the method is chosen based on a subjective observation. Figure B.1 shows an example of the process of preparing the image and measuring the projected area fraction.

To infer the volume fraction from the projected area fraction, it is necessary to have a known volume fraction as a reference; however the assumption of the particles being homogeneously distributed for density ratios equal to one is not strictly true. The projected area fractions for $\phi = 10$, 20, and 30% and $\rho_p/\rho = 1$ show some dependance on Stokes numbers, where the projected area fraction seems to increase with St. For this reason an image that corresponds to a Stokes number around 40 and density ratio equal to one is selected and used to calibrate the projected area

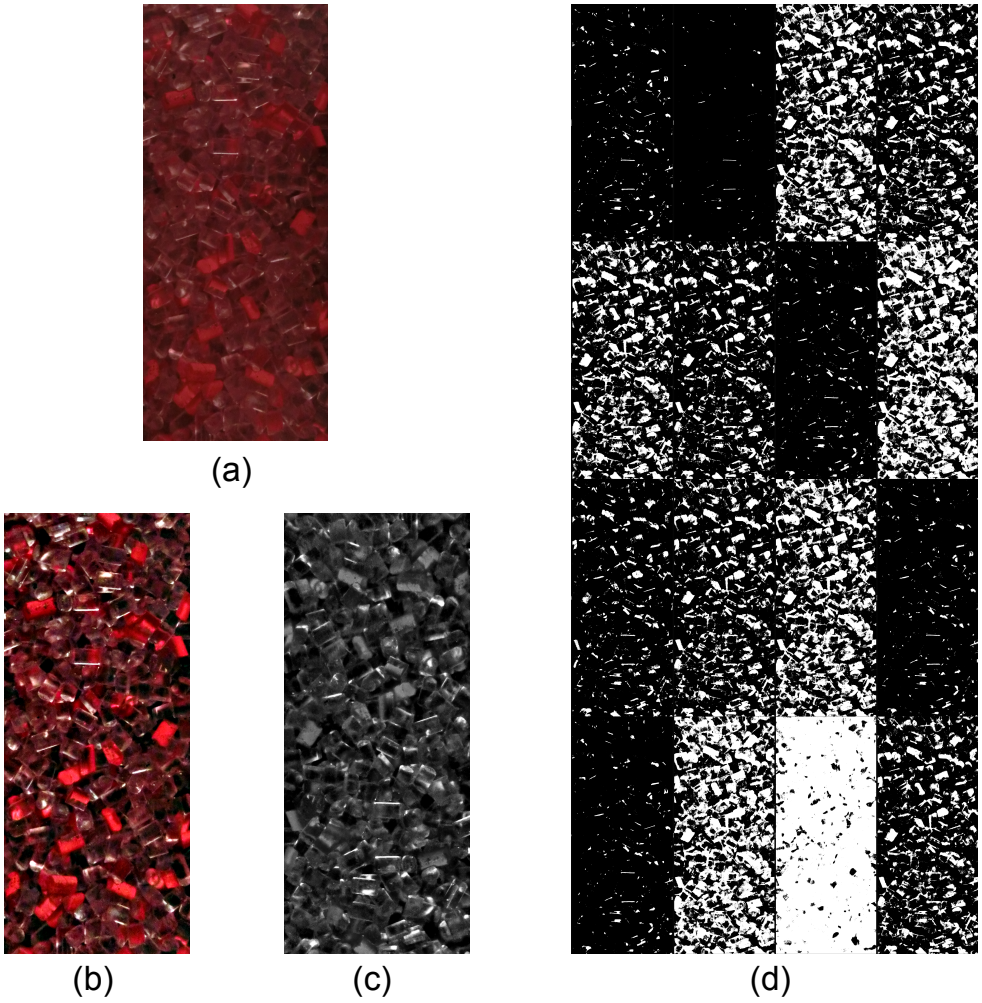

Figure B.1: Image processing example. (a) the image is filtered to correct for uneven lighting with a FFT bandpass filter, (b) the image is filer to correct for blurriness, (c) the image is convert to grayscale, and finally the image is segmented using 16 automatic thresholds methods and the method that best fit the data is chosen.

measurements. The volume fraction is not only inferred for the experiments with settling particles but also for the case with matched density. Figure B.2 shows the effective relative viscosity as a function of inferred volume fraction using the projected area for $\rho_p/\rho = 1$. The threshold method used to segment the images varied between loading fractions because a change in the light source position occurred every time the experiment was loaded with higher volume fractions. For most of the images corresponding to the same loading fraction the same threshold method was used to reduce bias in the results. For $\bar{\phi} = 10\%$, the inferred volume fraction shows the highest variability for $\rho_p/\rho = 1$. Notice that the inferred volume fraction can be higher than the loading fraction for high Stokes numbers; this can occur if there are differences in the particles density where some of the particles would sink while others would float, increasing in this way the particle concentration at the test section. Tests with polystyrene particles immersed in a matched density liquid were performed to study the neutrally buoyant condition. It was found that under no shear, approximately half of the particles would sink while the rest would float, and under slight shear of the flow the particles would distribute in an approximately homogeneous way. For higher loading fractions the change in volume fraction is negligible.

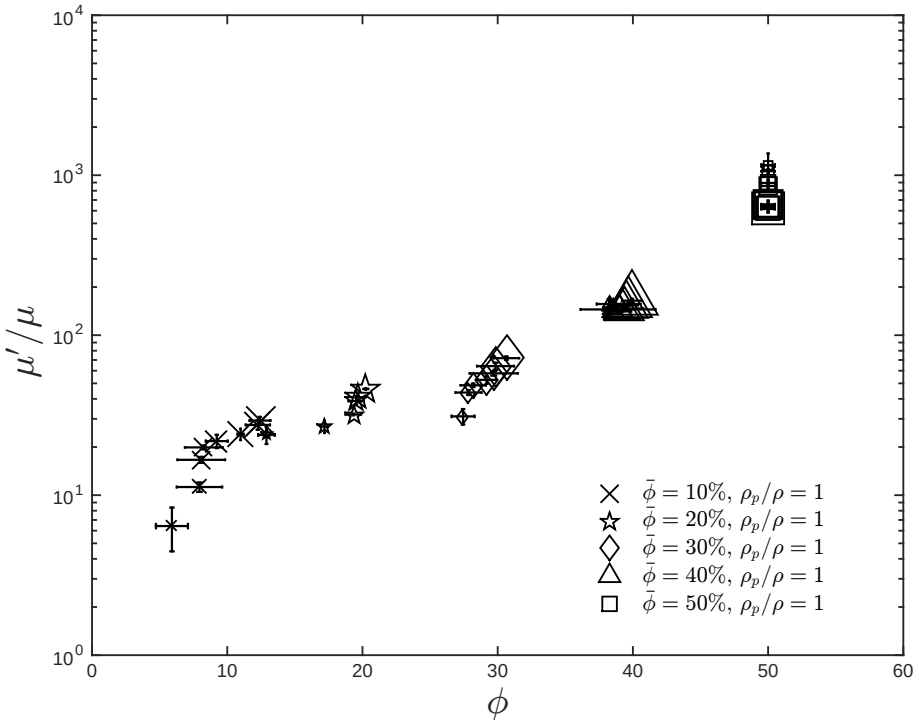

Figure B.2: μ'/μ as a function of the inferred volume fraction from projected area fraction for $\rho_p/\rho = 1$. The size of the symbols correspond to Stokes numbers magnitude.

Figure B.3 shows the inferred volume fraction from projected area fraction for $\rho_p/\rho = 1.05$. The change in volume fraction is larger than for the case with matched density. Similar to what was observed in the volume fraction predicted from the height reached by the particles, the volume

fraction increases with Stokes numbers for loading fractions lower than 30% and decreases with St for loading fractions higher or equal than 30%.

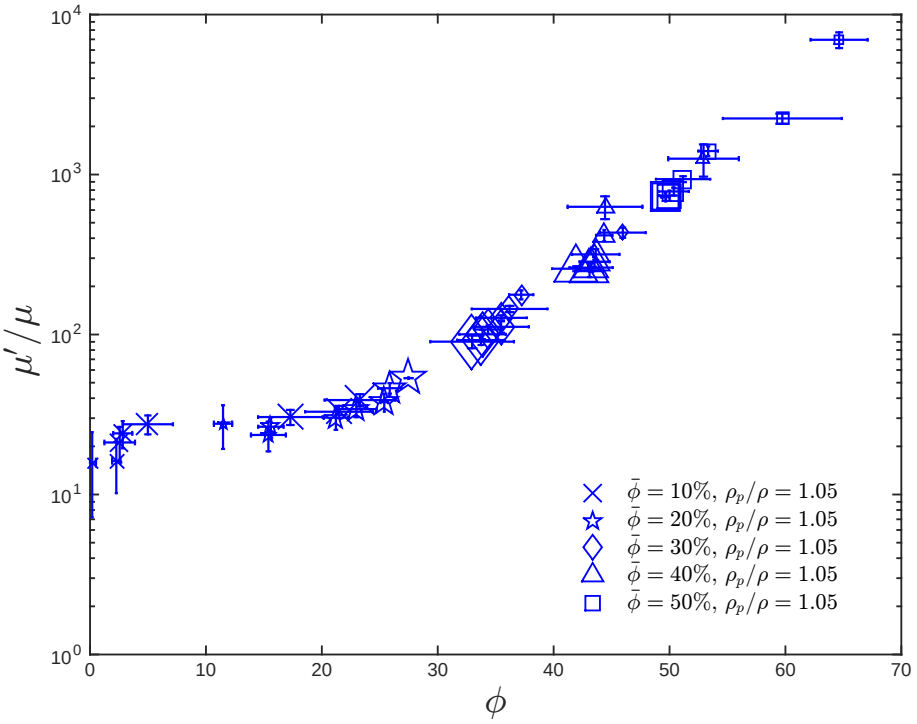

Figure B.3: Effective relative viscosity as a function of the inferred volume fraction from projected area fraction for $\rho_p/\rho = 1.05$. The size of the symbols correspond to Stokes numbers magnitude.

Figure B.4 shows the comparison between the effective relative viscosity for the two density ratios studied as a function of the inferred volume fraction. The effective relative viscosity coincides better for the volume fraction obtain from the projected area fraction than from the particles' height measurements. This might be due to an improve accuracy in the predicted volume fraction by considering a particles concentration gradient.

Figure B.5 shows the effective relative viscosity as a function of the inferred volume fraction. The change in volume fraction is similar to the one observed for the case without porous medium but same density ratio.

Finally, the effective relative viscosity results for the case with and without porous medium and difference density ratios are shown in Figure B.6. Unlike the results found using the particles height, the effective relative viscosity for the flow over porous medium coincides with the cases without porous medium and density ratios of 1.2 and 1.4.

These results suggest that better fits are obtained by using the projected area fraction.

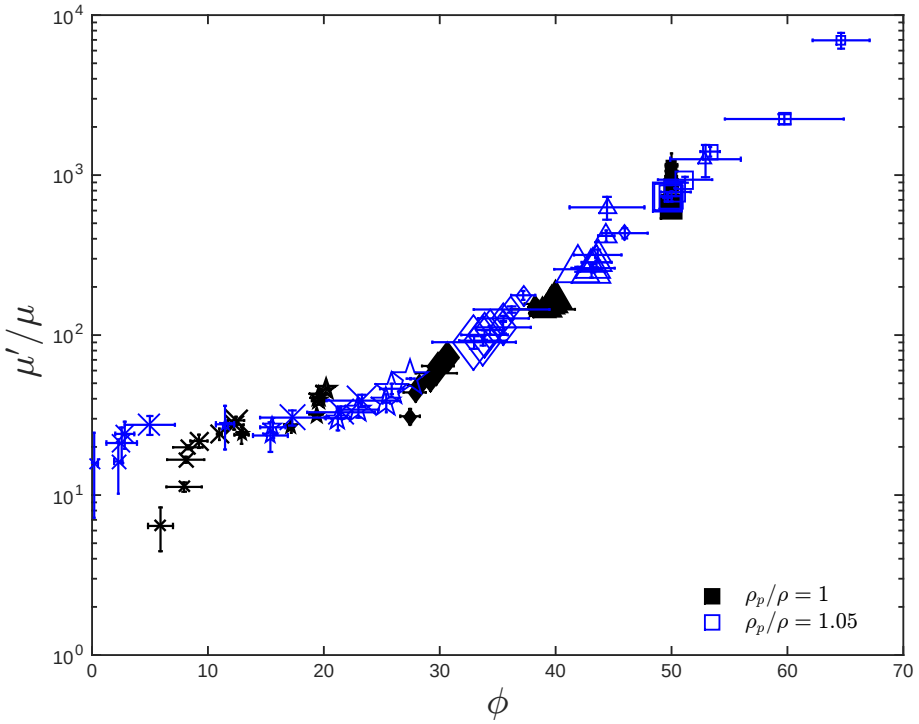

Figure B.4: Comparison between the effective relative viscosity as a function of the inferred volume fraction from projected area fraction for $\rho_p/\rho = 1$ and $\rho_p/\rho = 1.05$. The size of the symbols correspond to Stokes numbers magnitude.

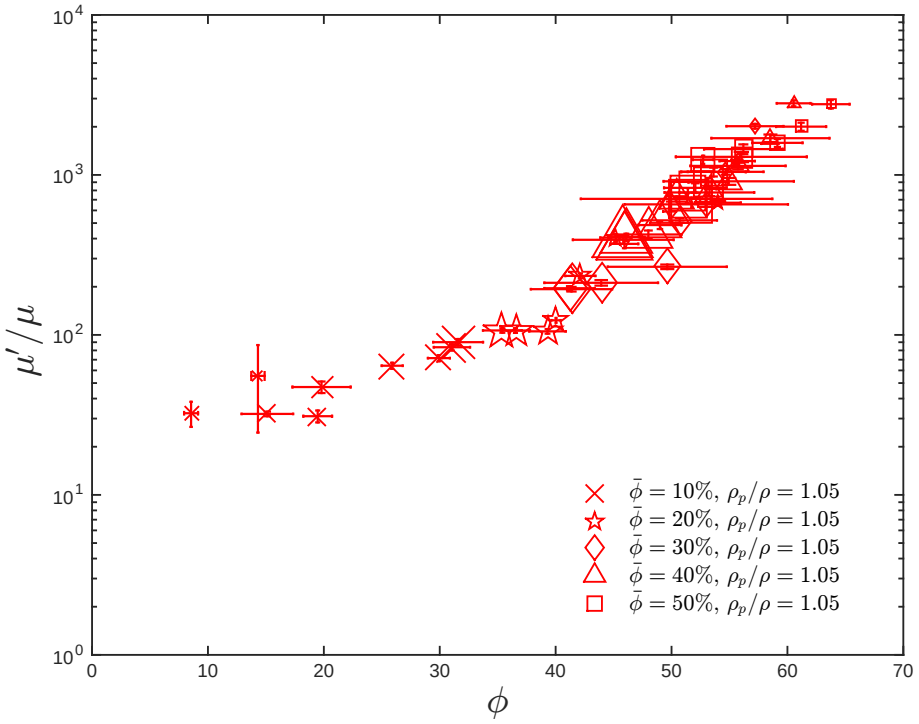

Figure B.5: Effective relative viscosity as a function of the inferred volume fraction from projected area fraction for flow over a porous medium and $\rho_p/\rho = 1.05$. The size of the symbols correspond to Stokes numbers magnitude.

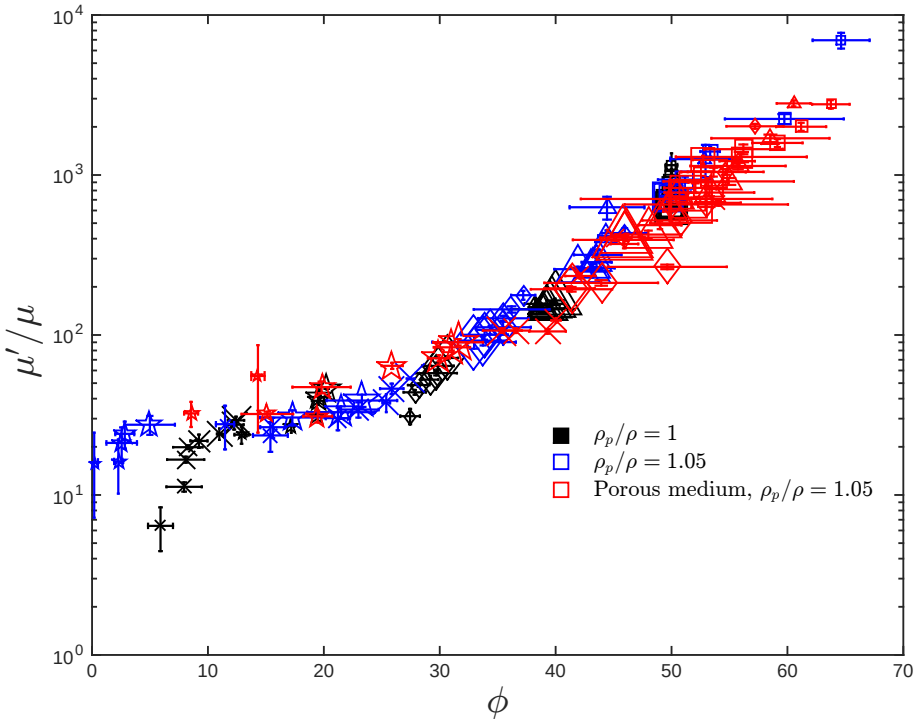

Figure B.6: Comparison between the effective relative viscosity as a function of the inferred volume fraction from projected area fraction for flow with and without a porous medium and $\rho_p/\rho = 1.05$ and $\rho_p/\rho = 1$. The size of the symbols correspond to Stokes numbers magnitude.

Appendix C

Rheological measurements with polyester particles

C.1 Motivation

To study the effect of higher density ratio as well as particles' size and shape effect, torque measurements using polyester particles were made. As described in Section 2.2 polyester particles are 1.33 times denser than the polystyrene particles used in the experiments described in Chapter 4 and 5. If the suspending liquid is water, the density ratio is 1.4. For these experiments the rough walls are the same as the ones used for the experiments with polystyrene (polystyrene particles glued to the walls). A description of experiments with polyester particles and three different suspending liquids is presented in the next section.

C.2 Polyester particles with $\rho_p/\rho = 1.4$

Figure C.1 shows the measured torque for loading fractions of 10 and 20% for polyester particles immersed in water ($\rho_p/\rho = 1.4$). The corresponding measured torques for pure water are also shown in Figure C.1. At low shear rates, the measured torques for the liquid-solid flow coincide with the measured torques for pure liquid. Approximately at $\dot{\gamma} = 60\ s^{-1}$, the measured torques start deviating from the pure liquid ones. Polyester particles are smaller than the polystyrene particles ($d = 2.93$ mm) and have a higher random loose packing ($\phi_{RLP} = 0.593$). When settled, the polyester particles do not reach the test section for loading fractions of 10 and 20%. For this reason the measured torques at low shear rates coincide with the pure fluid measurements. The torques increase in a non-linear way with shear rate.

Figure C.2 presents the measured torques for higher loading fractions of 30, 40 , and 50%. Unlike the results for polystyrene particles (see Figure 4.13), the torques not always increase with shear rate. For the highest loading fractions tested (40 and 50%), the measured torques show a drop for

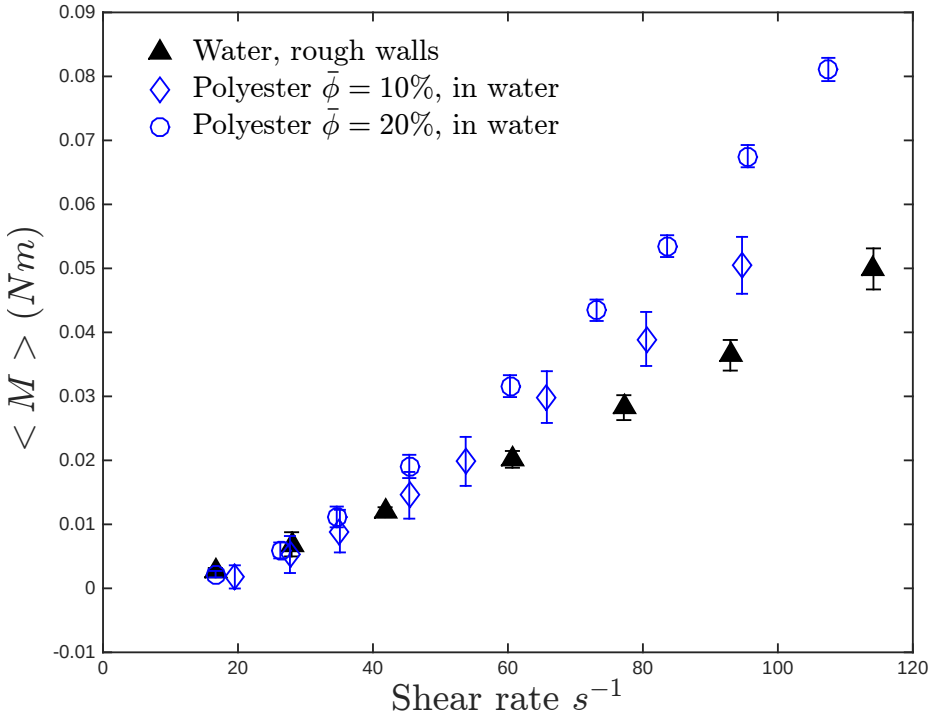

Figure C.1: Measured torques for polyester particles with $\rho_p/\rho = 1.4$ and for pure water. Error bars represents the combined uncertainty of the measurements.

shear rates higher than 30 s^{-1}. For $\bar{\phi} = 50\%$ the torques continue to decrease with shear rates. For $\bar{\phi} = 40\%$ the torques appear to reach a plateau for shear rates higher than 100 s^{-1}. For $\bar{\phi} = 30\%$, the torques show a slight drop at shear rates around 20 s^{-1} and they start increasing at shear rates around 60 s^{-1}. Visualizations of the flow show that these behaviors are a result of centripetal forces. For these higher density ratios, the centripetal forces due to the rotation of the outer cylinder are higher than the forces presented for lower density ratios. Under such forces, the particles are pushed away from the inner cylinder. Results of the visualization of the flow for polyester particles are presented later in Section C.5.

Figure C.3 shows the measured torques normalized with the corresponding laminar torques predicted from laminar theory. For the lowest loading fractions of 10 and 20, only the normalized torques corresponding to the Stokes number where particles reach the test section are shown. The normalized torques show a similar behavior as the case with settling polystyrene particles where $M/M_{laminar}$ increases for loading fractions lower than 30% and decreases for higher loading fractions. For $\bar{\phi} = 30\%$, the ratio of torques increases for Stokes numbers above 60. For $\bar{\phi} = 40\%$, the normalized torques appear to reach a plateau at Stokes numbers above 100. The only difference in behavior is that for $\bar{\phi} = 50\%$, the ratio of torques does not seem to reach a plateau and continues to decrease with the shear rate.

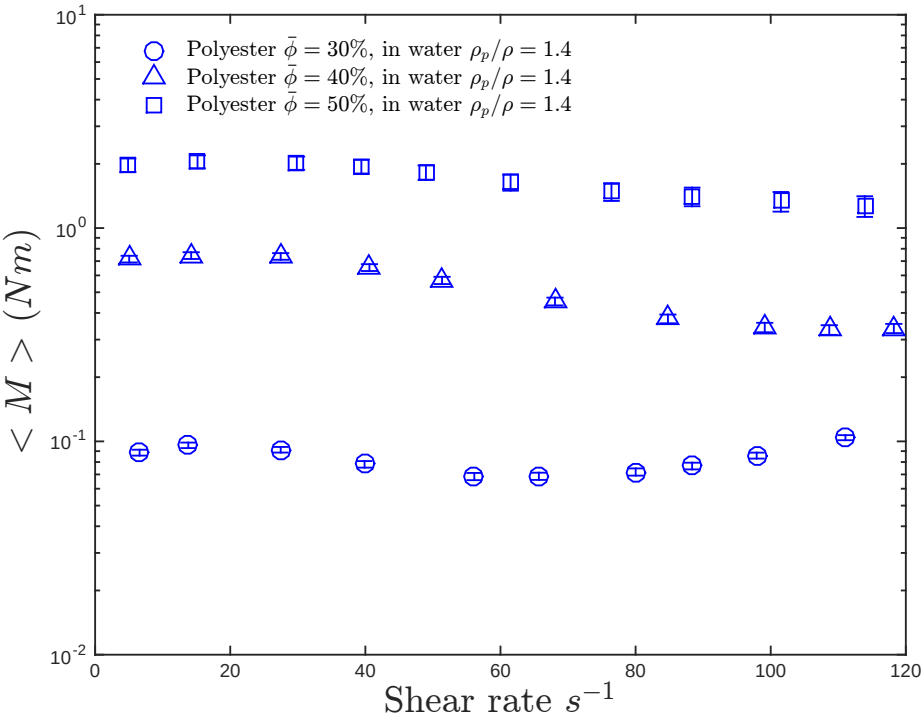

Figure C.2: Measured torques for polyester particles with $\rho_p/\rho = 1.4$ and for pure water. The loading fractions shown are 30, 40, and 50%. Error bars represents the combined uncertainty of the measurements.

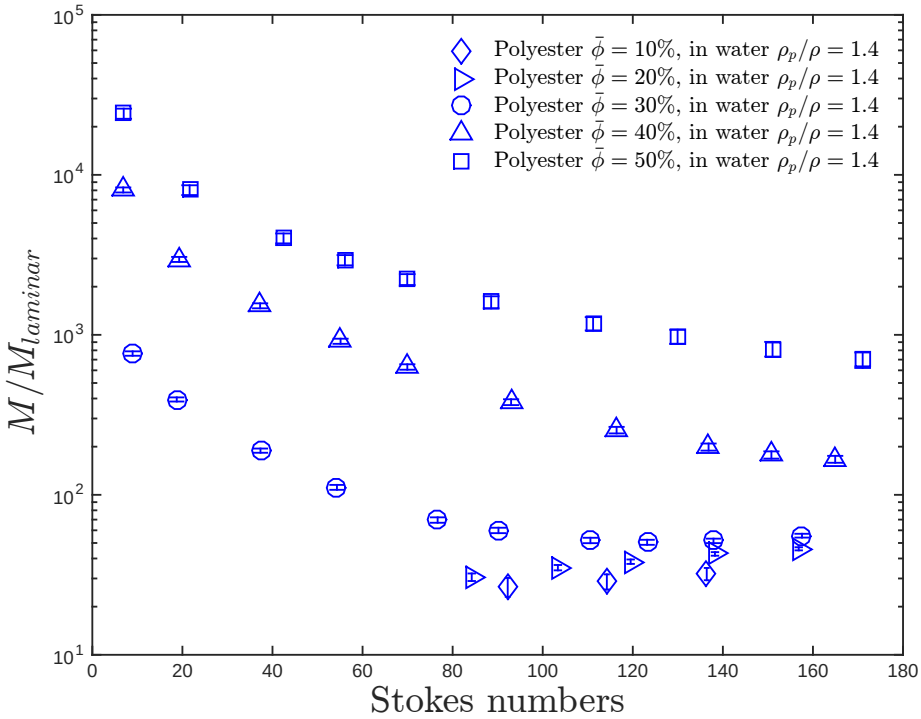

Figure C.3: Normalized torques for polyester particles with $\rho_p/\rho = 1.4$ and $\bar{\phi} = 10, 20, 30, 40$, and 50%. Only the results for the case where the particles reach the test section are shown. Error bars represents the combined uncertainty of the measurements.

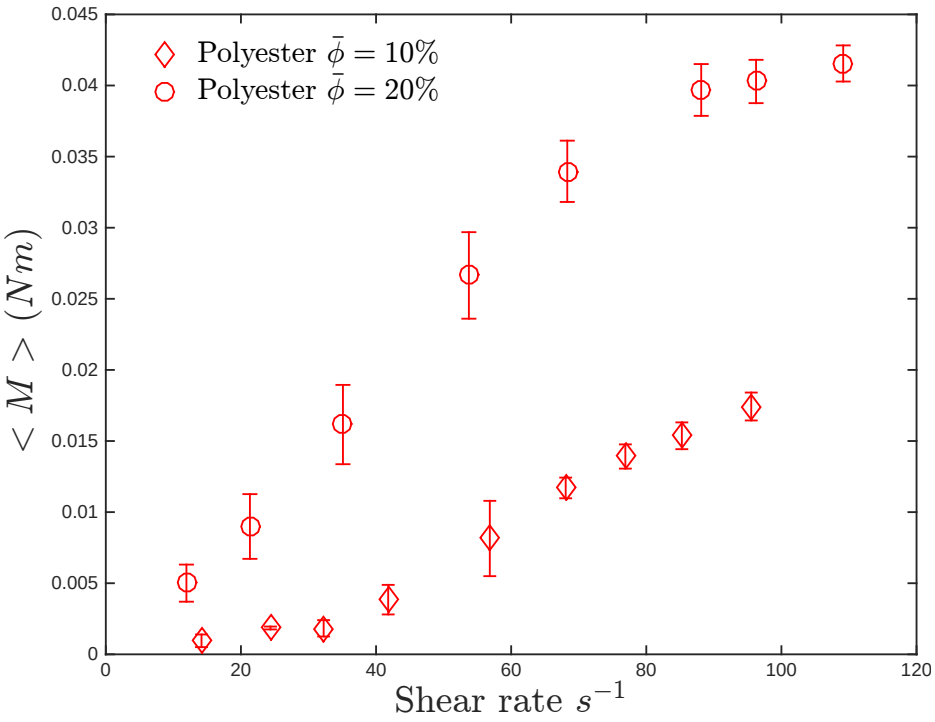

Figure C.4: Measured torques for polyester particles with $\rho_p/\rho = 1.2$ and $\bar{\phi} = 10$ and 20%. Suspending liquid is aqueous glycerine. Error bars represents the combined uncertainty of the measurements.

C.3 Polyester particles with $\rho_p/\rho = 1.2$

Experiments with polyester particles and a density ratio of 1.2 were performed using two different type of suspending liquids: aqueous glycerine and salt water. Both liquids have the same density but differ in viscosity, the former is approximately 7.7 times more viscous than the latter. This allows to study such density ratio at a wider range of Stokes numbers. The salt water density is measured directly with an hydrometer, while the viscosity is inferred from the work of Dessauges et al. (1980); Mao and Duan (2008) and Mao and Duan (2009) and considering a molality of 5.309 mol/Kg.

Figures C.4 and C.5 show the measured torques for loading fractions of 10 and 20% with aqueous glycerine and salt water as the suspending liquid, respectively. Visualization of the flows indicates that for the case with aqueous glycerine as the suspending liquid, the particles never reach the test section for $\bar{\phi} = 10\%$ and for $\bar{\phi} = 20\%$ the particles seem to reach the test section for shear rates higher than 50 s^{-1}.

For the case with salt water, the particles reach the test section at shear rates higher than 80 s^{-1} for $\bar{\phi} = 10\%$ and 35 s^{-1} for $\bar{\phi} = 20\%$. The measured torques don't increase linearly with the shear rate.

Figure C.6 show the measured torques as a function of shear rate for higher loading fractions of 30, 40, and 50%, and aqueous glycerine as the suspending liquid. The torques show a drop for shear

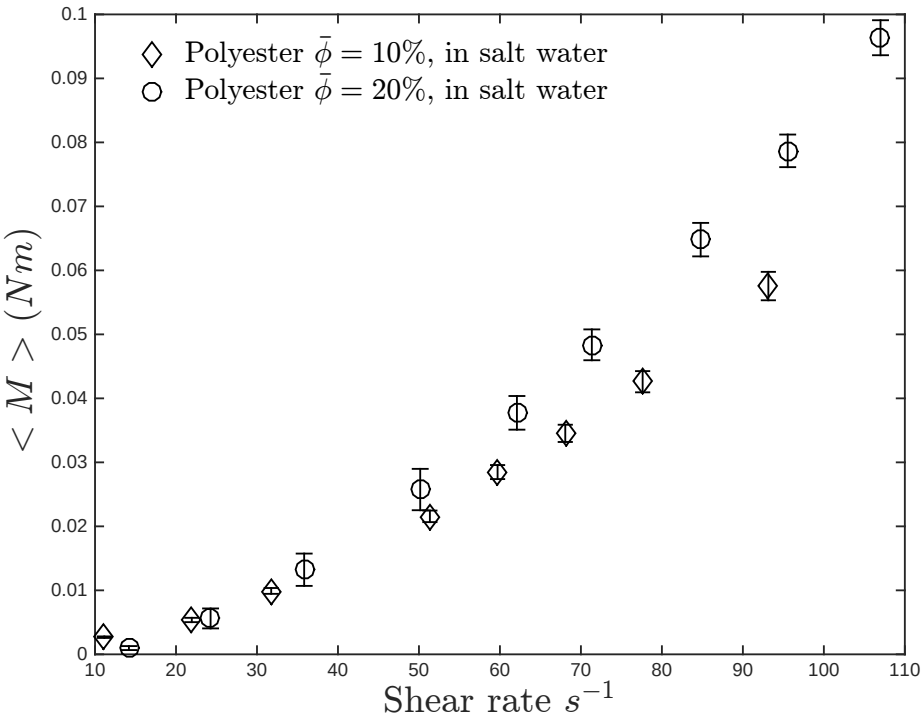

Figure C.5: Measured torques for polyester particles with $\rho_p/\rho = 1.2$ and $\bar{\phi} = 10$ and 20%. Suspending liquid is salt water. Error bars represents the combined uncertainty of the measurements.

rates higher than 40 s^{-1}. For loading fractions of 40 the torques reach a plateau for shear rates higher than 80 s^{-1}, and for the case with $\bar{\phi} = 30\%$ the torques start increasing again for shear rates higher than 80 s^{-1}, mean while for 50% the torques only continue to decrease with the shear rate.

Figure C.7 show the measured torques as a function of shear rate for higher loading fractions of 30, 40, and 50%, and salt water as the suspending liquid. Similarly to the measured torques using aqueous glycerine as the suspending liquid, the torques using salt water show a drop for shear rates higher than 40 s^{-1}. For $\bar{\phi} = 50\%$ the torques continue to decrease, while for $\bar{\phi} = 40$ and 30% the torques start increasing again for shear rates higher than 80 s^{-1}

Figure C.8 shows the normalized torques for all the loading fractions tested with the exception of $\bar{\phi} = 10\%$ because for such low loading fractions, visualization of the flow shows no presence of particles in the test section. For loading fraction of 20% the normalized torques decrease with Stokes number rather than increase. For the rest of the loading fractions the ratio of torques behave in the same way as for the case with $\rho_p/\rho = 1.4$ and water as the suspending liquid.

Figure C.9 presents the normalized torques for polyester particles immersed in salt water with a density ratio of 1.2 for all the loading fractions tested. Only the cases where the particles reach the test section are shown. Unlike the case with same density ratio but with aqueous glycerine as the suspending liquid, the ratio of torques for $\bar{\phi} < 30\%$ increases with shear rate. For the rest loading fractions (30, 40, and 50%) the normalized torques exhibit the same behavior as for the case

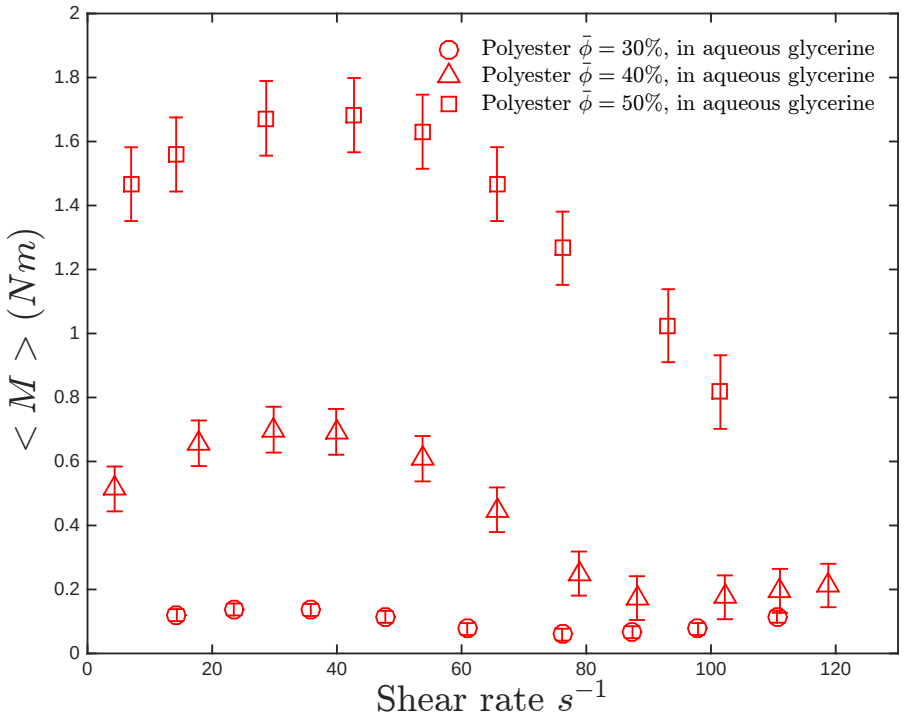

Figure C.6: Measured torques for polyester particles with $\rho_p/\rho = 1.2$ and $\bar{\phi} = 30$, 40, and 50%. Suspending liquid is aqueous glycerine. Error bars represents the combined uncertainty of the measurements.

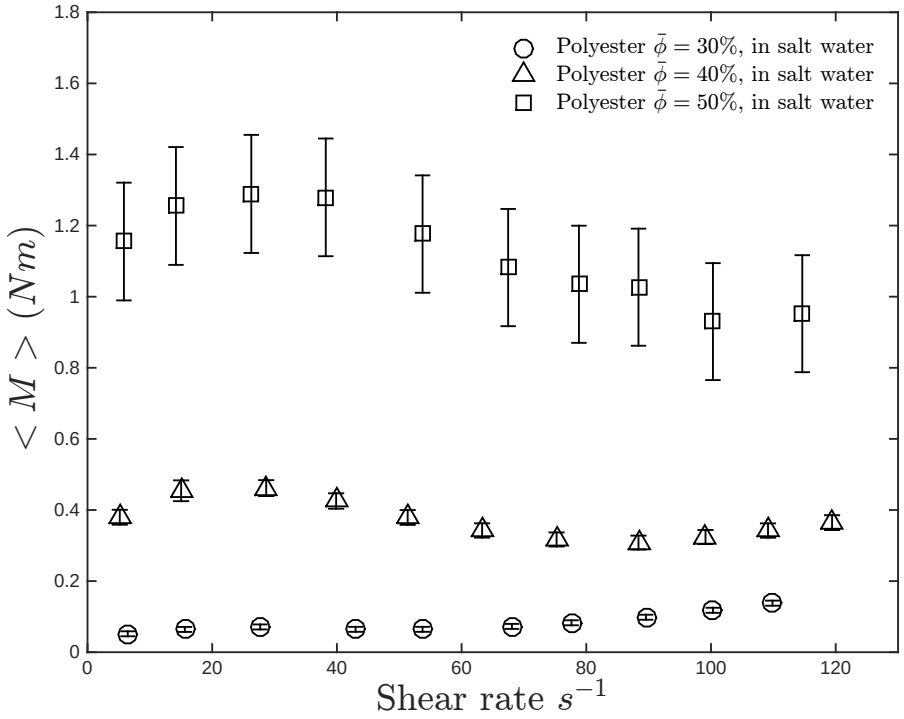

Figure C.7: Measured torques for polyester particles with $\rho_p/\rho = 1.2$ and $\bar{\phi} = 30$, 40, and 50%. Suspending liquid is salt water. Error bars represents the combined uncertainty of the measurements.

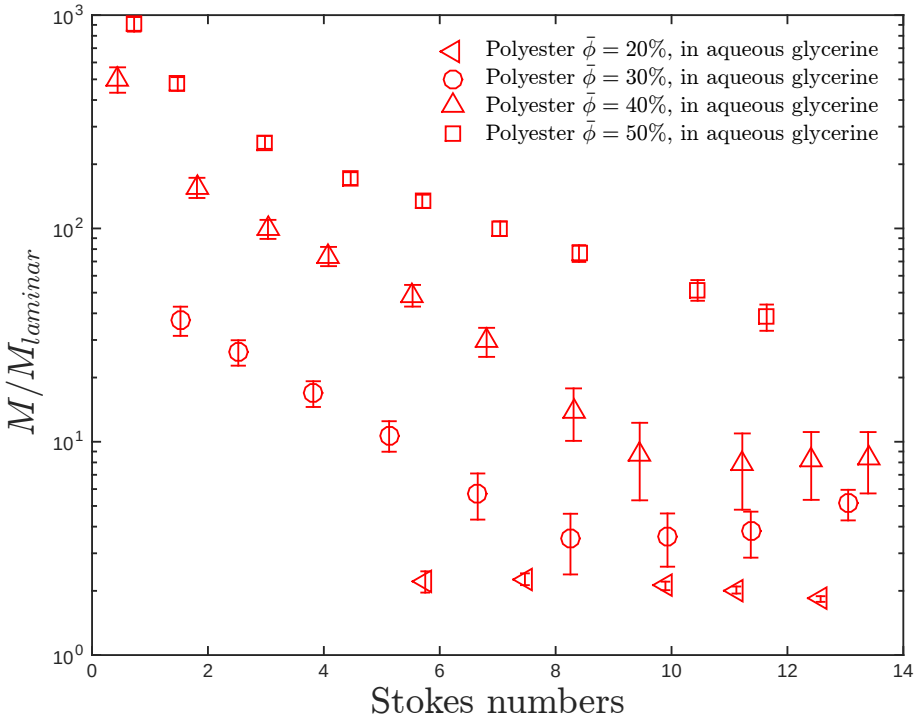

Figure C.8: Normalized torques for polyester particles with $\rho_p/\rho = 1.2$ and $\bar{\phi} = 20, 30, 40$, and 50%. The suspending liquid is aqueous glycerine. Only the results for the case where the particles reach the test section are shown. Error bars represents the combined uncertainty of the measurements.

with same density ratio but aqueous glycerine as the suspending liquid, and as for the case with $\rho_p/\rho = 1.4$ and water as the suspending liquid.

C.4 Direct comparison between same particles but different density ratios

Figure C.10 presents the normalized torques for $\bar{\phi} = 10$ and 20%, and for $\rho_p/\rho = 1.2$, and $\rho_p/\rho = 1.4$. The normalized torques for the case with aqueous glycerine as the suspending liquid is one order of magnitude lower than for the case with salt water as the suspending liquid, even though the density ratios are the same. The reason for this big difference is due to the presence of hydrodynamic effects. Figure C.11 shows the measured torques normalized by the corresponding laminar torques as a function of the modified gap Reynolds number which is defined in Section 2.4 for pure fluid and for loading fractions of 10% and 20% with water, salt water, and aqueous glycerine. For these low loading fractions, the visualizations show no presence of particles at the test section for the case with aqueous glycerine as the suspending liquid and $\bar{\phi} = 10\%$, and no presence of particles for water and salt water for shear rates lower than 65 and 85 s^{-1} and $\bar{\phi} = 20\%$, respectively. Therefore, the measured torques for these cases correspond to just the liquid. Deviation from the laminar

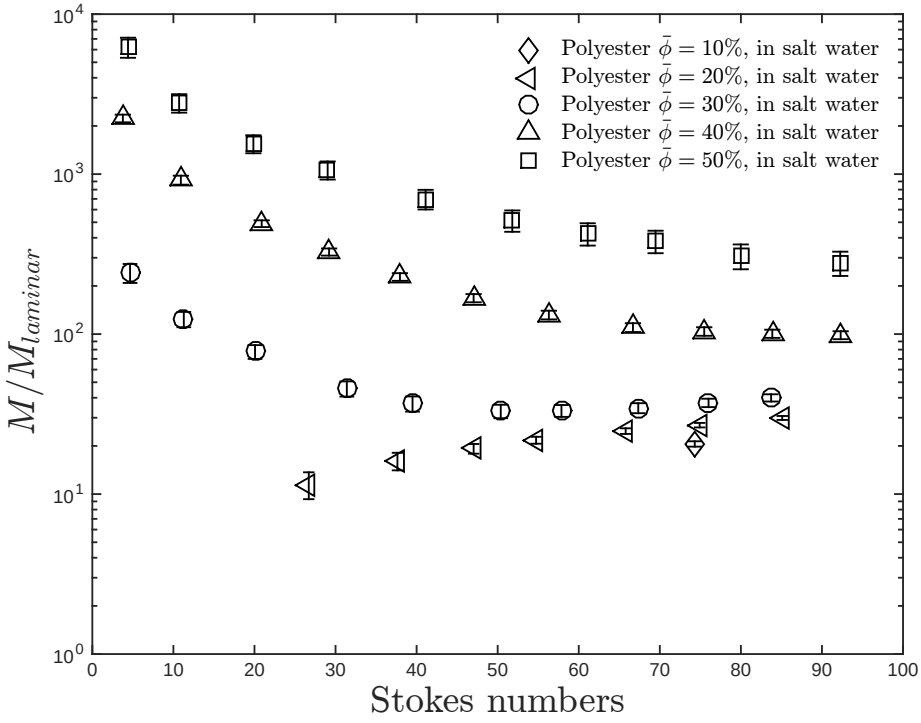

Figure C.9: Normalized torques for polyester particles with $\rho_p/\rho = 1.2$ and $\bar{\phi} = 20, 30, 40$, and 50%. The suspending liquid is salt water. Only the results for the case where the particles reach the test section are shown. Error bars represents the combined uncertainty of the measurements.

behavior is observed for the case with water and salt water, meanwhile for aqueous glycerine the normalized torques are closer to the laminar behavior; however the normalized torques for lower modified gap Reynolds numbers exhibit larger scatter. This is due to an increase in the uncertainty in the measurements of such low torques but as the torques increase with shear rate, the scatter decreases and a clear laminar behavior is observed. Figure C.12 shows the normalized torques as a function of Re_b^* for the present and previous pure fluid measurements from Koos (2009). Notice how the scatter observed for the torque measurements of $\bar{\phi} = 10$ and 20% in aqueous glycerine lies within the scatter observed in the previous measurements of Koos (2009). Therefore the experiments with water and salt water are likely to be affected by the presence of hydrodynamic instabilities.

Figure C.13 shows the normalized torques for loading fraction of 30% for $\rho_p/\rho = 1.4$ and $\rho_p/\rho = 1.2$. For the latter case, results using aqueous glycerine and salt water are shown. The behavior is the same for the three cases shown but the magnitudes do not coincide. For the experiments with $\rho_p/\rho = 1.2$ and aqueous glycerine as the suspending liquid, the ratio of torques is lower than for the case with the same density but higher Stokes number (salt water as the suspending liquid). Aside from the possible presence of hydrodynamics effects for the cases with higher Stokes numbers, the reason for these differences also include the effects of centripetal forces. Visualizations of the flow show that for the experiments with aqueous glycerine and water as the suspending liquid,

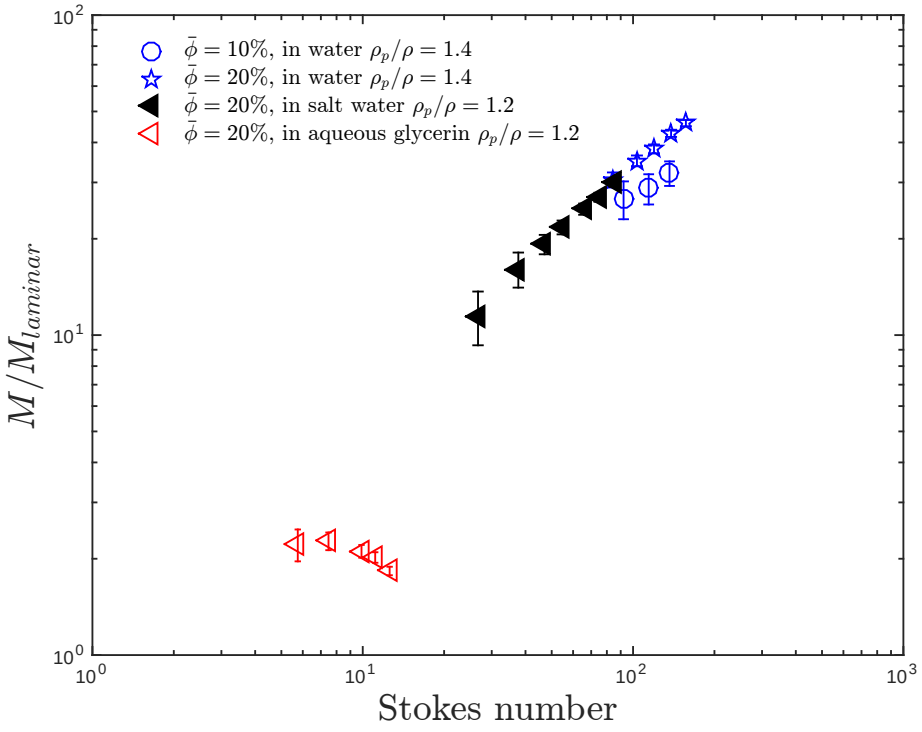

Figure C.10: Comparison between the $M/M_{laminar}$ for $\rho_p/\rho = 1.4$ and $\rho_p/\rho = 1.2$ and $\bar{\phi} = 10$ and 20%. Only the cases with particles present in the test section are shown.

the polyester particles move away from the inner wall. For the experiments with salt water, some particles stay close to the inner wall. This would lead to higher normalized torques but as seen in Figure C.13, the ratio of torques for the case with salt water is lower than the normalized torques for the case with water, where no particles are touching the inner cylinder for high Stokes numbers. The reason for this discrepancy is not clear, one possible explanation is that the hydrodynamic inertial effects present for the case with water as the suspending liquid are more pronounced than in the case with salt water. Further details on the flow visualizations is presented in the next section.

Figure C.14 shows the normalized torques for loading fraction of 40% and density ratios of 1.2 and 1.4. Similar to the case of $\bar{\phi} = 30\%$, the behavior for the three cases is the same and the ratio of torques only differ in magnitude, where the case with aqueous glycerine shows lower normalized torques than the experiments with water and salt water. The same behavior is found for $\bar{\phi} = 50\%$, as shown in Figure C.15.

C.5 Flow visualization for polyester particles

Visualization of the flow using water, salt water, and aqueous glycerine as the suspending liquid and polyester particles are presented in this section. The density ratio for the case with water is 1.4, and for aqueous glycerine and salt water the density ratio is 1.2.

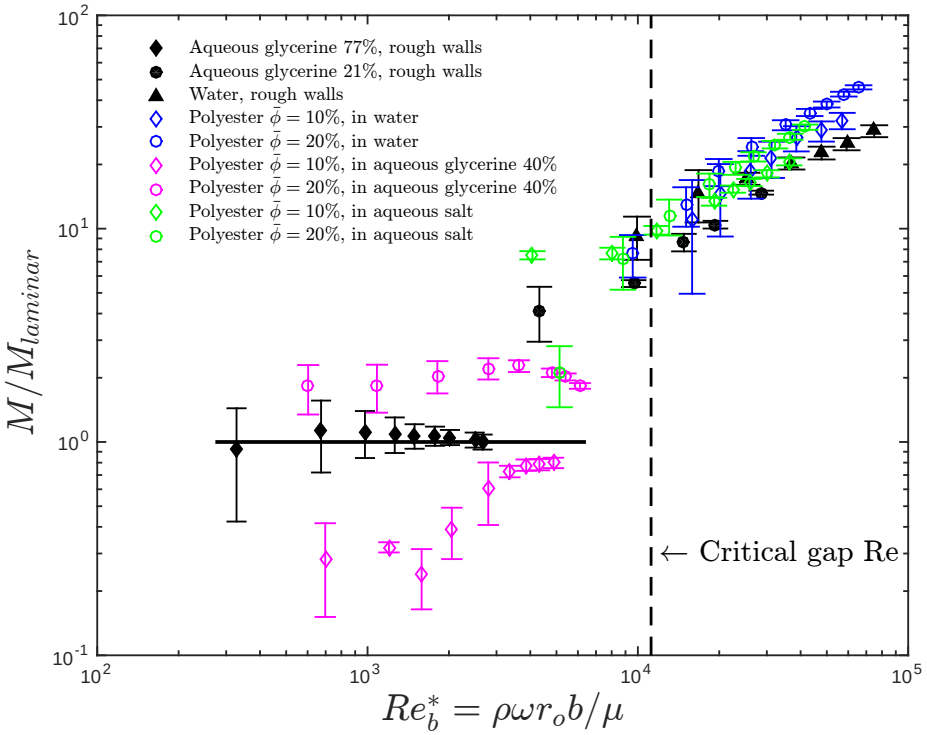

Figure C.11: Normalized torques for pure fluid and for low loading fractions of 10 and 20% where particles are not present in the test section. Vertical dashed line corresponds to the critical modified gap Reynolds number based on the work of Taylor (1936a) and considers the gap width for rough walls.

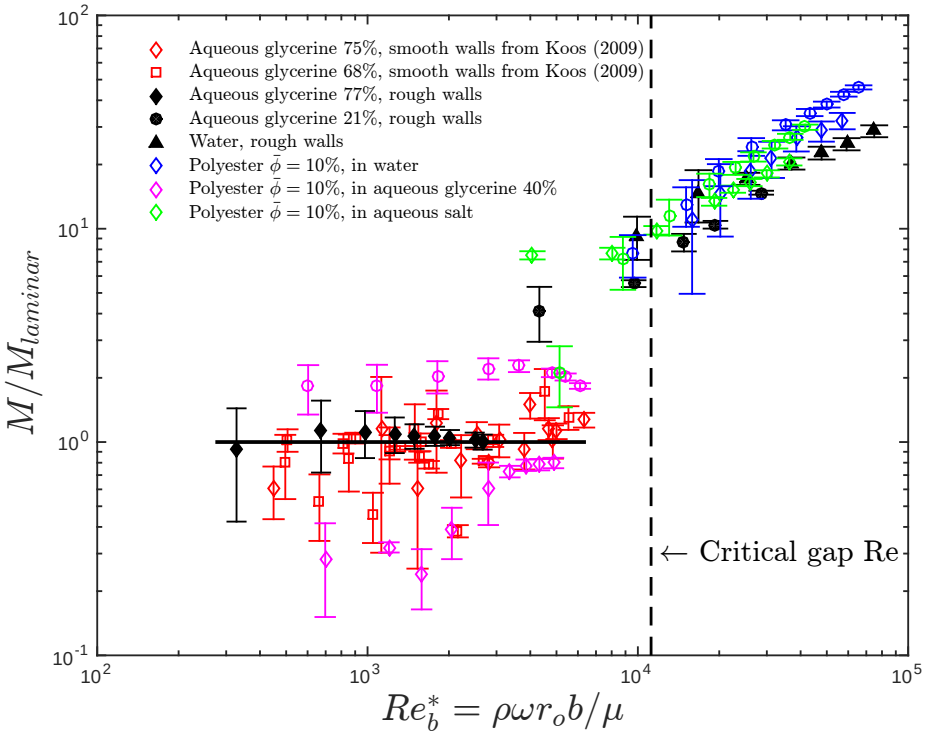

Figure C.12: Previous and present normalized torques for pure fluid and for low loading fractions of 10 and 20% where particles are not present in the test section. The previous torque measurements were done by Koos (2009) and used smooth walls. Vertical dashed line corresponds to the critical modified gap Reynolds number based on the work of Taylor (1936a) and considers the gap width for rough walls.

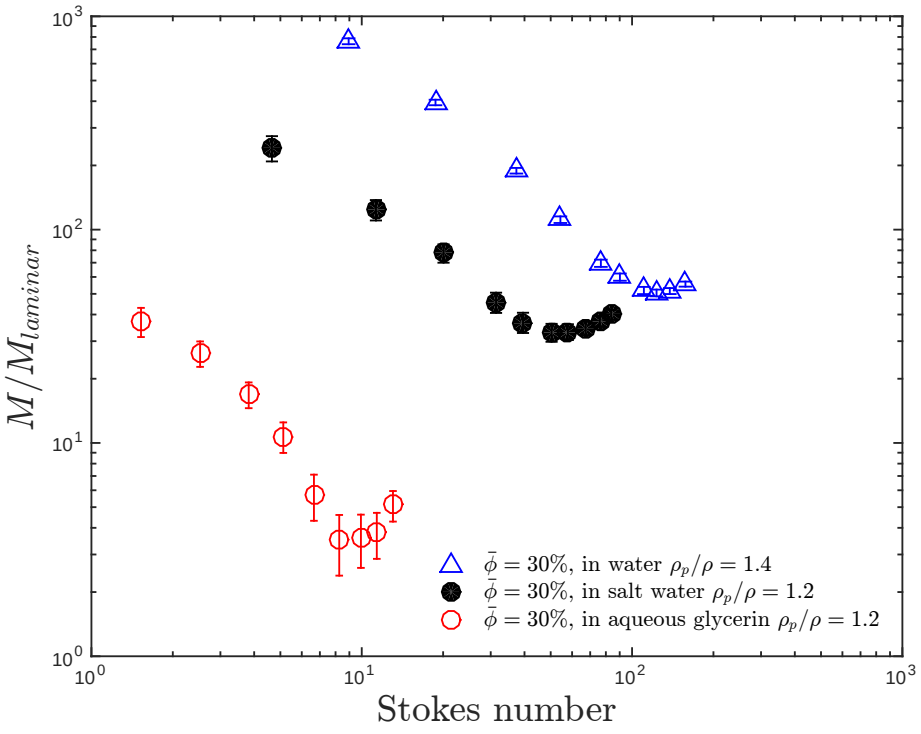

Figure C.13: Normalized torques for polyester particles and $\rho_p/\rho = 1.4$ and, $\rho_p/\rho = 1.2$ as a function of Stokes numbers for $\bar{\phi} = 30\%$. The suspending liquids are water, salt water, and aqueous glycerine.

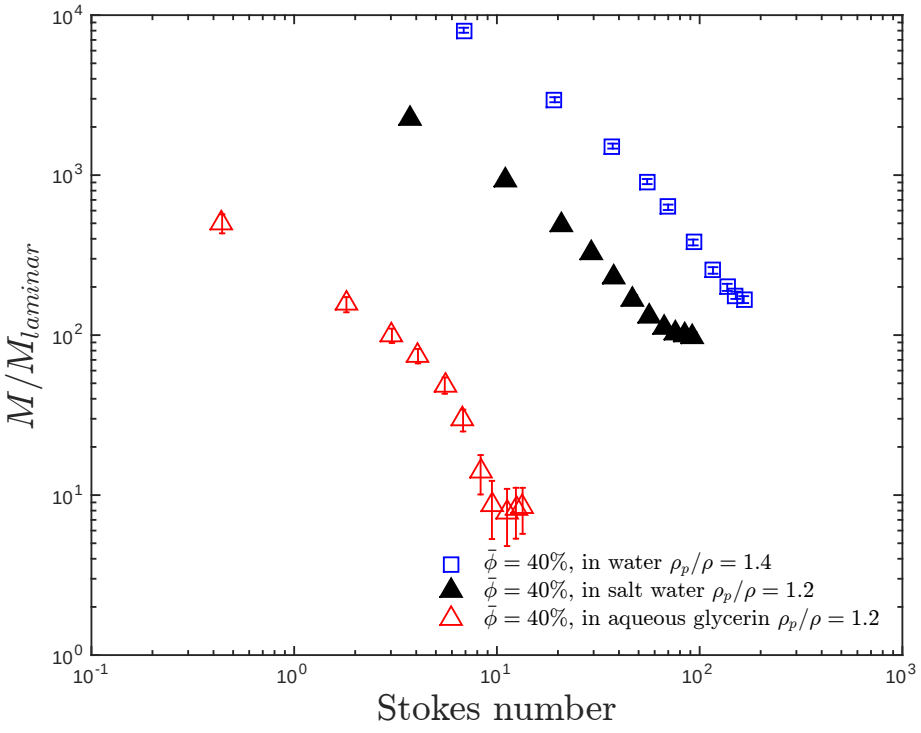

Figure C.14: Normalized torques for polyester particles and $\rho_p/\rho = 1.4$ and, $\rho_p/\rho = 1.2$ as a function of Stokes numbers for $\bar{\phi} = 40\%$. The suspending liquids are water, salt water, and aqueous glycerine.

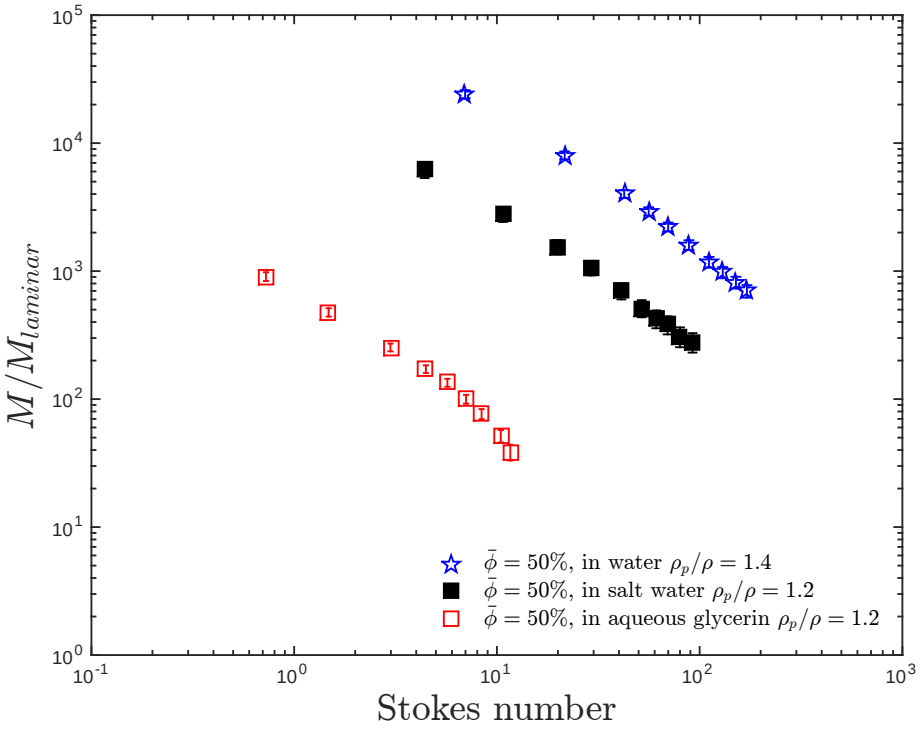

Figure C.15: Normalized torques for polyester particles and $\rho_p/\rho = 1.4$ and, $\rho_p/\rho = 1.2$ as a function of Stokes numbers for $\bar{\phi} = 50\%$. The suspending liquids are water, salt water, and aqueous glycerine.

Visualizations for $\rho_p/\rho = 1.4$

Figure C.16 shows the image sequence corresponding to a loading fraction of 10%, and for a density ratio of 1.4 at different Stokes numbers. The particles reach the test section height above certain Stokes numbers, but unlike the visualizations for polystyrene particles ($\rho_p/\rho = 1.05$) the polyester particles exhibit a radial migration and move towards the outer cylinder. The particles observed in Figure C.16 are not next to the inner cylinder but next to the outer one. Movies at different Stokes number show that the particles are touching the outer cylinder and as Stokes numbers increase, the polyester particles climb the outer wall and exhibit little interaction between each other. Therefore, the torque measurements for these loading fractions correspond to pure fluid measurements with a narrower annular gap in which the width decreases as more particles climb the outer wall.

For a loading fraction of 30%, the polyester particles are next to the inner wall at low Stokes numbers, and move away from the inner wall as Stokes increases. At the highest Stokes numbers there are no particles touching the test cylinder, and all the particles are pushed against the outer wall.

Similar results are found for volume fraction of 40 and 50%, as shown in Figures C.18 and C.19. At the highest Stokes numbers some of the polyester particles are touching the lower part of the test cylinder for $\bar{\phi} = 40\%$, and for $\bar{\phi} = 50\%$ the polyester particles are touching the test cylinder

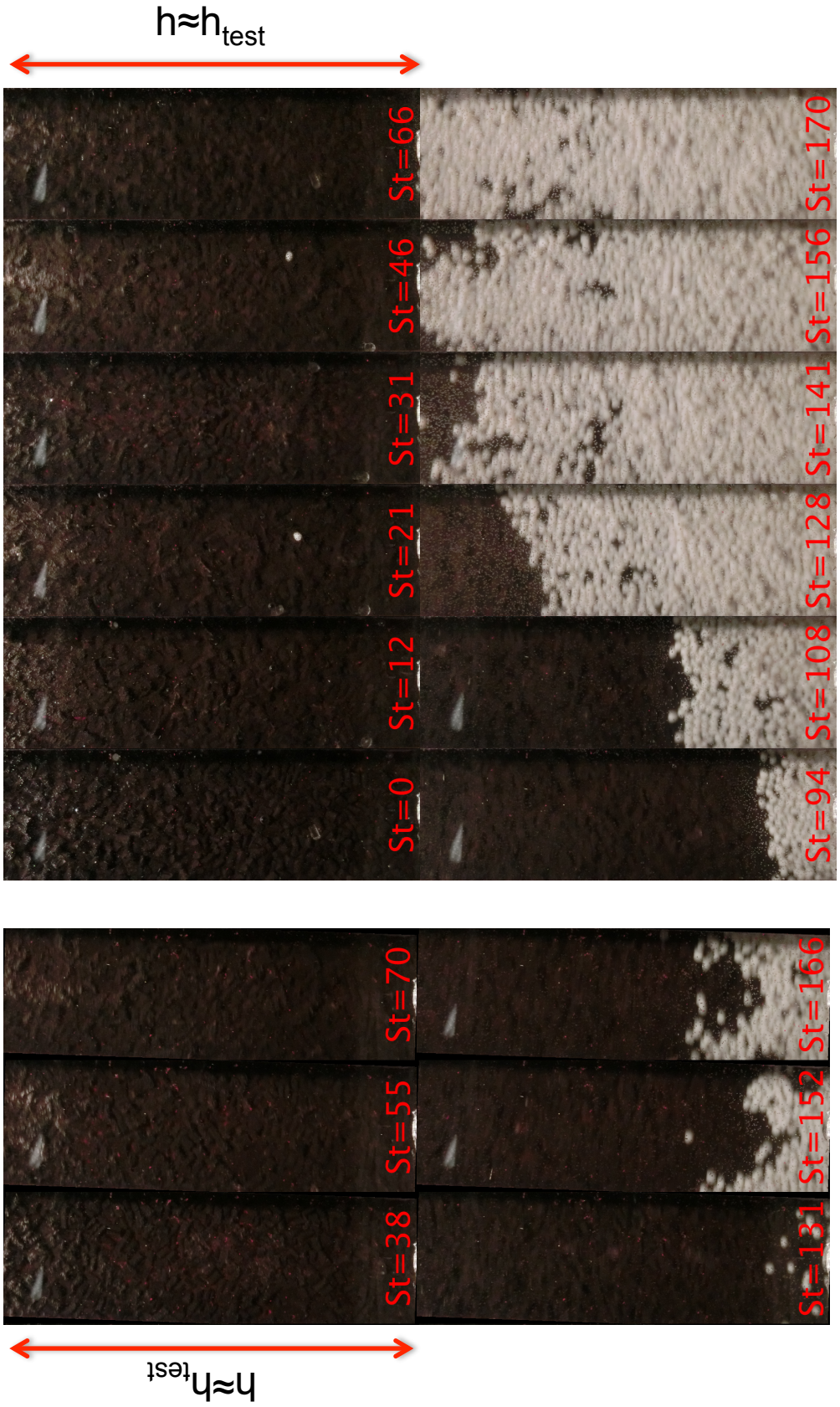

Figure C.16: Image sequence at different Stokes numbers for: (a) $\bar{\phi} = 10\%$ and (b) $\bar{\phi} = 20\%$. The density ratio for (a) and (b) is 1.4.

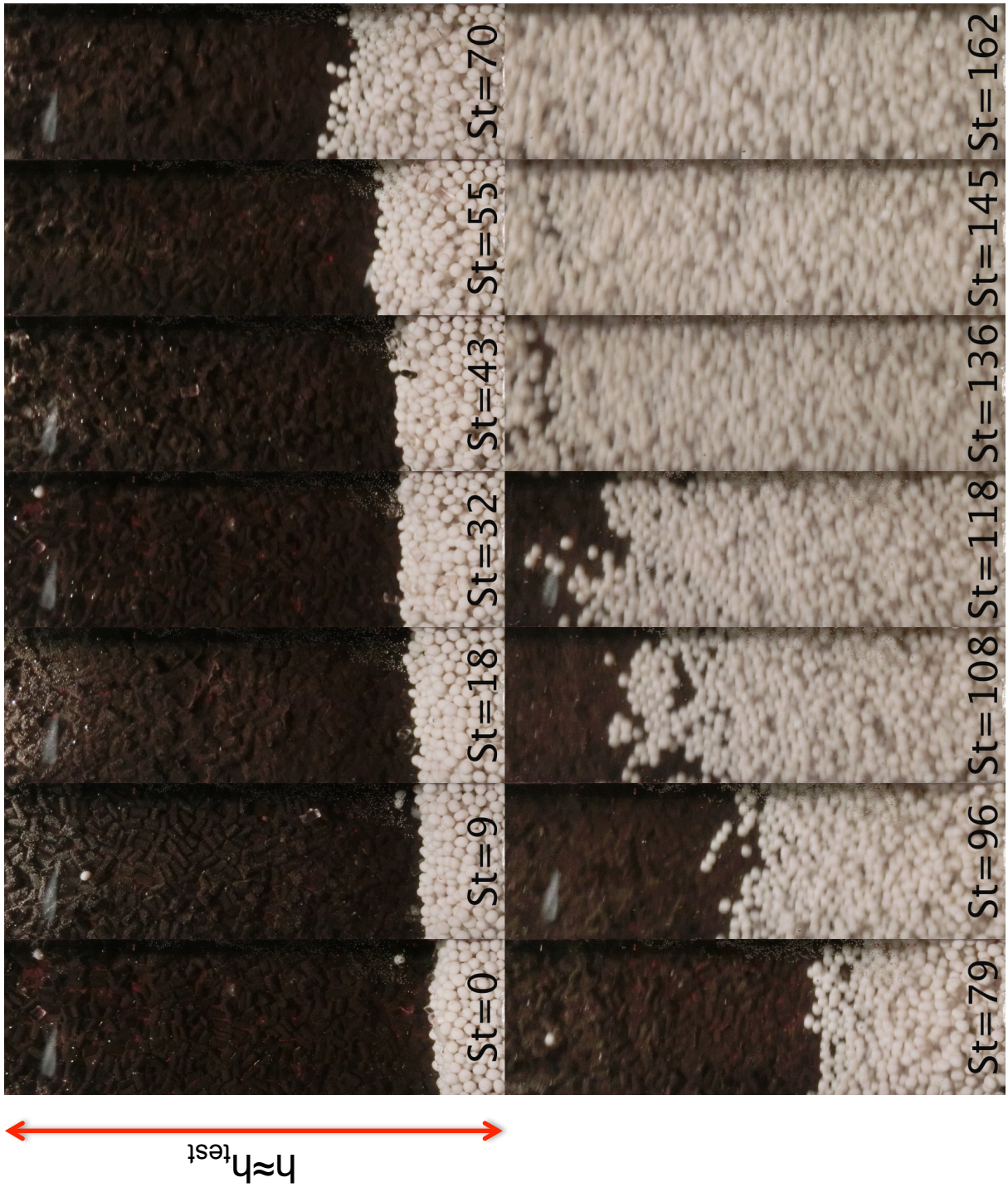

Figure C.17: Image sequence at different Stokes numbers for $\bar{\phi} = 30\%$. The density ratio is 1.4.

but their packing seem to have diminished.

Visualizations for $\rho_p/\rho = 1.2$

Figure C.20 shows the flow visualization for $\bar{\phi} = 10\%$, and a density ratio of 1.2 but different suspending liquids. The aqueous glycerine is 7.7 times more viscous than the salt water, leading to lower Stokes numbers. Only the images corresponding to the highest Stokes numbers tested for this loading fraction is shown. For the case with aqueous glycerine the particles never reach the test section, and for the case with salt water some particles climb the outer wall but do not touch the inner test section. The images for this visualization are blurry due to the opacity of the interstitial liquid, and the particles distance from the inner wall.

Figure C.21 shows the flow visualization for $\bar{\phi} = 20\%$ and a density ratio of 1.2 with different suspending liquids. For both cases the particles never touch the test section. When the suspending liquid is salt water, the presence of particles on the outer wall are indicated by the blurry white background on the pictures. When the polyester particles are touching the test section their image is sharp.

Figure C.22 shows the flow visualization for $\bar{\phi} = 30\%$ and $\rho_p/\rho = 1.2$ with salt water as the suspending liquid. At low Stokes numbers the particles do not exhibit strong radial migration but as Stokes numbers increases the particles begin to move away from the inner test section. However, not all the particles move away. This can be observed by the sharpness of the particles' images.

Figure C.23 shows the flow visualization for $\bar{\phi} = 30\%$ and $\rho_p/\rho = 1.2$ with aqueous glycerine as the suspending liquid. Similar to the case with salt water as the suspending liquid, the particles remain in contact with the test section wall at low Stokes numbers and migrate radially towards the outer cylinder. Unlike the case with salt water, the particles for this case stop touching the test cylinder wall at higher Stokes numbers. This results in a significant decrease of particle interactions because the particles are mainly pushed against the outer cylinder and follow the outer cylinder velocity.

Figure C.24 shows the flow visualization for $\bar{\phi} = 40\%$ and $\rho_p/\rho = 1.2$ with salt water as the suspending liquid. The radial migration of the particles makes the height reach by the particles next to the test section look constant. The way the particles migrate is similar to the one observed for the same parameters but $\bar{\phi} = 30\%$.

The radial migration for the same density ratio but more viscous fluid is significantly larger, as can be observed in Figure C.25. The majority of the particles are pushed against the outer cylinder and fewer particles remained touching the test section at the highest Stokes number.

Figure C.26 and C.27 show the flow visualization for $\bar{\phi} = 50\%$ and $\rho_p/\rho = 1.2$ with salt water and aqueous glycerine as the suspending liquid, respectively. Similar to the results found for this high loading fraction and $\rho_p/\rho = 1.4$, the particles packing seem to decrease with increasing Stokes

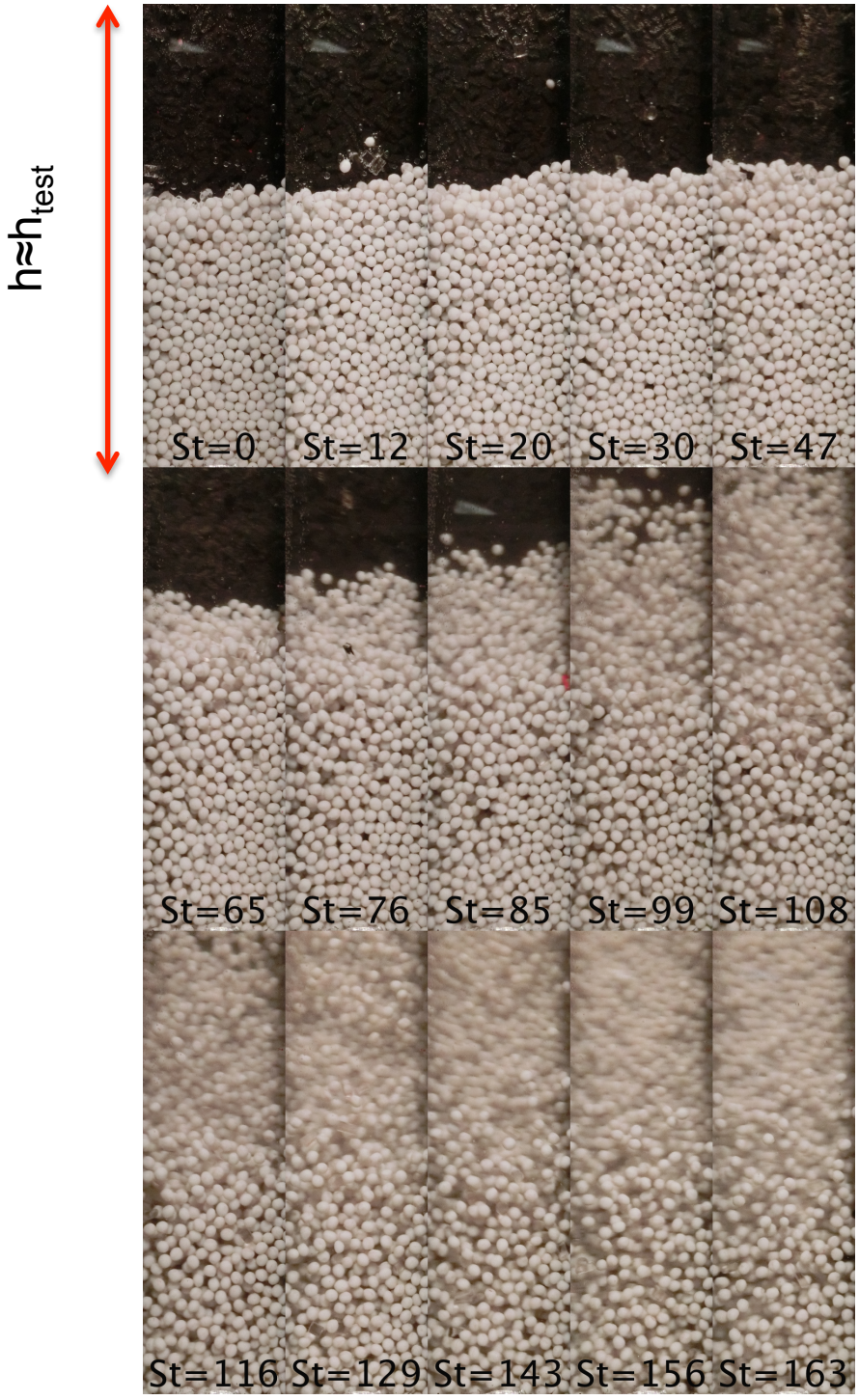

Figure C.18: Image sequence at different Stokes numbers for $\bar{\phi} = 40\%$. The density ratio is 1.4.

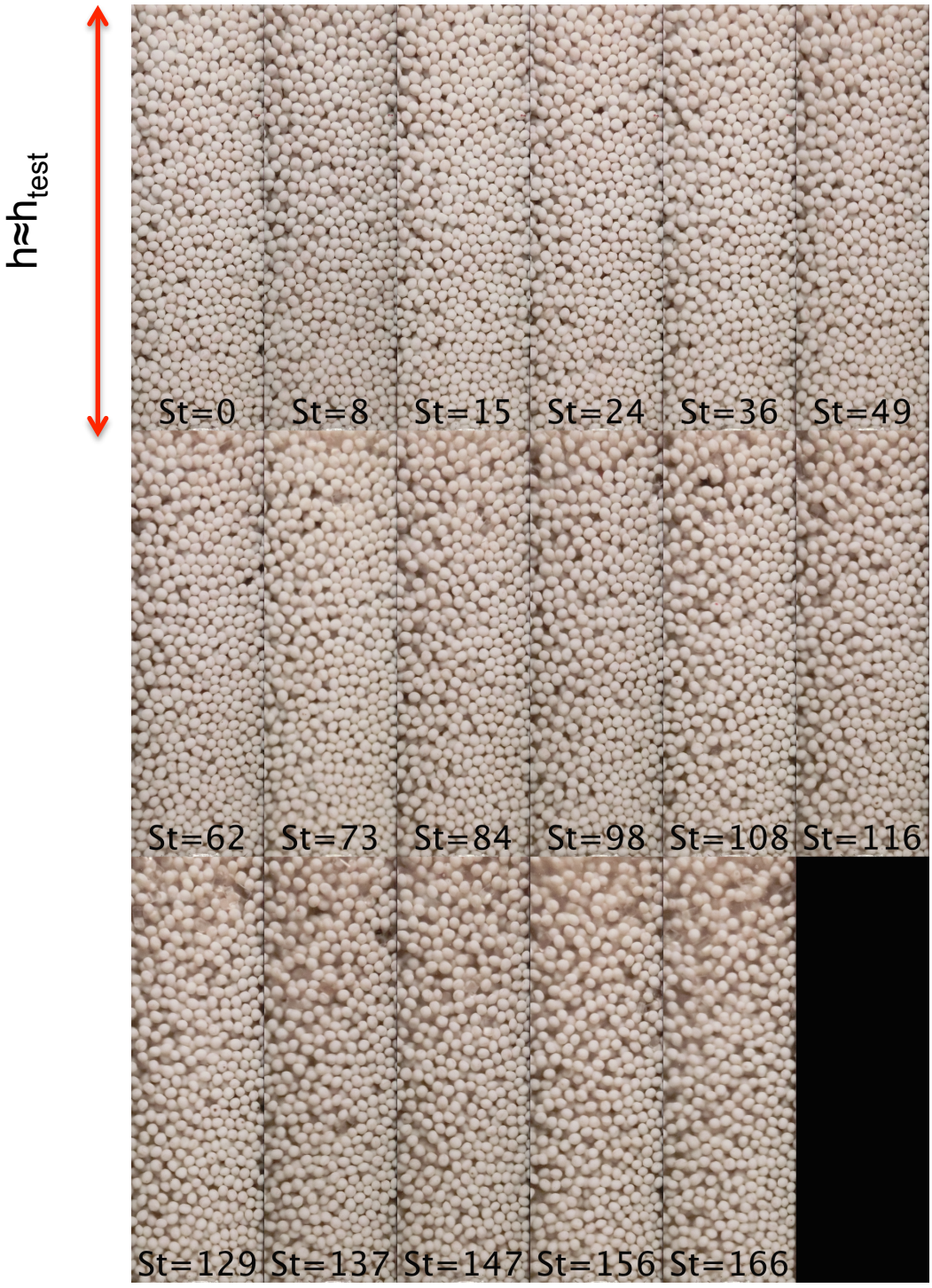

Figure C.19: Image sequence at different Stokes numbers for $\bar{\phi} = 50\%$. The density ratio is 1.4.

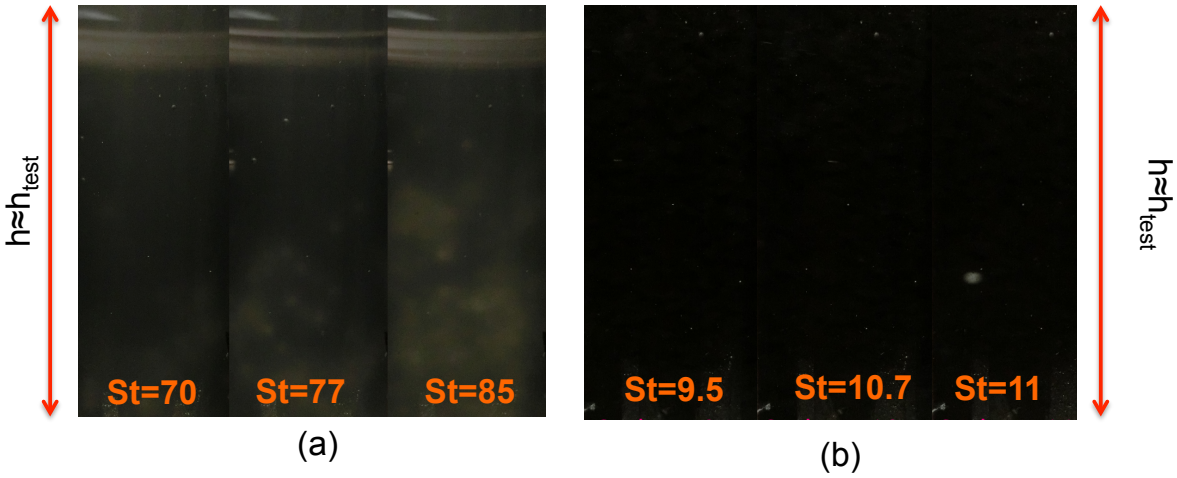

Figure C.20: Image sequence at different Stokes numbers for $\bar{\phi} = 10\%$. The density ratio is 1.2. (a) suspending liquid is salt water and (b) suspending liquid is aqueous glycerine.

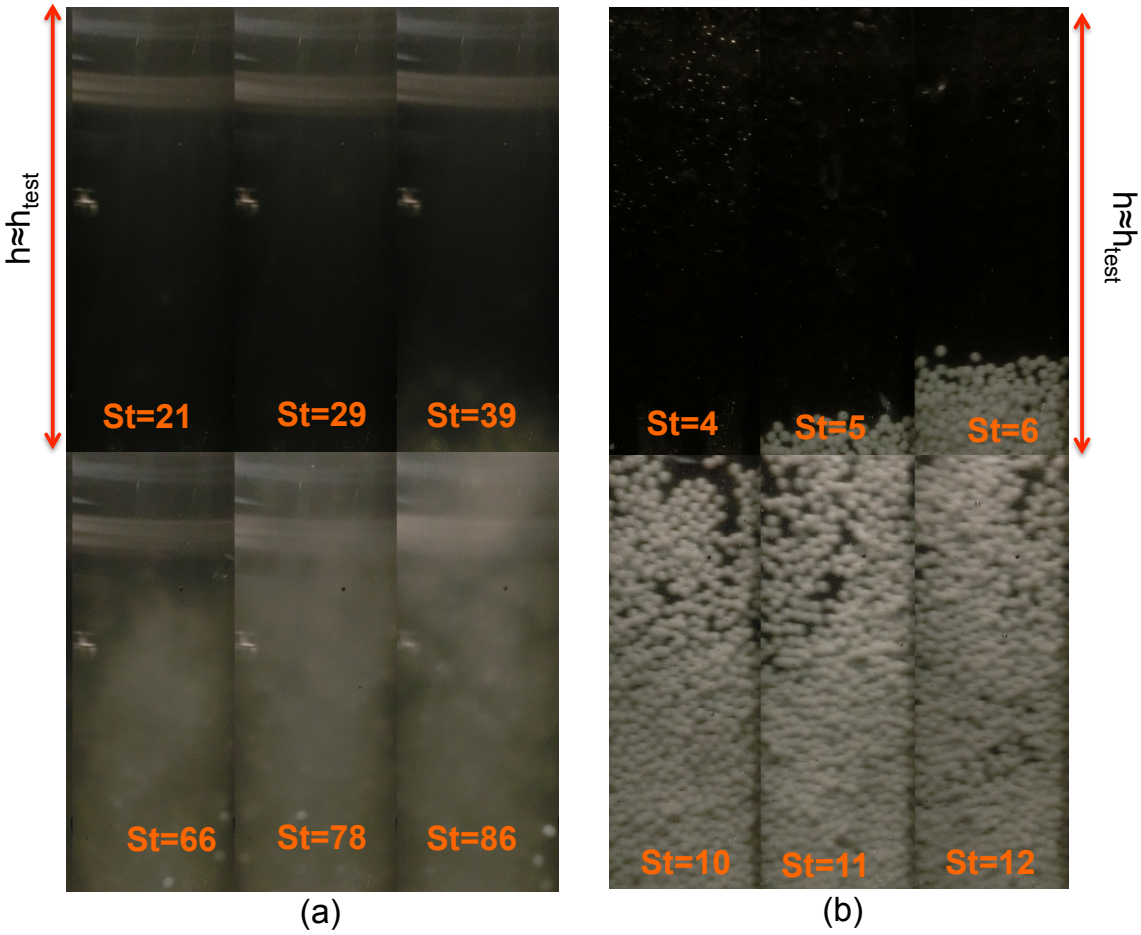

Figure C.21: Image sequence at different Stokes numbers for $\bar{\phi} = 20\%$. The density ratio is 1.2. (a) suspending liquid is salt water and (b) suspending liquid is aqueous glycerine.

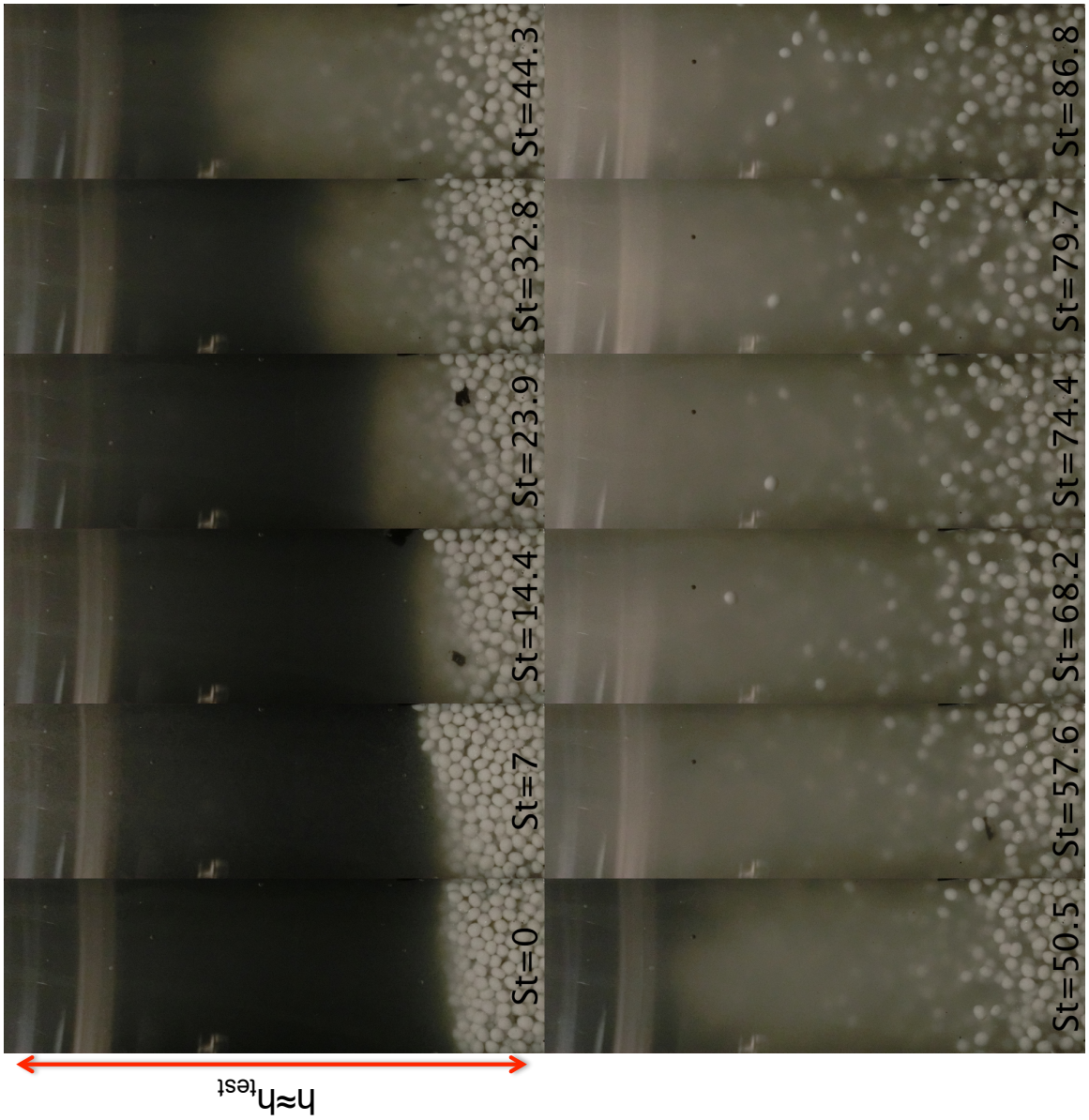

Figure C.22: Image sequence at different Stokes numbers for $\bar{\phi} = 30\%$. The density ratio is 1.2 and the suspending liquid is salt water.

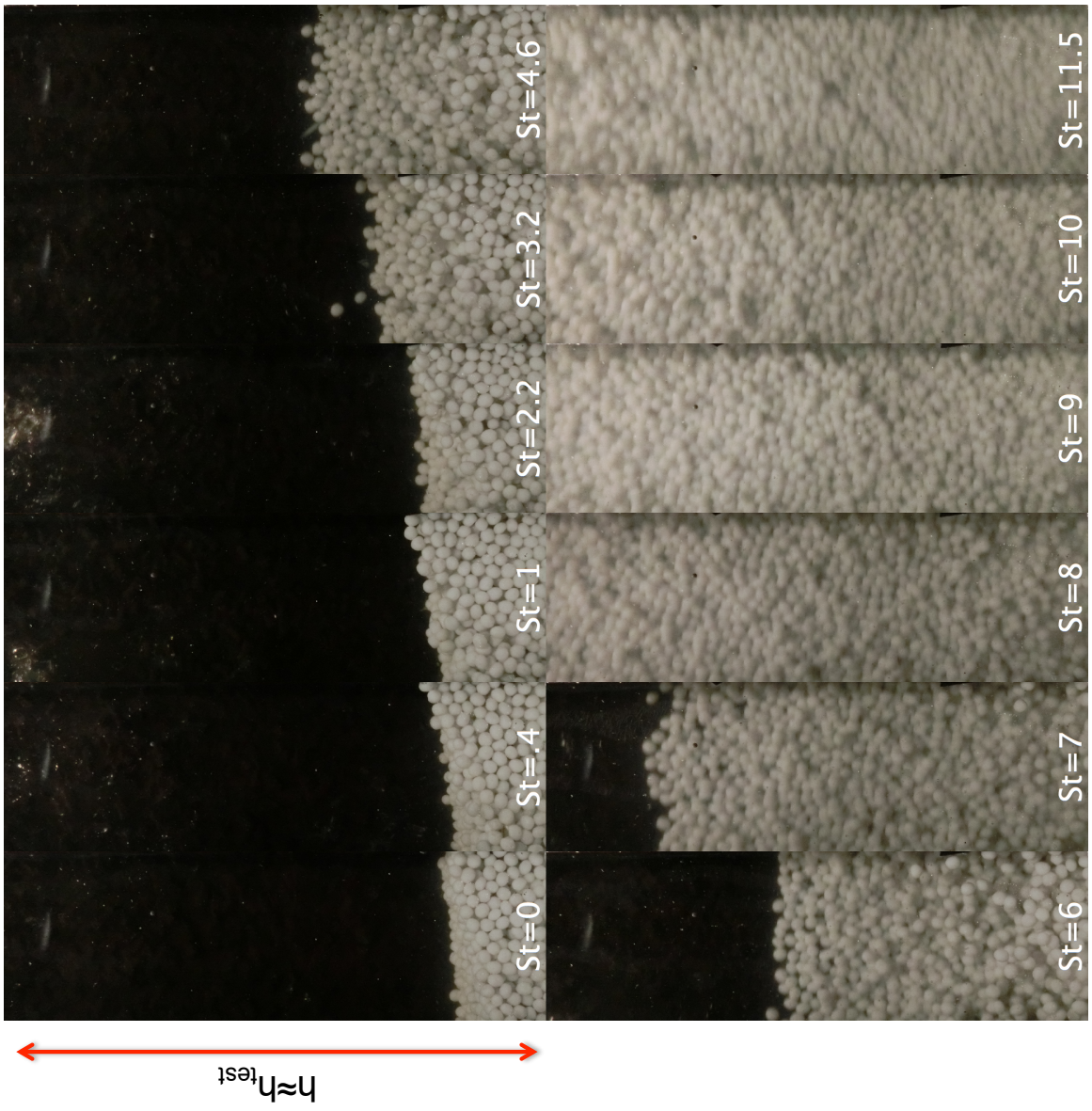

Figure C.23: Image sequence at different Stokes numbers for $\bar{\phi} = 30\%$. The density ratio is 1.2 and the suspending liquid is aqueous glycerine.

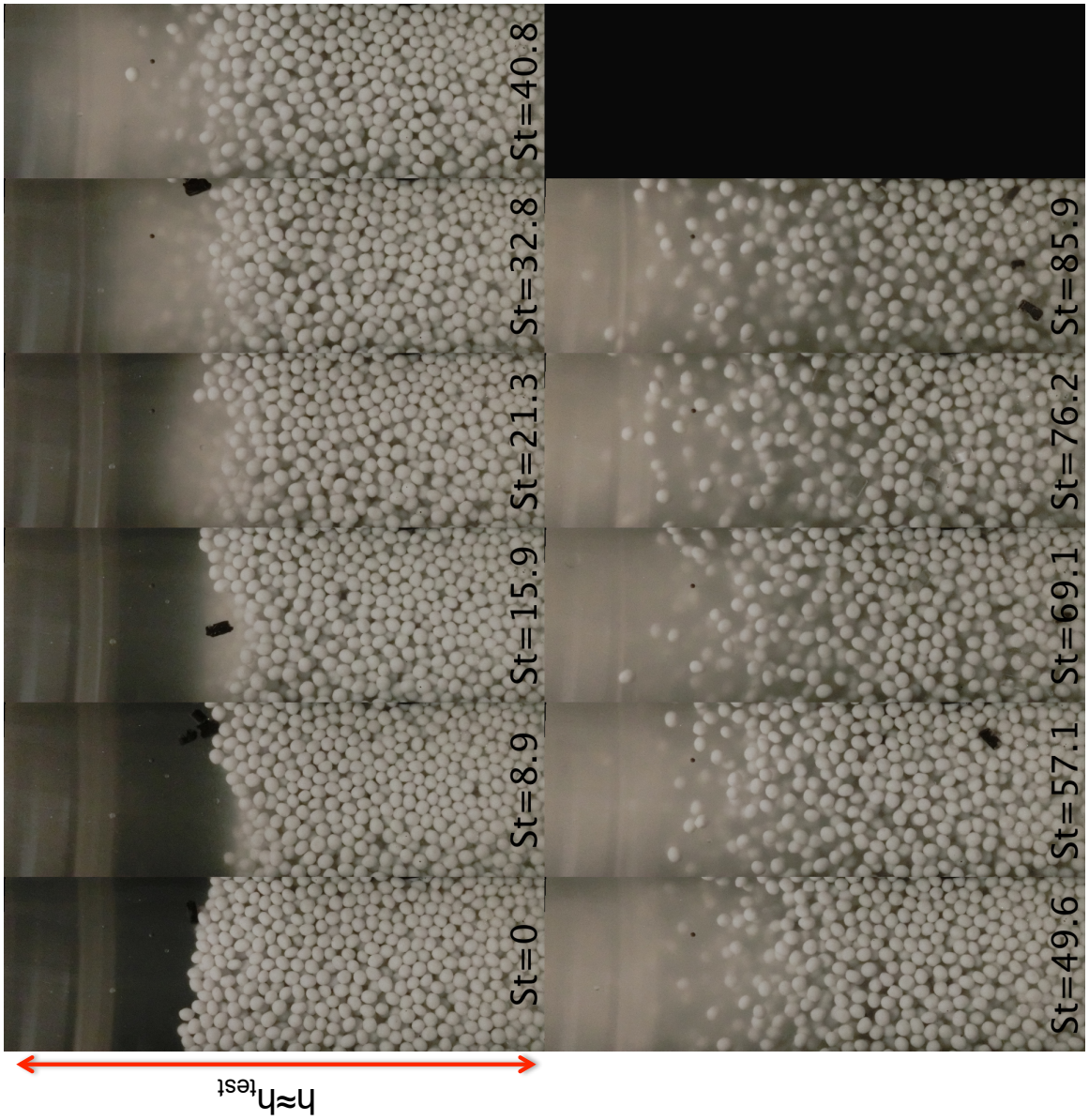

Figure C.24: Image sequence at different Stokes numbers for $\bar{\phi} = 40\%$. The density ratio is 1.2 and the suspending liquid is salt water.

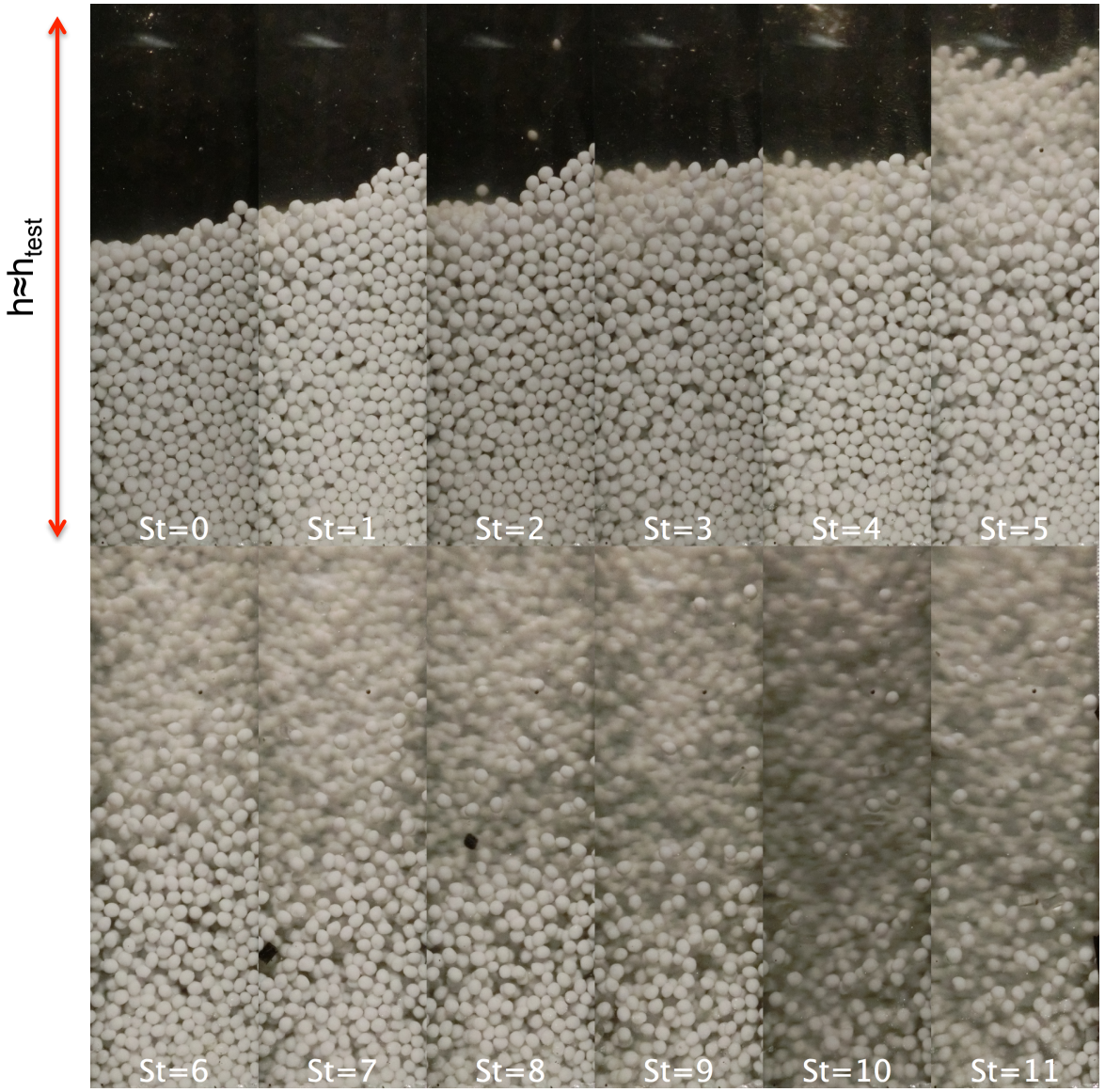

Figure C.25: Image sequence at different Stokes numbers for $\bar{\phi} = 40\%$. The density ratio is 1.2 and the suspending liquid is aqueous glycerine.

numbers and the particles are touching the test section.

C.6 Discussion

Because of the constraint on the visualization window height and the presence of radial migration, it is not possible to determine the effective volume fraction for these liquid-solid flows. What is possible to determine is the lack of particles next to the inner wall for loading fractions of 10 and 20% for the three cases studied. Through the flow visualization is possible to propose some reasons for the measured torque behavior. For the experiments with aqueous glycerine as the suspending liquid, the normalized torques are considerably lower than the normalized torques found for the same density ratio but with a less viscous liquid (salt water). Aside from having lower Stokes numbers and thus lower Reynolds stress, the flow visualization for this case show that the particles radial migration is considerably larger than for the case with salt water. This leads to measurements of pure fluid rather than measurements of the mixture for most of the Stokes numbers tested. This explains in part the lower normalized torques measured for the same density ratio and lower Stokes numbers. There is also the possibility that the experiments with higher Stokes numbers but same density ratio, are affected by hydrodynamic instabilities that increase the measured torques.

For the case with larger density ratio ($\rho_p/\rho = 1.4$) the particles also show a very similar significant radial migration than the one observed for the experiments with aqueous glycerine. The reason for this is not completely clear but one possible reason could be that even when the experiments with lower density ratio would experience lower centripetal forces, the viscosity of the fluid is higher (approximately 13.6 times higher than water) and therefore, the drag force too. Higher drag forces would push the particles towards the outer cylinder if the liquid itself is being pushed towards that direction. The reason why the experiments with salt water do not exhibit a strong radial migration might be because the particles in these experiments experience lower centripetal forces than for the case with $\rho_p/\rho = 1.4$ and the drag force would be less than for the case with the same density ratio but more viscous fluid.

The visualizations for the highest loading fraction of 50% does not show a strong difference in particle concentration and behavior among the three cases studied. However, the normalized torques does not have the same values. The reason for these differences is not clear, although the differences are less pronounced than the differences found for the lower volume fractions. It is possible that the salt water viscosity that was inferred from the work of Dessauges et al. (1980); Mao and Duan (2008) and Mao and Duan (2008) might not be completely accurate.

From the movies of the flow, the particle agitation next to the test section wall for the case with salt water seems to be higher than the one observed for the other two cases ($\rho_p/rho = 1.4$ and water as the suspending liquid, and $\rho_p/\rho = 1.2$ with aqueous glycerine as the suspending liquid).

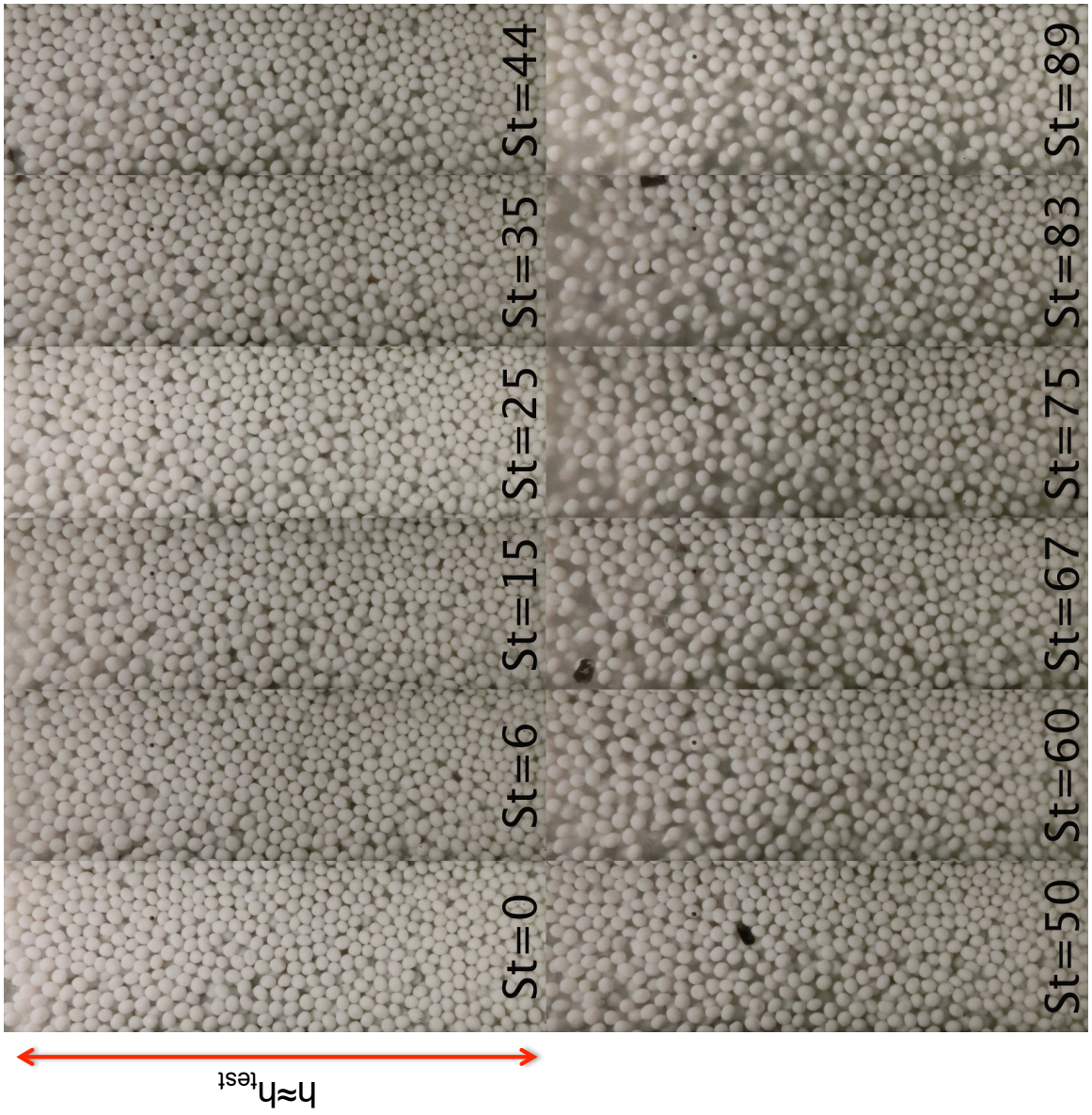

Figure C.26: Image sequence at different Stokes numbers for $\bar{\phi} = 50\%$. The density ratio is 1.2 and the suspending liquid is salt water.

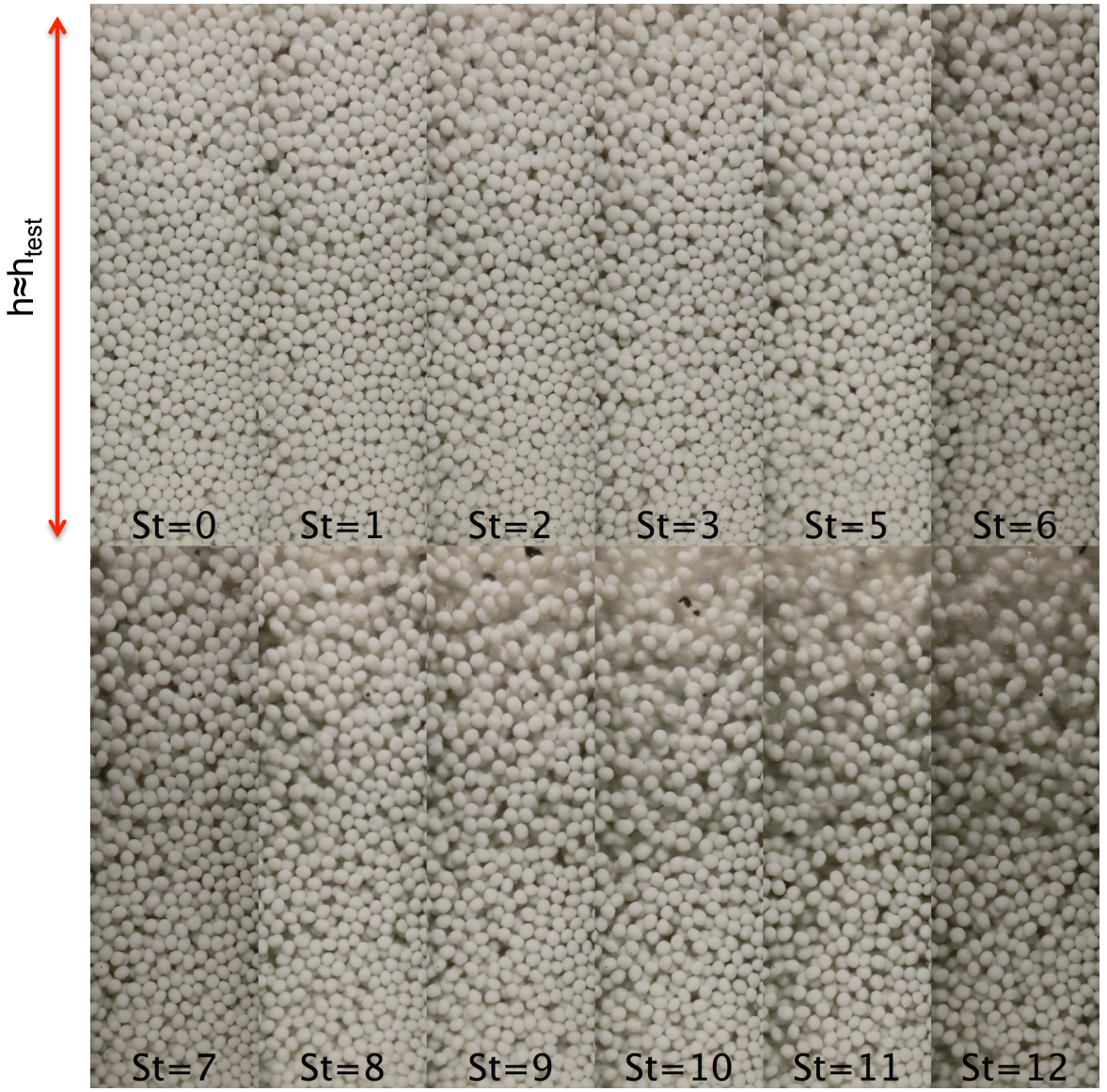

Figure C.27: Image sequence at different Stokes numbers for $\bar{\phi} = 50\%$. The density ratio is 1.2 and the suspending liquid is aqueous glycerine.

This would lead to higher normalized torques not only because of the particle interactions but also because the effective volume fraction is higher. However, the normalized torques for salt water are lower than for the case with $\rho_p/\rho = 1.4$. The reason for this is not clear and it might be an error in the calculation of the salt water viscosity.

Bibliography

B. Abedian and M. Kachanov. On the effective viscosity of suspensions. *International Journal of Ingeneering Science*, 48:962–965, 2010.

A. Acrivos. The rheology of concentrated suspensions of non-colloidal particles. In M. C. Roco, editor, *Particulate Two-Phase Flow*, chapter 5, pages 169–189. Butterworth-Heinemann, Boston, 1992.

A. Acrivos, R. Mauri, and X. Fan. Shear-induced resuspension in a couette device. *International Journal of Multiphase Flow*, 19:797–802, 1993.

A. Acrivos, X. Fan, and R. Mauri. On the measurements of the relative viscosity of suspensions. *Journal of Rheology*, 38(5):1285–1296, 1994.

A. Aguilar-Corona. *Agitation des particules dans un lit fluidise liquide. Etude experimentale.* PhD thesis, Institut National Polytechnique de Toulouse, Toulouse, France, 2008.

D. Andereck, S. S. Liu, and H. L. Swinney. Flow regimes in a circular couette system with independently rotating cylinders. *Journal of Fluid Mechanics*, 164:155–183, 1986.

R. A. Bagnold. Experiments on a gravity-free dispersion of large solid spheres in a Newtonian fluid under shear. *Proceedings of the Royal Society of London, Series A*, 225(1160):49–53, 1954.

H. A. Barnes. Shear-thickening ("dilatancy") in suspensions of nonaggregating solid particles dispersed in newtonian liquids. *Journal of Rheology*, 33:329–366, 1989.

H. A. Barnes. A review of the slip (wall depletion) of polymer solutions, emulsions and particle suspensions in viscometers: its cause, character, and cure. *Journal of Non-Newtonian Fluid Mechanics*, 56(3):221–251, 1995.

H. A. Barnes. Measuring the viscosity of large-particle (and flocculated) suspensions – a note on the necessary gap size of rotational viscometers. *Journal of Non-Newtonian Fluid Mechanics*, 94 (2–3):213–217, 2000.

C. H. Bennett. Serially deposited amorphous aggregates of hard spheres. *Journal of Applied Physics*, 43(6):2727–2734, 1972.

H. Bi and L. S. Fan. Existence of turbulent regime in gas–solid fluidization. *American Institute of Chemical Engineers Journal*, 38(2):297–301, 1992.

C. Bonnoit, T. Darnige, E. Clement, and A. Lindner. Inclined plane rheometry of a dense granular suspension. *Journal of Rheology*, 54:65–79, 2010.

T. Börzsönyi, T. C. Halsey, and R. E. Ecke. Avalanche dynamics on a rough inclined plane. *Physical Review E*, 78(11306), 2008.

F. Boyer, E. Guazzelli, and O. Pouliquen. Unifying suspension and granular rheology. *Physical Review Letters*, 107:188301–5, 2011.

J. F. Brady. Computer simulations of viscous suspensions. *Chemical Engineering Science*, 56:2921–2926, 2001.

J. F. Brady and G. Bossis. Stokesian dynamics. *Annual Review of Fluid Mechanics*, 20:111–157, 1988.

J. F. Brady, A. S. Khair, and M. Swaroop. On the bulk viscosity of suspensions. *Journal of Fluid Mechanics*, 554, 2006.

R. Buscall, I. J. McGowan, and C. A. Mumme-Young. Rheology of weakly interacting colloidal particles at high concentration. *Faraday Special Discussions of the Chemical Society*, 90:115–127, 1990.

R. Buscall, I. J. McGowan, and A. J. Morton-Jones. The rheology of concentrated dispersions of weakly attracting colloidal particles with and without wall slip. *Journal of Rheology*, 37(4): 621–641, 1993.

O. Cadot, Y. Couder, A. Daerr, S. Douady, and A. Tsinober. Energy injection in closed turbulent flows: Stirring through boundary layers versus inerial stirring. *Physical Review E*, 56:427–433, 1997.

C. Cassar, M. Nicolas, and O. Pouliquen. Submarine granular flows down inclined planes. *Physics of Fluids*, 17:103301–11, 2005.

C. Chang and R. L. Powell. Hydrodynamic transport properties of concentrated suspensions. *AIChE Journal*, 48(11):2475–2480, 2002.

X. Chen and M. Louge. Heat transfer enhancement in dense suspensions of agitated solids. part i: Theory,. *Internation Journal of Heat Mass Transfer*, 51(5108), 2008.

Nian-Sheng Cheng and Adrian Wing-Keung Law. Exponential formula for computing effective viscosity. *Powder Technology*, 129(1–3):156–160, 1 2003.

A. Chrzanowska, P. I. C. Teixeira, H. Ehrentraut, and D. J. Cleaver. Ordering of hard particles between hard walls. *Journal of Physics: Condensed Matter*, 13:4715–4726, 2001.

B. Clarke. Rheology of coarse settling suspensions. *Transactions of the Institution of Chemical Engineers and the Chemical Engineer*, 45(6), 1967.

D. Coles. Transition in circular Couette flow. *Journal of Fluid Mechanics*, 21:385–424, 1965.

S. L. Conway, T. Shinbrot, and B. J. Glasser. A Taylor vortex analogy in granular flows. *Nature*, 431:433–437, 2004.

P. Coussot and C. Ancey. Rheophysical classification of concentrated suspensions and granular pastes. *Physical Review E*, 59(4):4445–4457, 1999.

R. H. Davis, J. M. Serayssol, and E. J. Hinch. The elastohydrodynamic collision of two spheres. *Journal of Fluid Mechanics*, 163, 1986.

J. C. Van der Werff and C. G. de Kruif. Hard-sphere colloidal dispersions: the scaling of rheological properties with particle size, volume fraction and shear rate. *Journal of Rheology*, 33:421–454, 1989.

G. Dessauges, N. Mlljevic, and W. A. Van Hook. Isotope effects in aqueous systems. 9. Partial molar volumes of NaC/H_2O and $NaCl/D_2O$ solutions at 15, 30 and 45 $^\circ C$. *Journal of Physical Chemestry*, 84:2587–2595, 1980.

J. A. Dijksmann, E. Wandersmann, S. Slotterback, C. R. Berardi, W. D. Updegraff, M. van Hecke, and W. Losert. From frictional to viscous behavior: Three-dimensional imaging and rheology of gravitational suspensions. *Physical Review E*, 82:60301–4, 2010.

H. Egger and K. M. McGrath. Estimating depletion layer thickness in colloidal systems: correlation with oil-in-water emulsion coposition. *Colloids and Surfaces A: Physiochemical Engineering Aspects*, 275:107–113, 2006.

A. Einstein. On the theory of Brownian motion. *Annalen der Physik*, 19(4):371–381, 1906.

A. Fall, F. Bertrand, G. Ovarlez, and D. Bonn. Yield stress and shear banding in granular suspensions. *Physical Review Letters*, 103:178301–4, 2009.

J. L. Finney. Random packings and the structure of simple liquids: I. The geometry of random close packing. *Proceedings of the Royal Society of London, Series A*, 319(1539):5746–5746, 1970.

Y. Forterre and O. Pouliquen. Flows of dense granular media. *Annual Review of Fluid Mechanics*, 40:1–24, 2008.

N. A. Frankel and A. Acrivos. On the viscosity of a concentrated suspension of solid spheres. *Chemical Engineering Science*, 22:847–853, 1967.

F. A. Gadala-Maria and A. Acrivos. Shear-induced structure in a concentrated suspension of solid spheres. *Journal of Rheology*, 24:799–814, 1980.

R. A. Gore and C. T. Crowe. Modulation of turbulence by a dispersed phase. *Journal of Fluids Engineering*, 113(2):304–307, 1991.

S. A. Gulmus and U. Yilmazer. Effect of the surface roughness and construction material on wall slip in the flow of concentrated suspensions. *Journal of Applied Polymer Science*, 103(5):3341–3347, 2007.

H. Haddadi and J. F. Morris. Microstructure and rheology of finite inertia neutrally buoyant suspensions. *Journal Fluid Mechanics*, 749:431–459, 2014.

D. M. Hanes and D. L. Inman. Observations of rapidly flowing granular-fluid materials. *Journal of Fluid Mechanics*, 150:357–380, 1985.

D. P. Haughey and G. S. G. Beveridge. Local voidage variation in a randomly packed bed of equal-sized spheres. *Chemical Engineering Science*, 21(10):905–916, 1966.

L. Heymann, S. Peukert, and N. Aksel. On the solid-liquid transition of concentrated suspensions in transient shear flow. *Rheologica Acta*, 41:307–315, 2002.

R. L. Hoffmann. Discontinuos and dilatant viscosity behavior in concentratred suspensions. 1. observation of a flow instability. *Transactions of the Society of Rheology*, 16(1):155–173, 1972.

A. C. Hoffmnn and J. Kevelam. Model for the interparticle surface separation in concentrated mono- and polydisperse suspensions. *AIChE Journal*, 45:285–290, 1999.

N. Huang, G. Ovarlez, F. Bertrand, P. Coussot, and D. Bonn. Flow of wet granular materials. *Physical Review Letters*, 94(2):8301, 2005.

M. L. Hunt, R. Zenit, C. S. Campbell, and C. E. Brennen. Revisiting the 1954 suspension experiments of R.A. Bagnold. *Journal of Fluid Mechanics*, 452:1–24, 2002.

D. J. Jeffrey and A. Acrivos. The rheological properties of suspensions of rigid particles. *American Institute of Chemical Engineers Journal*, 22(3):417–433, 1976.

G. G. Joseph and M. L. Hunt. Oblique particle-wall collisions in a liquid. *Journal of Fluid Mechanics*, 510:71–93, 2004.

G. G. Joseph, R. Zenit, M. L. Hunt, and A. M. Rosenwinkel. Particle-wall collisions in a viscous fluid. *Journal of Fluid Mechanics*, 433:329–346, 2001.

R. P. King. *Introduction to practical fluid flow*. Butterworth-Heinemann, 2001.

E. Koos. *Rheological Measurements in Liquid-Solid Flows*. PhD thesis, California Institute of Technology, 2009.

E. Koos, E. Linares-Guerrero, M. L. Hunt, and C. E. Brennen. Rheological measurements of large particles in high shear rate flows. *Physics of Fluids*, 24(013302):1–19, January 2012.

I. M. Krieger and T. J. Dougherty. A mechanism for non-Newtonian flow in suspensions of rigid spheres. *Transactions of the Socieity of Rheology*, 3:137–152, 1959.

P. M. Kulkarni and J. F. Morris. Suspension properties at finite reynolds number from simulated shear flow. *Physics of Fluids*, 20:40602–12, 2008.

A. J. C. Ladd. Numerical simulations of particulate suspesions via a discretized boltzmann-equation. 1. theoretical results. *Journal of Fluid Mechanics*, 271:285–309, 1994.

S. H. Lee, H. T. Chung, C. W. Park, and H. B. Kim. Experimental investigation of the effect of axial wall slits on taylor-couette flow. *Fluid Dynamics Research*, 41, 2009.

E. J. LeFevre. Hard-sphere fluid. *Journal of Chemical Physics*, 59(10):497–493, 1973.

D. Leighton and A. Acrivos. Viscous resuspension. *Chemical Engineering Science*, 41:1377–1384, 1986.

D. Leighton and A. Acrivos. Measurement of shear-induced self-diffusion in concentrated suspensions of spheres. *Journal of Fluid Mechanics*, 177:109–131, 1987a.

D. Leighton and A. Acrivos. The shear-induced migration of particles in concentrated suspensions. *Journal of Fluid Mechanics*, 181:415–439, 1987b.

M. H. MacLaughlin. *An experimental study of particle-wall collision relating to flow of solid particles in a fluid*. PhD thesis, California Institute of Technology, 1968.

S. Mao and Z. Duan. The P, V, T, x properties of binary aqueous chloride solutions up to T=573 K and 100MPa. *Journal of Chemical Thermodynamics*, 40:1046–1063, 2008.

S. Mao and Z. Duan. The viscosity of aqueous alkali-chloride solutions up to 623 K, 1000 bar and high ionic strength. *International Journal of Thermophysics*, 30:1510–1523, 2009.

S. H. Maron and P. E. Pierce. Application of ree-eyring generalized flow theory to suspension of spherical particles. ii. flow in low shear region. *Journal of Colloid Science*, 11:80–95, 1956.

J. P. Matas, J. F. Morris, and É. Guazzelli. Transition to turbulence in particulate pipe flow. *Physical Review Letters*, 90(1):4501–4504, 2003.

M. Mooney. The viscosity of a concentrated suspension of spherical particles. *Journal of Colloid Science*, 6:162–170, 1951.

C. Moreland. Viscosity of suspension of coal in mineral oil. *Can. J. Chem. Eng.*, 41:24–28, 1963.

S. Mueller, E. W. Llewellin, and H. M. Mader. The rheology of suspensions in solid particles. *Proceedings of the Royal Society of London, Series A*, 466:1201–1228, 2010.

T. Mullin and T. B. Benjamin. Transition to oscillatory motion in the taylor experiment. *Nature*, 288:567–569, 1980.

C. S. O'Hern, S. A. Langer, A. J. Liu, and S. R. Nagel. Random packings of frictionless particles. *Physical Review Letters*, 88(7):5507–5510, 2002.

G. Ovarlez, F. Bertrand, and S. Rodts. Local determination of the constitutive law of a dense suspension of noncolloidal particles through magnetic resonance imaging. *Journal of Rheology*, 50 (3):259 – 292, 2006.

W. Pabst. Fundamental considerations on suspension rheology. *Ceramics-Silikaty*, 48:6–13, 2004.

W. Pabst, E. Gregorová, and C. Berthold. Particle shape and suspension rheology of short-fiber systems. *Journal of the European Ceramic Society*, 26(1–2):149 – 160, 2006.

S. J. Partridge. *The rheology of cohesive sediments*. PhD thesis, University of Bristol, 1985.

F. Picano, W. P. Breugem, D. Mitra, and L. Brandt. Shear thickening in non-newtonian suspensions: An excluded volume effect. *Physical Review Letters*, 111:98302–4, 2013.

D. Prasad and H. K. Kytömaa. Particle stress and viscous compaction during shear of dense suspensions. *International Journal of Multiphase Flow*, 21(5):775–785, 1995.

R. F. Probstein, M. Z. Sengun, and T. C. Tseng. Bimodal model of concentrated suspension viscosity for distributed particle sizes. *Journal of Rheology*, 38(4), 1994.

D. Quemada. Rheology of concentrated disperse systems and minimum enegy dissipation principle. *Rheologica Acta*, 6:82–94, 1977.

W. B. Russel and M. C. Gran. istinguishing between dynamic yielding and wall slip in a weakly flocculated colloidal dispersion. *Colloids Surf. A: Physiochemical Eng. Aspects*, 171:2000, 2000.

R. Rutgers. Relative viscosity of suspensions of rigid spheres in Newtonian liquids. *Rheologica Acta*, 2(3):202–210, 1962.

S. B. Savage and S. McKeown. Shear stresses developed during rapid shear of concentrated suspensions of large spherical particles between concentric cylinders. *Journal of Fluid Mechanics*, 127: 453–472, 1983.

H. Schlichting. *Boundary Layer Theory.* McGraw Hill, New York, 7^{th} edition, 1951.

G. D. Scott. Packing of spheres: Packing of equal spheres. *Nature*, 188:908–909, 1960.

G. D. Scott and D. M. Kilgour. The density of random close packing of spheres. *Journal of Physics D: Applied Physics*, 2(2):863–866, 1969.

A. Shapiro and R. Probstein. Random packings of spheres and fluidity limits of monodisperse and bidisperse suspensions. *Physical Review Letters*, Jan 1992.

A. Sierou and J. F. Brady. Rheology and microstructure in concentrted noncolloidal suspension. *Journal of Rheology*, 46:1031–1056, 2002.

F. Soltani and U. Yilmazer. Slip velocity and slip layer thickness in flow of concentrated suspensions. *Journal of Applied Polymer Science*, 70(3):515–522, 1998.

J. J. Stickel and R. L. Powell. Fluid mechanics and rheology of dense suspensions. *Annual Review of Fluid Mechanics*, 37(1):129–149, 2005.

G. I. Taylor. Fluid friction between rotating cylinders, I. Torque measurements. *Proceedings of the Royal Society of London, Series A*, 157(892):546–564, 1936a.

G. I. Taylor. Fluid friction between rotating cylinders, II. Distribution of velocity between concentric cylinders when outer one is rotating and inner one is at rest. *Proceedings of the Royal Society of London, Series A*, 157(892):565–578, 1936b.

D. G. Thomas. Transport characteristics of suspensions: Viii. a note on the viscosity of newtonian suspensions of uniform spherical particles. *Journal of Colloid Science*, 20:267–277, 1965.

S. Torquato, T. M. Truskett, and P. G. Debenedetti. Is random close packing of spheres well defined? *Physical Review Letters*, 84(10):2064–2067, 2000.

M. Trulsson, B. Andreotti, and P. Claudin. Transition from the viscous to inertial regime in dense suspensions. *Physical Review Letters*, 109:118305(5), 2012.

J.-C. Tsai and J. P. Gollub. Slowly sheared dense granular flows: Crystallization and nonunique final states. *Phys. Rev. E*, 70:031303, Sep 2004.

T. H. van den Berg, C. R. Doering, D. Lohse, and D. Lathrop. Smooth and rough boundaries in turbulent taylor-couette flow. *Physical Review E*, 68(036307), 2003.

V. Vand. Viscosity of solutions and suspensions. i theory. *Journal of Physical and Colloid Chemestry*, 52:277–299, 1948.

J. Wallner and U. Schaflinger. Viscous resuspension of a sediment caused by oscillating stratified flows. *Acta Mechanica*, 127:147–153, 1998.

S. G. Ward and R. L. Whitmore. Studies of the viscosity and sedimentation of suspensions. 1. the viscosity of suspension of spherical particles. *British Journal of Applied Physics*, 1:286–290, 1950.

F. Wendt. Turbulente strömungen zwischen zwei rotierenden konaxialen zylindern. *Ingenieur Archiv*, 4:577–595, 1933.

F. L. Yang and M. L. Hunt. Dynamics of particle-particle collisions in a viscous liquid. *Physics of Fluids*, 18, 2006.

K. Yeo and M. R. Maxey. Dynamics and rheology of concentrated, finite-reynolds- number suspensions in a homogeneous shear flow. *Physics of Fluids*, 25:533303–24, 2013.

U. Yilmazer and D. M. Kalyon. Slip effects in capillary and parallel disk torsional flows of highly filled suspensions. *Journal of Rheology*, 33(8):1197–1212, 1989.

I. E. Zarraga, D. A. Hill, and Jr. D. T. Leighton. The characterization of the total stress of concentrated suspensions of noncolloidal spheres in newtonian fluids. *Journal of Rheology*, 44(2), 1999.

G. Zeininger and C. E. Brennen. Interstitial fluid effects in hopper flows of granular materials. Technical report, ASME. Cavitation and Multiphase flow forum, New York, 1985.

R. Zenit, M. L. Hunt, and C. E. Brennen. Collision particle pressure measurements in solid-liquid flows. *Journal of Fluid Mechanics*, 353:261–283, 1997.

R. P. Zou and A. B. Yu. Evaluation of the packing characteristics of mono-sized non-spherical particles. *Powder Technology*, 88(1):71–79, 1996.